Dipl.-Ing. Nicolas Coniglio

Aluminum Alloy Weldability: Identification of Weld Solidification Cracking Mechanisms through Novel Experimental Technique and Model Development

BAM-Dissertationsreihe • Band 40
Berlin 2008

Die vorliegende Arbeit entstand an der BAM Bundesanstalt für Materialforschung und -prüfung.

Impressum

Aluminum Alloy Weldability:
Identification of Weld Solidification Cracking Mechanisms
through Novel Experimental Technique and Model Development

2008

Herausgeber:
BAM Bundesanstalt für Materialforschung und -prüfung
Unter den Eichen 87
12205 Berlin
Telefon: +49 30 8104-0
Telefax: +49 30 8112029
E-Mail: info@bam.de
Internet: www.bam.de

Layout: BAM-Arbeitsgruppe Z.64

ISSN 1613-4249
ISBN 978-3-9812354-3-2

Aluminum Alloy Weldability: Identification of Weld Solidification Cracking Mechanisms through Novel Experimental Technique and Model Development

Dissertation zur Erlangung des akademischen Grades

Doktor-Ingenieur
(Dr.-Ing.)

genehmigt durch die Fakultät für Maschinenbau
der Otto-von-Guericke-Universität Madgeburg

am 02.06.08 vorgelegte Dissertation

von Dipl.-Ing. Nicolas Coniglio

Thesis Committee: Prof. Dr.-Ing. A. Bertram
Prof. Dr.-Ing. T. Böllinghaus
Prof. C.E. Cross
Prof. S. Marya

Date of Examination: 23 October 2008

Abstract

The objective of the present thesis is to make advancements in understanding solidification crack formation in aluminum welds, by investigating in particular the aluminum 6060/4043 system. Alloy 6060 is typical of a family of Al-Mg-Si extrusion alloys, which are considered weldable only when using an appropriate filler alloy such as 4043 (Al-5Si). The effect of 4043 filler dilution (i.e. weld metal silicon content) on *cracking sensitivity* and *solidification path* of Alloy 6060 welds are investigated. Afterwards, *cracking models* are developed to propose mechanisms for solidification crack initiation and growth.

Cracking Sensitivity. Building upon the concept that silicon improves weldability and that weldability can be defined by a critical strain rate, strain rate-composition combinations required for solidification crack formation in the Al- 6060/4043 system were determined using the newly developed Controlled Tensile Weldability (CTW) test utilizing local strain extensometer measurements. Results, presented in a critical strain rate – dilution map, show a crack – no crack boundary which reveals that higher local strain rates require higher 4043 filler dilution to avoid solidification cracking when arc welding Alloy 6060. Using the established crack - no crack boundary as a line of reference, additional parameters were examined and their influence on cracking characterized. These parameter influences have included studies of weld travel speed, weld pool contaminants (Fe, O, and H), and grain refiner additions ($TiAl_3$ + Boron). Each parameter has been independently varied and its effect on cracking susceptibility quantified in terms of strain rate – composition combinations.

Solidification Path. Solidification path of the Al-6060/4043 system was characterized using thermal analysis and phase identification. Increasing 4043 filler dilution from 0 to 16% in Alloy 6060 arc welds resulted in little effect on thermal arrests and microstructure, no effect on solidification range, refinement in grain size from 63 to 51 μm, centerline columnar grains disappearance, and decreased cooling rate from 113 to 89 ℃/s. Moreover, in order to make direct comparison with literature, castings of controlled mixtures of alloys 6060 and 4043 were also investigated, thereby simulating weld metal composition under controlled cooling conditions. Castings showed a different trend than welds with small increases in silicon content (i.e. increase in 4043 filler dilution) resulting in huge effect on microstructure, no effect on liquidus temperature, drop in solidus temperature from 577℃ to 509℃, increase in quantity of interdendritic constituent from 2% to 14%, and different phase formation. Binary β-Al_5FeSi, Mg_2Si, and Si phases are replaced with ternary β-Al_5FeSi, π–$Al_8FeMg_3Si_6$, and a

low melting quaternary eutectic involving Mg_2Si, π, and Si. Also, variation of the cooling conditions in castings revealed the existence of a critical cooling rate, above which the solidification path and microstructure undergo a major change.

Cracking Model. Implementing the critical conditions for cracking into the Rappaz-Drezet-Gremaud (RDG) model revealed a pressure drop in the interdendritic liquid on the order of 10^{-1} atm, originating primarily from straining conditions. Since, according to literature, a minimum of 1,760 atm is required to fracture pure aluminum liquid (theoretical), this demonstrates that cavitation as a liquid fracture mechanism is not likely to occur, even when accounting for dissolved hydrogen gas. Instead, a porosity-based crack initiation model has been developed based upon pore stability criteria, assuming that gas pores expand from pre-existing nuclei. Crack initiation is taken to occur when stable pores form within the coherent dendrite region, critical to crack initiation being weld metal hydrogen content. Following initiation, a mass-balance approach developed by Braccini et al. (2000) revealed that crack growth is controlled by local strain rate conditions. Finally, a simplified strain partition model provides a link between critical strain rates measured across the weld and predicted at grain boundaries within the mushy zone. Although based on simplified assumptions, predicted and measured critical strain rate values are of the same order of magnitude. However, because of a longer mushy zone experienced at higher 4043 filler dilution related to a reduction in cooling rate, these models predict a lower weldability with increasing filler dilution, in contradiction with experimental observations. Combining the crack initiation and growth models suggests that hydrogen and strain rate, respectively, determine crack formation. An hypothetical hydrogen – strain rate map defines conceptually the conditions for cracking, suggesting better weldability at low weld metal hydrogen content. With the aid of the modified varestraint test (MVT) and a controlled hydrogen contamination system, results, presented in the form of ram speed – hydrogen map, revealed that hydrogen has little effect on crack growth, providing support to the proposed cracking models. However, a drop in weldability corresponding to the peak in weld metal hydrogen supersaturation suggests a different solidification cracking mechanism, where cavitation supports crack growth.

Acknowledgements

The present work was funded by and carried out at the Bundesanstalt für Materialforschung und –prüfung (BAM) laboratory in Berlin, Germany, during the 2005-2008 time frame.

I am grateful to Prof. C.E. Cross for having directed my thesis research. I am also grateful to Prof. Dr.-Ing. H. Herold and Dipl.-Ing. M. Streitenberger for my enrolment in the doctoral thesis program at the Institute for Materials and Joining Technology, Otto-von-Guericke-Universität Magdeburg, and to Prof. Dr.-Ing. T. Böllinghaus for the organization of the thesis defense.

I am grateful to BAM for internal support of this project, and specifically wish to thank R. Breu, P. Friedersdorf, A. Hannemann, C. Hesse-Andres, F. Köhler, M. Lammers, M. Marten, T. Michael, M. Richter, K. Scheideck, K. Schlechter, W. Österle, G. Nolze, I. Dörfel, R. Neumann, and H.-J. Malitte. Also, material donated by Outokumpu Stainless and Metallurg London was greatly appreciated.

I thank A. Cichon for the logistical support.

I thank the thesis committee, Prof. Dr.-Ing. A. Bertram, Prof. Dr.-Ing. T. Böllinghaus, Prof. C.E. Cross, and Prof. S. Marya, for evaluating the thesis manuscript.

Finally, this thesis is dedicated to Siegfried and Sonia Ramaut, my sister Charlène, my mother Evelyne, and my grand-mother Anna, to thank them for their support during all these years.

Table of Contents

1 Introduction

1.1 Aluminum Alloy Applications

Aluminum is one of the most abundant elements, constituting around 8 wt.% of the Earth's crust, and is second after steel among economically important metals. Strangely, even though copper, lead and tin were used for thousands of years, aluminum was only discovered in 1808 by Sir Humphrey Davy (Britain). This metal became economically interesting for engineering applications in 1886 with the discovery of industrial processes for the electrolytic reduction of alumina (Al_2O_3) into aluminum, independently developed by the American chemist Charles Martin Hall and the Frenchman Paul Héroult. The fascination exerted by aluminum at this time is well illustrated by a quote of Jules Vernes taken from "From the Earth to the Moon" (1865):

"This valuable metal possesses the whiteness of silver, the indestructibility of gold, the tenacity of iron, the fusibility of copper, the lightness of glass. It is easily wrought, is very widely distributed, forming the base of most of the rocks, is three times lighter than iron, and seems to have been created for the express purpose of furnishing us with the material for our projectile."

Indeed, aluminum has a remarkable combination of qualities that includes low density (one-third the density of steel), high ductility, high thermal and electrical conductivity, good corrosion resistance, attractive appearance, and non-toxicity. These reasons make aluminum widely used in transport and construction applications, for example to lighten vehicle structures for fuel-efficient engines in cars and trucks as well as for high speed rail and sea travel. In particular, aluminum alloys are used in automotive engineering applications in welded structures, even if these alloys are highly susceptible to a defect variously referred to as hot cracking, hot tearing, hot shortness, super-solidus cracking, solidification cracking, liquation cracking, or shrinkage brittleness. This major defect occurs above the solidus temperature, either upon solidification (solidification cracking) or upon remelting (liquation cracking). Its presence reduces the mechanical properties and is responsible of costly lost of defect materials. In particular, high-strength aerospace aluminum alloys, e.g. Alloys 7075 and 2024, are used in spacecraft structures, but are so highly susceptible to solidification cracking (Figure 1) that welding these alloys may simply be not allowed. Therefore, great research effort is expended to improve the weldability of aluminum alloys because i) these alloys are of competition with high strength steels

possessing better weldability, and ii) friction stir welding, a new solid-state joining process, can be used in particular to join aluminum alloys hardly weldable by conventional fusion welding, e.g. Alloys 7075 and 2024 [2].

1.2 Al-Mg-Si Alloy System

Even though a significant research effort has been especially expended over the last decades on predicting solidification crack formation, the mechanisms involved for its initiation and growth are today still not well understood. The present work aims to contribute to the research effort by focusing on the Al- 6060/4043 alloy system.

Alloy 6060 is typical of a family of Al-Mg-Si extrusion alloys, which are widely used in fabricated structures because of their good corrosion resistance, moderate strength, and good weldability, provided that an appropriate filler alloy is used. When welded autogenously, these alloys have been found highly susceptible to solidification cracking (Figure 2) [1,3-5]. Nevertheless, typical welding filler metals, such as Alloy 4043 (Al-5Si) or Alloy 5356 (Al-5Mg), shift the weld pool composition to an alloy regime that is less crack sensitive [6]. Normally, Alloy 5356 is selected for higher strength, whereas 4043 is selected for improved cracking resistance. However, the reason behind the important improvement in weldability when using 4043 (Figure 1) remains unclear.

Although it is well established that use of an appropriate filler metal improves weldability, the amount of filler dilution required to avoid cracking has never been a well defined quantity. Curiously, this has never been considered an important issue to industry, perhaps because standard welding practice routinely results in sufficient filler dilution to avoid cracking. This would particularly be true for gas-metal arc welding, where high filler dilution (30-60%) is common.

1.3 Objectives and Methodology

In the present thesis, the influence of weld metal silicon content (e.g. 4043 filler dilution) on Alloy 6060 weldability is investigated and mechanisms for solidification crack formation in aluminum welds are proposed. This work is planned in five stages:

Stage 1: Controlled Tensile Weldability (CTW) Test Development. A testing procedure was developed to characterize aluminum alloy weldability by means of the newly developed CTW test, utilizing local strain extensometer measurements.

Stage 2: Characterization of Al-6060/4043 Weldability. Making use of the CTW test, strain rate – composition combinations have been determined for solidification crack formation in Alloy 6060 arc welds. Results, presented in a critical strain rate – dilution map, define the critical amount of 4043 filler required to avoid solidification cracking when arc welding Alloy 6060, depending upon local strain rate. The influence of additional parameters, such as weld travel speed, weld pool contaminants (Fe, O, and H), and grain refiner additions ($TiAl_3$ + Boron), was characterized. Each parameter has been independently varied and its effect on cracking susceptibility quantified in terms of strain rate – composition combinations.

Stage 3: Characterization of Al-6060/4043 Solidification Path. With the aid of thermal analysis and phase identification, the solidification path was characterized for both 6060/4043 welds and castings, the latter simulating weld metal composition under controlled cooling conditions. Results are given regarding the effect of 4043 addition on phase formation, solidification range, solidification shrinkage, and grain structure.

Stage 4: Modeling Crack Initiation and Growth Mechanisms. By implementing experimental inputs (Stages 2 and 3) into cracking models, mechanisms are proposed for solidification crack initiation and growth. Also, a strain partition model is proposed, providing a link between predicted and measured cracking conditions. These models account for dissolved hydrogen.

Stage 5: Hydrogen Influence on Weldability. Since the proposed cracking models (Stage 4) suggest hydrogen to affect Alloy 6060 weldability, arc welding was performed with controlled hydrogen contamination. Threshold hydrogen values for solidification crack initiation were determined in restrained welds. Also, using the modified varestraint test (MVT), ram speed – hydrogen combinations required for solidification crack growth were defined.

The final conclusion summarizes the major outcomes of the present work, and a perspective for future works is presented.

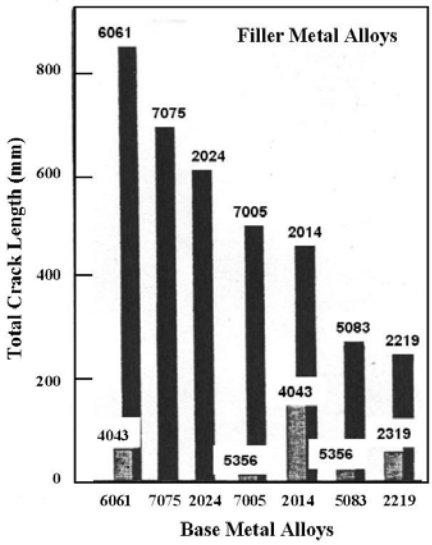

Figure 1: Total crack length for GMA aluminum weld metals with different aluminum filler using T-joint test [1].

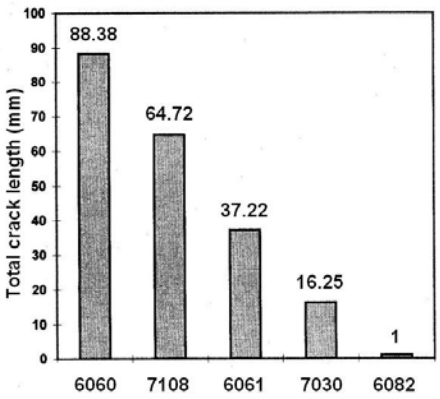

Figure 2: Total crack length in GTA aluminum weld metals using circular patch test [5].

2 Background

A background will be given that outlines important considerations in characterizing and predicting *solidification cracking.* Also solidification path and cracking susceptibility of *Al-Mg-Si alloys* will be detailed.

2.1 Solidification Cracking Phenomenon

Solidification cracking is complex in nature, involving interplay between thermal, mechanical, and metallurgical components. External factors, i.e. thermal (heat input, cooling rate) and mechanical factors (restraint intensity), affect the strain distribution around the weld. Inherent factors, i.e. metallurgical factors, define the inherent susceptibility of an alloy to cracking. The high solidification cracking susceptibility of aluminum alloys is believed to be due in part to the high solidification shrinkage coefficient (near 6% volume) as compared for example to iron (near 2% volume) [7]. It is also strongly dependent upon the alloy composition [6,8-11], with a typical Λ-shape curve for cracking susceptibility versus alloying content in binary and quasi-binary aluminum alloys (Figure 3). The underlying causes of solidification cracking being not well understood, it is still today a contentious subject. A literature review is provided below regarding *solidification cracking characteristics* and *modeling*, and *weldability characterization.*

2.1.1 Solidification Cracking Characteristics

Solidification cracking characteristics detailed below are based upon literature reviews from experimental investigations, especially *crack surface appearance* and *in-situ observations*.

2.1.1.1 Cracking Surface Appearance

Observing fracture surfaces should help in elucidating the mechanisms involved in weld solidification crack formation. Detailed fractographic studies have been conducted on cracks in stainless steels [12-19] and aluminum alloys welds [20,21] produced under a wide range of natural and artificial conditions, e.g. welds subjected to a rapid augmented strain using the varestraint or trans-varestraint test (described in paragraph 2.1.5.1.2). Fracture surfaces are generally covered by a smooth layer containing sometimes solid bridges that

connect opposite sides of the crack [22]. Examinations by scanning electron microscopy revealed three distinct surface appearances (Figure 4). Nearest from the weld pool at the time of cracking, the “Type D” surface exhibits a smooth dendritic appearance typical of solidification cracking in service welds (Figure 4b). Farthest from the weld pool at the time of cracking, the “Type F” surface displays a dominant flat surface with no distinguishable protuberances (Figure 4d). In between, the “Type D-F” surface is a narrow transient region with a pronounced globular appearance (Figure 4c). Regarding “Type D” surfaces, the lack of matching of the opposing crack surfaces and the smooth intact dendrite appearance could suggest that cracking formed in a liquid phase that covered completely the grain boundaries, as observed when “freezing” a propagating crack in Al-Si laser welds [23]. On the contrary, the usual correspondence between ridges and valleys on opposing “Type F” crack surfaces indicates that the intergranular liquid films were extremely thin and no longer fully covering the grain boundaries. “Type F” surfaces are observed in welds undergoing high applied strains and strain rates, but not in self-restraint welds. When subjugating aluminum welds to trans-varestraint tests (described in paragraph 2.1.5.1.2), “Type F” surfaces are found, with the aid of a plunged thermocouple in weld pool, to be generated at sub-solidus temperatures [20]. This suggests “Type F” surfaces to be associated with ductility dip cracks, whose formation is indeed favored at high applied strains and strain rates (Figure 5) [17].

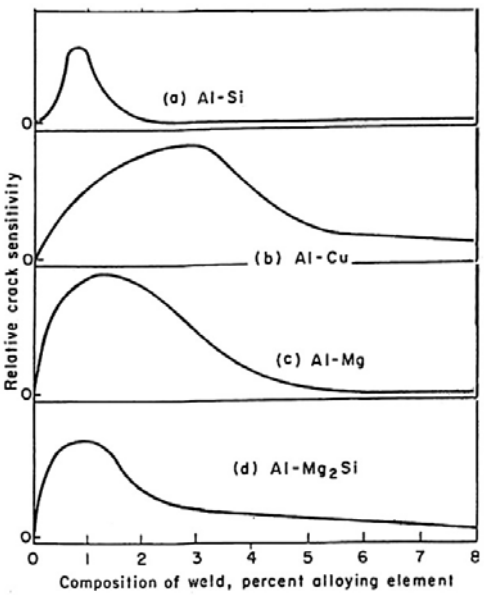

Figure 3: Solidification cracking susceptibility versus alloying content U-shaped cast bars of (a) Al-Si, (b) Al-Cu, (c) Al-Mg, and (d) Al-Mg_2Si binary alloys [11].

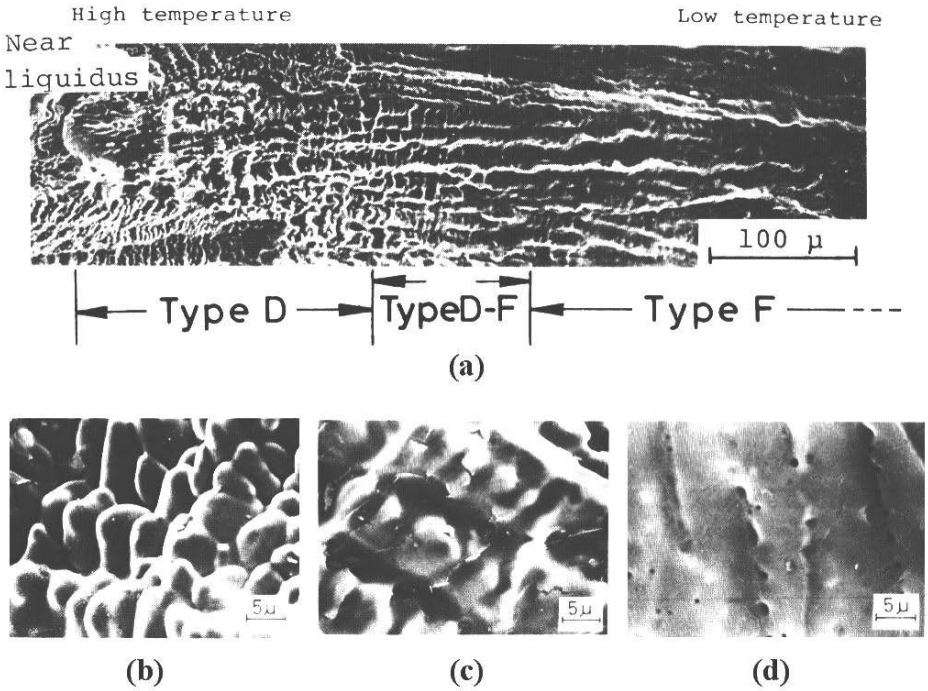

Figure 4: Feature of solidification crack surface of SUS 310S weld metal at (a) low and (b,c,d) high magnification: (a) general appearance, (b) Type D, (c) Type D-F, and (d) Type F [15].

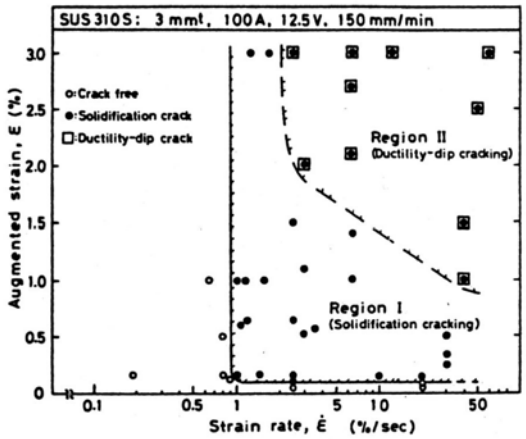

Figure 5: Strain rate dependence of hot crack ductility for SUS 310S stainless steel [17].

2.1.1.2 In-Situ Observations

In-situ observations of solidification crack formation have the advantage to relate the occurring events to post-mortem observations, e.g. crack surface features. Combining X-ray radiography and temperature measurement in steel and Al-4wt.%Cu castings, Pellini [24] detected solidification cracking to form between 0.85 and 0.95 solid fractions. Recently, a high-resolution camera coupled with a digital image correlation software enable direct observation of hot spot region in aluminum castings during solidification [25,26]. Solidification cracking was detected to form between 0.93 and 0.96 solid fractions in Al-0.5wt.%Cu casting [26]. Moreover, for constant casting conditions, local strains and strain rates are highly dependent upon the alloy composition, possibly due to different thermal contraction behavior, thus affecting the alloy cracking sensitivity [25,26].

In-situ observations were also performed during welding. In GTA steel welds, real-time radiography revealed that cracking initiated at an initial defect, later identified as a pore, about 0.4 second after the defect formation [19]. Pores were also observed ahead of the advancing crack tip in Al-Si laser welds [23]. Also, use of real-time radiography [19] and high speed cinematography [14,27,28] revealed that solidification cracking in GTA welds propagates through a liquid film at a fixed position, i.e. constant solid fraction, within the two-phase mushy zone, and must therefore grow at the same velocity as the weld torch [27]. However, this apparent “stable” crack growth is actually highly erratic with successive periods of rapid and slow crack growth [19].

In order to overcome the high temperatures encountered in aluminum welds, crack formation has been studied in solidifying succinonitrile-acetone (SCN) alloys [29,30], which have interesting properties: transparency, low melting point (58°C), solidification shrinkage similar to that of aluminum, and solidification in a dendritic structure. The SCN alloy solidified between two parallel transparent plates between which a stick was inserted previously to the solidification start, while submitted to a temperature gradient to promote uni-directional solidification. Pore formation was observed using an optical microscope and generated by pulling the growing dendrites with the stick at a controlled velocity in a direction transverse to the dendrite growth direction. Pores form in the liquid film along the grain boundaries only within a specific solid fraction range, high liquid feeding at low solid fractions and strain resistance due to extensive intergrain bridging at high solid fractions avoiding pore formation. The crack surface in SCN alloys reveals few small spikes resulting from a local plastic deformation of solid bridges or the meeting of two pores, similar pikes having been found on Al-Cu alloy solidification crack surfaces. Note that, since the melted SCN alloy was introduced between transparent plates in contact with air before testing, the plate surfaces contain gas embryos which could facilitate pore formation.

2.1.2 Solidification Cracking Models

During the last century, a number of fundamental theories and criteria were advanced to describe and characterize solidification crack formation, as indicated in recent reviews on the subject [31-34]. But none of these criteria is today universally accepted by the entire scientific community. Historically, one of the first solidification cracking models were proposed in the 1920´s and related the cracking sensitivity of a semi-solid material to its strength to fracture [35,36]: the faster the rise of strength with falling temperature, the lower the susceptibility to cracking. Starting the 1950´s, in-situ and crack surface observations revealed solidification crack formation to imply liquid film fracture at temperatures above the solidus. Today, with the availability of high computational performances, numerical simulations combine solidification cracking criteria and rheological behavior of semi-solid metals with the hope, one day, to predict cracking.

Assuming that all thermo-metallurgical conditions are held constant (e.g. constant alloy composition and cooling rate), it is useful to concentrate on what conditions are required to initiate and propagate cracking from a purely thermo-mechanical aspect. Over the years, research work has lead to the general belief that cracking results from the uniaxial tensile fracture of liquid films at grain boundaries within the two-phase mushy-zone [22]. Strains and stresses at the trailing edge of the weld pool can be either compressive or tensile, and arise from an interaction between the weld thermal experience (i.e. heating and cooling cycles), restraining forces, and solidification shrinkage [14,37,38,39]. Therefore, solidification cracking criteria, usually developed for casting and then adapted for weld metals, involve *critical stresses*, *strains*, or *strain rates* for cracking formation [34]. Most of these criteria are validated when reproducing the Λ-shape curves of cracking susceptibility versus alloying content for binary aluminum alloys (recall Figure 3).

2.1.2.1 Stress Based Models

Stress based models assume solidification cracking to form in a semi-solid material when applied tensile stresses exceed the material strength. Some experimental observations [37,38] and numerical simulations [14] suggest that tensile stresses at the trailing edge of the weld pool promote weld solidification cracking. Using the Moiré fringe analysis technique (described in paragraph 2.1.5.2.2), Chihoski [37,38] observed along Alloy 2014 GTA welds localized tensile and compressive regions (or cells), whose size and nature depend upon the experimental conditions. The cells are illustrated in Figure 6a in case of bead-on-plate GTA welds made at a welding speed of 8.5 mm/s. The compressive cell C_1 immediately in front of the weld pool is induced by the thermal expansion from preheat ahead

of the welding torch. The tensile cell T_S immediately behind the weld pool results from solidification shrinkage. The compressive cell C_2, behind T_S, is caused by the thermal contraction. In reaction to the compressive cells C_1 and C_2 form the tensile cells T_1 and T_2. Reducing the welding speed from 8.5 (Figure 6a) to 2.5 mm/s (Figure 6b) was found to increase weld solidification cracking susceptibility. This has been associated to the decrease in size of the compressive cell C_2 up to its disappearance, resulting in the weld mushy zone into tension (combination of tensile cells T_S and T_2). The development of a compressive cell surrounding the mushy zone should preclude crack formation [14]. Therefore, one suggested solidification cracking susceptibility index is simply proportional to σ/σ_{max}, where σ is local stress and σ_{max} is fracture stress [40].

2.1.2.1.1 Crack Initiation

Stress based models estimate the strength of grain boundary liquid films and consider a solidification crack to initiate when exceeding the fracture stress of these liquid films. One approach [41,42] considers a simplified geometry consisting in a liquid film trapped between parallel plates (Figure 7). Assuming total wetting, uniform distribution of the liquid, and negligible viscosity, the fracture stress σ_{fr} to separate two adjacent grains separated by a liquid is given by:

$$\sigma_{\mathrm{fr}} = \frac{2\gamma}{b} \tag{1}$$

, where γ is surface tension and b is liquid film thickness. Good agreement was found with measured fracture stresses at low solid fractions, i.e. thick liquid films.

Another approach [43] simulates the mechanical response of a semi-solid body to an external deformation. In a 2-D plane cut of a 3-D microstructure, the grains are assumed hexagonal in shape with a side length a. The fracture stress σ_{fr} of the liquid is related to the liquid surface tension γ, accumulated strain ε, liquid film thickness b, and solid fraction f_s by:

$$\sigma_{fr} = \frac{4\gamma}{3b}\left(1+\left(\frac{f_s^m}{1-f_s^m}\right)\varepsilon\right)^{-1} \tag{2}$$

, where m equals $\frac{1}{3}$ for 3-D equiaxed structure and $\frac{1}{2}$ for 3-D columnar structure.

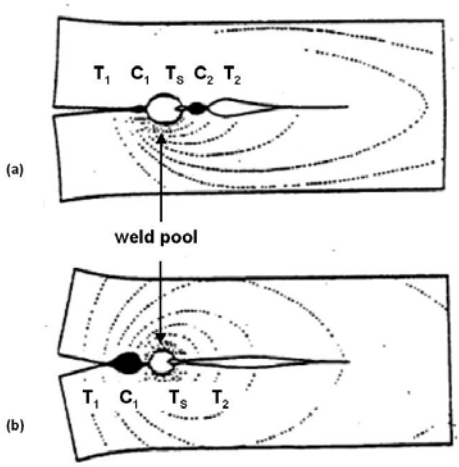

Figure 6: Transverse compressive and tensile cells around weld pool measured when welding at a torch travel speed of (a) 8.5 and (b) 2.5 mm/s. Note the disappearance of compressive cell C_2 at lower travel speed [37].

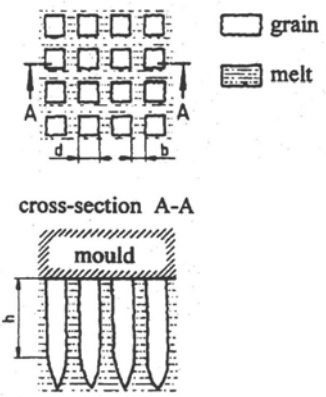

Figure 7: Schematic of a columnar grain structure as used by Dickhaus et al. to estimate stress to fracture [42].

2.1.2.1.2 Crack Growth

Stress based models characterize crack growth by applying solid state fracture mechanisms to liquid film rupture. One approach involves breaking bonds between the two sides of the opening crack to include surface energy effects [44]. The bonds were characterized using values having no physical meaning and the simulation was calibrated using data for crack growth in solid specimens. Another approach estimates the stress required for the propagation of a liquid-filled crack [45] based upon the Griffith criterion, which determines the energy required to grow a crack in a solid brittle material initiated at a stress concentrator. Modifying this criterion to consider the liquid film surrounding a grain as stress concentrator, the critical stress σ_c to propagate a crack at a constant temperature and solid fraction is given by:

$$\sigma_c = \sqrt{\frac{8G\gamma}{\pi(1-\nu)AV_L^{1/2}}} \tag{3}$$

, where A is a constant depending upon grain size and dihedral angle, G is shear modulus, γ is liquid surface tension, V_L is volume of liquid and ν is the Poisson's ratio. Good agreements were found between predicted and measured fracture stresses for Al-Sn binary alloys.

2.1.2.2 Strain Based Models

Strain based models traditionally assume the fracture in semi-solid materials to be strain limited. Strain accumulated in the mushy zone as a result of solidification shrinkage and thermal contraction serves to pull weld metal grains apart, resulting in the separation of grain boundary liquid films. Using the indentation technique (described in paragraph 2.1.5.2.2) along bead-on-plate GTA welds, Matsuda et al. [46,47] suggest that tensile strains at the trailing edge of the weld pool promote weld solidification cracking. Recently, with the aid of numerical simulations, welds in which cracking is experimentally observed were associated with higher accumulated strain along the weld centerline, according to simulative results [39,48]. Since accumulated strain is assumed, the *brittle temperature range*, i.e. the temperature range over which solidification cracking is likely to occur, and the *semi-solid material ductility* are believed to affect solidification crack formation.

2.1.2.2.1 Brittle Temperature Range (BTR).

The brittle temperature range (BTR) relates to the temperature range over which solidification cracking is likely to occur. It is argued that a large solidification range permits a large build-up of strain and thus a greater likelihood to crack [49]. While alloys with a large solidification range are often found more susceptible to cracking [22,50,51], there are exceptions where it clearly does not apply; e.g. aluminum-magnesium binary alloys have both a large solidification range and exceptional weldablility [50]. Therefore, research effort has been expended to determine the BTR within the solidification range.

Using hot tensile tests (described in paragraph 2.1.4) on Al-Si binary alloys, Singer and Cottrell [52] observed an abrupt drop in strength and a complete loss in ductility when exceeding the solidus temperature, due to the presence of liquid surrounding the grains. They also found a temperature, later referred to as the coherency temperature, above which the material consists of solid particles suspended in a continuous liquid and thus does not offer any mechanical resistance to deformation. Dendrite coherency point corresponds to the moment when dendrites begin to impinge upon another, causing the formation of a continuous solid network and thus an increase in strength when undergoing solidification below the coherency temperature [53]. The solidus – coherency point temperature range has been later referred to as the brittle temperature range (BTR). The shrinkage brittleness theory [49] argues that the developed solid network within the BTR hinders the liquid flow to compensate the shrinkage of the semi-solid material, associating a large BTR to a great likelihood to crack. Based upon the Al-Si equilibrium phase diagram, plotting the BTR range versus silicon content in Al-Si binary alloys reveals a Λ-shape curve, with a peak at

1.8 wt.% Si, close to the experimental cracking susceptibility curve (recall Figure 3). The displacement of the peak in cracking susceptibility towards lower alloying contents at higher cooling rates was associated to the suppression of diffusion processes which displace the BTR towards lower alloying contents [54]. Note that, at the time the work was done, non-equilibrium solidification was not well understood.

Further divisions of the BTR, successively proposed by the "generalized theory" [55] and the "modified generalized theory" [28], pointed out that solidification cracking should occur in regions combining both very low permeability (i.e. difficulty of liquid feeding) and low strength (i.e. non-extensive intergrain solid bridging). The modified generalized theory is illustrated in Figure 8. The BTR, i.e. between coherency temperature and solidus, is divided into three stages (2, 3(l), and 3(h)). The initial high amount of liquid present in the interstices of the solid network (stage 2) is reduced to a thin continuous liquid film (stage 3(h)) and finally to isolated liquid pockets (stage 3(l)). The initiation of a solidification crack appears unlikely during stage 2 because of the high permeability of the mushy zone (i.e. high liquid feeding), and during stage 3(l) because of extensive intergrain solid bridging (i.e. high strength). Therefore solidification cracking is likely to initiate during stage 3(h), where the alloy possesses both low permeability, low strength, and the lowest ductility within the BTR [56]. Once initiated, the crack propagates towards both stage 2 (in competition with liquid feeding) and stage 3(l), correlated to "Type D" and "Type F" crack surfaces, respectively [15].

The likelihood to crack is believed to depend not only upon the quantity but also upon the distribution of liquid at grain boundaries [55], which is characterized by the liquid wettability τ on solid grains (Figure 9), accordingly:

$$\tau = \frac{\gamma_{SL}}{\gamma_{SS}} = \frac{1}{2\cos(\phi/2)} \tag{4}$$

, where γ_{SS} and γ_{SL} are solid-solid and solid-liquid interface energies, and ϕ is dihedral angle. For good wettability, i.e. small dihedral angle ($\phi \approx 0°$), the liquid covers completely the grain boundaries, generating easy liquid flow (i.e. high liquid feeding). At high dihedral angle ($\phi \geq 90°$), the liquid concentrates as little pockets along the grain edges promoting extensive intergrain solid bridging (i.e. high strength). In between ($\phi \approx 60°$), the liquid is mostly present along the edges, resulting in low liquid feeding and low strength, and thus high susceptibility to solidification cracking. However, since the liquid film thickness cannot be infinitely thin, a minimum liquid amount is required to ensure complete coverage of the grain boundaries, even for ϕ equal to 0° [22]. For example, with ϕ equals 20°, 1 and 10% of liquid fraction covers respectively nearly 30 and 85% of the grain surfaces [57]. Furthermore, the liquid

distribution along grain boundaries has been shown to affect strength to fracture in semi-solid aluminum alloys 3104 and 5182 [58], suggesting that constitutive laws characterizing the rheological behavior of semi-solids and solidification cracking models should consider not the volume fraction of liquid but the fraction of grain boundary area covered with liquid.

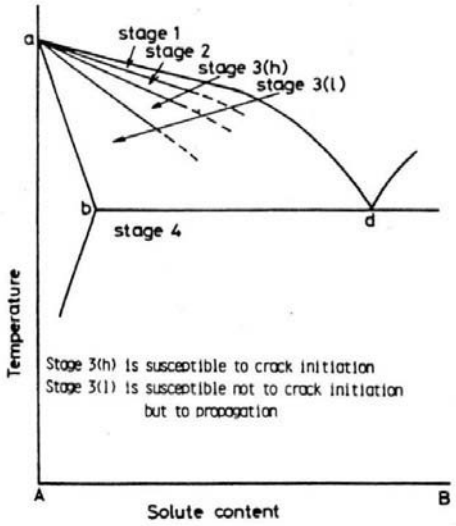

Figure 8: Correlation between solidification cracking and solidification path according to "modified generalized theory " [28].

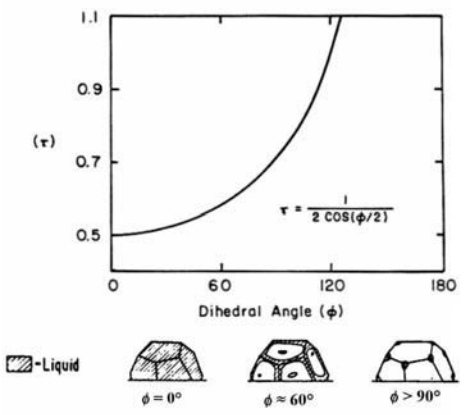

Figure 9: Relative interface energy (τ) versus dihedral angle (ϕ) and corresponding distribution of liquid at grain surface [55].

2.1.2.2.2 Semi-Solid Material Ductility.

Strain based models assume fracture in a semi-solid material to be strain limited. The "strain theory" [24] was the first theory to consider liquid films to withstand a limited local strain by introducing the liquid film concept, similar to the "shrinkage brittleness theory" [49]. Strain is assumed uniformly distributed above the coherency temperature (lack of coherence, Figure 10a) and at high solid fractions (high strength, Figure 10c). In between, strain is localized in the most vulnerable region to tensile strains within the mushy zone, i.e. at grain boundary liquid films (Figure 10b), where strains may be high enough to fracture the liquid.

Further developments were conducted using established characteristic ductility curves for specific alloys [12,16,56,59-62], ductility curves for some aluminum alloys being shown in Figure 11. These curves define not the strain at grain boundaries as considered by the strain theory (Figure 10), but the globally applied strain that can withstand a material over the solidification range bounded by liquidus and solidus temperatures. Therefore, one

suggested solidification cracking susceptibility index is simply proportional to $\varepsilon_{\theta\theta}/\varepsilon_{fr}$, where $\varepsilon_{\theta\theta}$ is accumulated plastic strain when reaching the solidus temperature and ε_{fr} is strain to fracture [63]. Note that minimum ductilities can vary between different tests from one order of magnitude, from 0.1 (Figure 11a) to 2% (Figure 11b).

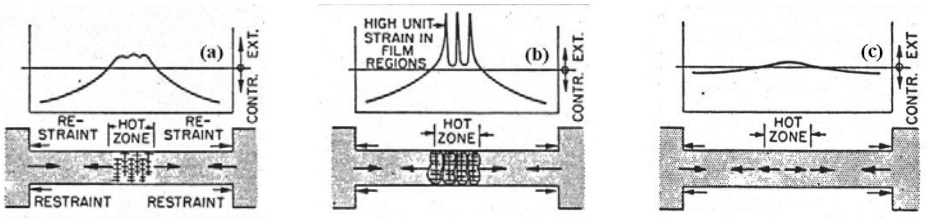

Figure 10: Strain distribution (extension and contraction) at different stages of solidification: (a) near liquidus, (b) slightly above solidus, and (c) at solidus [24].

Ductility based models recognized that strain rate is also an important factor, but only in so far as it serves to determine how much strain can be accumulated during the time of solidification. This concept was first suggested by Prokhorov [59] and later referred to as the critical strain rate for temperature drop (CST) [61]. It was argued that cracking occurs if the accumulated strain exceeds a ductility limit represented by characteristic ductility curves, as illustrated by line (c) in Figure 12a. Using this curve-strain build up concept, a critical rate of strain accumulation with temperature drop, characterizing the boundary between crack and no-crack conditions, is defined by the deformation curve tangent to the ductility curve, illustrated by line (b) in Figure 12a and dashed lines in Figure 12b. The rate of strain accumulation with temperature drop ($d\varepsilon/dT$) is related to the strain rate ($d\varepsilon/dt$), accordingly:

$$\frac{d\varepsilon}{dT} = \frac{dt}{dT} \cdot \frac{d\varepsilon}{dt} = \frac{\dot{\varepsilon}}{\dot{T}} \tag{5}$$

This criterion, applied for various weld metals [12,64-67], was in particular successfully used to evaluate the solidification cracking sensitivity of binary aluminum alloys [12]. Moreover, the ductility limit should be reached at higher temperatures with greater rates of strain accumulation, favoring “Type-D” upon “Type-F” crack surface [17].

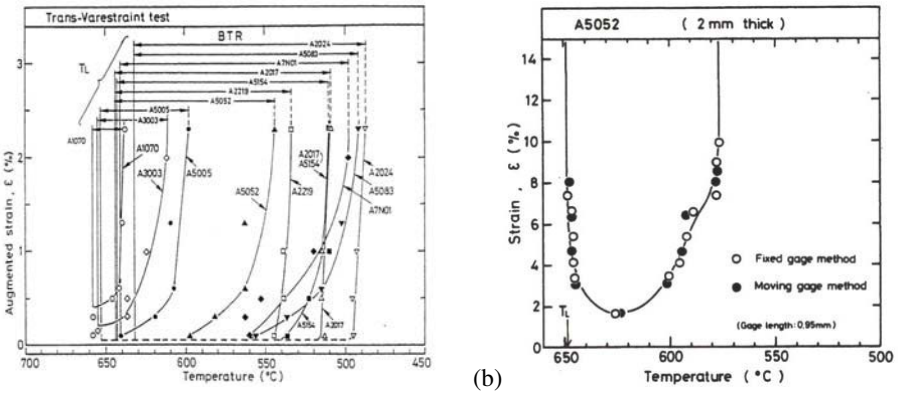

(a) (b)

Figure 11: Ductility curve comparison measured with MISO technique (described in paragraph 2.1.5.2.2) for aluminum alloys using (a) trans varestraint test [60] and (b) variable tensile test [62] (tests described in paragraph 2.1.5.1.2).

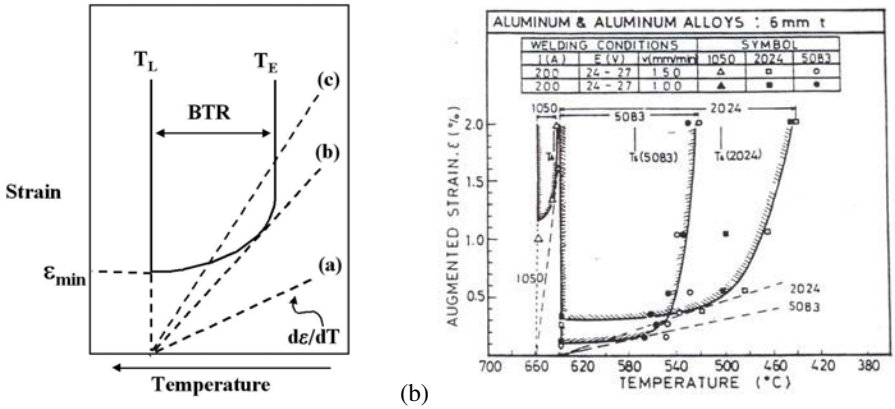

(a) (b)

Figure 12: Strain rate dependence of solidification crack ductility showing (a) general schematic and (b) for aluminum alloys [61].

Another approach [68] quantifies the ductility in the BTR by introducing the concept of "reserve of plasticity" (p_r) (Figure 13), which corresponds to the averaged integrated difference between the elongation to failure (ε_p) and the shrinkage/contraction (ε_{sh}) in the brittle temperature range (ΔT_{br}), i.e. between coherency (T_{coh}) and solidus (T_{sol}):

$$p_r = \frac{1}{\Delta T_{br}} \int_{Tcoh}^{Tsol} (\varepsilon_p - \varepsilon_{sh}) dT \tag{6}$$

The shrinkage is considered linear with temperature:

$$\varepsilon_{sh} = \alpha . \Delta T_{br} \tag{7}$$

, where α is the average thermal coefficient of linear contraction in the interval of solidification ΔT_{br}. The term p_r equals to the ratio between the interval of solidification ΔT_{br} and the surface *S* (Figure 13a) or *S1-S2* (Figure 13b). A good agreement for aluminum alloys was found between high values of p_r and low cracking susceptibility [69]. Note that strain based models, while popular and widely used, are not based upon any stated liquid fracture mechanism, which brings their validity into question.

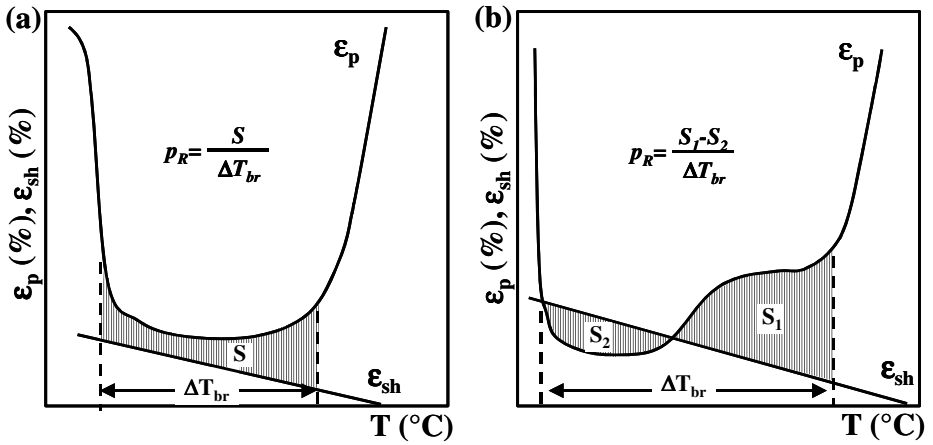

Figure 13: Shrinkage dependence for calculation of reserve of plasticity (p_r) using ductility curves [67].

2.1.2.3 Strain Rate Based Models

Over a long period of time (1940´s - present), weld solidification cracking has been believed to be a ductility limited phenomena, the ductility curves representing the boundary between crack and no crack. However, recent developments change this point of view. Strain rate, before just a secondary effect needed to achieve a critical strain, may actually play a more direct role in the liquid fracture mechanism, e.g. by controlling the interdendritic liquid pressure drop. The existence of a critical strain rate above which weld solidification cracking forms has been proven using the variable deformation rate (VDR) test [70], programmable deformation crack (PVR) test [71-75], and slow bending trans-varestraint test (SB-TVT) [17,60,76], these tests being described in paragraph 2.1.5.1.2. For example, with the aid of MISO measurements (described in paragraph 2.1.5.2.2) in SB-TVT tests, a critical strain rate for crack formation has been determined when welding aluminum alloys (arrows in Figure 14) and stainless steels (recall Figure 5), higher critical strain rate values representing greater resistance to cracking. Below are presented the *shrinkage - feeding theories* upon

which *strain rate based models* are developed. Note that here is considered liquid feeding, i.e. liquid flow through a dendritic solid network to avoid solidification crack formation, and not back-filling or healing, i.e. liquid flow filling an already existing crack as observed in welds when sufficient amount of liquid is present [11,14,23,28,49].

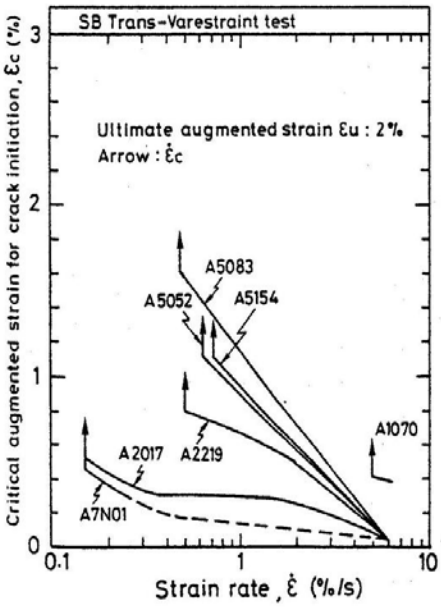

Figure 14: Strain rate dependence of solidification crack ductility for aluminum alloys [60].

2.1.2.3.1 Shrinkage - Feeding Theories

Shrinkage - feeding theories assume that the tendency to form solidification cracking hinges directly upon the ability to feed solidification shrinkage. When undergoing solidification, the liquid flow through the mushy zone, i.e. liquid feeding, is hindered by the developing dendritic solid network. The weld pool playing the role of the liquid supply, the further from the weld pool (i.e. the deeper in the mushy zone), the more difficult the feeding. Solidification cracking is believed to occur when liquid feeding becomes insufficient to compensate for the solidification shrinkage and thermal contraction.

The “shrinkage brittleness” theory [11] proposed a minimum amount of eutectic liquid required to avoid solidification cracking, arguing that more eutectic relates to more spacing between the dendrites and thus better feeding. Relating the calculated eutectic liquid amount with the cracking sensitivity of binary aluminum alloys in U-shape cast bars, results

suggest solidification cracking to be avoided for eutectic liquid amounts exceeding 12% by volume.

One approach [77] introduces the concepts of rate of shrinkage (ROS) and rate of feeding (ROF), solidification cracking being likely to form when the ROS value exceeds the ROF value. These terms are calculated by assembling the variables of importance into the following dimensionless form:

$$ROF = \left(\frac{\partial \ln V}{\partial t} \right)_{feeding} = \frac{f_L^2 \lambda_2^2 P_S}{24\pi c^3 \mu L^2} \tag{8}$$

$$ROS = \left(\frac{\partial \ln V}{\partial t} \right)_{shrinkage} = \frac{(\rho_O - \rho_S + akC_L)\dot{T} f_L^{(2-k)}}{\rho(1-k)m_L C_O} \tag{9}$$

, where V is volume, t is time, f_L is liquid fraction, λ_2 is secondary dendrite arm spacing, P_S is effective feeding pressure, c is dendrite network tortuosity, μ is liquid viscosity, L is length of porous network, ρ_L and ρ_S are liquid and solid densities, ρ is average density ($\rho = \rho_L f_L + \rho_S(1-f_L)$), ρ_O is liquid density at the melting point, a is composition coefficient of the liquid density ($\rho_L \approx \rho_O + aC_L$), C_L is composition of the liquid at the solid-liquid interface, C_O is alloy composition, $\dot{T}$ is average cooling rate during solidification, k is equilibrium partitioning coefficient, m_L is slope of the liquidus line. The effective feeding pressure (P_S) is considered as the sum of the atmospheric, capillary, and metallostatic pressures. The ROF value decreases with falling temperature because of the increasing tortuosity c with developing dendritic solid network. Applied to Al-5wt.%Si casting (Figure 15), cracking is likely to occur below 615°C, i.e. for ROS higher than ROF values. Moving the intersection point to lower temperatures should reduce the susceptibility to crack. This may be done by adding surface active elements, a negative gradient ($d\gamma/dT<0$, with T temperature and γ surface tension) driving naturally the liquid flow towards the dendrites root (lowest temperature) [78]. This results in a positive “pressure”, which is added to the effective feeding pressure P_S to increase the ROF value (Eq. 8).

Considering arguments of the generalized theory [55], Clyne and Davies [79] compare the time spent in the vulnerable zone (t_V) to the time spent in a recovery zone (t_R) by an alloy undergoing solidification (Figure 16). The vulnerable zone was stated to be between 0.90 and 0.99 solid fractions (i.e. hindered liquid feeding) and the recovery zone between 0.40 and 0.90 solid fractions (i.e. easy liquid feeding). The cracking susceptibility coefficient (CSC) is proposed as follows:

$$CSC = \frac{t_v}{t_r} = \frac{t_{99} - t_{90}}{t_{90} - t_{40}} \tag{10}$$

, where t_x is the time at x% solid fraction. Applied to cast Al-Mg binary alloys, the CSC criterion reproduced the Λ-shape curve for solidification cracking susceptibility versus magnesium content, but over-estimated the cracking susceptibility for Mg contents higher than 6 wt.% Mg.

Later, Katgerman [80] combined the CSC criterion (recall Eq. 10) with the shrinkage – feeding concept of Feurer (recall Eq. 8 and 9). The solid fraction, above which liquid feeding is insufficient and previously fixed at 0.90 in the CSC, is taken as the solid fraction at which the ROF and ROS curves intersect (Figure 15). This new criterion is found sensitive to composition, casting rate and ingot diameter for DC cast aluminum alloys [80].

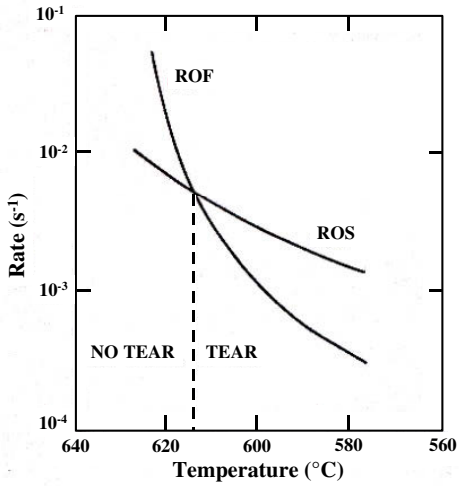

Figure 15: Calculated rate of feeding (ROF) and rate of shrinkage (ROS) for Al-5wt.%Si casting [77].

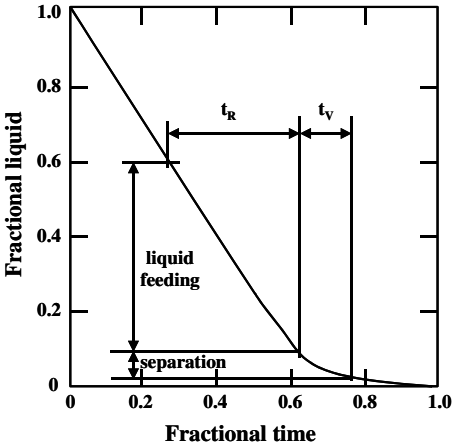

Figure 16: Relationship between liquid fraction, recovery duration (t_R) and vulnerability duration (t_V) [79].

2.1.2.3.2 Strain Rate Based Models

Strain rate based models put into mathematical form the shrinkage – feeding concepts of Feurer [77] and Campbell [22], while additionally accounting for deformation within the mushy zone incorporating a strain rate term. Strain rate is assumed to play a major role on both solidification crack *initiation* and *growth*, by controlling the liquid pressure drop within a semi-solid material.

Crack Initiation. Strain rate based models usually associate solidification crack initiation to the interdendritic liquid fracture, which occurs when the liquid pressure falls below some critical value. The first two-phase approach, accounting for the deformation of the solid phase, is the Rappaz-Drezet-Gremaud (RDG) theory [81]. This model estimates the interdendritic liquid pressure drop at the dendrite root due to insufficient liquid feeding to compensate solidification shrinkage and thermal contraction (Figure 17). The longitudinal component of the deformation is neglected, even if it might induce some suction or expulsion of liquid. Assuming a columnar structure and rigid solid phase, the maximum pressure drop (ΔP_{max}) due to localized transverse strain rate ($\dot{\varepsilon}$) is evaluated using a mass balance over the dendrite length:

$$\Delta P_{\max} = P_L - P_0 = \Delta P_{\varepsilon} + \Delta P_{sh} = \frac{(1+\beta)\mu}{G}\int_{TS}^{TL}\frac{E(T)}{K}dT + \frac{v_T\beta\mu}{G}\int_{TS}^{TL}\frac{1-f_S(T)}{K}dT \qquad (11)$$

, where $E(T) = \frac{1}{G}\int f_S(T)\dot{\varepsilon}(T)dT$, P_L and P_0 are liquid pressure at dendrite tip and root, μ is liquid viscosity, β is shrinkage factor, v_T is velocity of isotherms, G is thermal gradient, T_S and T_L are solidus and liquidus temperatures, K is mush permeability, $f_s(T)$ is solid fraction at the temperature T. The first term on the right hand side is the contribution of the deformation of the solid skeleton (ΔP_{ε}) to the liquid pressure drop, whereas the second one is the shrinkage contribution (ΔP_{sh}). Higher pressure drops are associated with higher solidification cracking susceptibility. The interdendritic liquid is assumed to fracture due to cavitation when the liquid pressure falls below some critical value. Applied to DC cast Al-Cu binary alloys, the RDG model predicts the Λ-shape curves for solidification cracking susceptibility versus copper contents with a peak at 1.4 wt.% Cu, and a liquid pressure drop (ΔP_{max}) on the order of 10^3 Pa under critical conditions for cracking. The RDG model was later successfully integrated into thermo-mechanical numerical simulations of DC cast [82] and laser welded [83] aluminum alloys. However, the lower bound in Eq. 11 is ill-defined, the calculation diverging as f_s tends towards unity, i.e. K towards zero. To overcome this problem, the lower bound has been taken at a fixed solid fraction of 0.98 [81] or at the zero ductility temperature (T_{ZDT}) [84], assuming that the strain resistance due to interdendritic bridging is sufficient to resist cracking beyond these points. Nevertheless, it was argued that the lower boundary should represent the temperature for grain coalescence, since cracking most often occurs along a single grain boundary. Indeed, the coherency at grain boundary is expected always to be less than within the grain because of the longer liquid film life for greater misorientation of the adjacent grains (Figure 18). A theoretical approach for pure substances [85] suggests

that approaching planar solid/liquid interfaces coalesce to a grain boundary at an undercooling (ΔT_b) is given by:

$$\Delta T_b = \frac{\Delta \Gamma_b}{h} = \frac{\gamma_{GB} - 2\gamma_{SL}}{\Delta s_f} \frac{1}{h} \tag{12}$$

, where h is thickness of an isolated solid-liquid interface, $\Delta \Gamma_b$ is difference between the grain boundary (γ_{GB}) and twice the solid-liquid (γ_{SL}) interfacial energy divided by the entropy of fusion (Δs_f). The coalescence occurs when $\Delta T_b < 0$.

A recent approach includes a 3-D granular model into a numerical simulation of a solidifying alloy [86], enabling interdendritic liquid films that appear discontinuous in 2-D to be continuous in 3-D. Results show that mainly one liquid path feeds the entire mush. Assuming no porosity is formed, computed liquid pressure drops vary from –0.17 MPa in the main feeding path up to –4 MPa in channels no longer fed.

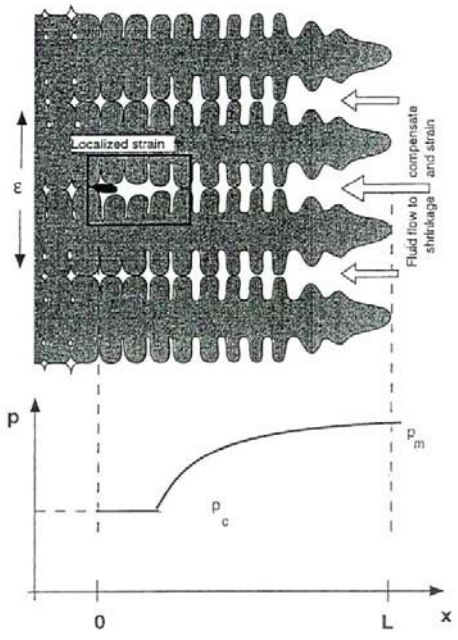

Figure 17: Schematics of solidification crack formation in between columnar dendrites resulting from localized strains. The pressure profile in interdendritic liquid is indicated [81].

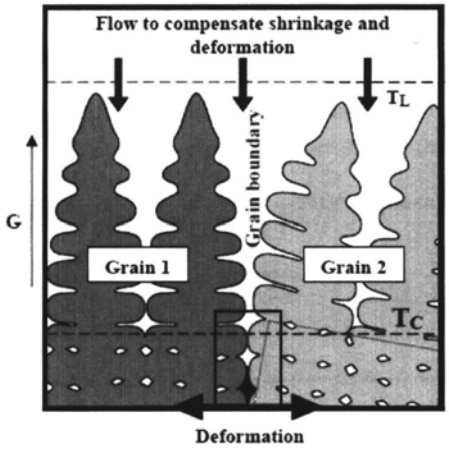

Figure 18: Schematics of solidification crack formation at boundary of disorientated grains [83].

The natural extension of the RDG criterion is the two-phase model proposed by Farup and Mo [87], which applies the RDG pressure drop concept to a 2-D microstructure, integrating a more rigorous rheological behavior to include thermally-induced deformation of the solid phase. The energy, liquid and solid momentum, and continuity equations are solved simultaneously. Major assumptions are no pore formation, equal pressures within the solid and liquid phases above coherency temperature, and incompressible solid skeleton below coherency temperature. Applying the two-phase model to a cast Al-4.5wt.%Cu binary alloy, the calculated pressure drop near the dendrite root is little sensitive to variations in solid fraction at the coherency temperature since the negative liquid pressure builds up near the very end of solidification. Further developments of the two-phase model included the plasticity of the solid phase [88] and existence of gas porosities [89], assuming pores to form in the liquid phase for dissolved hydrogen amounts greater than the saturation value given by Sievert´s law (detailed in paragraph 6.3.1.2). Applied to a DC cast AA5182 alloy, the latter model [89] revealed gas pores to participate to the feeding to compensate solidification shrinkage and thermal contraction, thus reducing the liquid pressure drop. The model also suggests that strains resulting from thermal contraction have only a small effect on liquid pressure drop values [90].

Another extension of the RDG criterion [81] is based upon simplified geometries simulating the columnar (Figure 19a) and equiaxed structures (Figure 19b), which consider the liquid film between two grains as a simple liquid slab embedded between two slabs of solid with properties assumed to be those of the mush [91,92]. Considering a material composed of parallel strips of liquid and solid phases, the global strain rate $\dot{\varepsilon}$, transverse to the solidification direction, is partitioned across a single grain boundary between liquid ($\dot{\varepsilon}_{\mathrm{L}}$) and solid ($\dot{\varepsilon}_{\mathrm{S}}$) strain rates, and equal pressures are assumed within the solid (σ_{S}) and liquid (σ_{L}) phases, accordingly:

$$\sigma_L = \sigma_S \text{ and } \dot{\varepsilon} = (1-\frac{h}{d})\dot{\varepsilon}_S + \frac{h}{d}\dot{\varepsilon}_L = f_s\dot{\varepsilon}_S + (1-f_s)\dot{\varepsilon}_L \qquad (13)$$

, where *d* is grain size, f_s solid fraction, and *h* liquid film thickness. The strain rate ($\dot{\varepsilon}_{\mathrm{S}}$) is estimated from an expression relating the rheological behavior of semi-solids to stress (σ). Using tensile and shear tests (described in paragraph 2.1.4), the visco-plastic behavior of the semi-solid Al-8 wt.% Cu binary alloy above 550°C was best fit by an equation of the form:

$$\sigma = \sigma_0 \exp(\alpha f_S)\exp\left(\frac{mQ}{RT}\right)(\dot{\varepsilon}_S)^m = K(T, f_s)\dot{\varepsilon}_S^m \qquad (14)$$

, where Q is activation energy, T is temperature, m is a strain rate sensitivity coefficient, σ_0 and α are material constants, and R is the gas constant. Equal pressures are assumed within the grain and at the grain boundary, i.e. the stress σ equals the liquid pressure drop originating from the strain rate ($\dot{\varepsilon}_{\mathrm{L}}$) as calculated using the RDG calculation (recall Eq. 11). Therefore, the critical strain rate to initiate a crack in a columnar ($\dot{\varepsilon}_{nd}$) and an equiaxed structure ($\dot{\varepsilon}_{ne}$) are explained as follows:

$$\dot{\varepsilon}_{nd} = \left[\frac{P_c}{K(T, f_s)}\right]^{1/m} \tag{15}$$

$$\dot{\varepsilon}_{ne} = \left(1 - \frac{h}{d}\right)\left[\frac{\frac{2}{3}P_c - P_m}{K(T, f_s)}\right]^{1/m} + \frac{h}{d}\frac{2k}{l_0^2}\frac{P_c}{\mu} \tag{16}$$

, where k is permeability of the mushy zone, l_0 is grain size, P_c is pressure at an oblate cavity interface, P_m is metallostatic pressure, μ is liquid viscosity.

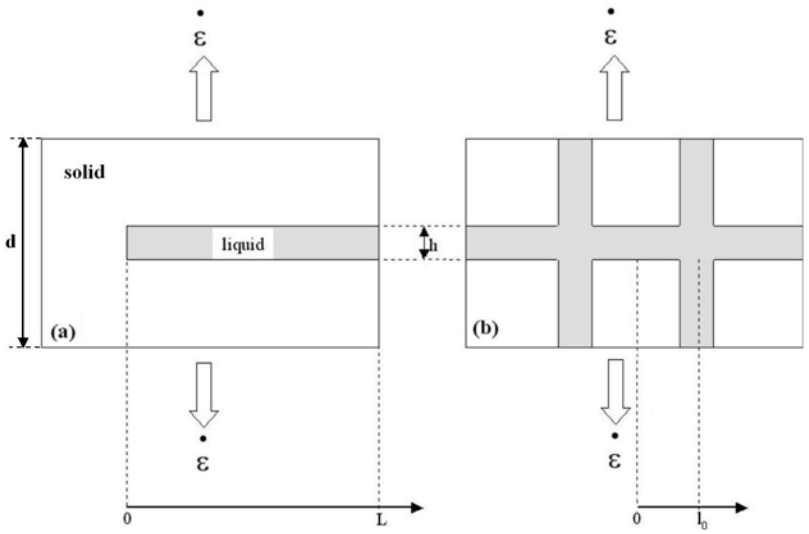

Figure 19: Schematic of (a) columnar and (b) equiaxed grain structure as considered by [91].

Crack Growth. Mechanisms for solidification crack growth have received less attention in the literature, since it has long been assumed that conditions appropriate for crack initiation will result in crack growth. This assumption follows weld in-situ observations,

which show that once initiated the crack follows the welding torch [27]. Therefore, one suggested solidification cracking susceptibility index is simply directly proportional to the amount of porosity [93], considering pores as potential sites from which a crack may grow. However, experimental work on DC cast Al-Cu binary alloys did not associate large amount of porosity with high solidification cracking susceptibility [94]. Note that different mechanisms are involved for pore expansion and crack growth, controlled by hydrogen diffusion and uniaxial tension, respectively [22].

Suyitno et al. [95], using a numerical simulation and integrating the semi-solid rheological behavior, assumed a circular cavity, i.e. pore, to form when liquid feeding cannot compensate the opening of the mush, providing crack initiation source. The pore of diameter d will grow into a crack when exceeding a critical stress σ_m given by a modified Griffith criterion, accordingly:

$$d = 4\gamma \frac{E}{\pi \sigma_m^2} \tag{17}$$

, where γ is liquid surface tension and E is Young modulus of the mush. The stress σ equals the liquid pressure drop originating from the straining conditions as calculated using the RDG criterion (recall Eq. 11). Applied to DC cast Al-4.5 wt.% Cu binary alloy, calculations reveal that higher strain rates are required to form a solidification crack than a micropore, represented by zone (C) and (B) in Figure 20, respectively.

Grandfield et al. [96] assumed the presence of an already existing void between the dendrites (Figure 21). The void interface may be assumed to grow as a crack if the sum of the pressures contributing to its growth (e.g. liquid pressure drop due to solidification shrinkage (ΔP_{sh}) and applied strain (ΔP_{ε}), and dissolved gas pressure (P_g)) exceeds the pressures contributing to its shrinkage (e.g. metallostatic pressure (P_m), surface tension pressure (P_γ), atmospheric pressure (P_a)):

$$(P_m + P_\gamma + P_a) - (\Delta P_\varepsilon + \Delta P_{sh} + P_g) \leq 0 \tag{18}$$

P_g was not taken into account. P_γ equals $2\gamma/r$, where γ is liquid surface tension and r pore radius. Assuming a perfect wetting of the liquid on solid dendrites, the pore diameter ($2r$) equals the interdendritic liquid film thickness. The sum ($\Delta P_\varepsilon + \Delta P_{sh}$) is calculated using the RDG pressure drop calculation (recall Eq. 11). The permeability K, used in the RDG calculation, was estimated based upon the secondary dendrite arm spacing λ_2:

$$K = \frac{\lambda_2^2}{180}\frac{(1-f_s)^3}{f_s^2} \tag{19}$$

, where f_s is solid fraction. Assuming the pore interface localted at the coherency point (temperature T_{coh} and solid fraction f_{scoh}), the critical strain rate for crack growth ($\dot{\varepsilon}_{\mathrm{crit}}$) is given by developing Eq. 18:

$$\dot{\varepsilon}_{crit} > \frac{\lambda_2^2}{180(1+\beta)B\mu L^2}\left[P_m + \frac{4\gamma}{(1-f_{scoh})\lambda_1}\right] - \frac{V\beta A}{(1+\beta)BL} \tag{20}$$

, where $A = \frac{1}{\Delta T_0}\int_{T_{eut}}^{T_{liq}} \frac{f_s^2}{(1-f_s)^2}dT$, $B = \frac{1}{\Delta T_0}\int_{T_{eut}}^{T_{liq}} \frac{f_s^2 F_s(T)}{(1-f_s)^3}dT$, $F_s(T) = \frac{1}{\Delta T_0}\int_{T_{eut}}^{T} f_s dT$,

$\Delta T_0 = T_{liq} - T_{eut}$, μ is liquid viscosity, λ_1 is primary dendrite arm spacing, β is shrinkage factor, V is growth velocity, G is thermal gradient, T_{liq} and T_{eut} are liquidus and eutectic temperatures respectively. Applied for horizontal direct chill cast magnesium alloys, the predicted critical strain rate ($\dot{\varepsilon}_{\mathrm{crit}}$) to grow a crack in a columnar structure equals $3.24 \cdot 10^{-3}$ s^{-1}.

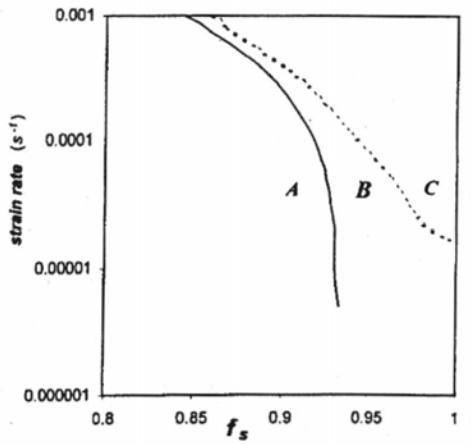

Figure 20: Strain rate – solid fraction conditions for (A) no micro-porosity and no cracking, (B) micro-porosity and no cracking, and (C) crack growth [95].

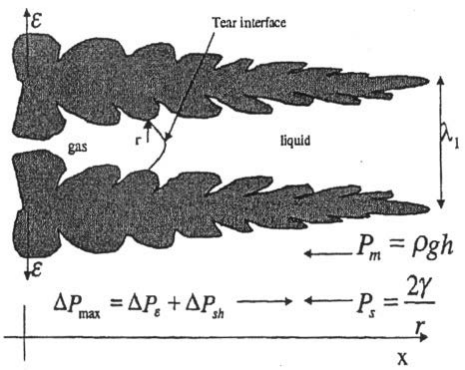

Figure 21: Schematic of model for crack growth used by [96] showing directions towards which pressures push pore interface.

Strain rate could also possibly play a direct role in propagating a crack, influencing the balance between transverse displacement, liquid feeding, and crack advancement [91,92]. Considering two grains separated by a liquid film of thickness h as depicted in Figure 22, the

transverse strain rate $\dot{\varepsilon}$ is compensated by both advancements of the crack $\dot{x}$ and the liquid feeding (flow rate v_L) in the form of a mass balance:

$$\dot{\varepsilon}(\lambda - x) = \dot{x}h + v_L h \tag{21}$$

, where $(\lambda\text{-}x)$ is the length of liquid film exposed to transverse strain in the region of dendrite coherency. Calculating the back-flow using Darcy´s law, the critical strain rate for crack growth $\dot{\varepsilon}_g$ is formulated as :

$$\dot{\varepsilon}_g = \left(1 - \frac{h}{d}\right)\left[\frac{\lambda - x}{\lambda}\left(\frac{\frac{2}{3}P_c - P_m}{K(T, f_s)}\right)\right]^{1/m} + \frac{h}{d}\frac{2K}{(\lambda - x)^2}\frac{P_c}{\mu} \tag{22}$$

, where d is grain size, P_c is pressure at an oblate cavity interface, P_m is metallostatic pressure, $K(T,f_s)$ as defined in Eq. 14, K is permeability of the mushy zone, and μ is liquid viscosity. This mass-balance approach was also developed for equiaxed structures using the simplified geometry depicted in Figure 19b. Applied to cast Al-8wt.%Cu binary alloys, it reveals that higher strain rates are required to grow a crack in equiaxed compared to columnar grain structures (Figure 23).

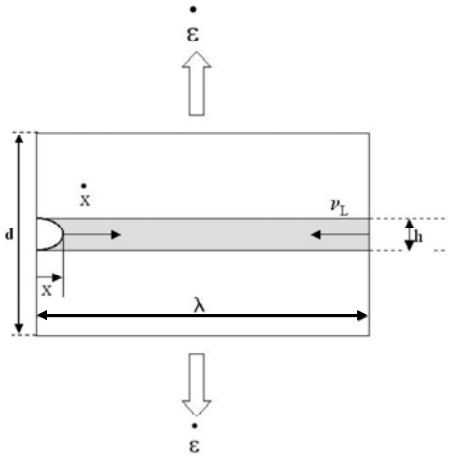

Figure 22: Schematic of grain boundary structure and crack interface as considered by [91].

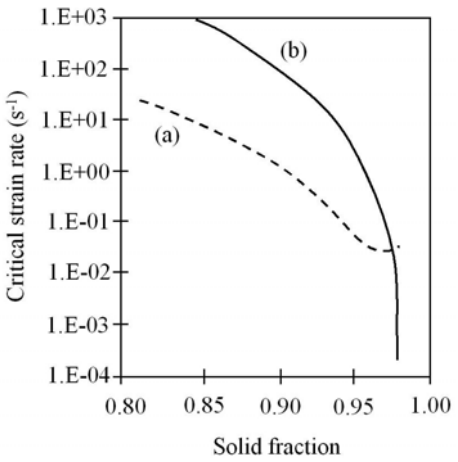

Figure 23: Critical strain rate for crack growth in cast Al-8wt.%Cu binary alloys with (a) columnar and (b) equiaxed microstructures [91].

2.1.2.4 Summary

Most solidification cracking models focus on conditions required for crack occurrence rather than on the mechanisms underlying crack initiation and growth. Over the years, the occurrence of solidification cracking in welds, for example, has been defined in terms of critical stress, strain, or strain rate. A majority suffer from one common fall in that they fail to address how the liquid is fractured. In particular, use has been made of long-held strain based models which do not have any physical basis regarding fracture mechanism. One notable exception to this is the RDG model, where the liquid fracture is specifically related to an interdendritic liquid pressure drop. Recent developments suggest that strain rate conceivably may play a direct role in fracture mechanism, since it controls the liquid pressure drop originating from local deformations. Implementing cracking models into numerical simulations of DC cast aluminum alloys [32,33,97] revealed that none of the models to date can predict crack occurrence, usually providing a relative ranking of alloys in terms of cracking susceptibility. This suggests that a model cannot predict solidification crack formation unless it addresses liquid fracture mechanisms, which are therefore discussed hereafter.

2.1.3 Liquid Fracture Mechanism

From the nature of solidification cracks, crack nucleation must involve liquid film fracture, which involves formation of a liquid-vapor interface, and may occur when the liquid pressure drop due to insufficient liquid feeding to compensate shrinkage falls below some critical value. The mechanism involved in initiating cracking remains to date ill-defined, and is usually related to either decohesion along oxides or pore formation. Pores (gas or vapor) are sometimes cited as potential crack initiation sites. Use of real-time radiography and scanning electron microscopy in fully austenitic welds [19] and investigations of pore surface in titanium welds [98] revealed solidification cracking to possibly form from a pore. However, evidence of porosity cannot always be found because liquid back-filling may cover the original crack surface. Pores, commonly present in aluminum welds, are believed to originate from dissolved hydrogen and/or incomplete liquid feeding of solidification shrinkage [22]. Likewise, mechanisms involved for pore formation in a liquid are far from being completely understood, leading to numerous suggested mechanisms [99], which are here classified into four categories: *homogeneous vapor pore nucleation* (i.e. pore cavitation), *heterogeneous vapor pore nucleation*, *gas pore nucleation*, and *pore formation from pre-existing nucleus*. At the end, the particular case of *porosity in aluminum welds* is reviewed.

2.1.3.1 Homogeneous Vapor Pore Nucleation

Homogeneous vapor pore nucleation involves spontaneous nucleation of vapor pores (i.e. cavitation) in the interior of a liquid solution. Liquids cannot sustain a tensile stress in equilibrium, but will become metastable when exposed rapidly to tension, with the desire to form vapor bubbles [100] which grow until the pressure of the system rises to the equilibrium vapor pressure. Since at least the 1940´s [101], liquids are known to withstand negative pressures (i.e. hydrostatic tension) of considerable magnitude. This reflects upon the difficulty in nucleating pores. Classical nucleation theory applied to vapor pore nucleation [102] defines cavitation to occur when the applied negative pressure, i.e. hydrostatic tension, exceeds the maximum stress a liquid can sustain. A work *W*, associated with the reversible homogeneous nucleation of a vapor bubble, is taken as the sum of the work required to form the volume *V* and area *A* of a spherical pore of radius *r:*

$$W = \gamma A + PV = \left(4\pi r^2\right)\gamma + \left(\frac{4}{3}\pi r^3\right)P \tag{23}$$

, where *P* is liquid pressure and γ is liquid surface tension. The work *PV* is negative for liquid under negative pressure, i.e. hydrostatic tension. Hence, *W* reaches a maximum value W_{max} equal to $W_{\max} = \frac{16\pi\gamma^3}{3P^2}$ for bubbles with a critical radius $r^* = \frac{-2\gamma}{P}$ (Figure 24). Bubbles with radii less than r^* require free energy for further growth and usually disappear without reaching the critical size r^*. Those with radii larger than r^* grow freely with decreasing free energy. Based upon calculations of rate of bubble formation, the fracture pressure is related to the forces required for simultaneous separation of all atomic bonds cut by a plane surface. The rate of bubble formation, i.e. formation of *n* bubbles in *t* seconds, is calculated from the classical nucleation theory, accordingly:

$$\frac{dn}{dt} = \left[\frac{Nk_BT}{h}\exp\left(\frac{-E_A}{k_BT}\right)\right]\cdot\exp\left(\frac{-W_{\max}}{k_BT}\right) \tag{24}$$

, where *N* is the number of molecules in the liquid, k_B is the Bolzmann´s constant, *T* is temperature, and E_A is free energy activation for the motion of an individual molecule of liquid past its neighbors into or away from the bubble surface. Considering the first bubble that forms to fracture the liquid, the fracture pressure P_t is taken as the minimum pressure giving one bubble in t seconds, dn/dt=1/t:

$$P_t = -\left[\frac{16\pi}{3}\frac{\gamma^3}{k_B T \ln(Nk_B Tt/h) - E_A}\right]^{1/2} \tag{25}$$

The fracture pressure P_t, corresponding to one vapor bubble per mole per second, is found nearly independent of the waiting time t and on the free energy activation E_A. Hence, a definite fracture pressure P_f for liquids is approximated by:

$$P_f = -\left[\frac{16\pi}{3k_B T}\frac{\gamma^3}{\ln(Nk_B T/h)}\right]^{1/2} \tag{26}$$

Eq. 26 has been applied to different liquids (Table 1). In particular, pure liquid aluminum at 660℃ is predicted to withstand negative pressures of considerable magnitude, i.e. 30,500 atm (3,050 MPa).

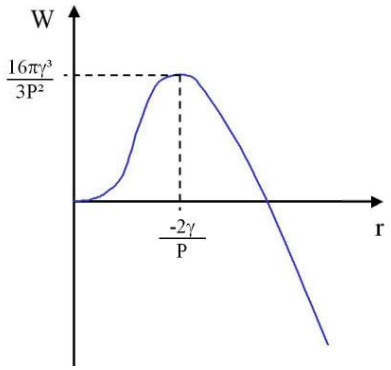

Figure 24: Work (*W*) to form a pore of radius (*r*) according to Eq. 23.

Table 1: Liquid Fracture Pressure P_f Predicted by Homogeneous Nucleation Theory [102]

Liquid	Temperature (℃)	Fracture Pressure P_f (atm)
Water	27	1,380
Aluminum	660	30,500
Iron	1,500	70,800

2.1.3.2 Heterogeneous Vapor Pore Nucleation

Most liquids experimentally exhibit tensile strengths at least one order of magnitude lower than theoretical values predicted by the homogeneous nucleation theory [102]. It is generally agreed that homogeneous nucleation of pores is extremely difficult and unlikely to occur in practice. The frequent occurrence of premature failure has been associated with

heterogeneous pore nucleation at the rough and irregular container surfaces [22], non-wettable foreign substrates [103], and/or the growing S/L interface [7]. This follows experimental investigations, showing the amount of porosity in aluminum castings to be increased with deliberate addition of oxides [103], and reduced when removing the inclusions by filtration [104]. However, the mechanism by which such inclusions or imperfections facilitate pore formation is not well understood.

In order to evaluate theoretical pressure for heterogeneous vapor pore nucleation at a liquid-solid interface, Fisher [102] considered a simplified geometry (Figure 25), assuming the vapor bubble at the liquid-solid interface bounded by a plane and a portion of a spherical surface. The liquid-solid (γ_{LS}), liquid-vapor (γ_{LV}), and solid-vapor (γ_{SV}) interfacial energies are related to the wetting angle (θ), accordingly:

$$\gamma_{LV}\cos\theta = \gamma_{SV} - \gamma_{LS} \tag{27}$$

The value to fracture at the solid-liquid interface ($P_{f(het)}$) is given by:

$$P_{f(het)} = P_{f(\mathrm{hom})} \quad x \quad 1.12\phi^{1/2} \tag{28}$$

, where $\phi = \frac{(2-\cos\theta)(1+\cos\theta)^2}{4}$, $P_{f(hom)}$ is fracture pressure required for homogeneous vapor pore nucleation. Heterogeneous nucleation is energetically favored over homogeneous nucleation on poorly wet substrates (i.e. high wetting angle θ), e.g. Al_2O_3 oxides wet by liquid pure aluminum with a measured wetting angle θ varying between 150.5° and 170° [105-108]. A value of 1,760 atm (176 MPa) is shown required for heterogeneous vapor pore nucleation on Al_2O_3 oxides, according to Eq. 28 (wetting angle 160°). Note that aluminum dendrites should not represent a favored site for heterogeneously fracturing the liquid, since the contact angle of a solid with the liquid from which it is growing is close to zero degrees [106].

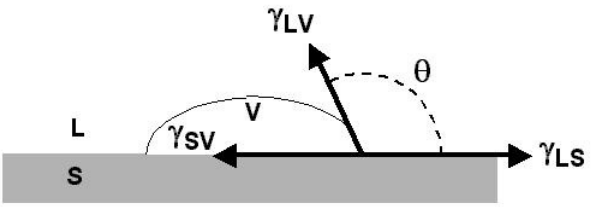

Figure 25: Scheme of heterogeneous nucleation of a vapor pore (*V*) on a solid (*S*) wetted by a liquid (*L*). Represented are wetting angle (θ) and interfacial energies between liquid-solid (γ_{LS}), liquid-vapor (γ_{LV}), and solid-vapor (γ_{SV}) [102].

2.1.3.3 Gas Pore Nucleation

Although several mechanisms for vapor pore nucleation have been postulated until recently, it remains unclear how a pressure drop of 1,760 atm can be achieved under normal solidification conditions [22]. This suggests the involvement of other mechanisms, in particular a possible beneficial effect of dissolved gas contributing to the internal pressure needed for liquid fracture [22,103,109,110]. From Campbell [110], the liquid fracture pressure (P_f) is taken to be the condition when the partial gas pressure (P_g) sufficiently exceeds all external pressures (P_e) to allow pore nucleation:

$$P_g - P_e = P_f \tag{29}$$

P_g is directly proportional to the square of the dissolved gas content in the liquid, according to the Sievert´s law (detailed in paragraph 6.3.1.2). Both calculations (e.g. by implementing the presence of dissolved gas into the nucleation theory, recall Eq. 26) and experiments showed dissolved gas to cause a negligible diminution (less than 0.5%) in the intrinsic strength of the liquids [111]. Indeed, in the absence of pre-existing gas cavities, bubble nucleation requires exceedingly high levels of supersaturation, in excess of 100 times or more [99]. This demonstrates that the nucleation theory simply cannot fulfill the fracture pressure requirement within castings, even when taking into consideration the partial gas pressure in addition to the shrinkage pressure drop and the presence of the most efficient foreign substrate in the liquid [22]. Nevertheless, the fact is that pores in castings are rather the norm than the exception. Therefore, this suggests that the discrepancy between theoretical and experimental values of the liquid tensile strength is not to be explicable in terms of dissolved gas, but must presumably be sought in the pre-existence of metastable pore nuclei in the liquid. This approach is detailed hereafter.

2.1.3.4 Pore Formation from Pre-Existing Nucleus

Water, supersaturated with a gas, was shown not to produce bubbles unless gas pockets are available on dust particles surfaces [101], these gas pockets acting as pre-existing nuclei from which a bubble could form. Consideration was also given to the stability criterion of a tiny bubble in the interior of liquid, which is dictated by [22]:

$$P_g - P_e = \frac{2\gamma}{r} \tag{30}$$

, where P_g is partial gas pressure, P_e is external pressure, γ is liquid surface tension, and r is pore radius. A gas embryo may expand as a result of decreasing external pressure (i.e.

small P_e) or supersaturated liquid (i.e. large P_g), enough to balance the high surface tension force of liquid, and will grow spontaneously when its radius exceeds the critical radius r^* that satisfies Eq. 30. In the presence of metastable gas cavities, the energy required for pore formation (Eq. 30) is very much lower than for the classical nucleation case (recall Eq. 28), given that less interfacial free energy is needed for the cavity to grow to a critical size when the system is made supersaturated [99]. Therefore, simulations of metal solidification usually consider a pre-existing pore nucleus, its nature being rarely specified, which becomes activated at a specific gas supersaturation [112,113]. In simulations of solidifying aluminum alloys, the nucleus is usually located at the surface of an oxide, from which a pore grows controlled by liquid pressure drop and gas segregation [114]. The pores start to grow as a sphere to minimize the energy associated with the gas/liquid interface, but may later become complex in shape since constrained by the developing surrounding solid dendrites.

2.1.3.5 Porosity in Aluminum Welds

In cast and welded aluminum alloys, porosity is a major defect often encountered, as revealed by high-resolution X-ray tomography in cast ingots of aluminum alloys [115]. Pore formation is influenced by several factors: *hydrogen contamination*, *alloy composition, process parameters*, and *inclusions*. Details are given below.

2.1.3.5.1 Hydrogen Contamination

Among the factors promoting porosity in cast and welded aluminum alloys, hydrogen is the only gas with significant solubility in the liquid phase, and thus the sole source of gas porosity [22,116]. Porosity was indeed reduced when lowering the hydrogen level [112,117], for example with the sparging of a gas (nitrogen, argon, or chlorine) into the aluminum alloy melt prior to casting [104]. Hydrogen in molten aluminum often results in porosity, because of the sharp drop in solubility when going from liquid to solid [116,118]. During solidification of pure aluminum, the solubility of hydrogen at the solid-liquid interface (660°C) drops from 0.69 to 0.036 ml/100g [116], resulting in a small partition coefficient (k_H=0.05), with hydrogen concentration increasing in the interdendritic liquid. Hydrogen contamination can arise from moisture and hydrogen in shielding gas, hydro-carbons (e.g. grease, machine oil), or hydrated oxide films present on metal surfaces. The contributions of different hydrogen sources to porosity were compared in case of Alloys 5083 and 6061 GMA welds with Alloy 5356 filler addition [119], and found in decreasing order of significance: hydrogen content in the filler metal, hydrogen solubility in weld metal (strongly dependent on alloy

composition), hydrogen content in shielding gas, and hydrogen content in base metal. Indeed, decreasing base metal hydrogen levels by vacuum degassing caused only a slight drop in weld porosity content [119].

When entrapped moisture enters the welding arc column, it decomposes and reacts either with Al (solid or liquid) to form Al_2O_3 (solid) and H_2 (gas) [116] or with Mg present in aluminum alloys to form MgO (solid) and H_2 (gas) [120]. Also possible for temperatures exceeding 815°C is the following reaction [120]:

$$Al_2O_3 \cdot H_2O + Mg \rightarrow MgAl_2O_4 + H_2 \tag{31}$$

The hydrogen is then transferred into the molten weld pool in accordance with Sievert´s Law. However, the role of hydrogen on cracking is not well understood, and it could conceivably have either positive or negative effects. Dissolved hydrogen should make it easier to cavitate, which is one of the possible mechanisms for crack initiation [22,116,121]. Pores may also serve to feed shrinkage, lowering the interdendritic liquid pressure drop [89], and hence reducing the susceptibility to solidification cracking.

2.1.3.5.2 Alloy Composition

Alloy composition affects both hydrogen solubility and solidification path, and thus has a major influence on porosity amount in cast and welded aluminum alloys. Lower hydrogen solubility and larger freezing range should favor porosity formation. This is well illustrated in Al-Mg binary alloys. A 6 wt.% magnesium addition almost doubles the hydrogen solubility in aluminum weld metal, from 0.70 ml/100g H_2 in commercially pure 1100 aluminum to 1.25 ml/100g H_2 in Al-6.5wt.%Mg binary alloy [120]. However, Al-Mg alloys are more sensitive to hydrogen porosity than high purity aluminum because of their large freezing range [116]. Therefore, and following from observations in nickel based alloy welds with nitrogen gas porosities [122], adding alloying elements that increase hydrogen solubility without increasing the solidification range should reduce the amount of weld metal porosity.

2.1.3.5.3 Process Parameters

The size, distribution, and amount of hydrogen pores generated in cast and welded aluminum alloys are dependent upon experimental conditions like solidification mode, cooling rate, degree of convective fluid flow, bead shape, shielding gas mixture, and external pressure. Porosity is strongly reduced in castings when lowering local solidification time (i.e. fast cooling rates) [112,117] and in welds when increasing the welding speed [120], possibly

due to the kinetics of pore nucleation and growth. On the other hand, higher heat inputs reduce weld metal porosity [120], probably because it ensures longer weld pool residence time and thus enables more bubbles to float up and escape, these bubbles absorbing the hydrogen dissolved in the weld pool. Also, flat welding produces welds contain less porosity than overhead welds, since gas bubbles can escape. Shielding gas also affects porosity amounts in GTA weld metal, this amount being reduced when using helium instead of argon, and even more reduced with a 65%He-35%Ar mixture [120]. Finally, higher external pressures reduce substantially porosity amount in aluminum weld metals [120,123], since higher pressures must be overcome to expand a pore.

2.1.3.5.4 Inclusions

Inclusions, e.g. intermetallic compounds and oxides, are known to affect the amount of porosity in cast and welded aluminum alloys, but the mechanisms involved are still not well known. In cast aluminum alloys, porosity depends not only on the hydrogen content, but also on the metal cleanliness, where higher amount of inclusions [123,124] or deliberate addition of oxides skimmed from the casting melt surface [103] increased the porosity amount. It was also proven that aluminum alloy melts rich in hydrogen are not capable of nucleating bubbles in the absence of inclusions [104], the porosity amount being reduced at a given hydrogen content when filtering the aluminum alloy melt to remove both metallic and non-metallic inclusions. These observations suggest that folded oxide films, formed due to turbulent mould filling, may provide suitable sites for heterogeneous pore nucleation [22,125]. Surface irregularities, like the rough and irregular surface of aluminum oxides, may trap air pockets, which could act as pore nucleation sites [103,126]. Hence, the surface of filler wire, which contains oxides and absorbed moisture, is a major source of hydrogen, because of the large surface-to-volume ratio, i.e. high quantity of surface oxide layer compare to the filler metal volume. Choosing filler electrode with bigger diameters should reduce the hydrogen contamination and the amount of oxides brought into the weld.

Embryos for pore formation may also be present on other insoluble foreign particles; for example, strontium and sodium additions increase the porosity amount, possibly due to a reduction of surface tension or an increase in inclusion content [109,124]. These foreign particles may be entrapped when the advancing solid/liquid interface exceeds a critical velocity [106,127], a critical welding speed being indeed found for austenitic chromium-nickel steel GMA welds above which porosity forms [128]. Numerical simulations show that the growth of the bubbles present on these entrapped particle surface require pressure drops on the order of several atmospheres, which can be attained in directional solidification when the

crevice is between the inclusion and the solid/liquid interface [106]. These models also suggest that improving the particles wettability should reduce the amount of porosity by enhancing the engulfment tendency. Considering grain refining $(Al,Ti)B_2$ particles, their wetting angle with liquid pure aluminum is close to 0°, which makes these particles easily engulfed, leading to a very short period with favorable conditions for pore growth [106]. In fact, $(Al,Ti)B_2$ particles do not affect significantly the porosity amount in aluminum castings [106,109]. Also, trace amounts of magnesium into aluminum alloys may improve the engulfment tendency of alumina inclusions due to the formation of a spinel layer ($MgAl_2O_4$), whose wettability with liquid aluminum is known to be good [106,107].

Analyzing porosity in Alloy 2219 welds made with electron beam and GTA welding processes, Fujii et al. [123] suggested porosity to possibly nucleate heterogeneously on aluminum oxides through the chemical reaction:

$$4Al(l)+Al_2O_3(s) \rightarrow 3Al_2O(g) \tag{32}$$

Addition of alloying elements that are more reactive than Al on Al_2O_3 particles (e.g. Li and Mg [107]) should help to avoid porosity by forming a new compound at the oxide surface, and thus avoid the reaction given by Eq. 32. However, this chemical reaction seems unlikely to occur in aluminum welds, since it is observed for temperatures near 2,000 K [107].

2.1.3.6 Summary

Even if the causes and effects of porosity have been extensively investigated, little is known about the mechanisms involved for nucleation and growth of gas bubbles in the weld pool. It is still uncertain whether nucleation of hydrogen bubbles occurs in the interior of liquid or along a particle surface, and what role is played by oxide inclusions, welding parameters, and solidification conditions. However, since numerous parameters can affect porosity as listed previously, hydrogen content cannot alone be associated with a given amount of porosity. A more fundamental approach to the porosity problem in aluminum welds is therefore needed.

2.1.4 Semi-Solid Material Behavior Characterization

Although the rheological behavior of semi-solid alloys is a major parameter when modeling solidification cracking, it is usually poorly known. *Tensile*, *shear*, and *compressive* tests have been developed over the years to characterize semi-solid materials, and can be conducted upon solidification or remelting, and under both isothermal or continuous cooling

conditions to simulate thermal cycles experienced in castings and welds [129]. However, reproducing weld thermal cycle usually presents difficulties due to the high heating and cooling rates concerned.

Hot tensile tests are very popular and often used upon flat shaped specimens to determine the strength to failure [42,49,52,130], although tensile experiments are difficult to carry out because the measured stresses are low and the amount of strain that can be achieved is limited. In order to reach higher deformations, shear tests have been developed. One configuration consists of sliding one part of a mould relatively to the other at a constant deformation rate [131]. In an other configuration, a four-blade vane is rotated at a constant rotation speed of 5 rpm into a semi-solid alloy (Figure 26) [132]. The torque required to rotate the vane is related to the yield stress assuming the shearing surface area to be the smallest cylinder including the vane when rotating. When undergoing solidification, the coherency temperature is evidenced by a sharp deviation of the torque-temperature curve, due to higher torques required to rotate the vane in a continuous solid skeleton.

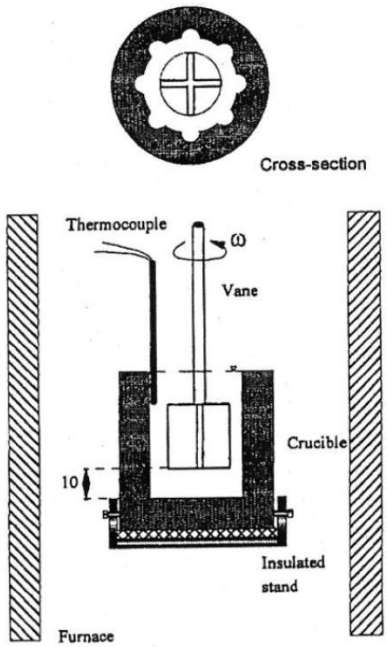

Figure 26: Schematic set-up of four-blade vane shear test [132].

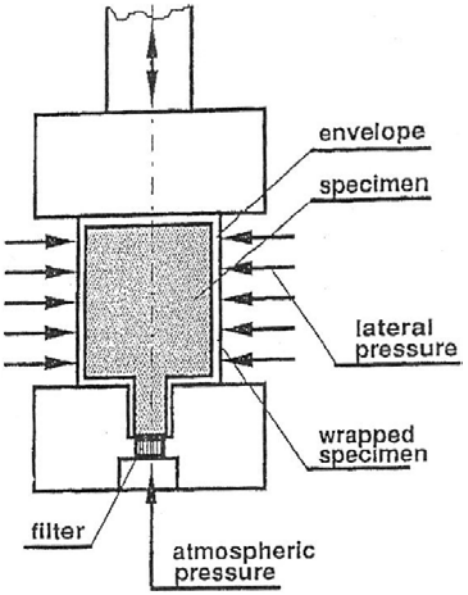

Figure 27: Schematic set-up of drained triaxial compressive test [133].

Also important are the compressive tests [133,134]. In particular, the drained triaxial compressive test (Figure 27) [133] consists of compressing a specimen wrapped into a deformable envelope with a superimposed controlled lateral pressure, in order to expel the

liquid and determine the volumetric strain and strain rate evolution. A filter enables the eutectic liquid to flow out during the densification of the specimen. Several properties can be characterized, like the densification behavior of the solid skeleton, the viscoplastic properties of the solid phase at elevated temperatures by expelling the eutectic liquid, or the liquid fraction – temperature relationship.

2.1.5 Weldability Characterization

Weldability characterization is required to evaluate the applicability of the solidification cracking models. The term "weldability" designates, in a given alloy, not only the ability to produce defect-free weld, but also to provide the required joint properties and quality. The weldability of an alloy is function of the environment (corrosion resistance and strength requirements), welding process, alloy composition, and joint design and quality (cracking and porosity tolerances). In the present work, "weldability" is examined in terms of susceptibility to weld solidification cracking. Since weldability is not a well-defined property, a lack of standard *testing techniques* and *quantification* exist, as detailed below, leading to possible poor correlation or even discrepancies between different studies.

2.1.5.1 Weldability Testing Techniques

A broad variety of weldability tests have been developed over the years and are specifically designed to generate cracking by promoting special straining conditions in the region undergoing solidification [51,135,136]. The weldability testing techniques can be classified into two categories: the *intrinsic weldability tests* promoting cracking by naturally occurring thermal contraction and solidification shrinkage, and the *extrinsic weldability tests* promoting cracking by external loading of the solidifying specimen.

2.1.5.1.1 Intrinsic Weldability Tests

"Intrinsic", also referred to as "representative", weldability tests somewhat represent the thermo-mechanical conditions experienced when welding an actual structure. These tests are self restraining, i.e. thermal contraction and solidification shrinkage induced by the specimen design and/or fixture promote cracking. The complex interactions involved in these tests make it difficult to isolate the metallurgical from the mechanical factors. The intrinsic tests include *casting tests* and *self-restraint welding tests*.

Casting Tests. The "weldability" of an alloy has been evaluated using casting tests, as it is generally assumed that the solidification cracking susceptibility in casting is representative of that in weld, even if large differences in mass, time, and temperature gradient exist. These tests consist in pouring the melted alloy into a pre-shaped mould that is made with a low thermal expansion and high melting point material. The pouring temperature has to be controlled since it affects the length of the cracks [137].

Different mould designs exist. The ring casting test consists of pouring the melt into a ring shape groove concentric with a core (Figure 28), the resistance of the core promoting cracks usually parallel to the solidification growth direction. This test has been abundantly used to study aluminum alloys [6,9,137]. The "harp" or "backbone mould" test consists in casting a "backbone" shape specimen in an horizontal [138] or vertical configuration [69] (Figure 29). The mold is designed to start solidification simultaneously at both the specimen edges towards the specimen center, thus promoting cracks perpendicular to the solidification direction at the specimen mid-length. The maximum length L or smallest diameter D for non-cracked specimens may be chosen as solidification cracking susceptibility indexes. The cast-pin test [139] consists of pouring the molten metal into a copper mold having a tapered cylindrical pin shape (Figure 30), promoting circumferential cracks. The severity of the test depends upon the diameters and length of the pin. A major drawback of these tests is the non-controlled solidification conditions. The Warrington test (Figure 31) was developed to overcome this problem, reproducing the thermal conditions experienced in direct-chill casting [140]. A water-cooled copper chill with a tapered conical portion is inserted to a pre-determined depth inside an internally tapered steel crucible placed in an open furnace and containing the molten metal. The water flow inside the copper chill controls the cooling rate conditions. The test is designed to provide a casting with 10 mm wall thickness.

Self-Restraint Welding Tests. These tests generate cracking in weld metal due only to their design. The patch test [141] consists in making a circular bead-on-plate weld (Figure 32). A continuous weld centerline crack initiates at an angle θ from start and propagates until the weld end. Small discontinuous cracks may form shortly before the angle θ. There are numerous versions of this test, as described in a review on the subject [142]. Another test, referred to as the T-test [8], consists in welding two plates in an "inverted T" configuration (Figure 33).

Figure 28: Schematic set-up of ring casting test (cross-section).

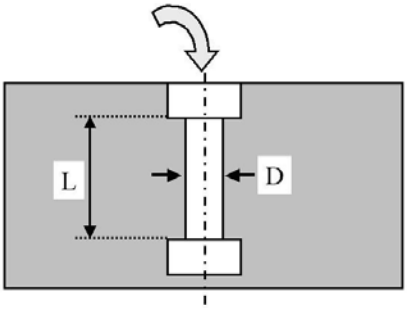

Figure 29: Schematic set-up of harp test (cross-section).

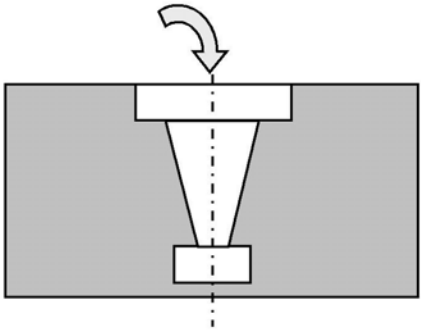

Figure 30: Experimental set-up of cast-pin test (cross-section).

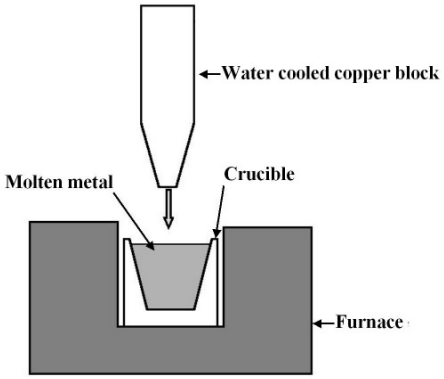

Figure 31: Schematic set-up of Warrington test (cross-section).

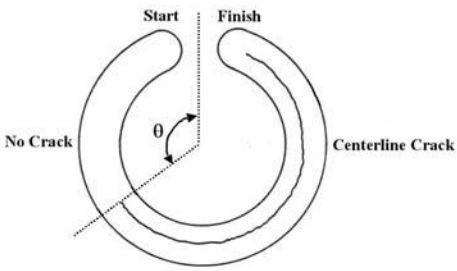

Figure 32: Experimental set-up of patch test (top view).

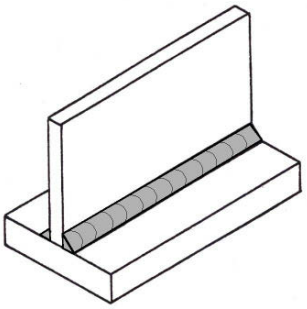

Figure 33: Schematic set-up of T-test.

The plate edge effect has also been used to generate cracks in bead-on-plate welds. The degree of restraint may be controlled by machining slots at the plates edges, the depth of the slots being either constant (Lehigh test) [143] or gradually increasing from one side of

the plate to the other (Houldcroft test, Figure 34) [144]. The minimum slot depth without crack formation is chosen as the solidification cracking susceptibility index. Especially, the Houldcroft test has been useful in evaluating compositional effects on Al-Zn-Mg alloys weldability [46,47], and is particularly interesting to investigate conditions required for both crack initiation (welding from left to right, Figure 34) and growth (welding from right to left, Figure 34). Similar in concept to the Houldcroft test, the fan-shaped cracking test [145] consists in welding along a plate centerline, the width of the plate gradually increasing from one side of the plate to the other. Another configuration, referred to as the free-edge test [48], consists in restraining only one edge of the specimen, the other being free (Figure 35), and was developed to evaluate the cracking susceptibility of aluminum bead-on-plate Nd:YAG laser welds. A critical distance a_{cr} between the weld and the free plate edge exists under which cracking occurs.

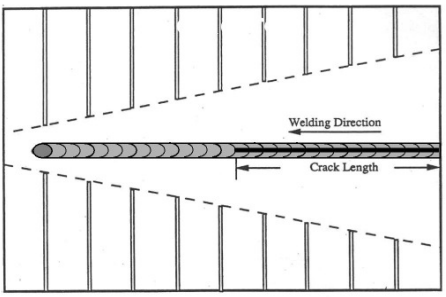

Figure 34: Experimental set-up of Houldcroft test (top view).

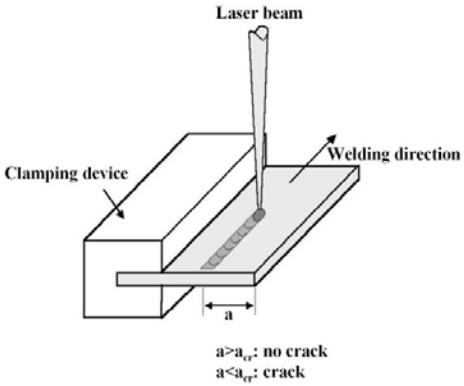

Figure 35: Schematic set-up of free edge test.

2.1.5.1.2 Extrinsic Weldability Tests

"Extrinsic", also referred to as "simulative", weldability tests seek to isolate the metallurgical from the mechanical factors by applying a controlled restraint, the weldability being directly related to applied strain or strain rate (crack versus no-crack) for a given alloy and welding condition. Unfortunately, the thermo-mechanical history is inherently different from the real-world welding conditions. These tests include *"relative moving plates"*, *"bent plate"*, and *"planar applied restraint"* tests.

"Relative Moving Plates" Tests. These tests consist of welding two plates in a butt-joint configuration while rotating one plate relative to the other at a constant angular speed

around an axis parallel (Murex test, Figure 36) [146] or perpendicular to the welding direction (variable deformation rate (VDR) test, Figure 37) [70]. The Murex test determines a critical angular speed ($\dot{\theta}$) to form a crack. In the VDR test, the weld is made towards the rotation axis. The angular speed ω is maintained constant, leading to a decreasing local deformation rate $\dot{\delta}$ as the welding torch advances. At a distance *L* from the rotation axis, $\dot{\delta}$ equals:

$$\dot{\delta} = \varpi \cdot \mathrm{L} \tag{33}$$

The deformation rate, calculated at the location where crack stopped, is taken as the critical value to grow a crack.

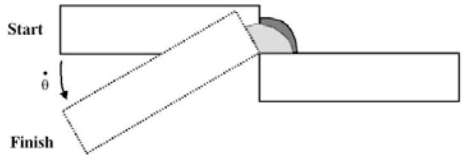

Figure 36: Schematic set-up of Murex test.

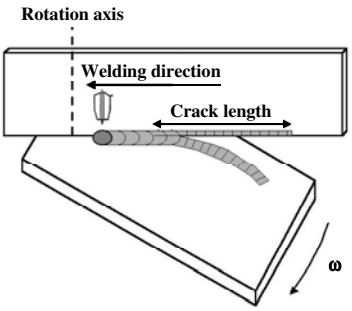

Figure 37: Schematic set-up of variable deformation rate test.

"Bent Plate" Tests. These tests consist in subjugating the solidifying weld pool during welding to controlled amounts of strain, by bending the specimen around a curved mandrel whose axis is either perpendicular (varestraint test, Figure 38) [147] or parallel (trans-varestraint test, Figure 39) [148] to the welding direction. The magnitude of the augmented applied strain (ε) is related to the radius of curvature of mandrel (*R*) and the specimen thickness (*t*), accordingly:

$$\varepsilon = \frac{t}{2R} \text{ x } 100\% \tag{34}$$

The varestraint and trans-varestraint tests were originally developed for a assumed "instantaneous" bending application, the controlled strain being applied in approximately 100 ms. Hence, the number of cracks is believed bounded by the number of grain boundaries and the length of each crack by the size of the mushy zone. This may not be always the case, with weld in-situ observations revealing crack growth even at high applied strain rates [27]. The use of MISO measurements (described in paragraph 2.1.5.2.2)

revealed actual strain rates in the weld up to 130 %/s [27,46,67,149], far exceeding the strain rates in real-world conditions (less than 8 %/s) [46] and the critical strain rate to form a crack (less than 5 %/s in arc welded aluminum alloys) [12,70,150]. This brings into question how these test results relate to real-world behavior. Moreover, the weld metal shows much higher strains (over 2%) and strain rates (over 100 %/s) than the applied strain (0.5 %) and strain rate (40 %/s) [27,62] as calculated with Eq. 34. These discrepancies suggest a hinging effect, whereby plastic deformation is concentrated in hot material along the weld seam, as shown schematically in Figure 40.

The original varestraint (Figure 38) and trans-varestraint (Figure 39) tests have since been developed into a variety of configurations. The slow bending trans-varestraint test [12,67], also referred to as the modified varestraint test (MVT) [135,151,152], consists of controlling the ram speed to reach lower applied strain rates. The spot varestraint test [153], used primarily for liquation cracking, consists of simultaneously bending “instantaneously” a stationary weld and extinguishing the torch (Figure 41), which generates cracks encircling the weld pool and crater cracks. This variant does not enable separation of the mechanical factors from the metallurgical ones (e.g. solidification shrinkage). Another variant, introduced for studying stainless steel laser weldability [154], consists of wrapping the weld coupon around a cylindrical mandrel during welding, imposing a fixed strain on the weld pool (Figure 42). Unlike the varestraint test, strain here is applied at an oblique angle to the welding direction. This test proved useful in comparing two different austenitic stainless steel alloys (alloys 309 and 304), establishing critical deformation rates needed to form cracks. However, it has numerous drawbacks, including the oblique (abnormal) angle for strain application and the inability to know or measure local strain or strain rate.

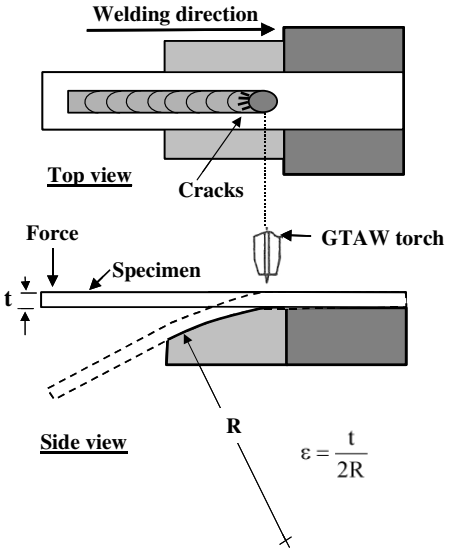

Figure 38: Schematic set-up of varestraint test.

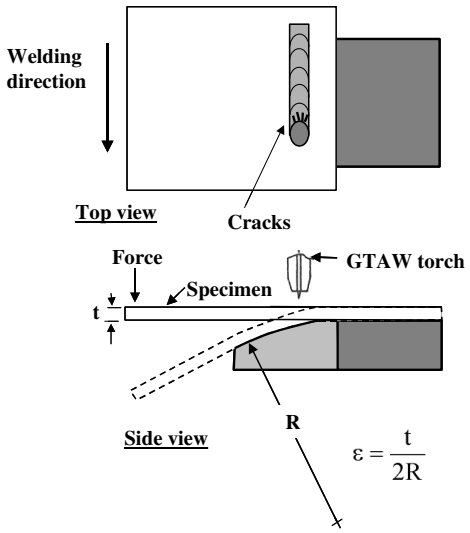

Figure 39: Schematic set-up of trans varestraint test.

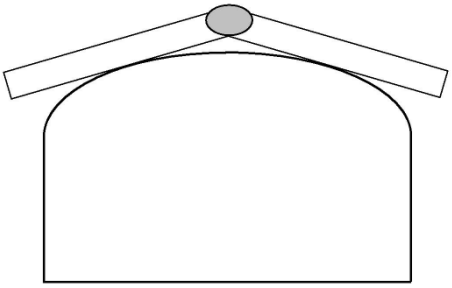

Figure 40: Schematic illustration showing hinge effect in trans-varestraint testing.

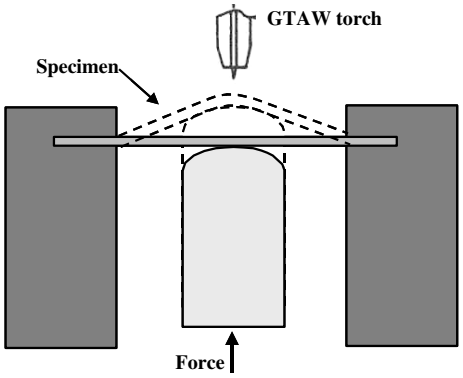

Figure 41: Schematic set-up of spot varestraint test.

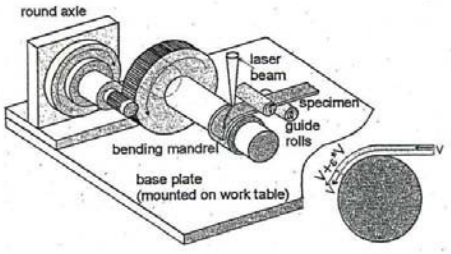

Figure 42: Schematic set-up of test developed for studying stainless steel laser welds [154].

"Planar Applied Restraint" Tests. These tests consist of applying a controlled restraint in the plane of the plate coupon. Pre-restraining the weld has been used to enhance strains during welding. This can be done by using a special welding fixture (Figure 43) allowing the welding to be performed under variable levels of restraint (by varying the height *H*) applied to aluminum welds [155]. Also possible is a pre-load applied transverse to the welding direction as in the Sigmajig test (Figure 44) [156] and the pre-loading tensile strain (PLTS) test (Figure 45) [157].

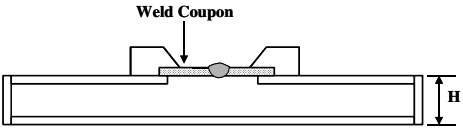

Figure 43: Schematic set-up of variable restraint box fixture [155].

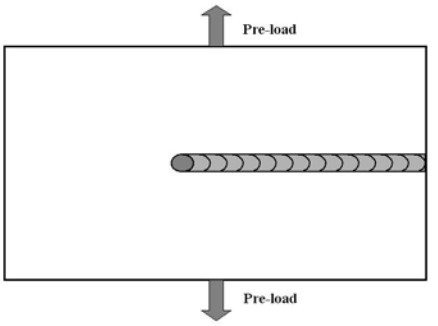

Figure 44: Schematic set-up of Sigmajig test (top view).

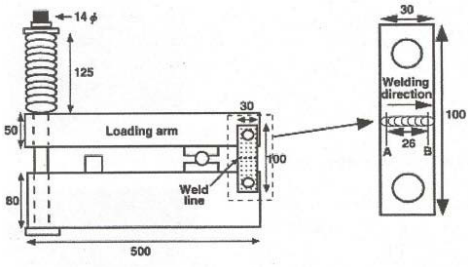

Figure 45: Schematic set-up of preloading tensile strain (PLTS) test [157].

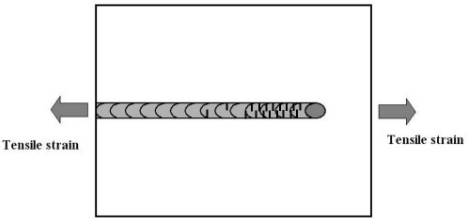

Figure 46: Schematic set-up of PVR test.

Also used was the application of a restraint during welding processing. The variable tensile strain test [150] consists of applying a displacement transverse to the welding direction and away from the weld, and was later successfully used with high deformation rates of 130 %/s around the weld to simulate the trans-varestraint test conditions [62]. The programmable deformation cracking (PVR) test [71-75] consists of applying a tensile strain during welding in the direction of welding while ramping up the strain rate (Figure 46), favoring cracking along grain boundaries perpendicular to the welding direction.

2.1.5.2 Weldability Quantification

Quantifying weldability is necessary at least to rank alloys, and at best to make explicit the conditions required for cracking. Even if a simple crack - no crack criterion can be used, other weldability indexes will hopefully lead to a finer ranking. While *crack length parametrics* permit only a relative ranking, *strain parametrics* relate to an actual cracking mechanism and hence can be used in the modeling of solidification cracking, allowing for future prediction of cracking.

2.1.5.2.1 Crack Length Parametrics

Crack length measurements are commonly used, often reported in terms of mean, maximum, or total accumulative crack length, as it is generally assumed that for fixed testing conditions, an alloy with higher cracking susceptibility should result in more extensive cracking [6,8-10,49]. However, problems can be encountered when attempting to rank weldability in terms of crack length, particularly for alloys with different thermal properties resulting in different weld pool shape. To overcome this problem, Lippold [51] related the maximum crack distance (MCD) in a trans-varestraint test to a corresponding temperature range with the aid of a thermocouple plunged into the weld pool. The MCD is obtained at high applied strain and measured normal to isotherms. The resulting value, or solidification cracking temperature range (SCTR), is believed to be independent of welding parameters and to represent a characteristic material-specific property reflecting relative weldability. A larger temperature range is related to higher solidification cracking susceptibility since it suggests the possibility for more strain build-up and a more difficult condition for liquid feeding.

To relate a crack distance in a trans-varestraint test to a corresponding temperature range requires the assumption of instantaneous bending in order to neglect the growth of the crack during bending. However, some investigations have demonstrated a problem with this assumption. A theoretical approach [76] relating crack length to the ductility of the mushy zone predicts longer cracks to form at higher welding speeds and lower applied strain rates, which agrees with in-situ observations of weld metal using the slow bending trans-varestraint test. A recent work [27] confirms these results with the aid of high speed photography observations in varestraint tests. For a 4% applied strain, a crack initiated in the mushy zone (at $f_s = 0.78$) at a local strain of 1%, and then grew simultaneously towards the weld pool and away from it. The advancing crack tip propagated at the velocity of the welding torch (3.3 mm/s), maintaining its relative position to a constant solid fraction ($f_s = 0.78$) and terminated as the applied strain dissipated. The retreating crack tip grew at a higher velocity

and terminated when it intersected the advancing solidus temperature. During the period of the 4% strain application (approx. 120 ms), the weld pool advanced of 0.4 mm, which is the same order of magnitude as the measured crack length of 0.7 mm. This demonstrates that the MCD measurements cannot be related to a characteristic temperature range (e.g. SCTR) in any straight forward manner, and becomes even more mis-representative of a characteristic temperature range at low applied strain rates and high torch travel speeds.

2.1.5.2.2 Strain Parametrics

Assuming that all thermo-metallurgical factors are held constant (e.g. constant alloy composition and cooling rate), it is useful to concentrate on the thermo-mechanical conditions required for crack formation. Measuring local strain in the vicinity of the mushy zone behind a moving weld pool is one key to the establishment of critical cracking conditions, verification of numerical simulations, and eventual prediction of cracking behavior, since solidification cracking models can estimate the cracking susceptibility of a material based upon local strain conditions. Such measurements pose some unique challenges primarily associated with the high temperatures encountered in welding. Therefore different methods have been developed.

Strain can first be measured using extensometers [158] or an LVDT [72] spanned across the weld and connected to small diameter pins attached to opposite sides of the joint, either above or below the plate surface. Strain is measured as the welding torch passes between the affixed pins.

Other methods consist of real-time observations of a “pattern” located at the surface of the specimen, as micro-vickers indentation marks [46], scribe marks [37], or moiré-fringe analysis of grid patterns [159,160]. One method, referred to as the digital image correlation (DIC) technique [161,162], employs the computer aided tracking of a random speckle pattern painted onto the plate surface prior to welding. The speckle pattern is created either by using coherent light with a laser beam to create a grainy pattern on the object surface by a diffraction effect or by applying on the specimen surface a paint containing speckles. Images of the same pattern at two different instants are correlated to calculate the strain distribution over the analysis area, for example by using the algorithm developed by Sutton et al. [162]. One technique, referred to as measurement by mean of in-situ observation (MISO), has been specially developed to measure strain across few grains within the weld mushy zone making use of small particles present on the weld surface [56,62,149]. The relative movement of these particles is tracked using high speed photography, typically providing an effective gage length between 0.9 and 1.7 mm. The chosen discontinuities, always on opposite sides of the

crack, may be either fixed at the crack initiation site (“fixed gage method”) or different at each instant and located at the crack tip (“moving gage method”). These optical techniques have the advantages to be non-contacting and insensitive to the temperature changes, but usually require flat surfaces and optical access to the specimen.

2.2 Al-Mg-Si Alloy System

The present work investigates the solidification cracking susceptibility of controlled mixtures of alloys 6060 and 4043, principally belonging to the Al-Mg-Si alloy system. Details are given below regarding the *solidification path* and *weldability* of the Al-Mg-Si alloy system.

2.2.1 Solidification Path

It has long been observed that the solidification cracking susceptibility of aluminum alloys is strongly dependent upon the alloy composition and solidification path. Equilibrium phase diagrams for Al-Mg and Al-Si binary alloys (Figures 47 and 48) reveal, for the aluminum end, simple solidification paths involving the intermetallic phases Mg_5Al_8 and Si, respectively. Equilibrium phase diagram for Al-Mg-Si ternary alloy system (Figure 49) consists of a quasi-binary line occurring at a fixed magnesium-silicon ratio (Mg/Si = 1.73). Alloys that meet this criterion behave like a binary system consisting of α-aluminum and Mg_2Si. Using the quasi-binary as a line of reference, alloys rich in silicon will form Si in addition to Mg_2Si, whereas alloys rich in magnesium will tend to form Mg_5Al_8 [163]. The alloy examined in this study, Alloy 6060 (0.6 wt.% Mg + 0.4 wt.% Si) welded with 4043 filler metal (5 wt.% Si), resides on the silicon-rich side of the quasi-binary line.

However, due to the presence of the impurity iron, the phase reactions that actually occur are considerably more complex, as observed as early as 1927 [164]. Iron is the most common impurity present in commercial aluminum alloys. Even at low concentrations, iron plays a significant role in aluminum solidification, due to its low solid solubility in aluminum (0.05 wt.% Fe at 655°C) and strong tendency to partition (equilibrium partition ratio: k_{Fe} = 0.03). While normally present in small amounts around 0.2 wt.% (0.3 wt.% Fe max in 6060 extrusions; 0.8 wt.% Fe max in 4043 filler metal [165]), iron tends to form numerous different intermetallic compounds with aluminum and silicon, thereby affecting the solidification sequence [166].

Equilibrium phase diagram for Al-Fe binary alloys (Figure 50) reveals, for the aluminum end, simple eutectic solidification involving the intermetallic phase $FeAl_3$. In Al-Mg-Fe ternary

alloys, the microstructure consists simply of intermetallic phases Al_5Mg_8 and $AlFe_3$, with no ternary compound being formed [163]. In Al-Si-Fe ternary alloys, numerous intermetallic phases may form near the equilibrium conditions, like β–Al_5FeSi (long needles), α–Al_8Fe_2Si (Chinese script), δ–$FeSi_2Al_4$ at high Si content and γ–$FeSiAl_3$ at high Fe and Si contents [163,167,168].

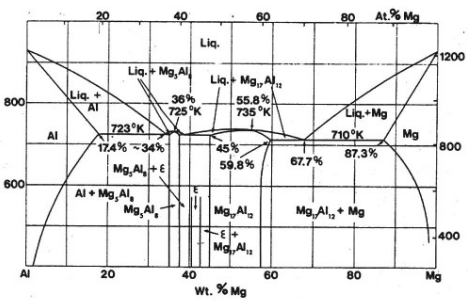

Figure 47: Al-Mg equilibrium phase diagram [163].

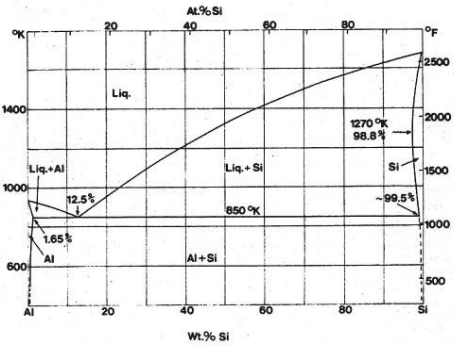

Figure 48: Al-Si equilibrium phase diagram [163].

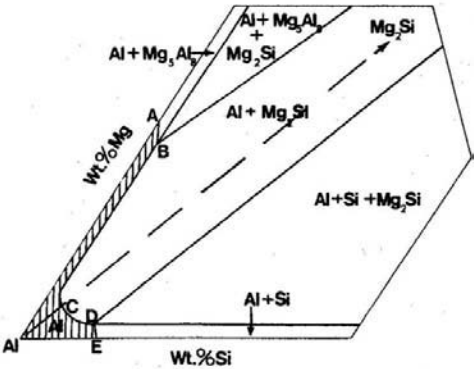

Figure 49: Ternary phase equilibrium diagram for Al-Mg-Si showing solidus surfaces and quasi-binary line (dashed) [163].

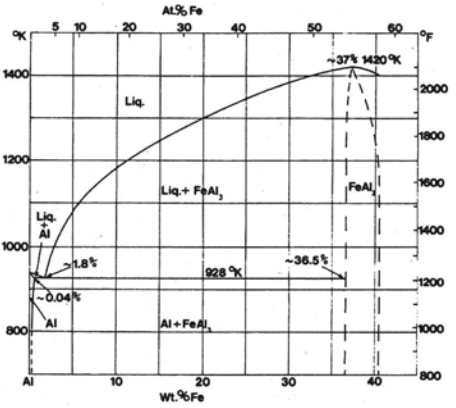

Figure 50: Aluminum end of Al-Fe equilibrium phase diagram [163].

When casting an Al-Mg-Si-Fe quaternary alloy typical of Alloy 6060 welded with a 4043 filler, phases normally expected are detailed in Table 2, and include β-Al_5FeSi, α-Al_8Fe_2Si and π-$Al_8FeMg_3Si_6$ phases in addition to Mg_2Si and Si [53,163,167-172], and corresponding reactions suggested in Table 3. Metastable intermetallic phases might also form, like α´, α´´, α_T, q_1. Moreover, the nature, size, morphology, and amount of these intermetallics depend upon the alloy composition and cooling rate conditions [53,169,170].

Indeed, higher iron contents favor the "binary" over the "ternary β–phase" (Table 3) [163]; lower Fe:Si ratios favor the β–Al_5FeSi over the α–Al_8Fe_2Si phases [163,173]; higher cooling rates reduce the size of the intermetallic phases, shift the reaction forming the "ternary β phase" towards higher Fe contents, and disperse the β–Al_5FeSi particles [53,163,169,170]; low (0.1 °C/s) and high cooling rates (20 °C/s) favor the β–Al_5FeSi over the α–Al_8Fe_2Si, but the β–Al_5FeSi is inhibited at intermediate cooling rates (10 °C/s) [174]; finally, higher casting superheat favors the α–Al_8Fe_2Si over the β–Al_5FeSi phases [167], probably related to the transformation of γ–Al_2O_3 into α–Al_2O_3 inclusions, where γ–Al_2O_3 inclusions possibly serve as effective nucleation sites for the β–Al_5FeSi phase [174].

Table 2: Phases to be Expected in Al-Mg-Si-Fe Quaternary System for Composition Range Corresponding to Alloy 6060 with Alloy 4043 Filler Addition [163,171,172]

Phase	Structure	Lattice Parameters (10^{-10}m)				Composition	Appearance
		a	b	c	Angle (°)		
α-Al [163,172]	FCC	4.049	/	/	/	100 wt% Al	White
Primary Si [163]	FCT	5.431	/	/	/	100 wt% Si	Dark gray
β-AlFeSi[163,171] (Al_5FeSi)	Monoclinic	6.12	6.12	41.50	α=91.0°	59wt%Al+18wt%Si+3wt%Mn+21wt%Fe or 55-63wt.%Al+25-30wt%Fe +12-15wt%Si	Gray needles
β*-AlFeSi [171] β´-AlFeSi [172]	Monoclinic	8.90	4.90	41.60	β=92.0°	-	Gray needles
Mg_2Si [163]	Cubic	6.35-6.40	/	/	/	63.2wt%Mg+36.8wt%.Si	Black
π-AlFeSi [163] $FeMg_3Si_6Al_8$	Hexagonal	6.63	/	7.94	/	38-47wt%Al+11-12wt%Fe +14-23wt%Mg+18-34wt%Si	Light Gray
α-AlFeSi [171] (Al_8Fe_2Si)	Hexagonal	12.30	/	26.30	/	62wt.%Al+9wt%.Si+9wt.%Mn+20wt.%Fe or 55-64wt%.Al+30-33wt%.Fe +6-12wt%.Si	Chinese Script
α-AlFeSi [163]	Body-centered cubic	12.56	/	/	/		Chinese Script
α-AlFeSi [163]	Primitive cubic	12.52	/	/	/		Chinese Script
α´-AlFeSi [171]	Hexagonal	12.30	/	26.20	/		Chinese Script
α´´-AlFeSi or q_1-AlFeSi [163]	C-centered orthorhombic	12.70	36.20	12.70	/		Chinese Script
α_T -AlFeSi [163]	C-centered monoclinic	27.95	30.62	20.73	β=97.74°		Chinese Script

Table 3: Invariant Reactions to be Expected in Al-Mg-Si-Fe Quaternary System for Composition Range Corresponding to Alloy 6060 with Alloy 4043 Filler Addition [63].

Reactions	Temperature (°C)
Liq → Al + Si	577
Liq → Al + Mg_2Si	595
Liq + $FeAl_3$ → Al + α-Al_8Fe_2Si	630
Liq + α-Al_8Fe_2Si → Al + β-Al_5FeSi ("binary β phase")	612
Liq → Al + β-Al_5FeSi + Si ("ternary β phase")	575
Liq → Al + Mg_2Si + Si	555
Liq → Al + Si + Mg_2Si + π-$Al_8FeMg_3Si_6$	554
Liq + β-Al_5FeSi → Al + Si + π-$Al_8FeMg_3Si_6$	567

2.2.2 Weldability

The influence of composition on cracking susceptibility of high purity Al-Mg-Si ternary alloys was examined by Jennings et al. [6] using a ring casting test (Figure 51). A ridge of high cracking susceptibility is observed along the Al-Mg_2Si quasi-binary line (Mg/Si=1.73, weight ratio) with a peak in cracking susceptibility occurring at 0.4 weight percent Si and 0.3 weight percent Mg. Alloy 6060 sits close to this peak, and hence should have a high susceptibility to cracking, something that has been verified in circular patch tests (recall Figure 2). The weld metal composition is shifted to a less crack sensitive region when diluted with Alloy 4043 (recall Figures 1 and 51), changing primarily the silicon content, increased with higher filler dilution (Figure 51).

The weldability of Al-Mg-Si alloys is also strongly affected by the alloy composition, i.e. *magnesium*, *silicon*, and *iron* contents. Other factors examined in this study could conceivably have an effect on weld solidification cracking susceptibility: *grain refinement*, *travel speed*, and *oxygen contamination*. Details regarding these possible interactions are discussed below.

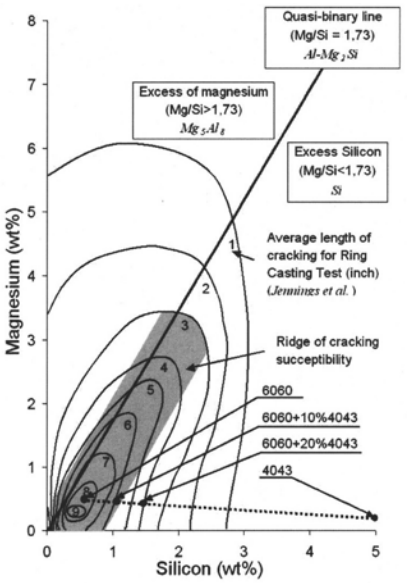

Figure 51: Quasi-binary line superimposed on ring casting data of Jennings et al. [6] showing solidification cracking susceptibility for Al-Mg-Si ternary alloy system.

2.2.2.1 Role of Magnesium

Addition of magnesium slightly decreases the solidification shrinkage [163], increases the melted alloy viscosity [163], and reduces the solid solubility of iron in aluminum [168]. Weldability of Al-Mg binary alloys has been investigated using U-shaped cast bars [11], T-joint test with GMA welds [8], ring casting and restraint GTA welds (Figure 52) [10], and quantified based upon crack length parametrics. The Λ-shape curves for cracking susceptibility versus magnesium content revealed a peak in solidification cracking susceptibility varying with the process: near 1 wt.% Mg with T-joint [8] and ring casting tests (Figure 52a) [10], 1.5 wt.% Mg with U-shaped cast bars (recall Figure 3c) [11], and 4 wt.% Mg with restrained welds (Figure 52b) [10]. It was noted that the casting superheat affects the grain structure and the peak amplitude, but not the peak position (Figure 52a).

Use has also been made of slow bending trans-varestraint test [12]. Measuring local strains with the MISO technique in GTA welds, the peak in solidification cracking susceptibility is found near 1 wt.% Mg with a critical strain rate of 0.25 %/s (Figure 53). In comparison, the critical strain rate at the peak in cracking susceptibility was found less than 0.1 %/s for welded Al-Cu binary alloys [12], demonstrating the good weldability of Al-Mg alloys in spite of their large solidification range. However, this apparent discrepancy between long solidification range and good weldability may not be so contradictory in regards to in-situ

observations in Alloy 5053 (Al-4.4Mg-0.8Mn) promoted using the slow bending trans-varestraint test [75]. The crack is observed not to extend to the assumed lowest bound of the BTR, i.e. the solidus, possibly due to early high strength build-up, thus resulting in a smaller BTR than expected.

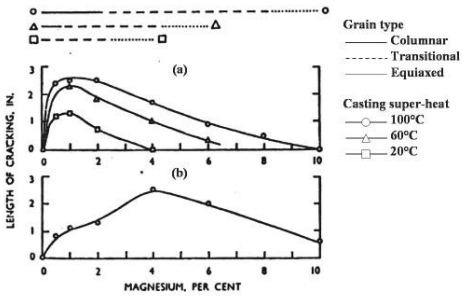

Figure 52: Cracking susceptibility of Al-Mg binary alloys using (a) ring castings and (b) restrained welds [10].

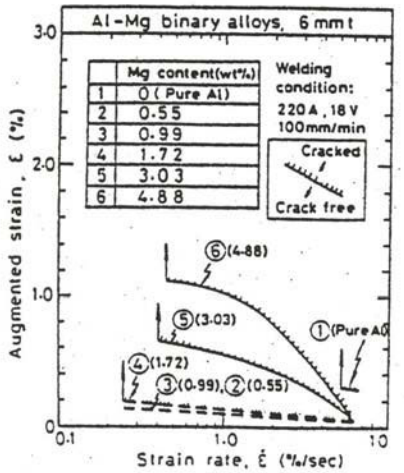

Figure 53: Strain rate dependence of solidification crack ductility for Al-Mg binary alloys [12].

2.2.2.2 Role of Silicon

First investigated in 1856 by Saint Claire-Deville [163], silicon is today commonly added to cast aluminum alloys since it improves the castability, is fairly inexpensive, and is one of the few elements that may be added to aluminum without increasing its density [168]. Silicon addition reduces the viscosity of molten aluminum for silicon contents higher than 1.65 wt.% Si (silicon solubility in molten aluminum) [163]. The expansion of silicon when solidifying results in a reduction in solidification shrinkage from 6.6 % for pure aluminum to 4.4 % for Al-11.6wt.%Si [175] to finally reach zero shrinkage at 25 wt.% Si [163]. With the aid of the four-blade vane shear test (recall Figure 26), silicon additions to Al-1Mg and Al-5Mg binary alloys is observed to postpone the dendrite coherency (Figure 54), which was attributed to a larger amount of eutectic liquid phase [132]. However, it does not affect the alloy strength at the end of solidification because of the similar morphologies of the dendrites. Silicon was also found to refine the grain structure within cast aluminum alloys [176].

Weldability of Al-Si binary alloys has been investigated in U-shaped cast bars [11], ring castings and restrained welds [10] and quantified using crack length parametrics. Results revealed a peak in solidification cracking susceptibility near 0.5 wt.% Si with ring castings and restrained welds (Figure 55) [10], and near 1 wt.% Si in U-shaped cast bars (recall Figure 3a) [11].

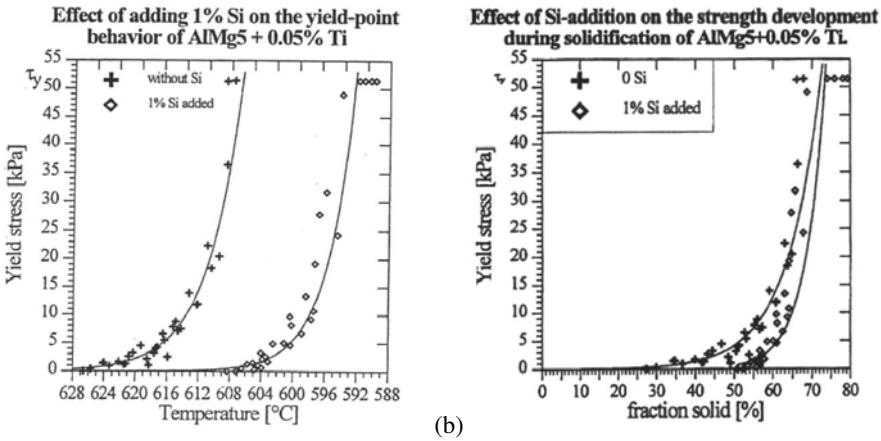

Figure 54: Effect of adding 1% silicon in Al-5Mg alloy regarding strength development versus (a) temperature and (b) solid fraction [132].

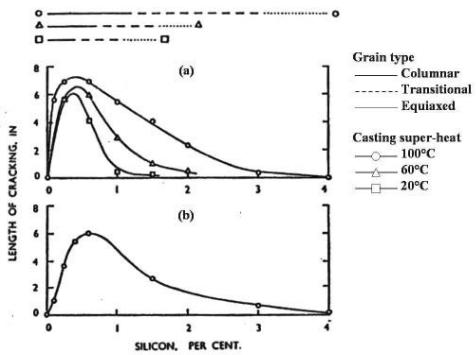

Figure 55: Cracking susceptibility of Al-Si binary alloys using (a) ring castings and (b) restrained welds [10].

2.2.2.3 Role of Iron

Iron, even when present at low impurity levels, plays an important role in determining solidification microstructure as noted above. Although normally found at around 0.20 weight percent (0.30 wt.% max.) in most wrought aluminum alloys, iron has a 0.80 weight percent

maximum limit in the 4043 filler alloy [165]. It is normally considered an undesirable element due to its resulting in reduced mechanical properties and corrosion resistance, where both problems are tied largely to the formation of coarse, iron-bearing intermetallic phases that are cathodic relative to the aluminum matrix [118]. The addition of iron increases the viscosity of molten alloys, has a grain refinement effect in some Al-Mg alloys, and decreases the solidification shrinkage linearly from about 6% for pure aluminum to approximately 3% for an Al-5wt.%Fe binary alloy [163]. Iron reduces the solubility of titanium and boron in aluminum, so that less of these elements are needed to promote grain refinement [163]. It is purposely added to die-casting alloys to prevent the casting from sticking to the die [168]. Manganese is commonly added to neutralise the effect of iron and modify the morphology and type of intermetallic phases, additions of Mn basically expanding the α-Al_8Fe_2Si phase over the β-Al_5FeSi phase [167].

Regarding weldability, ring castings and restrained welds revealed that high purity Al-Fe binary alloys have a low susceptibility to solidification cracking [10]. Concerning high purity Al-Fe-Si alloys ternary alloys, ring castings (Figure 56) and restrained welds (Figure 57) revealed a low solidification cracking susceptibility at high iron contents [9], and especially no cracking in welds for Fe:Si ratio higher than unity (Figure 57). Since high iron contents favor the binary β-Al_5FeSi (forming at a temperature over 600°C) over the ternary β-Al_5FeSi (forming at temperatures lower than 580°C) [177], it has been suggested that high temperature binary β impairs liquid feeding, which in turn leads to porosity formation in castings, and may also serve as effective pore nucleation sites [167,168,177]. However, the general consensus is that binary β improves resistance to solidification cracking [177], whereby needles serve to bridge dendrites, reducing strain localization in the mushy state and increasing the alloy strength at high temperatures [168].

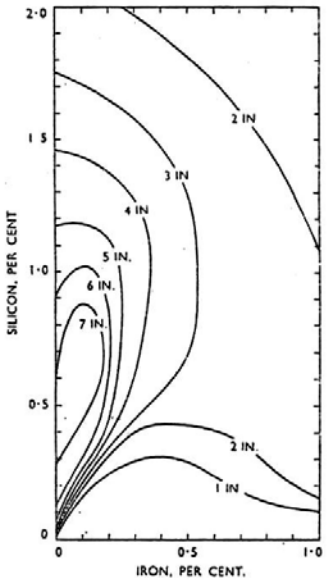

Figure 56: Mean crack length (in inches) on ring castings of Al-Fe-Si ternary alloys versus iron and silicon contents [9].

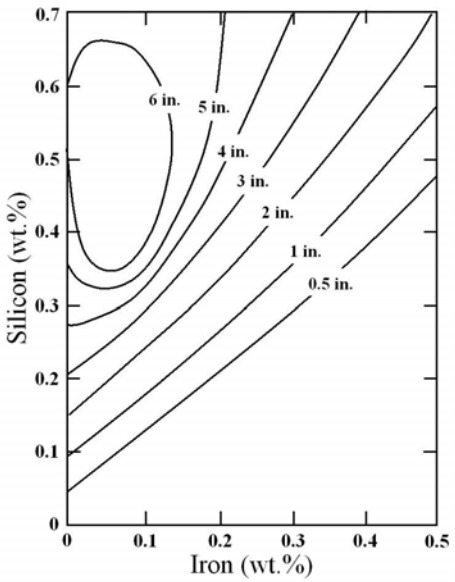

Figure 57: Mean crack length (in inches) on restrained welds of Al-Fe-Si ternary alloys versus iron and silicon contents [9].

2.2.2.4 Grain Refinement

Grain size directly affects the strain distribution within the weld mushy zone, grain structure refinement increasing the number of grain boundaries, thereby reducing the strain seen by each boundary. Reduced cracking susceptibility of aluminum alloy 7108 [5], Al-6wt.%Cu binary alloy [140], and Al-2.2Li-2.7Cu [178] with addition of grain refiners scandium [5], titanium-boron, i.e. TiBor [5,140], titanium [178], and zirconium [178] have been related to grain refinement. Using the circular patch test, cracking in Alloy 7108 [5] was avoided when adding a minimum of 0.25 wt.% Sc or (0.02 wt.% Ti + 0.004 wt.% B), corresponding respectively to a grain size of 80 and 180 μm. Note that the grain size in a 7108 weld without TiBor and Scandium was 290 μm. Using the Warrington test, cracking in Al-6 wt.% Cu binary alloy [140] was avoided when adding a minimum of (0.005 wt.% Ti + 0.001 wt.% B), and was attributed to the change from coarse columnar to refined equiaxed grain microstructure. However, the mechanisms by which TiBor particles promote grain refinement remain not well understood [179].

Addition of grain refiners can also affect the rheological behavior of the semi-solid material. Hot tensile test [31] and four-blade vane shear test [132] revealed that addition of Al-5Ti-1B master alloy increases the ductility of semi-solid Al-1.5wt.%Cu alloy [31] and

postpones the strength development of Al-Cu binary alloys (Figure 58) [132]. The difference in slope of the curves beyond the coherency temperature (Figure 58) is attributed to the difference in dendrite morphology. In refined microstructures, the small and round grains easily rearrange by sliding one against the other, resulting in a slow development of strength. In non refined columnar structures, the large and highly branched grains entangle in each other, hindering grain rearrangement. The strain accommodation also occurs by the deformation of the dendrites themselves, causing a rapid increase in strength.

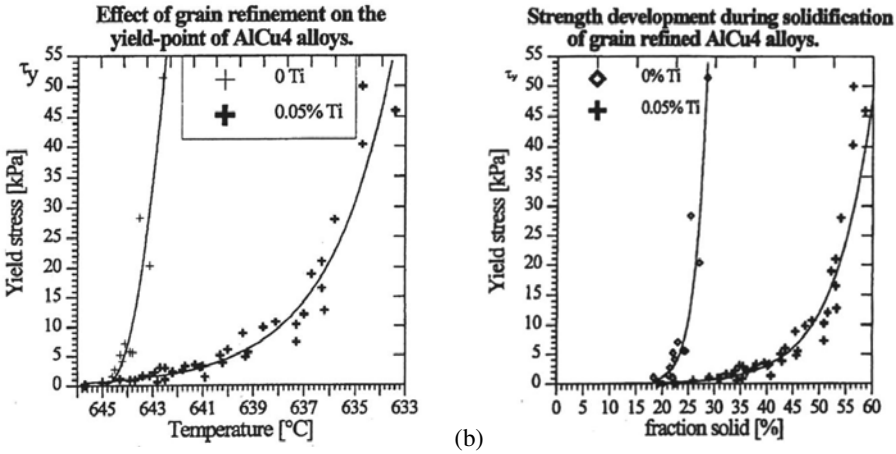

Figure 58: Effect of grain refinement on Alloy Al-4wt.%Cu strength development versus (a) temperature and (b) solid fraction [132].

2.2.2.5 Travel Speed

Strain and stress fields around the weld pool have been experimentally observed and simulated [14,37,38,39,70,180-182], their nature (tensile or compressive) and magnitude depending upon weld processing parameters as well as restraining conditions. The influence of torch travel speed on weld solidification cracking has been extensively studied, but is not well understood [37,38,70,180-182]. Some studies have observed an improvement in weldability when increasing the torch travel speed [37,38,70,181]. These measurements were made for the GTA process and travel speeds between 2.5 and 13 mm/s. Chihoski [37,38] experimentally observed compressive and tensile cells around a moving weld pool. At high travel speeds, a compressive cell is located at the mushy zone, thereby avoiding cracking (recall Figure 6a). With decreasing travel speed, this compressive cell diminishes and is replaced with a tensile cell, favoring crack formation (recall Figure 6b). However, some simulations [182] and experimental observations [180] show an increase in cracking

susceptibility with increasing travel speed. But in these situations, the welding speeds are high; between 50 and 100 mm/s for laser welding [180] and between 16 to 25 mm/s for GTA welding [182].

Weld travel speed also influences the weld pool shape, which is known to have a strong effect on weldability [183]. Increasing weld travel speed modifies the weld pool shape from round to teardrop, which favors centerline columnar grain formation with grain boundaries orientated normal to transverse strains, and thus a greater likelihood to cracking. This counters Chihoski´s observations [37] where high torch travel speed should improve weldability. Therefore, both weld pool shape and local strain cells must be considered when determining solidification cracking susceptibility.

Weld travel speed may also affect the weld microstructure, where faster welding speeds imply higher undercooling and thus favor equiaxed structures. The weld microstructure is believed to be dependent upon undercooling conditions, represented by the diffusion coefficient of the solute in the liquid term (*D*) multiplied by the temperature gradient (*G*) and divided by the square root of the dendrite growth rate (*R*) [184]. Increasing the dendrite growth rate *R* favors the equiaxed over the columnar structure (Figure 59).

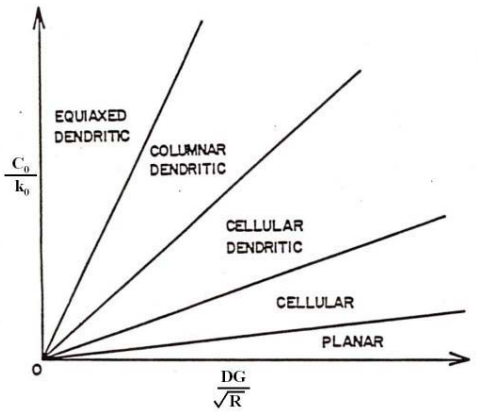

Figure 59: Schematic representing influence of nominal solute content (C_0), distribution coefficient (k_0), diffusion coefficient of solute in liquid (D), temperature gradient in liquid (G), and growth rate (R) on grain microstructure in solidified weld metals [184].

2.2.2.6 Oxygen Contamination

Oxygen contaminations is typically unavoidable, because this element is always present in the vicinity of the molten weld pool, for example with humid air aspirated into the shielding gas. Molten aluminum has a strong tendency to form aluminum oxides. These oxides have a density close to that of molten aluminum, and hence tend not to separate if

mixed. Entrapped oxide films may influence the cracking susceptibility, providing sites for crack nucleation due to decohesion [22]. Such oxide films may also impair the fluidity and feeding ability of the alloy [118], or affect the solidification path, serving as sites for phase nucleation [172]. Above 750°C, the γ-Al_2O_3 will be present, which acts as the preferred nuclei for β-Al_5FeSi needles [174]. The α-Al_2O_3 oxide suppresses nucleation of the β-phase, which as noted before is the phase believed to promote porosity.

3 Statement of Problem

Despite a huge amount of literature on solidification cracking, only limited work has been devoted to understanding the mechanisms for crack initiation and growth. During the last 50 years, strain was believed to control solidification crack formation, without any physical basis in cracking mechanism. Although recent developments have suggested that strain rate may play a more direct role in controlling weld solidification crack formation, the nucleation and growth of cracks are still largely unexplored subjects, mostly because welding research has concentrated on the engineering aspects of this subject (e.g. weldability testing and crack length measurement), while ignoring the underlying science. Hence, the solidification cracking criteria to date are not based upon any firmly established mechanisms, and thus fail to accurately account for cracking behavior. Among the more puzzeling aspects of solidification cracking, the present work addresses the following unanswered questions:

- How much 4043 filler is needed to avoid weld solidification cracking?
- How do local strain rate measurements relate to weldability?
- Can solidification cracking be regarded in terms of nucleation and growth?
- What role does hydrogen and porosity play on solidification crack formation?

The present thesis aims to make advancements in addressing these four posed questions. In order to reach this objective, weldability characterization and solidification cracking modeling were performed on the 6060/4043 aluminum alloy system, as detailed in the following sections.

4 Experimental Approach

A schematic outlining the experimental approach is shown in Figure 60. A novel experimental technique using the controlled tensile weldability (CTW) test was developed to characterize the weldability of the 6060/4043 system. Also investigated was the solidification path of Alloy 6060 for different 4043 filler additions and cooling rates. The measured weldability characteristics and solidification path of the 6060/4043 alloy system were then implemented into cracking models in order to identify the mechanisms involved for solidification crack formation. At the end, the effect of weld metal hydrogen content on Alloy 6060 weldability was investigated since the proposed cracking models suggest that hydrogen plays a major role in solidification crack formation.

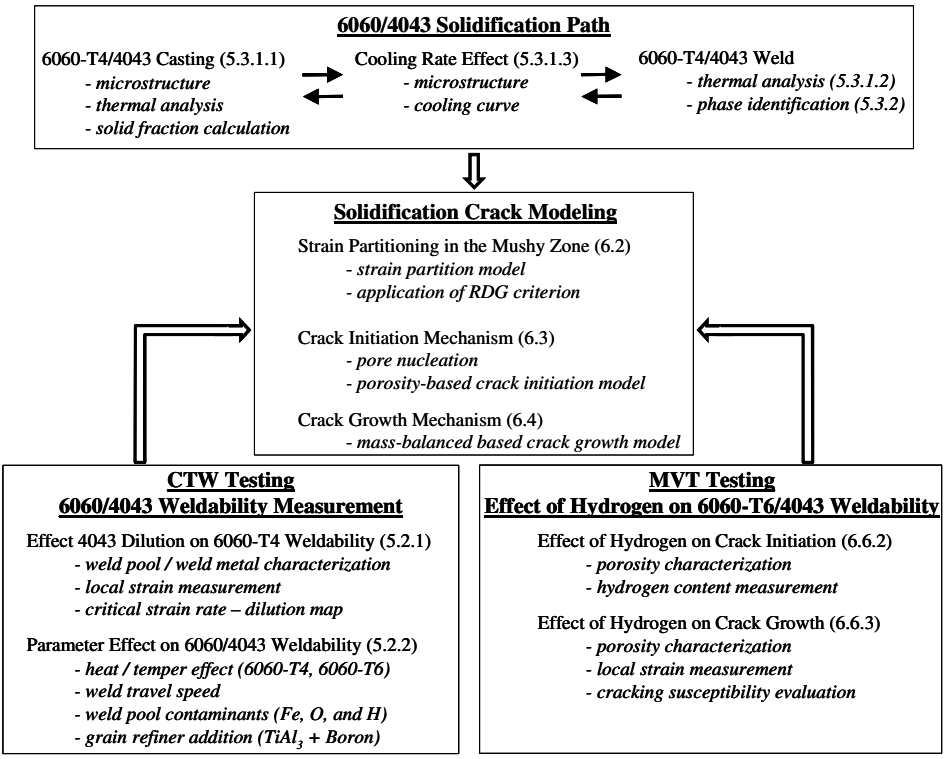

Figure 60: Schematic of experimental approach. Numbers in brackets indicate corresponding paragraphs .

4.1 Controlled Tensile Weldability (CTW) Test

4.1.1 Description

Solidification cracking susceptibility was studied by means of a newly developed Controlled Tensile Weldability (CTW) test shown in Figure 61, consisting of a horizontal tensile test apparatus (500 kN load capacity) that can apply a plane tensile strain during welding, transverse to the welding direction, at a controlled strain rate. The concept of this test is to vary the local strain rate in the vicinity of the mushy zone, by systematically varying the globally applied strain rate (i.e. cross-head speed). By looking for crack-no crack conditions, one can identify the critical local strain rate needed for crack formation. The concept for such a test is not new, with different variations appearing in the literature [72,150]. In comparison, for example, the Programmable Deformation Cracking (PVR) test consists of applying a tensile strain during welding, in the direction of welding, while ramping up the strain rate [72]. The point at which cracking is first observed defines a critical strain rate. While such tensile tests can be used to apply a global strain at a fixed strain rate during welding, of more importance is the local strain and strain rate (i.e. in the mushy zone or vicinity), which is not the same as global strain values and hence must be measured separately.

4.1.2 Test Procedure Development

4.1.2.1 Material

Weld coupons 120 mm in length were cut from 40 mm x 4 mm extruded bars of 6060-T4 and 6060-T6 (Table 4), with a respective hardness of 40 and 83 HV0.5. In preparation for testing, each coupon was welded to two load-transfer aluminum plates (300 mm x 150 mm x 8 mm, Figure 61b), suitable for clamping into the headstock of the CTW machine. Following testing, coupons are cut out and the load-transfer plates reused.

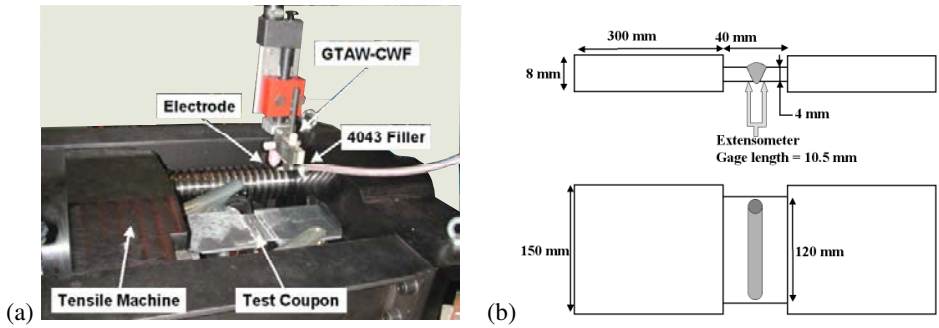

Figure 61: (a) Overview of CTW test machine and (b) dimensions of test coupon showing test coupon joined to two load-transfer plates.

Table 4: Measured Chemical Analysis for Aluminum Alloy 6060-T4, 6060-T6, and 4043 (wet chemical analysis for 4043 filler wire and spectrometry for 6060 base metal)

Aluminum Alloy	Composition (wt.%)									
	Si	Mg	Fe	Mn	Cu	Cr	Ni	Zn	Ti	Zr
6060-T4	0.42	0.59	0.19	0.020	0.012	0.004	0.004	0.009	0.020	0.001
6060-T6	0.51	0.51	0.21	0.040	0.027	0.003	0.003	0.044	0.020	0.001
4043	5.30	0.002	0.22	0.003	0.018	0.002	0.005	0.005	0.003	0.002

Table 5: Base Welding Parameters for GTAW-CWF Process

Parameter	Value
Current	110 A
Voltage	17.8 V
Arc Gap	2 mm
Electrode Diameter	3.2 mm
Electrode Type	Tungsten + 1% LaO_2
Electrode Tip Angle	30°
Torch Gas	Helium
Gas Flow Rate	0.33 L/s
Polarity	DCEN
Torch Travel Speed	4 mm/s
Wire Diameter	0.8 mm
Wire Feed	0-41.7 mm/sec

4.1.2.2 Welding Parameters

Welding was performed using the gas-tungsten arc, cold-wire feed process (GTAW-CWF). The base welding parameters, held constant throughout this study, are listed in Table 5. Arc voltage was kept constant using an arc voltage control system, maintaining a 2 mm arc gap corresponding to a 17.8 V arc voltage. Parameters were developed to obtain a full penetration, bead-on-plate weld. Welds were made both with and without 4043 filler wire (0.8 mm diameter). Filler wire speed was varied from 0.0 to 41.7 mm/s in incremental steps of 8.3 mm/s. Prior to welding, the oxide layer on the test coupon was chemically

removed (etch E1 applied at room temperature for 15 minutes, Table 6), followed by degreasing with acetone.

Table 6: Etchants used for Oxide Removal and Metallographic Analysis

Etchant	Description
E1	869mL H_2O, 125mL HNO_3 65%, 6.25mL HF 48%
E2	100mL H_2O, 66mL HCl, 66mL HNO_3, 16mL HF
E3	100mL H_2O, 4g $KMnO_4$, 1g NaOH
E4	H_2O + 1% NaOH

4.1.2.3 CTW Test Sequence

The CTW test sequence is summarized in Table 7. A pre-load of 15 kN was applied prior to welding to compensate for thermal expansion of the weld coupon during welding, maintaining it in tension even at a 0 mm/s transverse cross-head speed. The arc was initiated by touch contact between the electrode and the weld coupon. In a 100 mm long weld, the transverse cross-head speed was applied 30 mm after the start of welding. Local strain was measured at weld mid-length. At the end of the weld, the arc was abruptly extinguished, providing information as to the shape of the weld pool. Each individual test was run at a constant applied strain rate, where the tensile transverse cross-head speed was varied from 0.000 to 0.083 mm/s in incremental steps of 0.017 mm/s per test. This globally applied strain rate resulted in variations in local strain rate (i.e. region adjacent to weld pool), which was measured with an extensometer.

Table 7: CTW Test Sequence

Step Number	Distance from the Weld Start (mm)	Related Action
1	0	Start weld
2	30	Start cross-head travel
3	50	Electrode at the top of the extensometer
4	90	Stop cross-head travel
5	100	Stop weld

4.1.2.4 Local Strain Measurement

An extensometer was attached underneath the weld coupon, in the path of the weld at mid-length (Figure 61b), to measure the transverse strain across the weld mushy zone during the welding process, and referred to as the local strain. When attached to the bottom surface of a weld, the extensometer can be placed directly at the location of desired measurement, but this requires use of through-thickness welds and a thin plate (i.e. plane strain) to provide useful information. The gage length of the extensometer was 10.5 mm,

spanning across an 8 mm wide weld bead. The extensometer output was recorded at a 100 Hz frequency during the entire test using *CATMAN 4.5* computer software for data acquisition and a *Spider 8* analog-to-digital converter. Local strain rates were calculated from these recorded strains and, with incrementally increased applied strain rate for each succeeding test, the critical local strain rate for cracking was identified when cracks were first observed.

Strain and strain rate values were examined at the coherency temperature (i.e. as the mushy zone passes over the extensometer), corresponding to the point during solidification where the secondary arms of adjacent dendrites first begin to coalesce. This is normally taken to be the region where cracking initiates [53], and can be determined experimentally from thermal analysis corresponding to the first arrest in the cooling curve following the beginning of α-Al dendrite solidification [49]. Coherency represents a sharp reduction in interdendritic liquid feeding and thus a change in heat removal. The position of coherency relative to the torch along the weld centerline was determined from weld pool size (i.e. distance between torch and trailing weld pool boundary) and cooling rate measurements (i.e. time between liquidus and coherency temperatures). The position of the torch relative to the extensometer was determined from time of travel.

4.1.2.5 DIC Measurement

The Digital Image Correlation (DIC) method was used as a supplementary method to measure the local strain at the bottom surface of the weld (Figure 62). When using light optics, this method is best suited for use on the bottom surface of the weld, where arc light and gas fumes cannot interfere with speckle resolution. The DIC method consisted of covering the bottom surface with paint speckles (Figure 62b). Their movement was recorded in three dimensions by means of two cameras (Figure 62a). Local transverse strains were then calculated and mapped over a photo of the weld coupon at the corresponding instant. The mapped strain field over the weld was used to determine the influence of gage length on measured strains and calculated strain rates.

4.1.2.6 Temperature Measurement

Thermal analysis of the welds at 0% and 16% 4043 filler dilution was accomplished by welding over a thermocouple embedded in the plate. A hole, 0.6 mm diameter and 1 mm deep, was drilled from the bottom side of the weld coupon, in the path of the weld at weld mid-length. A sheathed and electrically grounded Type-K thermocouple (0.5 mm outer dia.)

was pre-placed inside this hole (friction fit) prior to welding. The thermocouple output was recorded at a 200 Hz frequency during solidification using *CATMAN 4.5* computer software for data acquisition and a *Spider 8* analog-to-digital converter.

(a) 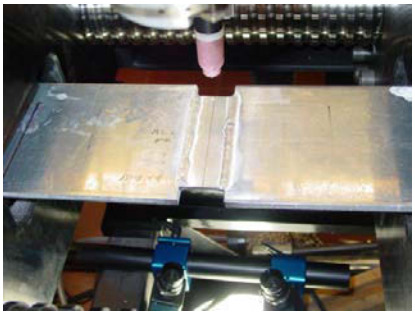 (b) 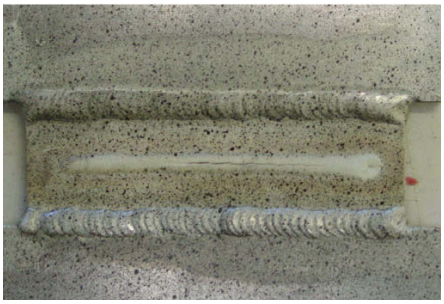

Figure 62: (a) DIC set-up using two cameras to observe CTW test specimen and (b) bottom view of test sample after welding with paint speckle.

4.2 Weldability Measurement

4.2.1 Critical Strain Rate – Dilution Mapping

The critical strain rate to form cracks was compared for several different filler metal dilutions between 0 and 20% 4043. Filler dilution is an important concept in determining weld pool composition, approximated using Eq. 35:

$$\text{filler dilution} = \frac{B+C}{A+B+C} \quad x \quad 100\% \tag{35}$$

, where *A* is cross-sectional melted area of the 6060 base metal, and *B+C* is difference between the total area of the weld metal and *A* (Figure 63).

In CTW testing, for each dilution level the transverse cross-head speed was incremented in steps of 0.017 mm/s from 0.000 mm/s to 0.068 mm/s, noting the value where cracking first occurred. Because of the fixed incremental step of transverse cross-head speed (0.017 mm/s), the exact location of the crack-no crack boundary lies somewhere within this fixed step. This corresponds to the difference between the highest measured strain rate without cracking and a strain rate slightly greater than that required to form a crack. Hence, the accuracy for determining the critical strain rate, for a given filler dilution, is limited by the magnitude of this step. Data was plotted as a critical strain rate – dilution map, demarking the region between crack and no-crack conditions.

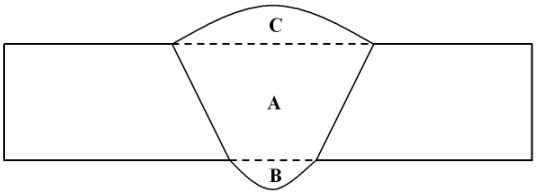

$$\text{filler dilution} = \frac{B+C}{A+B+C} \times 100\ (\%)$$

Figure 63: Illustration for filler dilution calculation from weld metal cross-section.

4.2.2 Minor Element Effects

4.2.2.1 Inserts

The objective was to vary weld metal composition using inserts having a controlled composition (Table 8). Inserts were machined from cast ingots made from controlled mixtures of 6060-T6 with master alloys (e.g. Al-5Ti-B or Al-10Fe). These inserts were then pre-welded into 6060-T6 CTW coupons in preparation for CTW weldability testing.

Table 8: Measured Wet Chemical Analysis and Emission Spectrometry for Aluminum Alloys 6060, 4043, and Controlled Mixtures of 6060-T6 with Master Alloys Al-10Fe and Al-5Ti-B (wt.%): (a) Insert 6060+Tibor (6060+15%(Al-5Ti)), (b) Weld Pool 6060+Insert (6060+Tibor), (c) Insert 6060+Fe (6060+15%(Al-10Fe)), and (d) Weld Pool 6060+Insert (6060+Fe)

	Composition (wt.%)									
	Si	Mg	Fe	Mn	Cu	Cr	Ni	Zn	Ti	Zr
(a)	0.43	0.43	0.18	0.03	0.02	0.003	0.003	0.04	0.77	0.001
(b)	0.50	0.50	0.21	0.04	0.03	0.003	0.003	0.04	0.14	0.001
(c)	0.43	0.43	1.68	0.03	0.02	0.003	0.003	0.04	0.02	0.001
(d)	0.50	0.50	0.43	0.04	0.03	0.003	0.003	0.04	0.02	0.001

Controlled mixtures of 6060-T6, 6060+15%(Al-5Ti-B), and 6060+15%(Al-10Fe) were cast. The composition of the resulting ingots, when using master alloys, differs from 6060 respectively for titanium (0.77 wt.% instead of 0.02 wt.%) and iron (1.68 wt.% instead of 0.20 wt.%). The casting mold is shown in Figure 64, with inside dimensions 140 mm x 10 mm x 30 mm, and mold thickness 10 mm. All mold materials with direct exposure to molten aluminum were pre-coated with boron-nitride spray. Each cast heat weighed approximately 130 grams and was melted in a graphite crucible placed inside an electric furnace held at 800°C. Oxide dross was skimmed just prior to casting, and the melt was rigorously stirred in order to ensure thorough mixing with the master alloy. In the case of

Al-5Ti-B, 6060-T6 was thoroughly melted before adding the Tibor master alloy, in order to reduce time exposure of $TiAl_3$ particles in the melt, and thus minimize particle dissolution and promote efficient grain refinement. Five inserts (2 mm x 2 mm x 140 mm) were machined from each cast ingot. For purposes of providing an experimental control, inserts of cast 6060 material were also prepared, left untreated with any master alloy.

Square grooves (2 mm x 2 mm) were machined along the centerline of 6060-T6 CTW test coupons (i.e. extrusions) to receive the inserts (Figure 65). Prior to assembly, the oxide layer was chemically removed by etching both weld coupon and insert (etch E1, Table 6), followed by degreasing with acetone. The insert was forced into the groove (hammer taps) and pre-welded using the welding parameters listed in Table 9. Variable polarity current was used here to help to remove oxides at the weld surface. The pre-weld consisted of a bead-on-plate, partial penetration weld (6 mm wide and 3 mm thick), which completely melted the insert.

Table 9: GTA Welding Parameters for Pre-Welding Inserts

Parameter	Value
Positive Electrode / Duration	+80 A /20%
Negative Electrode / Duration	- 220 A /80%
Frequency	50 Hz
Arc Gap	1.5 mm
Electrode Diameter	3.2 mm
Electrode Type	Tungsten + 2% ThO_2
Electrode Tip Angle	30°
Torch Gas	Argon
Gas Flow Rate	0.3 L/s
Polarity	Variable polarity
Torch Travel Speed	4 mm/s

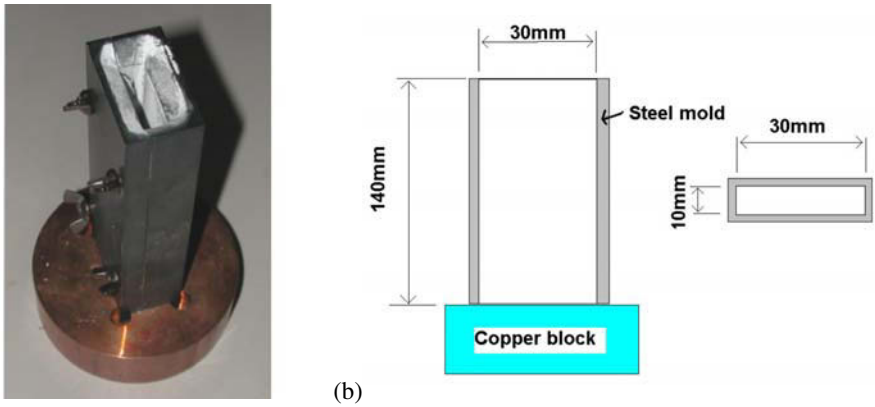

Figure 64: Casting mold (a) photograph and (b) schematic, used to obtain ingots for weld insert production.

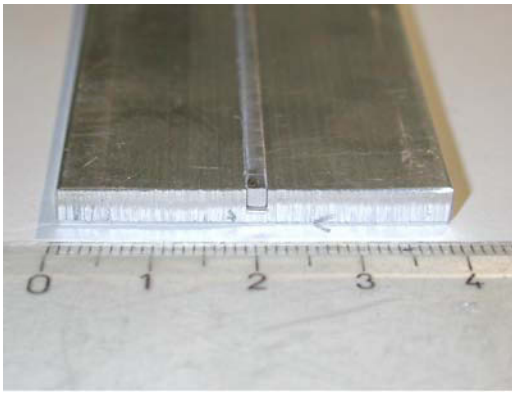

Figure 65: Insert placed into groove of 6060-T6 coupon before pre-weld.

4.2.2.2 Shielding Gas

In the case of controlled oxygen and hydrogen contamination, helium flow rate was maintained constant (0.33 L/s) and mixed with gases from pre-mixed bottles of either Ar+2%H_2 or Ar+1%O_2. Because of the effect of gas additions in changing the weld heat input, current was varied in order to maintain a constant weld pool size. Ar+2%H_2 flow rate was fixed at 0.27 L/s to obtain a sufficient amount of dissolved hydrogen in aluminum to promote limited interdendritic pore formation. Regarding oxygen contamination, Ar+1%O_2 flow rate was fixed at 0.03 L/s, corresponding to the maximum gas flow rate possible while maintaining arc stability. At a 0.08 L/s Ar+1%O_2 flow rate, the arc became highly erratic, likely due to the large quantity of aluminum oxides formed on the weld pool.

4.3 Solidification Path

In realization of the importance of solidification range and liquid feeding to cracking, the solidification path was characterized using thermal analysis techniques combined with metallographic observations and phase identification using SEM and TEM. While there is now popular use of thermodynamic based software for phase prediction, it is of course important to also perform experimentation to confirm solidification behavior. It is understood that the possibility also exists to predict these phase relationships using commercially available thermodynamic software. However, available phase prediction software does not take into account the presence of iron, which can have a profound effect on solidification structure. Details are given below.

4.3.1 Simulation of Weld Metal Composition

Castings of controlled mixtures of Alloys 6060 and 4043 were investigated, thereby simulating weld metal composition under controlled cooling conditions. Because of the extensive metallurgical data in the literature concerning aluminum castings, this allowed a direct comparison to be made with expected behavior. The effect of cooling rate on solidification path was investigated in order to extend the results to welding.

4.3.1.1 Experimental Equipment

Extruded bars of alloy 6060-T4 were melted and pre-weighed amounts of 4043 filler wire were then added (Table 4). Experimental equipment (Figure 66) comprised a cylindrical graphite mold with embedded thermocouples and a cylindrical stainless steel block to extract heat out the bottom. The graphite mold had an inside diameter of 19 mm, outside diameter of 40 mm, and a height of 60 mm. The stainless steel block had an outside diameter of 80 mm and a height of 30 mm. Three Type-K thermocouples (0.2 mm diameter), labeled T_w, T_{wc}, and T_c, were placed at the centerline of the mold at respective distances of 0 (i.e. against the block), 3, and 30 mm from the stainless steel block, and calibrated using 99.999 weight percent pure aluminum. All mold materials with direct exposure to molten aluminum were pre-coated with boron-nitride spray. The heat sink placed at one end of the mold promotes unidirectional, non-equilibrium solidification.

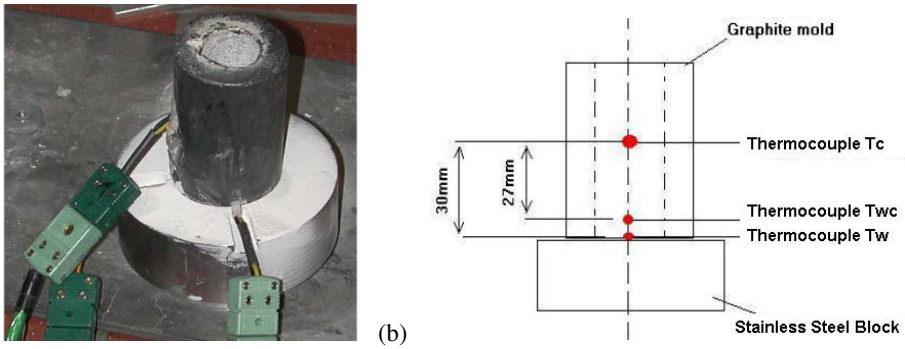

Figure 66: Experimental equipment (a) photograph and (b) schematic, showing graphite mold, stainless steel block, and thermocouple locations.

Thermocouples were strategically pre-placed (Figure 66) in order to facilitate the thermal analysis methods described in the next section. Thermocouple T_c was used to collect data for the cooling rate method, the temperature variance method, and to make solid fraction calculations. Thermocouples T_w and T_{wc} were used to evaluate the temperature

difference method. Slowly cooled castings were investigated in this analysis to facilitate the collection of thermal data, to make phase identification easier (i.e. produce coarse phases for metallographic analysis), and to establish the limitations of these different techniques. Each of these analytical methods will be briefly discussed below.

4.3.1.2 Test Sequence

Each cast sample weighed approximately 45 grams and was melted in a graphite crucible placed inside an electric furnace held at 800°C. The molten alloy was superheated to 780°C. The melt was rigorously stirred in order to ensure thorough mixing between the two alloys (6060 and 4043). Oxide dross was skimmed just prior to casting. The three thermocouple outputs were recorded at a 50 Hz frequency during solidification using *CATMAN 4.5* computer software for data acquisition and a *Spider 8* analog-to-digital converter.

4.3.1.3 Cooling Rate Variation

It is intended that this work will serve as a basis for future studies to characterize the effect of cooling rate on phase selection. The rapid cooling of welding may result in deviations from equilibrium phase formation. Solidified alloy specimens have been examined in this study in two different forms, both as castings and as weld metal, in order to intentionally vary the cooling rate during solidification and compare the resulting microstructures. Castings of Alloy 6060 were made with the equipment shown in Figure 66, but using blocks of different materials attached to the bottom of the cylinder to extract heat at different rates. Block materials included ceramic (fireclay), stainless steel, and copper, which when combined with the use (or not) of a boron-nitride coating, allowed a total of 6 different cooling rates to be examined. Only the thermocouple labeled T_c (Figure 66) was used to monitor the cooling rate of the casting.

4.3.2 Thermal Analysis

Three different thermal analyses were used to characterize the solidification of 6060/4043 alloys and will be referred to here as: cooling rate, temperature difference, and temperature variance methods. Also, a solid fraction calculation was made based upon cooling rate data. These techniques follow from work done by Bäckerud et al. for aluminum castings [53,169,170] and Alexandrov et al. for welds [185,186]. These methods are

founded on the principle that thermal arrests observed during cooling correspond to phase formation and the release of latent heat. All four techniques were used to characterize the solidification of aluminum alloys in casting, while only the cooling rate and temperature variance methods were used to characterize aluminum welds.

4.3.2.1 Cooling Rate Method

The cooling rate method [53,169,170] is the most widely used method for investigating solidification of metals and alloys, because of its simplicity of application and setup. Temperature at a central location in a casting is recorded as a function of time and the first derivative of this temperature (i.e. cooling rate) is calculated and displayed as a function of time. Thermal arrests on cooling, caused by the release of latent heat, indicate new phase formation. This is indicated with even higher sensitivity by observing abrupt changes in the first derivative (cooling rate) curve, allowing for higher precision in determining the temperature of phase formation.

4.3.2.2 Temperature Difference Method

The temperature difference method [53,169,170], also known as Differential Thermal Analysis (DTA), uses two thermocouples: one placed close to the mold wall and one placed some distance from the mold wall, in line with the heat flow. This method provides a different approach for detecting phase formation, which serves to both complement and help verify the cooling rate method. It has been found in some instances to have higher sensitivity, and is particularly useful in indicating the coherency temperature.

The difference in temperature between the two thermocouples is calculated for each moment in time. The thermocouple at the wall will always be slightly lower in temperature and, when solidification occurs, the latent heat released inside the casting will tend to reduce this temperature difference. Thus, an abrupt change in temperature difference is taken to indicate phase formation. The first derivative of this difference is used to identify thermal arrests.

4.3.2.3 Temperature Variance Method

The temperature variance method, also referred to as Single Sensor-Differential Thermal Analysis (SS-DTA), has been successfully applied to welding, making use of a

single thermocouple to measure phase transformations in ferrous based alloys [185,186]. It has proven useful in identifying phase reactions and solidification ranges in welds [186].

The cooling curve is approximated (i.e. curve-fit), done using a third degree polynomial in the present study, and then the variation between measured and curve-fit values are compared over time. Again, taking a first derivative of this variation serves to help identify arrests. Due to the stepped nature of most solidification cooling curves (i.e. plateaus), only isolated portions of a cooling curve can be readily curve-fit.

4.3.2.4 Solid Fraction Calculation

The method presented here was used only in the casting since it does not take into account an external source of heat during the alloy solidification. The amount of solid that forms over time as a result of cooling, expressed in terms of solid fraction-versus-temperature, can be obtained from cooling rate curves [53]. This calculation is based upon the heat flow equation for conduction:

$$\rho Cp \frac{dT}{dt} = \nabla(k\nabla T) + \rho\Delta H \frac{dfs}{dt} \tag{36}$$

, where ρ is density, C_p is specific heat, T is temperature, t is time, k is heat conductivity, ΔH is latent heat, and f_s is solid fraction. Basically, latent heat is partitioned during solidification according to how much solid has formed (df_s/dt), thus affecting the cooling rate (dT/dt) accordingly. Solving Eq. 36 for solid fraction:

$$fs = \frac{1}{\Delta H} \sum_{t=0}^{t} (Cp\Delta(\frac{dT(t)}{dt})) \tag{37}$$

Here the cooling rate difference term $\Delta(dT(t)/dt)$ represents the difference between the observed cooling rate and a hypothetical base line (approximated), representing the cooling rate for zero latent heat. A graphical representation is shown in Figure 67. Appropriate values for latent heat and specific heat are selected.

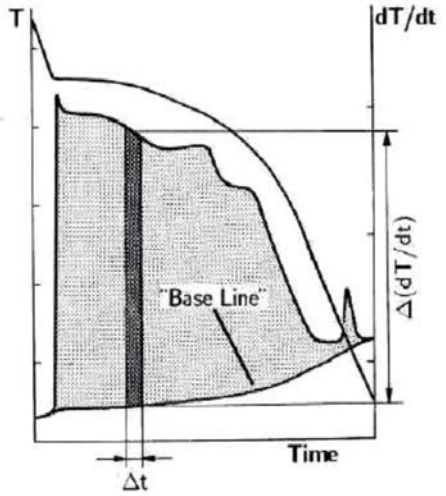

Figure 67: Schematic showing difference between measured cooling rate and baseline approximation [53].

4.3.3 Metallographic Analysis

4.3.3.1 Casting

After casting, samples were cut 25 mm from the end closest to the stainless steel block. The cross sections were ground and polished to 1 μm and then chemically polished using a slightly basic solution of colloidal silicon dioxide. The microstructure was examined using optical microscopy.

4.3.3.2 Weld

Metallographic cross-sections were cut transverse to the weld, at weld mid-length. These sections were ground and polished to 1 μm and then chemically polished using a slightly basic solution of colloidal silicon dioxide. The microstructure was examined using optical metallography and scanning electron microscopy (SEM). The phases were identified using transmission electron microscopy (TEM). Electron backscattered diffraction (EBSD) was employed to help define grain boundaries for grain size measurement. Grain size was measured using a line-intercept technique, taking a mean value of four line-intercept measurements. Other polished cross sections were etched with the Etch E3 (Table 6) for

45 seconds at room temperature to reveal the weld pool size and geometry, and the etch E4 (Table 6) for 10 minutes between 55 and 60°C to dissolve the aluminum dendrites and observe in three-dimensions the intermetallic phases using SEM.

4.4 Effect of Hydrogen on Weldability

When dealing with dissolved gas in aluminum alloys, the only gas to consider is hydrogen [116]. The effect of weld metal hydrogen content on solidification cracking susceptibility is a little explored subject, and was investigated in the present work with Alloy 6060-T6 welds made without 4043 filler.

4.4.1 Effect of Hydrogen on Solidification Crack Initiation

4.4.1.1 Test procedure

The effect of hydrogen contamination on weld solidification crack initiation, i.e. pore formation, was investigated in restrained welds using the experimental equipment shown in Figure 68. Welds 380 mm in length were made on 400 mm long weld coupons, which were cut from 40 mm x 4 mm extruded bars of 6060-T6 (Table 4). Full penetration, bead-on-plate, gas-tungsten-arc (GTA) welds made using weld parameters given in Table 10. Prior to welding, the oxide layer on the test coupon was chemically removed (etch E1 applied at room temperature for 15 minutes, Table 6), followed by degreasing with acetone. The arc was initiated at 10 mm from the edge of the plate.

Hydrogen contamination was achieved by adding controlled amounts of hydrogen to the shielding gas using a pre-mixed bottle of Ar+2%H_2. Helium flow rate was maintained constant (0.33 L/s) while Ar+2%H_2 flow rate was varied between 0.000 and 0.083 L/s. The shielding gas was flowing 30 seconds before starting the weld to flush the tubes of other gas contaminations. Because of the effect of gas additions in changing the weld heat input, arc length was varied in order to maintain a constant 17.8 V arc voltage.

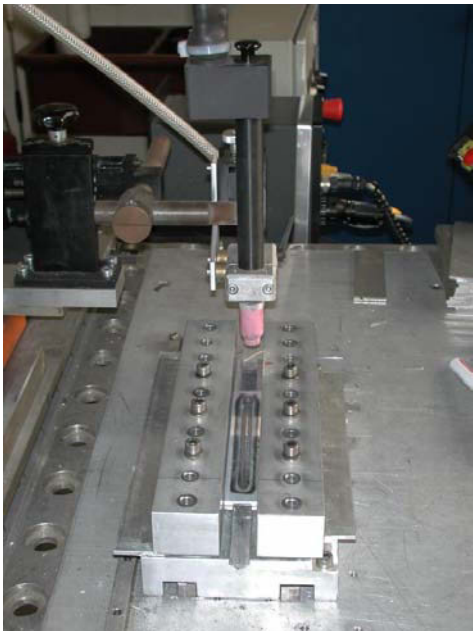

Figure 68: Overview of experimental set-up to investigate solidification crack initiation.

Table 10: GTA Welding Parameters for Investigating Solidification Crack Initiation

Parameter	Value
Current	125 A
Voltage	17.8 V
Arc Gap	2 mm
Electrode Diameter	3.2 mm
Electrode Type	Tungsten + 1% LaO_2
Electrode Tip Angle	30°
Torch Gas	Mixture He and (Ar+2%H_2)
Gas Flow Rate	He (0.33 L/s) + Ar+2%H_2 (0.000-0.083 L/s)
Polarity	DCEN
Torch Travel Speed	4 mm/s

4.4.1.2 Weld Porosity Characterization

Weld metal porosity was characterized using metallography and X-ray radiography. Metallographic cross-sections were cut transverse to the weld, at weld mid-length. These sections were ground and polished to 1 μm and then chemically polished using a slightly basic solution of colloidal silicon dioxide. The microstructure was examined using optical metallography at magnification 50x, corresponding to an area of approximately 2 mm x 2 mm. Eight areas were required to cover the whole weld cross-section. Porosity

amount was evaluated as the ratio between the total pore cross-sectional area and weld cross-sectional area.

4.4.2 Effect of Hydrogen on Solidification Crack Growth

4.4.2.1 Description

The effect of hydrogen contamination on weld solidification crack growth was investigated using the Modified Varestraint Test (MVT) shown in Figure 69, consisting of bending at a controlled speed the weld coupon around a mandrel (with a block radius of 250 mm) whose axis of curvature is parallel to the welding direction (i.e. trans-varestraint configuration). This test is used here in a manner similar to the slow bending trans-varestraint test [12,67], where the local strain rate in the vicinity of the mushy zone is varied by systematically varying the globally applied strain rate (i.e. ram speed) which allows a critical ram speed to be determined.

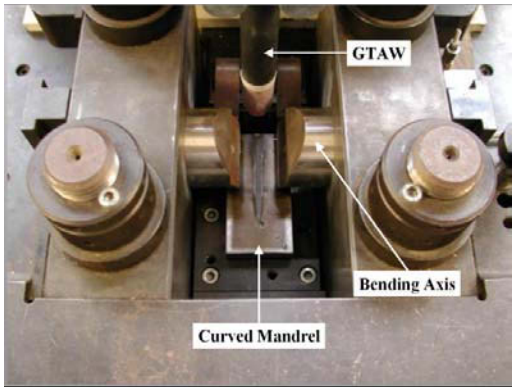

Figure 69: Overview of MVT test machine.

4.4.2.2 Test Procedure Development

4.4.2.2.1 Welding Parameters

Weld coupons 120 mm in length were cut from 40 mm x 4 mm extruded bars of 6060-T6 (Table 4). Partial penetration, bead-on-plate, gas-tungsten-arc (GTA) welds made using weld parameters given in Table 11. Two series of tests were performed using two welding currents, 95 and 105 A. Prior to welding, the oxide layer on the test coupon was chemically removed (etch E1 applied at room temperature for 15 minutes, Table 6), followed by degreasing with acetone.

Table 11: GTA Welding Parameters for Investigating Solidification Crack Growth

Parameter	Value
Current	95 – 105 A
Voltage	17.8 V
Arc Gap	2 mm
Electrode Diameter	3.2 mm
Electrode Type	Tungsten + 1% LaO_2
Electrode Tip Angle	30°
Torch Gas	Mixture He and (Ar+2%H_2)
Gas Flow Rate	He (0.33 L/s) + Ar+2%H_2 (0.00-0.10 L/s)
Polarity	DCEN
Torch Travel Speed	4 mm/s

Hydrogen contamination was achieved by adding controlled amounts of hydrogen to the shielding gas using a pre-mixed bottle of Ar+2%H_2. Helium flow rate was maintained constant (0.33 L/s) while Ar+2%H_2 flow rate was varied between 0.00 and 0.10 L/s. The shielding gas was flowing 30 seconds before starting the weld to flush the tubes from other gas contaminations. Because of the effect of gas additions in changing the weld heat input, arc length was varied in order to maintain a constant 17.8 V arc voltage.

4.4.2.2.2 MVT Test Sequence

The MVT test sequence is defined as follows. The specimen was placed on the mandrel and the bending yokes were lowered into contact with the specimen. The arc was initiated 10 mm from the edge of the plate. In a 100 mm long weld, the controlled ram speed was applied 50 mm after the start of welding, promoting a local strain transverse to the welding direction. The bending process continues until the applied displacement reaches the ultimate value previously decided. Meanwhile the arc travels steadily onwards and is extinguished 10 mm from the end of the plate. Each individual test was run at a constant

applied ram speed, which was varied from 0.05 to 0.11 mm/s in incremental steps of 0.01 mm/s per test.

4.4.2.2.3 Strain Measurement

This globally applied bending resulted in variations in transverse local strain rate (i.e. region adjacent to weld pool). The augmented strain applied on the specimen surface was measured for ram speeds between 0.05 to 0.11 mm/s, without welding, with a strain gage attached to the specimen at mid-length. The strain gage output was recorded at a 100 Hz frequency using *CATMAN 4.5* computer software for data acquisition and a *Spider 8* analog-to-digital converter. Strain rates were calculated from these recorded strains. The strains measured should be a good approximation of the strain around the weld during testing according to Arata et al. [12] who found a good correlation between strains gage measurements without welding and strains measured with the indentation recording film technique during welding.

4.4.3 Hydrogen Measurement

Hydrogen content in aluminum alloys was measured using the hot extraction technique initially developed by Ransley et al. in 1955 [116], a suitable and accurate method for determining hydrogen amount present in solid state materials. Hydrogen is extracted by heating a sample in a vessel under a controlled nitrogen atmosphere and at a temperature close to, but below the solidus in order to avoid any melting. A continuous flow of nitrogen transports the extracted hydrogen to a calibrated thermal conductivity detector (TCD). A TCD consists of an electrically-heated wire or thermistor, whose temperature depends on the thermal conductivity of the surrounding gas. Changes in thermal conductivity, such as when organic molecules displace some of the carrier gas, cause a temperature variation in the element, which is sensed as a change in resistance. The TCD is not as sensitive as other detectors, but it is non-destructive. The relationship between the TDC output (in mV) and the hydrogen amount (in ml) was calibrated by injecting into the vessel controlled volumes of hydrogen (0.1, 0.3, and 0.5 ml). The influence of specimen preparation on hydrogen measurements was also investigated. Test duration was chosen based upon hydrogen diffusibility calculations. Analysis was made on base metal coupons of 4 mm x 15 mm x 40 mm cut from extruded bars of 6060-T4 and 6060-T6 (Table 4), and on 40 mm long weld coupons cut along and close to the weld edges.

5 Results and Discussion

5.1 CTW Test Development

The CTW test was developed for GTA aluminum welds to include local extensometer strain measurements in the vicinity of the weld pool. However, extensometer measurements are limited to one fixed position and do not enable an overview of the strain distribution over a large surface. Therefore, *digital image correlation (DIC) measurements* were made and compared to extensometer measurements. Also discussed here is the affect of *extensometer location* on strain measurements.

5.1.1 Digital Image Correlation (DIC) Measurements

Extensometer measurements are defined by a fixed location along the weld and a fixed gage length. The possibility exists for a much more thorough strain characterization using a digital image correlation (DIC) technique and employing the computer aided tracking of a random speckle pattern painted onto the plate surface prior to welding [162]. The DIC measurements were performed on Alloy 6060 CTW test coupons welded without 4043 filler and with no applied cross-head speed. At a given instant, the calculated transverse strains are mapped in a window of 20 mm wide and 40 mm long superposed on a photo of the weld at the same instant (Figure 70a). The torch travels from the top to the bottom of the photo. The red transverse line locates the weld pool. Along this line, the transverse strains are plotted (Figure 70b), with a value of “1,000” on the point index corresponding to 20 mm. A constant increase in strain was observed over a distance of 11 mm centered on a 6 mm wide weld pool. Noting strain ε, transverse distance x, and time t, the straight lines correspond to $d\varepsilon/dx \approx$ constant, which leads to $d\varepsilon/dt \approx$ constant within the immediate vicinity of the weld. The measured strain rate is also approximately constant for a gage length under 11 mm. Thus, the gage length of 10.5 mm chosen for extensometer measurements appears to represent strain rates at the fusion line. Under constant experimental conditions, the strains measured with the extensometer (between –2.22 and +0.11 %) are found close to the strains measured with the DIC technique (between –2.26 and +0.32 %, Figure 70a).

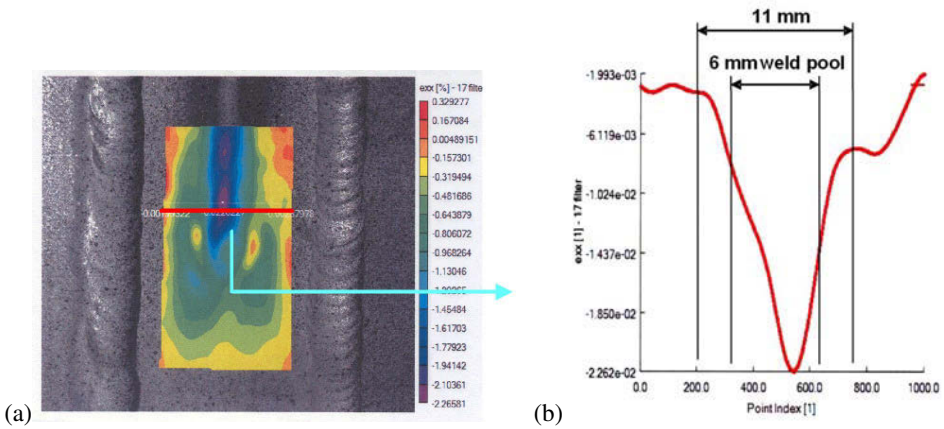

Figure 70: (a) Light optical DIC measurements made on bottom side of plate during autogenous, full-penetration, bead-on-plate GTA welding of aluminum 6060 plate. Note black paint speckle pattern sprayed onto plate prior to welding. (b) Strain across mushy zone of weld pool showing a constant outward displacement with distance from weld centerline.

5.1.2 Extensometer Measurements versus Location

Since extensometer measurements are defined by a fixed position, the location of the extensometer along the weld could affect strain measurements. In executing the CTW test sequence (Table 7), the extensometer was positioned at weld mid-length. However, ideally the best place to measure strain is at the crack initiation site, which was found to always occur at the point where the mushy zone sits when strain is first applied, 25 mm after the weld start. Therefore, a few select strain rate measurements were made at the observed crack initiation site to correlate these measurements with those measured at weld mid-length (Table 12), the standard location selected for strain measurement in this study. These values show good agreement (less than 0.05 %/s difference), except for one condition at high cross-head speed (0.083 mm/s), far exceeding the critical conditions for crack formation. Ideally, the standard sequence should be modified for future tests, to relocate the extensometer to the 25 mm position.

Table 12: Comparison Between Strain Rates Based Upon Extensometer Measurements Made 25 mm from Weld Start and at Weld Mid-Length

Cracking susceptibility	Dilution (%)	Cross-head speed (mm/s)	Measured strain rate (%/s)	
			25 mm from weld start	Weld mid-length
No crack	0	0	-0.18	-0.20
Crack	0	0.033	-0.09	-0.06
No crack	17	0.033	-0.05	+0.00
Crack	17	0.083	+0.26	+0.55

5.2 Weldability Measurements

Using the Controlled Tensile Weldability (CTW) test, the amount of 4043 filler dilution required to avoid crack formation was determined for different local strain rate and experimental conditions. Strain rate was identified as an important parameter to monitor, in particular, because of its direct relationship to cracking mechanisms [81,91]. A new approach to crack evaluation was taken whereby a strain rate versus dilution map was developed to identify critical conditions needed for cracking.

5.2.1 6060/4043 Weldability

The 6060/4043 weldability characterization was investigated on 6060-T4 base alloy using the CTW test. Weld pool shape was characterized, local strain was measured, and the calculated local strain rate was chosen as the solidification cracking susceptibility index. Results are presented using the new "critical strain rate – dilution mapping" concept and discussed.

5.2.1.1 Local Strain Measurement

An example of strain measurement made during a CTW test is presented in Figure 71a, shown as a function of time with the CTW test sequence superimposed from Table 7. Since strain is measured with an extensometer spanned across the weld, a negative strain rate shows that the material is moving toward the weld centerline, and a positive strain rate reveals that it is moving away. The negative strain between 5 and 15 seconds is likely due to thermal expansion in the test sample caused by heating ahead of the advancing weld torch [37]. Figure 71b shows the calculated strain rate from point (3) to point (4) during weld solidification. Time has been set to zero in Figure 71b, corresponding to step 3. Although a continuous centerline crack is formed under the test conditions presented in Figure 71, the irregularity in the curve (at 1 second, Figure 71b) likely represents erratic crack growth, as has been observed by other researchers [19,27].

The repeatability of the CTW test results was examined for the test conditions 11% 4043 filler dilution and 0.033 mm/s cross-head speed. Performing the CTW test three times for these fixed test conditions resulted in a variation in measured strain rates between +0.10 and +0.11 %/s (± 0.005 %/s), demonstrating good repeatability within 10%.

The local strain rate value is taken at the coherency point, 1.7 seconds behind the torch (torch is at point (3), Figure 71b). Indeed, strain measurements were made at the point

where the mushy zone (coherency point) passes between the extensometer. The weld pool temperature was recorded during solidification to know where the mushy zone and coherency point were located relative to the torch position. Thermal analyses (detailed in paragraph 5.3.1.2) measured the liquidus at 660°C and coherency point at 624°C for Alloy 6060. Weld pool shape measurements (detailed in paragraph 5.2.3) revealed a distance from the electrode to the fusion line along weld centerline of 6 mm, corresponding to 1.5 seconds for a 4 mm/s welding speed. Adding the temperature drop from liquidus to coherency temperature in approximately 0.2 second (thermal analysis in paragraph 5.3.1.2), the coherency temperature along the weld centerline is reached 1.7 seconds after the passage of the welding electrode.

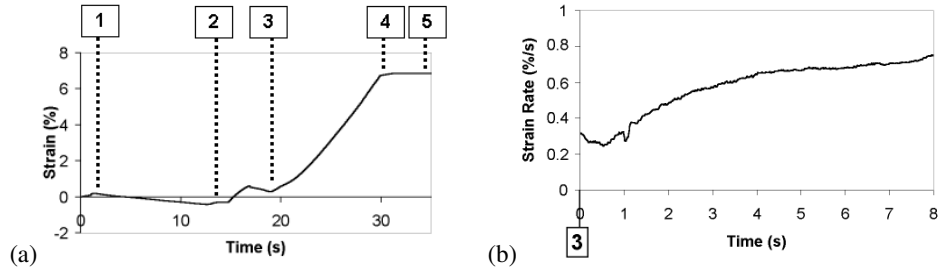

Figure 71: (a) CTW test sequence superimposed on measured strain and (b) first derivative of strain-time curve in (a), for test conditions 6060+ 9% 4043 filler dilution and 0.067 mm/s cross-head speed.

Additional strain rate plots are compared in Figures 72 and 73 showing respectively the influence of cross-head speed and dilution on cracking susceptibility. Both the liquidus and coherency temperatures are indicated to identify the region of interest to solidification cracking. A general trend is observed for strain rate over time, whereby it either continuously increases (for the case of crack formation), or it first increases and then plateaus (for the case of no crack formation). In case of cracking, the increase in crack length over time reduces the specimen resistance to the applied transverse cross-head speed, and thus the local strain rate continues to increase. In case of no cracking, a plateau appears once welding is complete and the thermal condition is stabilized.

For a fixed filler dilution of 9% (Figure 72), the cross-head speed is observed to have a direct effect on strain rate. Increasing the cross-head speed increases the local strain rate, as to be expected. For a cross-head speed up to 0.033 mm/s (curves (a), (b), (c)) no cracking was observed. Over 0.050 mm/s (curves (d) and (e)), a continuous centerline crack was formed, with a crack forming instantaneously with the application of strain. The critical condition for crack formation is bounded by the curves (c) and (d), where the maximum local strain rate measured without cracking (point A) corresponds to a value close to the critical

strain rate required to form cracking. When considering mechanisms for crack formation, one must be careful to distinguish between crack nucleation and growth. However, it is not known at this point which of these two phenomena is actually being represented here by these observed critical strain rate conditions.

Figure 73 illustrates the influence of filler dilution on strain rate and cracking susceptibility, in this case for a cross-head speed of 0.050 mm/s. A continuous centerline crack formed with up to 9% filler dilution (curves (a), (b), (c)), but with 11% filler dilution (curve (d)) only discontinuous, i.e. small successive, cracks were formed. For welds made with over 14% filler dilution (curves (e) and (f)) no cracking was observed. As was the case in Figure 72, crack-free welds exhibited lower strain rates. Irregularities are observed on strain rate curves that are close to the critical conditions needed to form cracking (curve (d) in Figure 72; curve (c) in Figure 73), suggesting that crack growth is erratic.

Filler dilution affects local strain rates even for uncracked welds (Figure 73, curves (e) and (f)). This could be due to the lower cooling rate at higher filler dilution (as shown in the next section) resulting in lower rates of solidification shrinkage and thermal contraction, or an increased weld pool width (detailed in paragraph 5.2.3) in relation to a fixed extensometer gage length (10.5 mm). Since the strain field is not necessarily uniform in the mushy zone and surrounding base metal, the use of an extensometer to monitor strain has its limitations. It is suggested that optical methods for strain measurement, for example the MISO technique in the weld metal [62] or digital image correlation (DIC) analysis of the surrounding base metal (recall Figure 70), could have advantages over extensometer measurements.

Negative local strain rates were sometimes measured at low (or zero) applied tensile cross-head speeds. For example, a tensile cross-head speed of 0.017 mm/s for a filler dilution of 9% resulted in a negative (i.e. compressive) local strain rate (Figure 72 curve (b)). This suggests the existence of local compressive cells behind the weld pool, formed in reaction to thermal and shrinkage stresses [37], which should preclude crack formation [14].

5.2.1.2 Critical Strain Rate – Dilution Map

Recall from Eq. 35, filler dilution was calculated and plotted as a function of filler wire speed as shown in Figure 74. Filler dilution was found to vary between 0 and 16% for filler wire speeds between 0 and 41.7 mm/s. For each filler dilution examined, the weld metal composition is given in Table 13, showing that silicon is the primary alloying element affected by filler dilution.

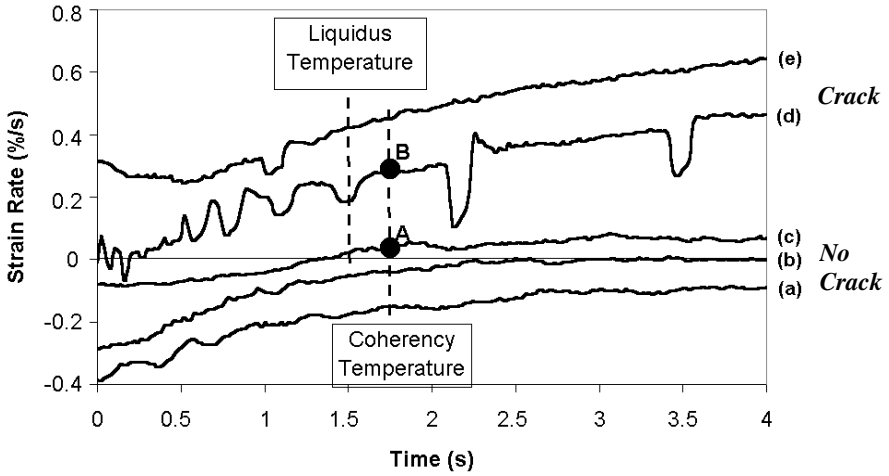

Figure 72: Strain rate measurements for a filler dilution of 9% and a cross-head speed of (a) 0, (b) 0.017, (c) 0.033, (d) 0.050, (e) 0.067 mm/s. Note the points A (insufficient strain rate to form crack) and B (sufficient strain rate to form crack).

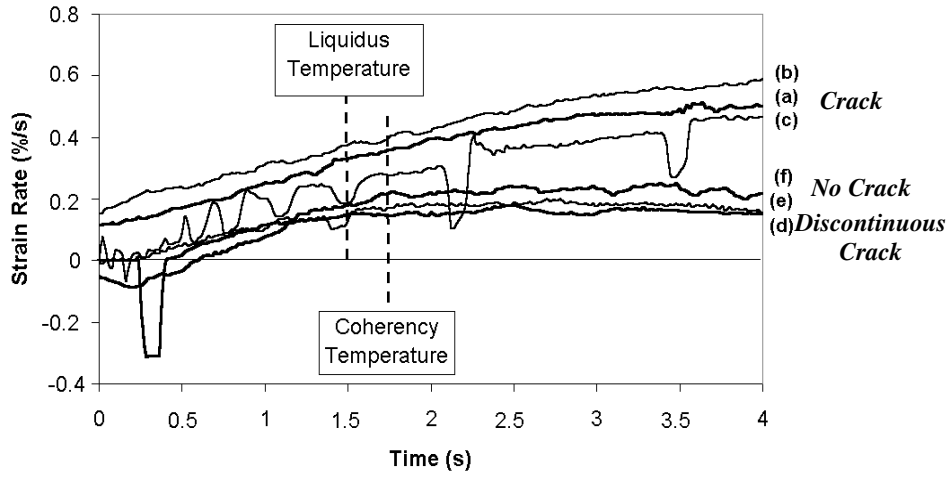

Figure 73: Strain rate measurements for a cross-head speed of 0.050 mm/s and a filler dilution of (a) 0%, (b) 5%, (c) 9%, (d) 11%, (e) 14%, (f) 16%.

Table 13: Measured Chemical Analysis for Aluminum Alloy 6060 and 6060/4043 Mixtures (wet chemical analysis for 4043 filler wire and spectrometry for 6060 base metal)

Aluminum Alloy	Composition (wt.%)									
	Si	Mg	Fe	Mn	Cu	Cr	Ni	Zn	Ti	Zr
6060-T4	0.42	0.59	0.19	0.020	0.012	0.004	0.004	0.009	0.020	0.001
6060+05% 4043	0.66	0.56	0.19	0.019	0.012	0.004	0.004	0.009	0.019	0.001
6060+09% 4043	0.86	0.54	0.19	0.018	0.013	0.004	0.004	0.009	0.018	0.001
6060+11% 4043	0.96	0.53	0.19	0.018	0.013	0.004	0.004	0.009	0.018	0.001
6060+14% 4043	1.10	0.51	0.19	0.018	0.013	0.004	0.004	0.008	0.018	0.001
6060+16% 4043	1.20	0.50	0.19	0.017	0.013	0.004	0.004	0.008	0.017	0.001
4043	5.30	0.002	0.22	0.003	0.018	0.002	0.005	0.005	0.003	0.002

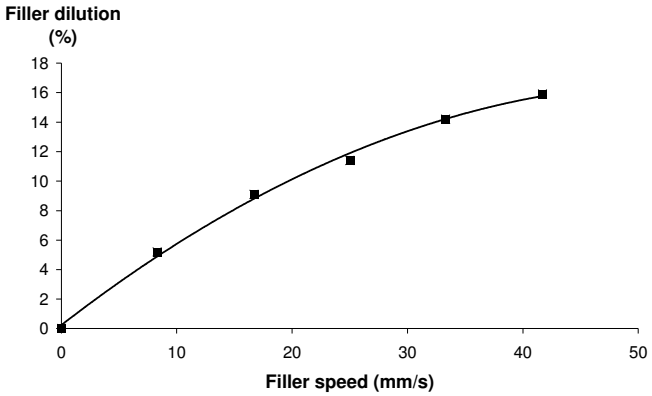

Figure 74: Calculated filler dilution as a function of filler wire speed.

The type of crack encountered in CTW testing is plotted as a function of cross-head speed and filler speed (Figure 75a), and local strain rate and filler dilution (Figure 75b). Since the strain is measured with the extensometer spanned across the weld (recall Figure 61), a negative strain rate reveals that the material is moving toward the weld centerline, while a positive strain rate shows that it is moving away. A border (approximated with dashed line) is established between crack and no-crack conditions, with discontinuous cracking occurring near the crack – no crack boundary. The position of the border reflects the influence of thermo-mechanical factors, where alloys with poor weldability have low critical strain rates. Its slope reveals the effect of thermo-metallurgical factors, i.e. effect of 4043 filler dilution on weldability. E.g. a vertical boundary would show that the filler does not affect weldability. Results show that more filler dilution, i.e. greater weld metal silicon content, is needed at higher strain rate to avoid cracking. Solidification cracking forms at a local strain rate of –0.06 %/s at 0% 4043 filler dilution and +0.35 %/s at 16% 4043 filler dilution.

As can be seen in the strain rate - dilution map, cracking that occurs at low 4043 dilutions involves a negative critical strain rate (i.e. inward movement of material to feed

shrinkage). At first hand this appears counter intuitive, but may actually reflect upon the material's very poor weldability. Even with the inward movement of base material, the low compressive local strain rate (–0.06 %/s) does not entirely compensate for solidification shrinkage, still permitting tensile strains in the mushy zone.

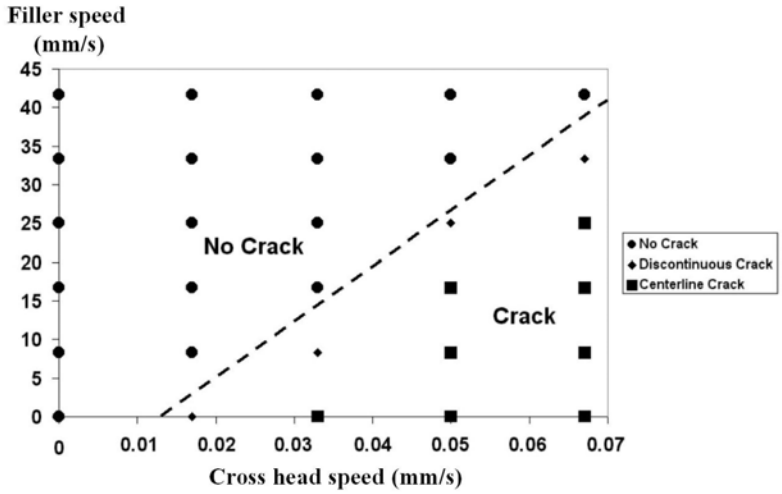

(a)

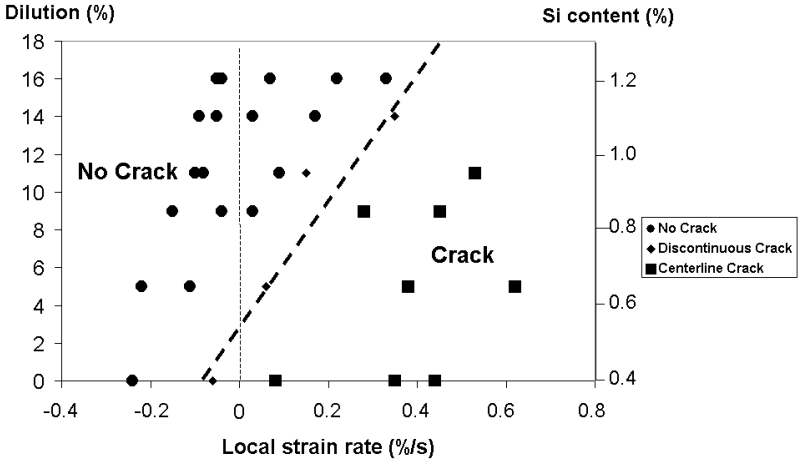

(b)

Figure 75: Cracking susceptibility of Alloy 6060 (a) for variable 4043 filler speed shown as a function of cross-head speed and (b) for variable 4043 filler dilution shown as a function of local strain rate.

Critical strain rates measured using the CTW test for crack formation are compared in Table 14 and 15 against values obtained with other tests taken from the literature, including the variable tensile strain test using an extensometer [150], the slow bending

trans-varestraint test using the Vickers indentation technique [12], and the variable deformation rate (VDR) test [70]. Strain rates are found to reflect directly upon weldability, where alloys with relatively poor weldability have low (or in some cases negative) critical strain rates (Table 14). These values are typically on the order of a few tenths of a percent per second, for each of the different testing methods. In comparison, observations made in aluminum alloy cast bar with the aid of a high-resolution camera and a digital image correlation software reveal that local strains rates around 0.4, 0.7, and 1.2 %/s were sufficient to promote cracking in respectively AA3104, Al-0.5wt.%Cu, and AA6111 cast aluminum alloys [25]. The critical deformation rates measured with the CTW and VDR tests differ from one order of magnitude (Table 15), suggesting that the conditions to initiate a crack (CTW) differ from the one to stop a crack (VDR). However, care should be taken when comparing these results, whose differences may reflect upon different welding conditions and gage lengths.

Table 14: Critical Strain Rates Required for Solidification Crack Formation

Test	Welding Speed (mm/s)	Aluminum Alloy Base Metal/Filler Metal	Critical Strain Rate for Crack Formation (%/s)
CTW Test (present study)	4	6060/4043 (0%)	-0.06
		6060/4043 (5%)	0.06
		6060/4043 (9%)	0.17
		6060/4043 (11%)	0.22
		6060/4043 (14%)	0.30
		6060/4043 (16%)	0.35
Variable Tensile Strain Test [150]	5	5052	0.15
		5083	0.20
Slow Bending Trans-Varestraint Test [12]	1.7	2017	0.15
		5083	0.47
		2219	0.50
		5052	0.64
		5154	0.70
		1070	5.00

Table 15: Critical Deformation Rates Required for Solidification Crack Formation

Test	Welding Speed (mm/s)	Aluminum Alloy Base metal/filler metal	Critical Deformation Rate for Crack Formation (mm/s)
CTW Test (Present study)	4	6060/4043 (0%)	-0.006
		6060/4043 (5%)	0.006
		6060/4043 (9%)	0.017
		6060/4043 (11%)	0.023
		6060/4043 (14%)	0.032
		6060/4043 (16%)	0.037
Variable Deformation Rate test [70]	4	1100/1070	0.15
	6.7	1100/1070	0.25
	10	1100/1070	0.40
	13.3	1100/1070	0.50
	6.7	5052/1070	0.05
	6.7	5083A/5183B	0.18

5.2.2 Minor Element Effects

The weld parameter and minor element effects were investigated on a 6060-T6 base alloy, a different heat of material than the 6060-T4 previously studied. Using the CTW test, local strain rates were calculated from the local strain extensometer measurements. The extensometer was maintained at the weld mid-length. The results are presented using the new “critical strain rate – dilution mapping” concept. A fixed incremental step (0.017 mm/s) was chosen to cover a wide range of cross-head speeds. Thus, the condition between crack and no-crack is not precisely defined, but lies somewhere within this fixed step. The crack – no crack boundary was first compared with the one found for alloy 6060-T4 (Figure 75b). The effect of weld parameter and minor elements is afterwards investigated and discussed.

5.2.2.1 Heat / Temper Effect

Aluminum 6060 extrusions from two different heats and tempers were evaluated with the CTW test using the same base welding parameters (Table 5). A critical strain rate – dilution map comparing 6060-T4 and 6060-T6 is shown in Figure 76. 6060-T6 has been studied at 0 and 17% 4043 filler dilution, whereas data for 6060-T4 exists from previous work (Figure 75b). A large difference in critical dilution is observed at high strain rates, where higher 4043 dilution is required to avoid cracking in 6060-T6. For example, at a local strain rate of 0 %/s, 7% 4043 filler dilution is required to avoid cracking in 6060-T4, while 17% filler dilution is required for 6060-T6. It is not known at this point whether this difference in

weldability is due to differences in hardness (40 and 83 HV0.5) or composition (Table 4). Also, grain size in 6060-T4 weld metal (51 and 63 µm for 0 and 16% 4043 respectively), which is more weldable, is bigger than in 6060-T6 weld metal (43 and 39 µm for 0 and 17% 4043 respectively).

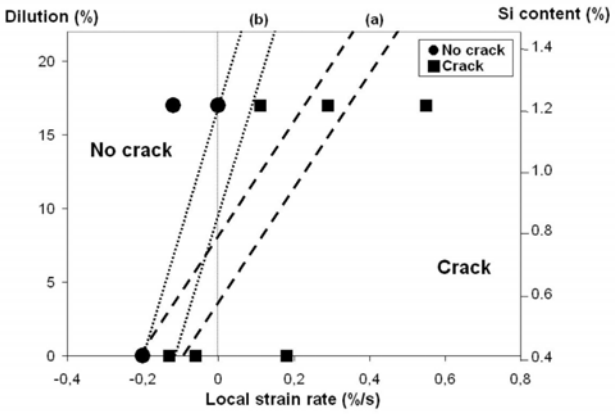

Figure 76: (a) 6060-T4 and (b) 6060-T6 crack-no crack boundaries on critical strain rate – dilution map with measurements realized on 6060-T6 at 0% and 17% 4043 filler dilution.

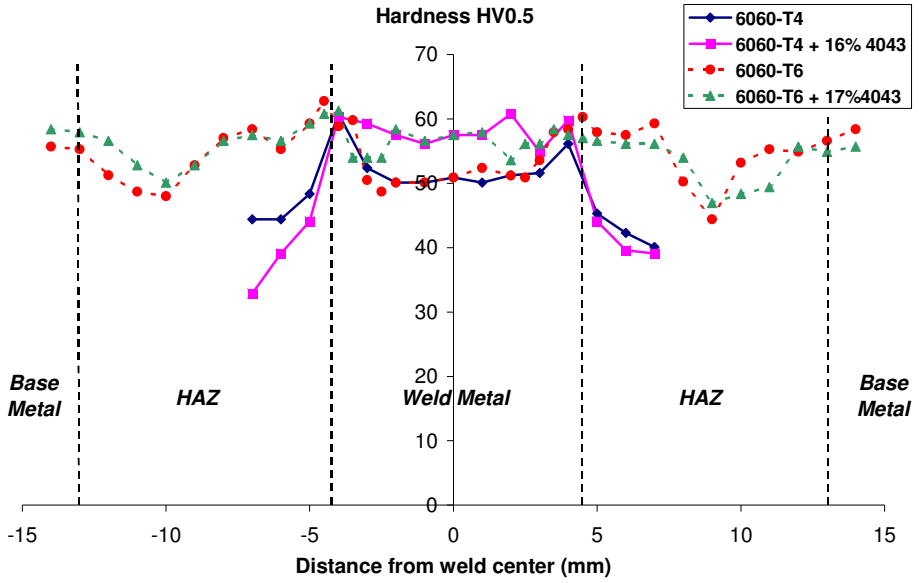

Figure 77: Hardness measurements on weld cross sections for both 6060-T4 and 6060-T6 base metals at low and high 4043 filler dilutions.

Initial surface hardnesses of base metal extruded plates were 40 and 83 HV0.5 for 6060-T4 and 6060-T6 respectively. Hardness measurements on weld cross-sections (Figure 77) reveal similar hardnesses for the two base metal welds made in same experimental conditions, with an increase in weld metal hardnesses from approximately 52 to 58 HV0.5 when increasing 4043 filler dilution. Also observed was a decrease in hardness in the heat affected zone, from approximately 57 to 41 HV0.5 with higher filler additions, probably due to smaller temperature gradient, i.e. longer time under heat, as seen in the next section. This demonstrates, however, how material with the same alloy designation can exhibit different weldability depending on specific conditions. This also reflects upon restraint, where the higher strength material (T6) provides higher restraint, thus influencing the interaction between global and local strain behavior.

5.2.2.2 Travel Speed Effect

CTW tests were made on aluminum 6060-T6 using the base parameters (Table 5), but varying the weld travel speed. In addition, the welding current was varied so as to maintain a constant weld pool size. Weld travel speed was run at 2, 4, and 6 mm/s, and the current was varied respectively from 80 to 145 A. Data for 4 mm/s was obtained from a previous test (Figure 75b). Filler dilutions studied were 0%, and either 18% or 16% 4043 respectively for 2 and 6 mm/s weld travel speeds. The crack – no crack boundaries for these conditions are compared against the boundary found using the base weld parameters (Table 5), i.e. 4 mm/s weld travel speed and 110 A, as shown in Figures 78 and 79. Increasing weld travel speed should improve weldability following the relationship of Chihosky [37,38], and this appears to be the case, but only at high filler dilutions. Specifically, at 18% 4043 filler dilution, solidification cracking occurs for a +0.12 %/s local strain rate at 2 and 4 mm/s weld travel speed, while no crack occurs at +0.25 %/s strain rate for a 6 mm/s travel speed. On the other hand, 6060-T6 is less weldable at 0% 4043 filler dilution with increasing weld travel speed. This is likely due to a change in weld metal grain structure, where stray centerline grains were observed to occur only at 4 and 6 mm/s weld travel speed. With the exception of bigger grains at 6 mm/s welding speed and no filler, grain size in 6060-T6 did not significantly vary between welding speeds of 2 mm/s (42 and 41 μm for 0 and 18% 4043 respectively), 4 mm/s (43 and 39 μm for 0 and 17% 4043 respectively), and 6 mm/s (49 and 39 μm for 0 and 16% 4043 respectively).

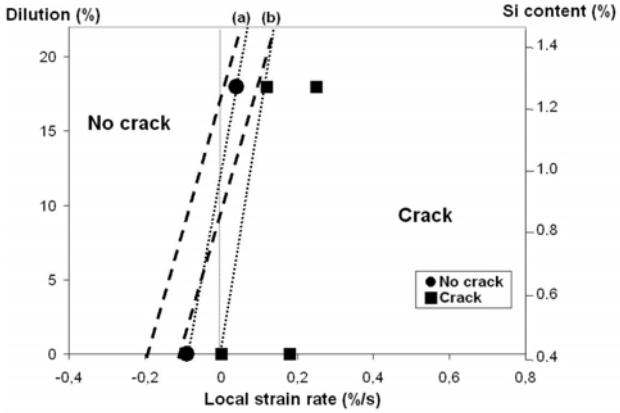

Figure 78: Critical strain rate – dilution map comparing crack-no crack boundaries at weld travel speeds of (a) 4 mm/s and (b) 2 mm/s when welding 6060-T6. Data points are shown for 2 mm/s.

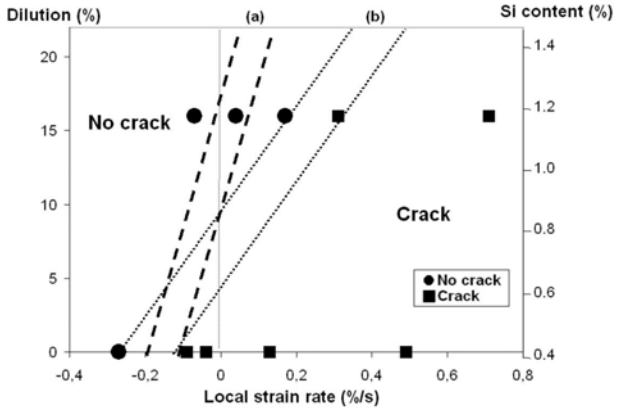

Figure 79: Critical strain rate – dilution map comparing crack-no crack boundaries at weld travel speeds of (a) 4 mm/s and (b) 6 mm/s when welding 6060-T6. Data points are shown for 6 mm/s.

5.2.2.3 Insert Effect

Weld coupons with 6060 inserts containing no extra alloying elements were evaluated with CTW testing thus providing a control to determine the influence of the insert and corresponding weld coupon preparation on weldability. The base welding parameters were used (Table 5), but the current was decreased to 95A to maintain a constant weld pool size. Cracking susceptibility was measured for 0 and 17% 4043 filler dilution. Figure 80 compares the crack-no crack boundary for 6060-T6 with base welding parameters and 6060-T6 with 6060 inserts. A slight difference is observed which may come from the methodology to determine these boundaries (i.e. fixed increasing step of the cross-head speed). The use of

inserts appears to have no significant influence on the crack - no crack boundary. Thus, weldability differences due to insert alloy additions (following sections) will be assumed to represent the effect of the alloy addition, and not the insert itself.

5.2.2.4 Iron Impurity Effect

Inserts at high iron content were machined from a 6060+1.7%Fe ingot (Table 8). The influence of iron content on cracking susceptibility was first observed during the casting of ingots. While 6060 ingots cracked at the base of the pouring spout, there was no cracking in 6060+1.7%Fe ingots. This supports observations of Lu and Dahle [177], where high iron content prevented cracking in cast Al-Mg-Si alloys. The welding parameters were the same as those used for 6060 inserts. The 4043 filler dilutions studied included 0% and 20%. The weld pool composition resulting from using the high iron insert had a corresponding high iron content (i.e. increase from 0.2 to 0.4 wt.% Fe) as given in Table 8. The crack - no crack boundaries are compared in Figure 81. Further investigations are needed to better define these boundaries, but it appears there is little effect of iron.

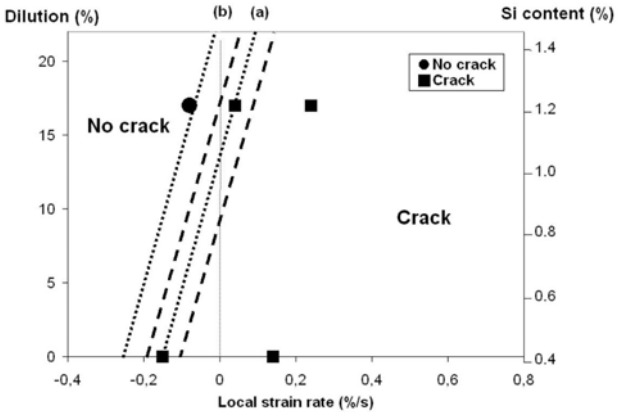

Figure 80: Critical strain rate – dilution map comparing crack-no crack boundaries for (a) 6060-T6 and (b) 6060-T6 with 6060 insert. Data points are shown for 6060 inserts.

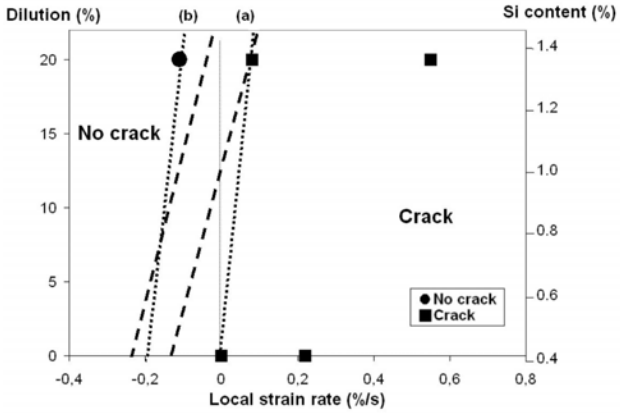

Figure 81: Critical strain rate – dilution map comparing crack-no crack boundaries for 6060-T6 with (a) 6060 insert and (b) 6060+1.7%Fe insert. Data points are shown for 6060+1.7% Fe insert.

5.2.2.5 Grain Refiner Effect

Titanium plus boron are the standard grain refiners for most aluminum alloys [163]. CTW tests were performed with inserts high in Tibor content machined from a 6060+0.8%Ti+0.16%B ingot (Table 8). A few scattered macro-pores were observed in the weld cross-sections. The influence of Tibor on cracking susceptibility was first observed in cast ingots, where 6060 ingots cracked at the base of the pouring spout, and 6060+0.8%Ti+0.16%B ingots did not crack. The welding parameters were the same as those used for 6060 inserts. The 4043 filler dilutions studied were 0% and 15%. The weld pool composition with the Ti rich insert differed by its higher titanium content (from 0.02 to 0.14 wt.% Ti) as given in Table 8. Crack-no crack boundaries are compared for both insert compositions in Figure 82. The grain refiner addition significantly improved weldability, particularly at low 4043 filler dilutions. This is not surprising considering the potent effect of refinement reported for aluminum weldability improvement [5]. Also, stray centerline grains present in 6060-T6 without 4043 filler addition were not present in autogeneous welds with high titanium contents (grain refinement). The important improvement of weldability at low 4043 filler dilution may be due to both grain refinement and stray grain disappearance. Moreover, it seems that Tibor improves weldability with more efficiency than 4043, the boundary being completely moved to higher strain rates for all dilutions. Finally, the boundary is almost vertical, revealing that 4043 filler dilution has little influence on the weldability of grain refined 6060 welds. In essence, the grain refinement resulted from Tibor seems to exceed any metallurgical effects resulting from 4043 filler dilution.

This suggests that it may prove feasible to develop a filler that is high in grain refiner, while low in Si. It is interesting to note that, despite a Ti content in 4043 filler very low (0.003 wt.% Ti) compared to the initial Ti content in 6060-T6 (0.02 wt.% Ti), increasing 4043 filler dilution promotes grain refinement (as shown in paragraph 5.2.3.1), in agreement with the refined grain structure found when adding silicon in cast aluminum [176]. Indeed, grain size in welds with Ti rich inserts was reduced to 29 µm for both 0 and 16% 4043, in comparison with non-refined welds (43 and 39 µm for 0 and 17% 4043 respectively). Thus, improved grain refinement should be achieved with increasing 4043 filler dilution, which may explain why the crack - no crack boundaries tend to be closer at high 4043 filler dilutions (Figure 82).

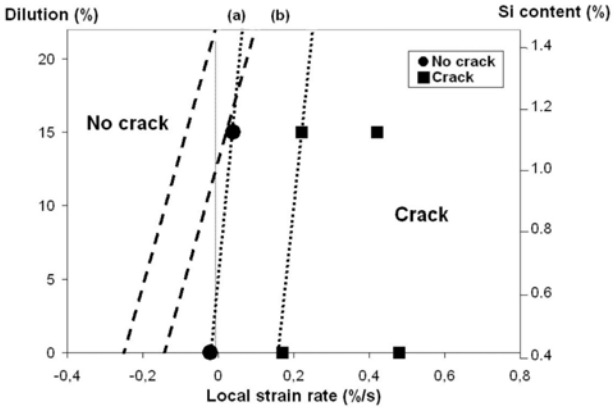

Figure 82: Critical strain rate – dilution map comparing crack-no crack boundaries for 6060 –T6 with (a) 6060 insert and (b) 6060+0.8%Ti insert. Data points are shown for 6060+0.8%Ti insert.

5.2.2.6 Oxygen Contamination Effect

CTW tests were performed using an oxygen-containing shielding gas (flow rate: 0.33 L/s He + 0.03 L/s Ar+1%O_2). This required a decrease in the welding current to 100 A to keep a constant weld pool size. Filler dilutions of 0% and 18% 4043 were studied. High quantities of oxides were observed at the weld surface. Crack - no crack boundaries are compared between normal and oxygen-containing gas in Figure 83, where use of oxygen is found to slightly improve weldability. At 18% filler dilution and a local strain rate of +0.09 %/s, a crack should occur when welding with helium, but does not initiate with oxygen added to the helium. This trend goes counter to the belief that oxygen forms oxides films that can nucleate cracks [22]. However, it may just be that a heavy oxide is formed at the pool surface and does not get mixed into the weld pool.

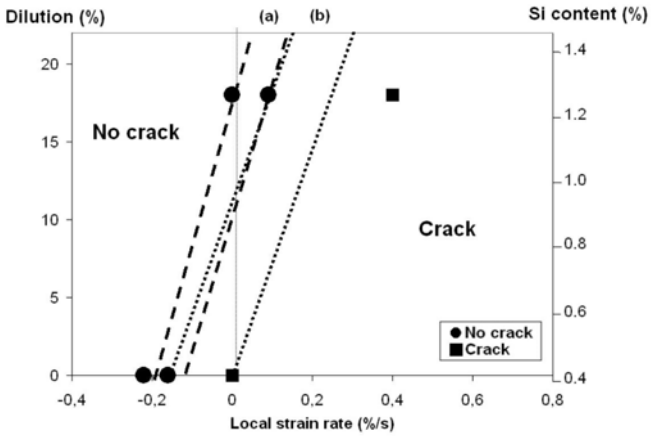

Figure 83: Critical strain rate - dilution map comparing crack-no crack boundaries for 6060-T6 welded with (a) 0.33 L/s He and (b) 0.33 L/s He + 0.03 L/s (Ar+1%O_2). Data points are shown for He+(Ar+1%O_2) shielding gas.

5.2.2.7 Hydrogen Contamination Effect

CTW tests were performed using a hydrogen-containing shielding gas (flow rate : 0.33 L/s He + 0.27 L/s Ar+2%H_2). This required a decrease in the welding current to 105 A to keep a constant weld pool size. Filler dilutions were studied at 0% and 18% 4043. Limited interdendritic pores were observed in the weld cross section (Figure 84). Since no oxides were observed on the weld surface, it is assumed that hydrogen served as an effective reducing element. Crack - no crack boundaries are compared between welds made with helium and helium-argon-hydrogen in Figure 85. Hydrogen is found to improve weldability, especially at high 4043 filler dilution. In fact, at 18% filler dilution and +0.15 %/s local strain rate, 6060-T6 cracked when welded with helium, but did not crack when welded with helium-argon-hydrogen. This suggests that hydrogen pores may be feeding shrinkage and thus reducing the pressure drop. This leads to an interesting choice between having cracking or porosity.

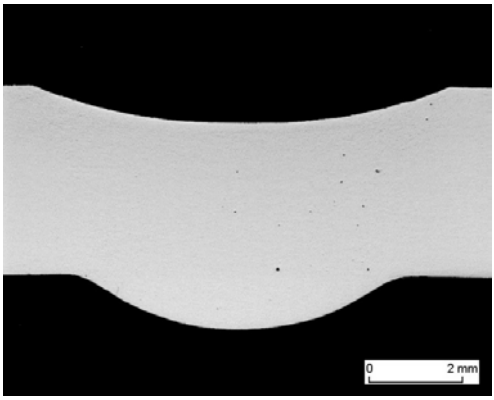

Figure 84: Unetched weld cross sections of 6060-T6 coupon made with He+Ar+H_2 and 0% 4043 filler dilution revealing interdendritic pores.

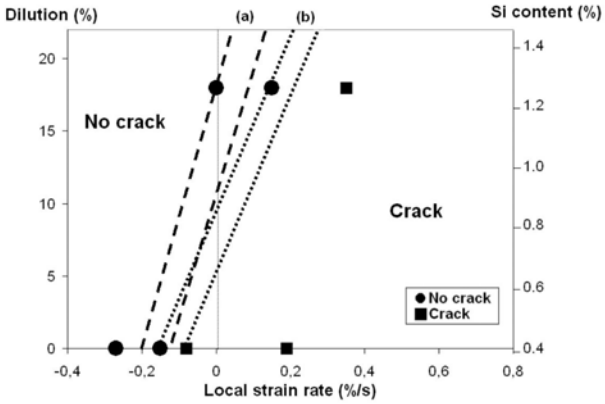

Figure 85: Critical strain rate – dilution map comparing crack-no crack boundaries for 6060-T6 welded with (a) 0.33 L/s He and (b) 0.33 L/s He + 0.27 L/s (Ar+2%H_2). Data points are shown for He+(Ar+2%H_2) shielding gas.

5.2.2.8 Sensitivity of CTW Test

The CTW test appears sensitive to small variations in alloy composition and welding conditions. In examining this subject, the sensitivity and limitations of this new weldability test have been established. Some of the inherent problems associated with this test are discussed below.

Crack Boundary. The nature of the crack-no crack boundary for the 6060/4043 alloy system is such that variations in filler dilution of 0 to roughly 17% corresponds to a maximum difference in critical strain rate, expressed in terms of cross-head speed, of roughly

0.1 mm/s. In terms of test sensitivity, it would be preferable that this number be much larger. As it is, this means that test increments approaching 0.01 mm/s are needed to accurately identify the location of a boundary (i.e. one tenth of the full range). In this work, increments of 0.017 mm/s were used, which only roughly determined the boundary for each experimental condition. Thus, the use of finer increments should be considered for future tests on this alloy. Other alloy systems will likely exhibit their own unique sensitivity to strain rate.

Interacting Factors. As is usual for welding experiments, it is difficult to vary one parameter systematically and not have numerous other factors change indirectly. For CTW testing, the use of 4043 filler changes not only the silicon content of the weld metal, but increases the size and shape of the weld bead. Thus, it becomes difficult to separate the metallurgical effects from the mechanical. Likewise, variations in travel speed or changes in shielding gas will alter the heat input and, although corrected with adjustments to current, there may be subtle changes to pool shape that can affect grain structure. Thus, it becomes difficult to know if the effect of travel speed on weldability is due to a change in local strain rate or grain structure. The application of modeling may help to answer these questions in the future.

5.2.3 Weld Pool / Weld Metal Characterization

5.2.3.1 6060-T4 / 4043 Weld Metal

Application of Etch E2 at room temperature for 1 minute (Table 6) revealed the grain structure and weld pool shape from the top surface as shown in Figure 86. Weld pool shape was approximately constant for different 4043 filler dilutions, with distances A, B, and C summarized in Table 16. Of particular importance is distance B, approximately 6 mm, which represents the distance between the electrode and the fusion boundary along the weld centerline. Thus, with a torch travel speed of 4 mm/s, solidification along the weld centerline starts approximately 1.5 seconds after passage of the electrode.

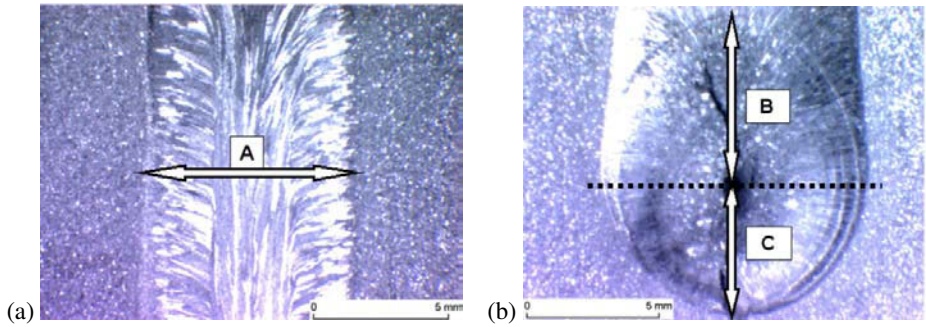

Figure 86: Weld pool measurements from top surface: (a) width- A, (b) distance behind electrode- B, and distance in front of electrode- C.

Table 16: Weld Pool Measurements for Al 6060-T4 According to Figure 86

Filler Dilution (%)	Top Width: A (mm)	Distance Behind Electrode: B (mm)	Distance in Front of Electrode: C (mm)
0	7.5	6.1	4.7
5	7.8	6.0	4.6
9	8.0	6.3	4.8
11	8.1	6.3	4.7
14	8.1	5.9	4.6
16	8.1	5.9	4.8

Observation of 6060-T4 weld metal microstructure from the top surface reveals stray centerline grains for autogenous welds (i.e. with no 4043 filler added, Figure 87a). These stray grains are no longer observed with as little as 5% filler dilution (Figure 87b), with additional increases in filler dilution causing further grain refinement (Figures 87b-f). However, it is not clear whether the higher silicon content, shown to promote grain refinement in aluminum castings [176], or the mechanical disturbance when adding filler alloy eliminates stray grains.

Metallographic transverse cross-sections taken from the weld mid-length were examined for all 4043 filler dilutions, and weld bead dimensions were measured as summarized in Table 17. An example of weld cross-sections made on Alloy 6060-T4 coupons with 0 and 16% 4043 filler dilution are compared in Figure 88, showing an increase in weld bead thickness from 4.2 to 5.0 mm and bead width from 7.5 to 8.1 mm. Cross sectional area also increased with filler dilution from 25.1 to 31.7 mm^2 and overbead curvature changed from –0.068 (concave) to +0.011 mm^{-1} (convex). The change in curvature from concave to convex occurred between 11 and 14% filler dilution, and is reported to provide better cracking resistance [187], although the reason for this remains unclear.

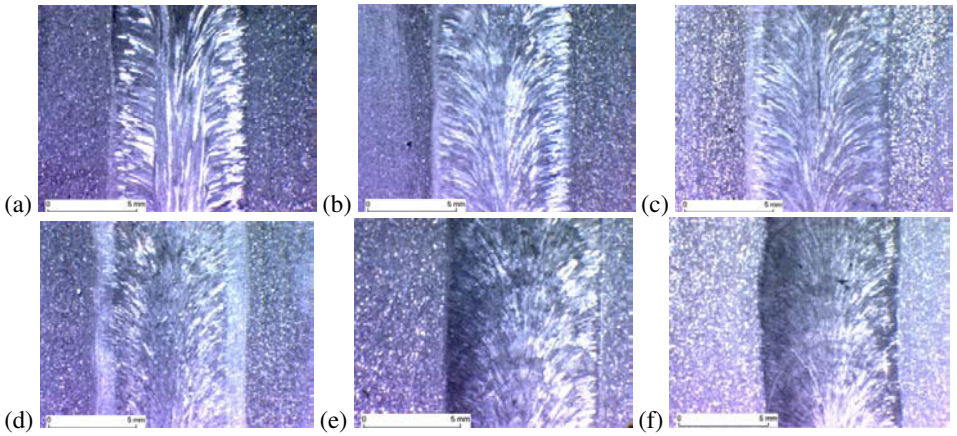

Figure 87: Grain structure at top surface of weld metal for Al 6060-T4 with (a) 0%, (b) 5%, (c) 9%, (d) 11%, (e) 14%, (f) 16% 4043 filler dilution.

Table 17: Characteristic Dimensions of Weld Metal for Al 6060-T4 Depending on Filler Dilution

Filler Wire Speed (mm/s)	Filler Dilution (%)	Cross Section Area (mm^2)	Bead Thickness (mm)	Root Width (mm)	Over-Bead Width (mm)	Over-Bead Curvature (mm^{-1})
0	0	25.1	4.2	5.5	7.5	-0.068
8.3	5	25.5	4.4	5.1	7.8	-0.023
16.7	9	25.9	4.6	5.4	8.0	-0.031
25.0	11	28.0	4.7	5.4	8.1	-0.007
33.3	14	29.0	4.9	5.7	8.1	0.007
41.7	16	31.7	5.0	6.5	8.1	0.011

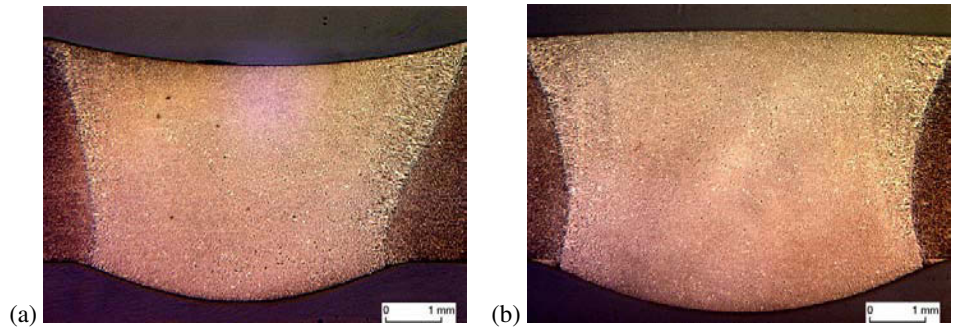

Figure 88: Weld metal cross-sections for a) 6060-T4 and b) 6060-T4+16% 4043, for the case of zero cross-head speed.

Grain size measurements for weld cross-sections were made for 0% and 16% 4043 dilution with the aid of Electron Backscattered Diffraction (ESBD) to help delineate grain boundaries as shown in Figure 89. Increasing 4043 dilution from 0 to 16% promotes small refinement in grain size (from 63 to 51 μm), which may contribute at least in part to improved

weldability, based upon previous studies [5,178]. Moreover, observing the crack tip reveals the intergranular nature of crack propagation (Figure 90).

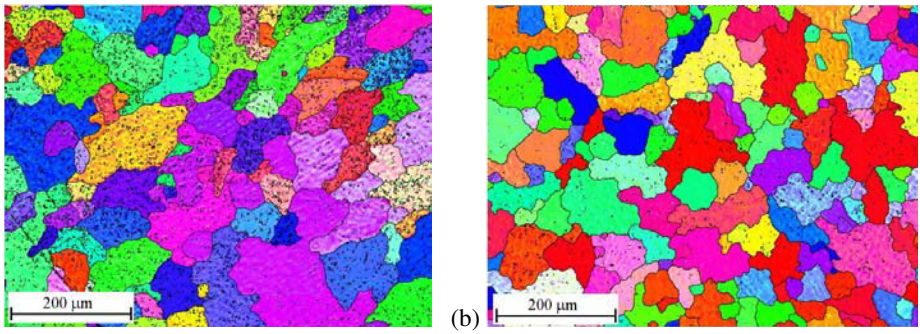

Figure 89: SEM-EBSD micrographs for Al- 6060-T4 weld metal cross-section with (a) 0% 4043 and (b) 16% 4043 filler dilution.

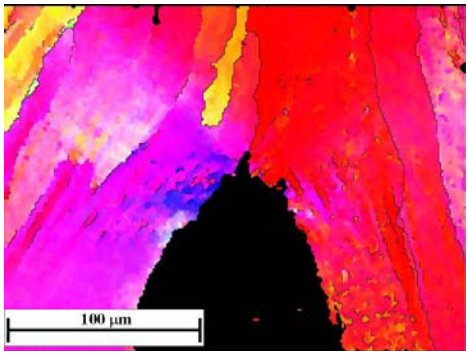

Figure 90: SEM-EBSD micrograph of crack tip for Al- 6060 with 0% 4043 filler dilution and 0.033 mm/s cross-head speed.

5.2.3.2 Minor Element Effects

Tables 18 to 25 reveal the different weld pool shape measurements realized for all the studied experimental conditions. They explicitly relate the calculated filler dilution to the 4043 filler feeding speed, the weld pool shape measurements according to Figure 86, and dimensional cross sectional characteristics of the weld pools. Each table corresponds to one experimental condition at low and high 4043 filler dilutions. For all the welding conditions, the dimensional characteristics of the weld pool were: top width 8 mm, and distance behind electrode 6 mm, with a deviation of $\pm$ 1 mm.

Metallographic transverse cross-sections were cut from the mid-length of the weld. Weld bead dimensions were measured in all experimental conditions (Tables 18 to 25) and

remained almost constant. Cross-sections for all experimental conditions revealed similar weld pool shapes. More detailed weld metal dimensions for 0% 4043 filler dilution are : 8 mm overbead width, 6 mm underbead width, 4 mm centerline thickness, and 24 to 27 mm² cross-sectional area. For 17% 4043 filler dilution these dimensions are : 8 mm overbead width, 6 mm underbead width, 5 mm centerline thickness, and 28 to 32 mm² cross-sectional area.

Table 18: 4043 filler dilution and dimensional characteristics for CTW welds of alloy 6060-T6. Distances (A), (B), (C) are according to Figure 86

Base metal	Filler Wire Speed (mm/s)	Filler Dilution (%)	Top Width (A) (mm)	Distance behind electrode (B) (mm)	Distance in front of electrode (C) (mm)
6060-T6	0	0	7.5	6.3	5.6
6060-T6	41.7	17	7.8	5.9	5.3
Cross Section Area (mm²)	**Bead Thickness (mm)**	**Root Width (mm)**	**Over-Bead Width (mm)**	**Over-Bead Curvature (mm^{-1})**	
26.1	4.8	5.8	7.8	-0.066	
31.5	5.0	6.9	8.1	+0.009	

Table 19: 4043 filler dilution and dimensional characteristics for CTW welds of alloy 6060-T6 with 6060 insert. Distances (A), (B), (C) are according to Figure 86

Base metal	Filler Wire Speed (mm/s)	Filler Dilution (%)	Top Width (A) (mm)	Distance behind electrode (B) (mm)	Distance in front of electrode (C) (mm)
6060-T6	0	0	8.0	5.6	6.1
6060-T6	41.7	17	7.9	6.0	5.0
Cross Section Area (mm²)	**Bead Thickness (mm)**	**Root Width (mm)**	**Over-Bead Width (mm)**	**Over-Bead Curvature (mm^{-1})**	
24.2	4.3	5.7	8.1	-0.056	
28.7	5.1	6.0	8.0	+0.025	

Table 20: 4043 filler dilution and dimensional characteristics for CTW welds of alloy 6060-T6 with 6060+1.7%Fe insert. Distances (A), (B), (C) are according to Figure 86

Base metal	Filler Wire Speed (mm/s)	Filler Dilution (%)	Top Width (A) (mm)	Distance behind electrode (B) (mm)	Distance in front of electrode (C) (mm)
6060-T6	0	0	8.3	6.0	6.4
6060-T6	41.7	20	7.5	5.1	5.5
Cross Section Area (mm²)	**Bead Thickness (mm)**	**Root Width (mm)**	**Over-Bead Width (mm)**	**Over-Bead Curvature (mm^{-1})**	
26.7	4.3	5.7	8.5	-0.053	
29.6	5.3	6.5	7.6	+0.025	

Table 21: 4043 filler dilution and dimensional characteristics for CTW welds of alloy 6060-T6 with 6060+0.8%Ti insert. Distances (A), (B), (C) are according to Figure 86

Base metal	Filler Wire Speed (mm/s)	Filler Dilution (%)	Top Width (A) (mm)	Distance behind electrode (B) (mm)	Distance in front of electrode (C) (mm)
6060-T6	0	0	8.9	6.2	6.3
6060-T6	41.7	15	9.0	6.0	5.6
Cross Section Area (mm²)	**Bead Thickness (mm)**	**Root Width (mm)**	**Over-Bead Width (mm)**	**Over-Bead Curvature (mm^{-1})**	
25.2	4.3	4.5	8.4	-0.025	
28.7	5.1	5.1	7.9	+0.015	

Table 22: 4043 filler dilution and dimensional characteristics for CTW welds of alloy 6060-T6 welded at a torch travel speed of 2 mm/s. Distances (A), (B), (C) are according to Figure 86

Base metal	Filler Wire Speed (mm/s)	Filler Dilution (%)	Top Width (A) (mm)	Distance behind electrode (B) (mm)	Distance in front of electrode (C) (mm)
6060-T6	0	0	8.2	6.6	7.2
6060-T6	20.8	18	8.3	6.3	6.7
Cross Section Area (mm^2)	**Bead Thickness (mm)**	**Root Width (mm)**	**Over-Bead Width (mm)**	**Over-Bead Curvature (mm^{-1})**	
25.7	4.0	6.3	8.3	-0.074	
28.5	5.2	6.1	8.1	+0.000	

Table 23: 4043 filler dilution and dimensional characteristics for CTW welds of alloy 6060-T6 welded at a torch travel speed of 6 mm/s. Distances (A), (B), (C) are according to Figure 86

Base metal	Filler Wire Speed (mm/s)	Filler Dilution (%)	Top Width (A) (mm)	Distance behind electrode (B) (mm)	Distance in front of electrode (C) (mm)
6060-T6	0	0	7.3	5.4	5.6
6060-T6	62.5	16	7.2	5.4	4.3
Cross Section Area (mm^2)	**Bead Thickness (mm)**	**Root Width (mm)**	**Over-Bead Width (mm)**	**Over-Bead Curvature (mm^{-1})**	
25.1	4.2	6.5	7.6	-0.107	
30.1	5.1	6.7	7.9	-0.015	

Table 24: 4043 filler dilution and dimensional characteristics for CTW welds of alloy 6060-T6 welded with He+(Ar+1%O_2) shielding gas. Distances (A), (B), (C) are according to Figure 86

Base metal	Filler Wire Speed (mm/s)	Filler Dilution (%)	Top Width (A) (mm)	Distance behind electrode (B) (mm)	Distance in front of electrode (C) (mm)
6060-T6	0	0	8.2	5.8	6.4
6060-T6	41.7	18	7.6	6.0	6.4
Cross Section Area (mm^2)	**Bead Thickness (mm)**	**Root Width (mm)**	**Over-Bead Width (mm)**	**Over-Bead Curvature (mm^{-1})**	
27.6	4.2	7.1	8.4	-0.108	
29.1	5.1	6.4	7.6	+0.000	

Table 25: 4043 filler dilution and dimensional characteristics for CTW welds of alloy 6060-T6 welded with He+(Ar+2%H_2) shielding gas. Distances (A), (B), (C) are according to Figure 86

Base metal	Filler Wire Speed (mm/s)	Filler Dilution (%)	Top Width (A) (mm)	Distance behind electrode (B) (mm)	Distance in front of electrode (C) (mm)
6060-T6	0	0	8.7	5.9	6.2
6060-T6	41.7	18	8.4	5.8	6.0
Cross Section Area (mm^2)	**Bead Thickness (mm)**	**Root Width (mm)**	**Over-Bead Width (mm)**	**Over-Bead Curvature (mm^{-1})**	
26.4	4.3	6.7	8.8	-0.084	
31.4	5.1	6.4	8.5	+0.015	

5.2.4 Summary

The newly developed CTW test has been successfully used to investigate the 6060/4043 weldability, evaluated in terms of critical strain rate – dilution maps. This new approach to weld development using in-situ strain rate measurement and new composition-strain rate maps helps define the boundary between crack and no-crack conditions and can

be used to characterize boundary variations for changes in weld travel speed, weld pool contaminants (Fe, O, and H), and grain refiner additions ($TiAl_3$ + Boron). Especially, small additions of oxygen or iron were found to have little or no effect on weldability. Improvements in weldability were experienced with the addition of hydrogen or a grain refiner, or with the use of faster travel speeds. The weldability improvement in autogenous welds at low welding speed (recall Figure 78) and high titanium content (recall Figure 82) were associated with the disappearance of stray centerline grains, suggesting that this change in grain structure plays a major role in improving weldability with filler addition, according to Figure 87. Supporting this hypothesis are the more vertical crack – no crack boundaries in critical strain rate – dilution maps when no change in grain microstructure occurs (recall Figures 78 and 82).

Although the CTW test is some regard unique in its application of controlled transverse global strain rate, what is of particular importance here is the measurement of local strain rate critical to crack formation. The same approach could be accomplished using other established weldability tests incorporating tensile tests (e.g. VTS [150] or PVR [72]) or pre-stress applied in the plane of the test specimen (e.g. Sigmajig [156] or PLTS [157]). Weldability tests that do not lend themselves to this approach are those involving bending (e.g. Slow-Bending Transvarestraint Test [12]), where the strain rate is not uniform throughout the duration of the test or through the test specimen. The disadvantage of strain rate analysis is that it adds to test complexity and is time consuming. However, expressing cracking susceptibility in terms of a critical parameter directly related to a cracking mechanism has the advantage of providing a more meaningful representation of weldability. Of particular importance is the possibility to use this data in the modeling of cracking mechanisms, allowing for future prediction of cracking.

5.3 Solidification Path

In realization of the importance of solidification range and liquid feeding to cracking, the solidification path was characterized using thermal analysis techniques combined with metallographic observations and phase identification. Details are given below.

5.3.1 Thermal Analysis

The thermal analysis and solidification path determination of Alloy 6060 diluted with variable amounts of 4043 was investigated first in *casting*, simulating the weld metal composition. The detected reactions were identified based upon the alloy microstructure and

literature data. The results were then used to determine the solidification path in *welds*. Finally, the *effect of cooling rate* on microstructure and phase selection was investigated in order to correlate castings and welds. Results will be discussed in terms of their relevance to existing cracking models.

5.3.1.1 6060 / 4043 Casting

Solidification path of controlled mixtures of Alloys 6060 and 4043 (given in Table 26) was investigated in casting, simulating the weld metal composition. Comparing the *microstructure* and *thermal analysis* results with literature data, the solidification path was characterized. Slowly cooled castings were investigated in this analysis to facilitate the collection of thermal data, to make phase identification easier (i.e. produce coarse phases for metallographic analysis), and to establish the limitations of the different thermal analysis techniques.

Table 26: Measured Chemical Analysis for Aluminum Alloy 6060 and 6060/4043 Mixtures (wet chemical analysis for 4043 filler wire and spectrometry for 6060 base metal)

Aluminum Alloy	Composition (wt.%)									
	Si	Mg	Fe	Mn	Cu	Cr	Ni	Zn	Ti	Zr
6060-T4	0.42	0.59	0.19	0.020	0.012	0.004	0.004	0.009	0.020	0.001
6060+02% 4043	0.52	0.58	0.19	0.020	0.012	0.004	0.004	0.009	0.020	0.001
6060+08% 4043	0.81	0.54	0.19	0.019	0.012	0.004	0.004	0.009	0.019	0.001
6060+10% 4043	0.91	0.53	0.19	0.018	0.013	0.004	0.004	0.009	0.018	0.001
6060+20% 4043	1.40	0.47	0.20	0.017	0.013	0.004	0.004	0.008	0.017	0.001
4043	5.30	0.002	0.22	0.003	0.018	0.002	0.005	0.005	0.003	0.002

5.3.1.1.1 Microstructure

Microstructures for the two extremes in alloy composition (6060 versus 6060+20%4043) are compared in Figure 91. Here the large white areas are α-aluminum dendrites and the numerous different interdendritic phases have been labeled based upon descriptions available in the literature [163,171,188] and upon thermal analysis performed in this study. It is clear that by dilution with 4043, which shifted primarily only the silicon content (Table 26), there is a significant change in the appearance and constitution of interdendritic phases between 6060 and 6060+20%4043, i.e. for silicon content shifted from 0.4 to 1.4 weight percent.

Coarse needles of β–Al_5FeSi are observed in both microstructures (Figures 91a and 91b), as are particles of Mg_2Si and Si. However, the specific reactions which produced these phases is likely different, as will be discussed in the next section. Note that a fine speckled

eutectic is observed only in Figure 91b, which contains much smaller particles of Mg_2Si and Si than are observed in Figure 91a.

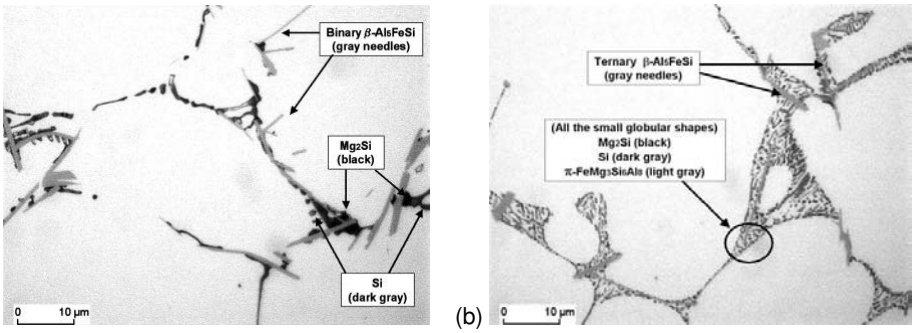

Figure 91: Comparison of cast structures for (a) 6060 and (b) 6060+20%4043 highlighting the different phases.

5.3.1.1.2 Thermal Analysis

Thermal analysis was used to reveal the influence of 4043 filler dilution on the solidification process and thermal arrests. The resulting cooling curves are compared in Figure 92 for the aluminum alloy 6060 and the add-mixture 6060+20%4043. The time t=0s was chosen as the time when the temperature at the stainless steel heat-sinking block, T_w, reached 680°C upon cooling. Thermal arrests are observed on each curve, marked 1 to 10, and are identified in Table 27 as corresponding to a particular phase reaction which was identified based upon limited phase identification and information available in literature [6,163,171]. The range of temperatures shown correspond to the beginning and end of the observed peaks.

Some reactions have weak thermal arrests, which may be attributed to either low latent heats or signal noise. It should be noted that many of these thermal arrests are close to one another, making precise identification impossible. There is also a problem with sensible heat which, when added to the latent heat, serves to mask the arrest. Another concern involves temperature measurement accuracy. All thermocouples were made from the same spool of chromel/alumel wire, several of which were calibrated using 99.999% pure aluminum. The melting point was found to consistently be 7-8°C below the expected 660°C, with the ice point remaining at 0°C. Corrections were made to experimental measurements by applying a multiplicative factor (1.01) to all temperature curves. In summary, the over-all accuracy of a thermal arrest indication is a combination of the ability to detect the arrest (i.e. above the noise level) and assign a correct temperature.

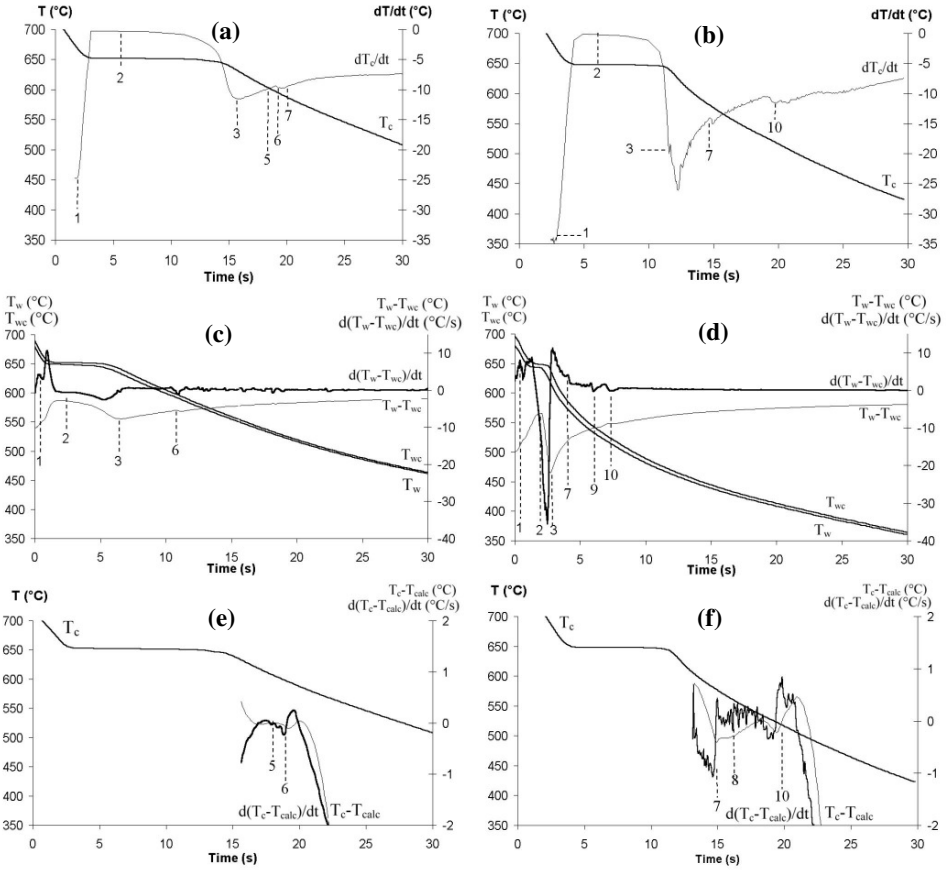

Figure 92: Application of (a,b) cooling rate, (c,d) temperature difference, and (e,f) temperature variance methods to Alloy 6060 cast metal with (a,c,e) 0% 4043 and (b,d,f) 20% 4043 filler addition. Numbered arrests correspond to numbered reactions in Table 27.

Each thermal method (cooling rate, temperature difference, and temperature variance) had its own limitations and advantages, sometimes confirming and other times complementing arrests from other methods. The cooling rate method gave indications for all reactions, but worked best for indicating the liquidus and α-aluminum dendrite plateau temperature. The temperature variance method was only applicable after the coherency point, where the temperature curve becomes globally smooth and can be easily curve-fit. The temperature difference method is harder to setup (i.e. involving two in-line thermocouples) and did not work in all cases. However, this method was consistently the most useful in detecting the coherency point, with an accuracy dependent upon the distance between the two thermocouples (T_w and T_{wc}).

Table 27: Phase Reactions in the Al-Mg-Si-Fe Quaternary System for Composition Range corresponding to Variable 4043 Filler Dilution in 6060 Cast Base Metals, Identified using Cooling Rate [(a)], Temperature Difference [(b)], and Temperature Variance [(c)] Methods. Numbered Reactions Correspond to Numbered Arrests in Figure 92.

No.	Phase Reactions	Thermal Arrests (°C)				
		6060	**6060+ 02% 4043**	**6060+ 08% 4043**	**6060+ 10% 4043**	**6060+ 20% 4043**
1	L+$TiAl_3$→α(Al)	666 [a] 665 [b]	666 [a] 668 [b]	667 [a] 665 [b]	666 [a] 663 [b]	666 [a] 667 [b]
2	L→α(Al)	653-650 [a] 653-649 [b]	652-650 [a] 652-647 [b]	650-648 [a] 651-648 [b]	651-649 [a] 649-645 [b]	649-647 [a] 650-647 [b]
3	Coherency Point	638-637 [a] 642-640 [b]	642-640 [a] 639-638 [b]	639-637 [a] 642-640 [b]	639-638 [a] 641-639 [b]	640-639 [a] 642-641 [b]
4	L->α(Al)+ α(Al_8Fe_2Si)	------	--------	--------	---------	---------
5	L→α(Al)+β (Binary β)	609-597 [a] 608-604 [c]	607-600 [a] 614-607 [c]	605-600 [a]		
6	L→ α(Al)+Mg_2Si	597-590 [a] 597-590 [b] 596-589 [c]	592-588 [a] 597-588 [b] 600-588 [c]	600-584 [a] 595-586 [b] 596-589 [c]	594-586 [a] 598-586 [b] 592-585 [c]	
7	L→α(Al)+Si	587-578 [a]	588-577 [a] 588-577 [c]	586-575 [c]	586-578 [a] 586- 579 [b] 585-575 [c]	584-577 [a] 585-577 [b] 582-577 [c]
8	L→α(Al)+Si+ β (Ternary β)			551-536 [a] 552-544 [c]	556-551 [c]	564-556 [c]
9	L+β→α(Al)+Si+π			536-532 [a] 544-536 [c]	538-524 [a] 542-537 [c]	539-534 [b]
10	L→Mg_2Si+Si+α(Al)+π (Quaternary Eutectic)			521-513 [a] 516-512 [b] 521-512 [c]	524-516 [a] 521-513 [b] 523-514 [c]	524-511 [a] 521-512 [b] 524-509 [c]
11	End Solidification	578 [a] 590 [b] 589 [c]	577 [a] 588 [b] 577 [c]	513 [a] 512 [b] 512 [c]	516 [a] 513 [b] 514 [c]	511 [a] 512 [b] 509 [c]

Concerning the effect of 4043 filler dilution, its addition is seen to have little influence on the thermal characteristics of the primary α-aluminum dendrite formation and interdendritic coherency (arrests 1 to 3). In contrast, the interdendritic reactions change significantly with 4043 filler dilution: from high temperature reactions (614-577°C) at low filler dilution, to low temperature reactions (585-509°C) at high filler dilution. This leads to an increase in the solidification range from 88 to 157°C, and to the replacement of the eutectic reactions forming binary β needles, Mg_2Si, and Si, to reactions involving ternary β needles and π phase. The quaternary eutectic (arrest 10) corresponds with a major change in

microstructure, where a very fine multi-phase interdendritic constituent is observed to occur (Figure 91b).

5.3.1.1.3 Solid Fraction Calculation

Recall from Eq. 37, the solid fraction calculation is based upon the difference in cooling rates between measured and baseline values, where the baseline represents heat transfer for conditions of zero latent heat. In this case, the base line was approximated using two straight lines tangent to the liquid and solid cooling rate curves, respectively, as indicated in Figure 93.

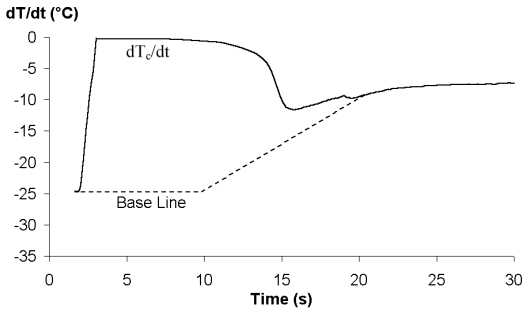

Figure 93: Baseline as defined in this study for Alloy 6060.

Solid fraction was evaluated according to Eq. 37 using the physical property values listed in Table 28. Calculated solid fraction values at the end of solidification were found to vary between 0.93 and 0.96 for different alloy mixtures. A multiplication factor, in the range 1.04 to 1.07, was applied to obtain the desired solid fraction of 1 at the end of solidification. The need for this multiplication factor may be attributed to: i) uncertainty in physical property values C_p and ΔH, ii) coarse approximation for the baseline, or iii) variations in sensible heat contained within each cast specimen. Sensible heat will affect the cooling rate, which may indirectly affect the solid fraction calculation.

Table 28: Physical Property Constants for Pure Aluminum used for Solid Fraction Calculations [118]

Parameter	Symbol	Value
Liquid Specific Heat	C_p(liquid)	1,273 J/(kg·K)
Solid Specific Heat	C_p(solid)	1,278 J/(kg·K)
Specific Heat	C_p	$f_s \cdot C_p$(solid) + (1-f_s)·C_p(liquid)
Latent Heat	ΔH	380 kJ/kg

Calculated solid fraction versus temperature curves are compared in Figure 94. Curves for pairs (a)-(b) and (c)-(d) are respectively similar and represent only small

differences in filler dilution (2%). However, the difference between curves (a) and (e) is significant and represents a 20% difference in filler dilution. Increasing 4043 filler dilution tends to shift the curves down and to the left. The downward shift is the direct consequence of the decrease in solidus temperature, as discussed in the thermal analysis. The shift to the left represents a decrease in the amount of primary α-aluminum and a corresponding increase in the amount of interdendritic liquid. Indeed, the solid fraction at the coherency temperature (near 640°C, Table 26) drops from 0.94 to 0.78 for increasing filler dilution from 0 to 20% (Figure 95). Moreover the solid fraction, when the first interdendritic reaction begins, decreases from 0.98 at 609°C (0% filler dilution) to 0.86 at 585°C (20% filler dilution). Note that such a high solid fraction at the coherency point has been observed in other low alloyed aluminum alloys, as for example the coherency point for cast Al-0.5wt.%Cu binary alloy was found at 0.90 solid fraction [26].

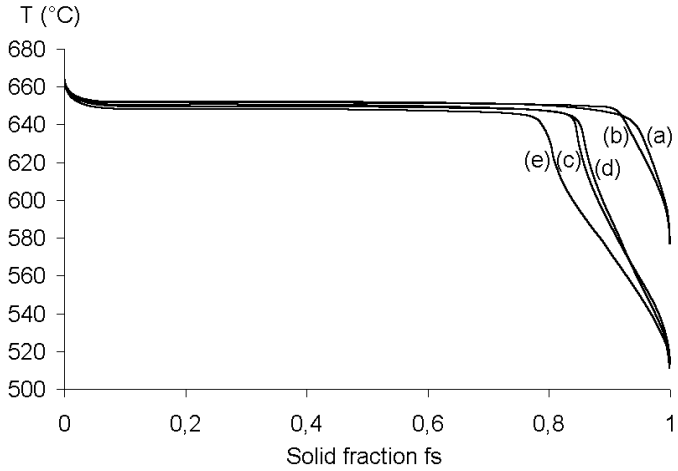

Figure 94: Solid fraction versus temperature curves for alloys: (a) 6060, (b) 6060+02%4043, (c) 6060+08%4043, (d) 6060+10%4043, and (e) 6060+20%4043.

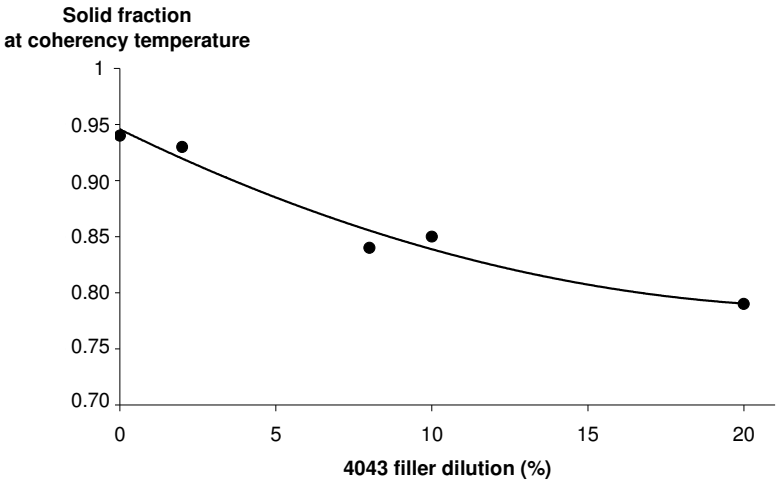

Figure 95: Solid fraction at coherency temperature versus 4043 dilution in cast Alloy 6060-T4.

5.3.1.1.4 Relevance to Solidification Cracking

Increasing 4043 filler dilution in the weld metal is known to increase the resistance to solidification cracking, although the reason for this remains unclear. Previous work has shown that 4043 filler dilution is needed to avoid cracking when welding 6060 aluminum, even under low restraint conditions. If weld solidification follows the same trend observed here for castings, there will be a concurrent increase in both solidification range and quantity of interdendritic liquid with increased dilution. Depending upon which of numerous models for cracking is examined, the observed solidification behavior can have different implications regarding prediction of cracking resistance.

It is argued that longer solidification time increases the accumulated strain experienced in the mushy zone, thus a greater likelihood for cracking [24,49,59,189] and that a longer mushy zone length, i.e. longer distance to feed, associated with greater solidification range, hinders liquid feeding ability [77,81]. In contrast, a more opened dendritic structure associated with a larger quantity of interdendritic liquid should prove easier to feed shrinkage, precluding cracking [77,81], and is also less prone to coherency, an important requirement for stress models [14,190].

Increased silicon content with higher filler dilution (Table 26) is also likely to reduce solidification shrinkage [163,168]. This behavior is believed due to the volume expansion of silicon as it solidifies, compensating in part for the solidification shrinkage of aluminum [168]. Alloy 6060 castings have demonstrated this, where the shrinkage cavity is reduced when increasing 4043 filler dilution (Figure 96a and 96b), even at high cooling rates (54 °C/s) on

additional in-house castings (Figure 96c and 96d). A reduction in solidification shrinkage should improve weldability, according to the shrinkage-feeding concept of Feurer [77].

5.3.1.1.5 Summary

From the thermal analysis of cast 6060-4043 mixtures, increased silicon content favors lower temperature phase reactions and the formation of Si and π phases. The solidification range was found to significantly increase with silicon, as did the quantity of interdendritic eutectic liquid generated. The solidification path determined in 6060/4043 castings will help to characterize the solidification path of Al- 6060/4043 welds, as detailed hereafter.

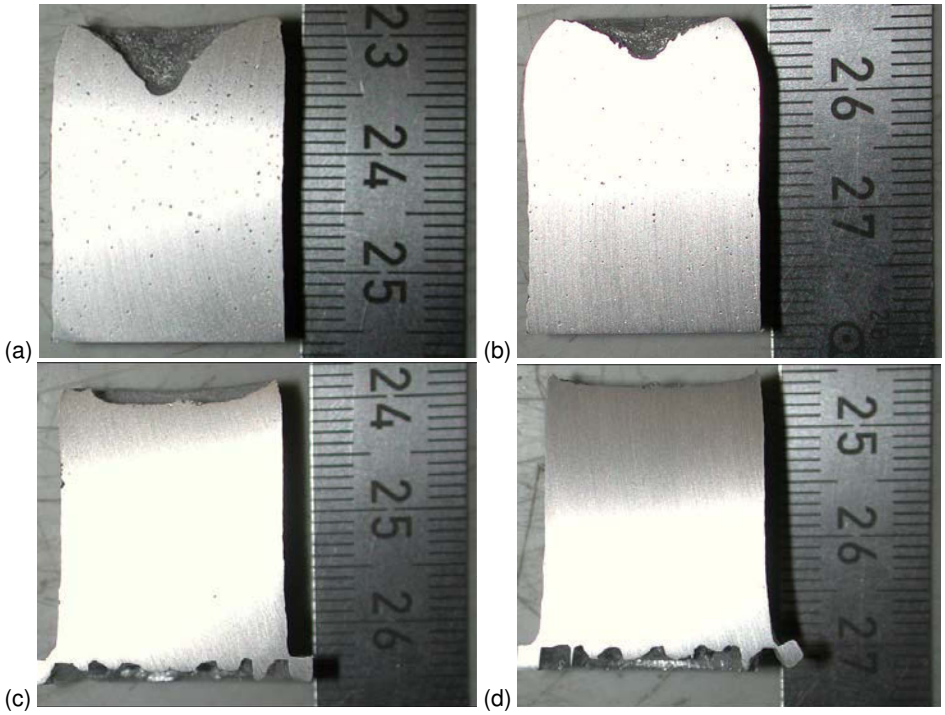

Figure 96: Shrinkage cavity observed in castings of (a,c) 6060 and (b,d) 6060+20%4043. Cooling rate (a,b) 9℃/s and (c,d) 54 ℃/s between 750 and 500℃.

5.3.1.2 6060 / 4043 Weld

The solidification path was characterized by examining cooling curves for low and high filler dilutions in welds (Figure 97). The observed thermal arrests on each curve are identified in Table 29 as corresponding to a particular phase reaction based upon thermal

arrest behavior characterized previously for 6060/4043 castings (recall Table 26). Some reactions have weak thermal arrests, which may be attributed to either low latent heats or signal noise.

Thermal analysis show some notable differences in solidification path between Alloy 6060 welds (Table 29) and castings (Table 27). Increasing 4043 filler dilution decreases the coherency point by approximately 12°C, decreases the start temperatures for all the other reactions up to 20°C, and had little effect on solidification start and stop. The decrease in coherency temperature at higher silicon contents agrees with other investigations (recall Figure 54). The phase reactions occurring at lower temperatures with higher filler dilution are probably due to higher undercooling of reactions involving silicon.

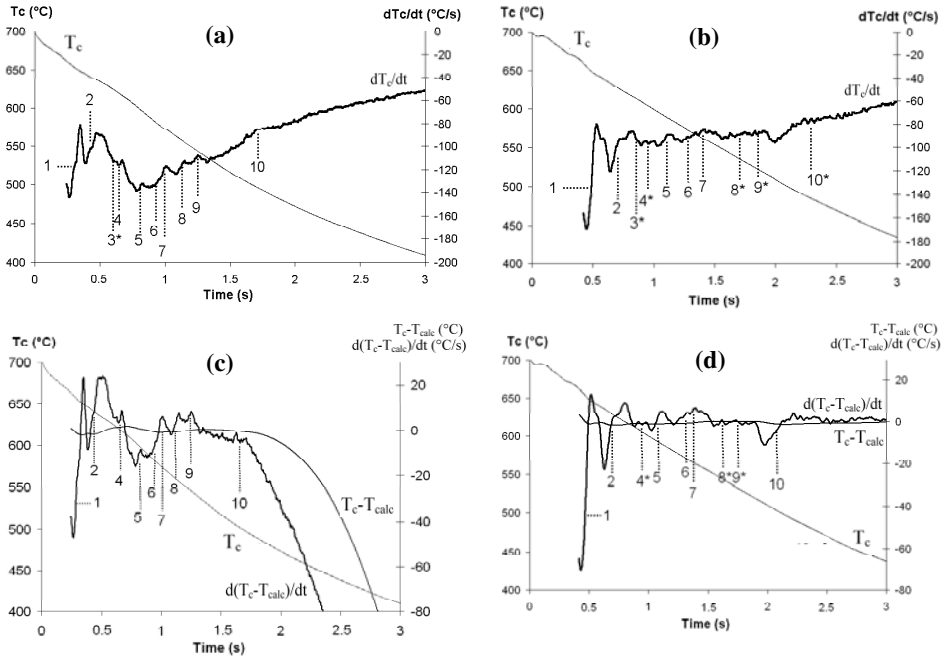

Figure 97: Application of (a,b) cooling rate and (c,d) temperature variance methods to Alloy 6060 weld metal with (a,c) 0% and (b,d) 16% 4043 filler dilution. Numbers arrests correspond to numbered reactions in Table 29.

A thermal arrest for α-Al_8Fe_2Si was observed in the weld metal but not the casting (i.e. reaction 4). Evidence in the literature shows that fast cooling rates promote α- Al_8Fe_2Si formation at the expense of β- Al_5FeSi [53,163,169,170,174]. Also, the low melting reactions (reactions 8-10) were not observed for castings at low silicon, but were observed in low silicon weld metal, probably due to incomplete eutectic reactions at higher temperatures

(reactions 4-7) making more solute available for lower temperature reactions. This results in an unaffected solidification range with 4043 filler dilution (≈ 165°C). This is also suggested by the micrographs of the weld cross-sections with and without 4043 (Figure 98). Unlike 6060/4043 castings (Figure 91), weld microstructure appears unaffected by 4043 filler dilution.

Reaction 5, involving β–Al_5FeSi needle formation, is less detectable with high filler dilution, possibly due to less binary β needles solidification at higher silicon content (i.e. higher Si:Fe ratio), similarly to what has been observed in cast Al-Si binary alloys [177]. The absence of long β needles at grain boundaries (Figure 98), to either block liquid feeding or act as high strength solid bridges at high temperatures, may explain the little effect of weld metal iron content on Alloy 6060 weldability (recall Figure 81). As to be noted, when considering the cooling curves after the α-Al solidification (reaction 2 in Table 29), the maximum cooling rate is measured at 601°C (138°C/s) and 597 °C (98°C/s), respectively for 0 and 16% 4043 filler dilution, which corresponds in both cases to the start of the binary β phase formation (reaction 5 in Table 29). Note that peritectic reactions (e.g. reaction 9) are unlikely to occur to completion under rapid cooling conditions.

Table 29: Phase Reactions in the Al-Mg-Si-Fe Quaternary System for Composition Range corresponding to Variable 4043 Filler Dilution in 6060 Weld Base Metals, Identified using Cooling Rate [(a)] and Temperature Variance [(b)] Methods. Numbered Reactions Correspond to Numbered Arrests in Figure 97

No.	Phase Reactions	Thermal Arrests (°C)	
		6060	6060+16%4043
1	L+$TiAl_3$→αAl)	659-648 [(a)] 660-649 [(b)]	654-644 [(a)] 659-645 [(b)]
2	L→α(Al)	645-636 [(a)] 646-632 [(b)]	632-614 [(a)] 636-618 [(b)]
3	Coherency Point	624 [(a)]	612 [(a)]
4	L→α(Al)+α(Al_8Fe_2Si)	619-616 [(a)] 620-616 [(b)]	608-604 [(a)] 610-602 [(b)]
5	L→α(Al)+β (Binary β)	601-595 [(a)] 603-596 [(b)]	596-585 [(a)] 597-587 [(b)]
6	L→α(Al)+Mg_2Si	585-580 [(a)] 587-580 [(b)]	577-568 [(a)] 580-569 [(b)]
7	L→α(Al)+Si	579-571 [(a)] 579-572 [(b)]	566-560 [(a)] 566-563 [(b)]
8	L→α(Al)+Si+ β (Ternary β)	562-554 [(a)] 563-556 [(b)]	547-541 [(a)] 549-534 [(b)]
9	L+β→α(Al)+Si+π	549-543 [(a)] 550-544 [(b)]	537-516 [(a)] 529-519 [(b)]
10	L→Mg_2Si+Si+α(Al)+π (Quaternary Eutectic)	507-494 [(a)] 507-496 [(b)]	511-488 [(a)] 511-491 [(b)]
11	End Solidification	494 [(a)] 496 [(b)]	488 [(a)] 491 [(b)]

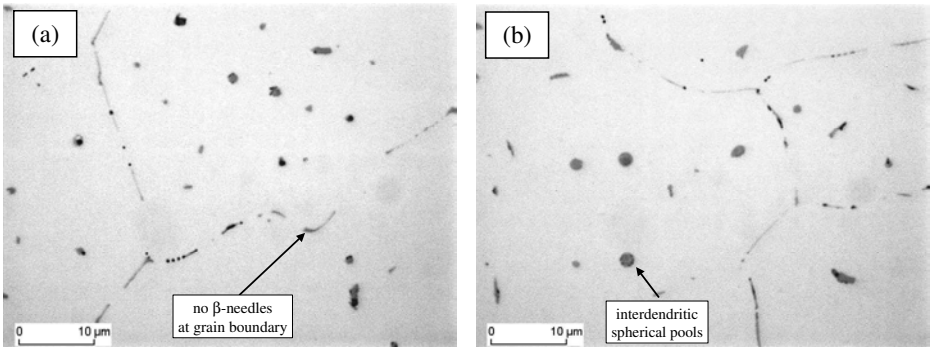

Figure 98: Micrographs for Al- 6060 weld metal with (a) 0% and (b) 16% 4043 filler dilution.

Increased 4043 filler dilution from 0 to 16% resulted in a decrease in weld cooling rate during solidification from 113℃/s to 89℃/s. This may possibly be related to a release in latent heat associated with greater amounts of silicon or interdendritic constituent, or to a larger weld pool associated with the use of 4043 filler (recall Table 17), either case resulting in a higher quantity of heat to remove during solidification. Since the solidification range remains constant (Table 29), the lower cooling rates with increase in filler dilution (from 0 to 16% 4043) are associated with higher solidification duration (from 1.5 to 1.9 seconds) and longer mushy zone (from 6.0 to 7.6 mm). Considering the shrinkage feeding theory of Feurer [77], a lower cooling rate reduces the rate of shrinkage and thus decreases the cracking susceptibility. However a longer mushy zone hinders the liquid feeding ability, and thus increases the cracking susceptibility. The improvement in weldability when adding 4043 to 6060 welds suggests that the reduced amount of shrinkage overcomes the effects due to the reduced liquid feeding ability.

5.3.1.3 Cooling Rate Effect

To develop a better understanding of weldability requires knowledge of how welds solidify, including the solidification path and phase formation. The microstructure observed in weld metal is often considerably different from that observed in castings, for the same alloy. The goal of this study was to examine the evolution of alloy 6060 solidification microstructure as a function of cooling rate, providing a link between casting and weld. Details are given below.

5.3.1.3.1 Limitations in Thermal Analysis

Thermal analysis of cast specimens has been found limited under high cooling rate conditions. Indeed, the magnitude of thermal arrests associated with reactions were not detectable, where the latent heat released during phase formation produced too small a deviation in cooling curves compared to signal noise and heat extraction rate. The signal noise is believed to come from the casting test configuration (recall Figure 66), where solidification near the heat sink block starts before the casting of the molten metal was completed, resulting in high liquid flow turbulences around the thermocouple T_c. Indeed, thermal analysis could be made in welds at high cooling rates.

5.3.1.3.2 Cooling Curve – Microstructure Relationship

Cooling curves for cast Alloy 6060 are compared in Figure 99, curves (a) to (f), for cooling rates between 6 and 58 °C/s measured as an average between 640 and 500 °C, i.e after the plateau associated with aluminum dendrite formation. Also included is a cooling curve for the 6060 gas-tungsten arc weld thermally isolated to reduce cooling rate, the cooling rate measured with a plunged thermocouple being 42 °C/s (i.e. close to the fastest cooled casting), curve (g) in Figure 99. The plateau associated with aluminum dendrite formation is gradually diminished for increasing cooling rates, reflecting upon a fixed quantity of latent heat being removed. In the case of the weld, with a smaller liquid volume and quantity of latent heat, a plateau is not observed at all. Specifically, the solidification time for these castings is found to go from approximately 17 s (at 6 °C/s) to 3 s (at 50 °C/s).

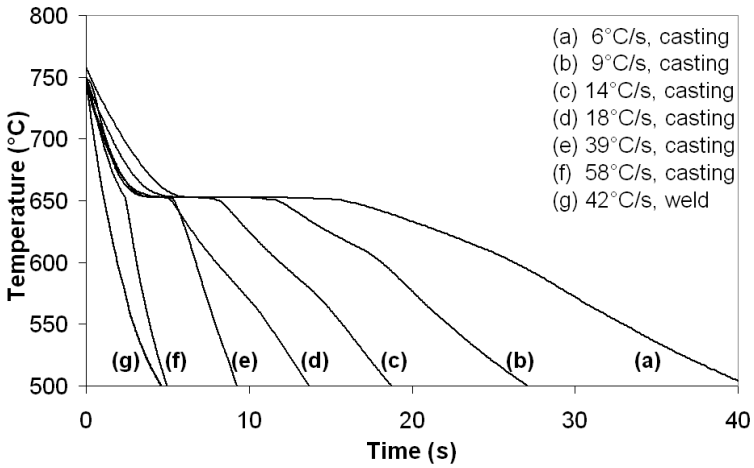

Figure 99: Cooling curves for Alloy 6060 castings and weld.

Micrographs corresponding to three different cooling rates plus the weld from Figure 99 are compared in Figure 100, all shown at the same magnification. Figure 100a corresponds to 6 °C/s and can be characterized as having coarse constituent particles all around the periphery of the dendrites. These phases include gray β needles and dark Mg_2Si and Si particles. Figure 100b corresponding to 39 °C/s is similar to Figure 100a, except that the constituent phases are slightly smaller in dimension, and less continuous around the dendrite periphery. Between cooling rates of 39 and 58 °C/s, there exists a marked change in microstructure typified by Figure 100c and Figure 100d, for cast and weld metal, respectively. In this new arrangement in microstructure, the dendrites are no longer outlined by the constituent phases, in fact making dendrite boundaries hard to distinguish. Instead, constituent particles are localized in small globular pools distributed more-or-less uniformly throughout the grain (1-2 μm dia. pools; 6-8 μm pool spacing). Within these globular pools there is often a mixture of two or more different phases (e.g. see paragraph 5.3.2). In contrast to this unique interdendritic distribution, there remains a nearly continuous distribution of second phases along grain boundaries. This abrupt shift in interdendritic phase distribution when increasing the cooling rate, reflects upon the ability to nucleate and grow constituent phases, and probably a limited time available for elements to diffuse in liquid. With shorter solidification times, the number of nucleation events becomes limited and the undercooling at which nucleation occurs will be greater. The time and space available for growth also becomes limiting factor. The globular pools distributed along the dendrites at high cooling rates may also be associated with a change in dendrite shape, with more developed secondary dendrite arms at higher cooling rates (recall Figure 59) [184].

However, care should be given when comparing castings and welds, since such a comparison cannot be based only upon the cooling rate (dT/dt), but also requires the knowledge of the growth rate (R) and temperature gradient (G), the cooling rate being equal to the product ($G \cdot R$). Considering the weld with a cooling rate of 42°C/s (curve (g) in Figure 99) and a growth rate of 4.0 mm/s, i.e. equal to the welding speed, the calculated temperature gradient equals 10.5 °C/mm. In the casting with a cooling rate of 9 °C/s (curve (b) in Figure 99) and a temperature gradient of 2.7 °C/mm measured between the thermocouples T_c and T_{wc} (recall Figure 66), the calculated growth rate is equal to 3.2 mm/s. It clearly shows that, with similar cooling rates, growth rate and temperature gradient in castings and welds can differ.

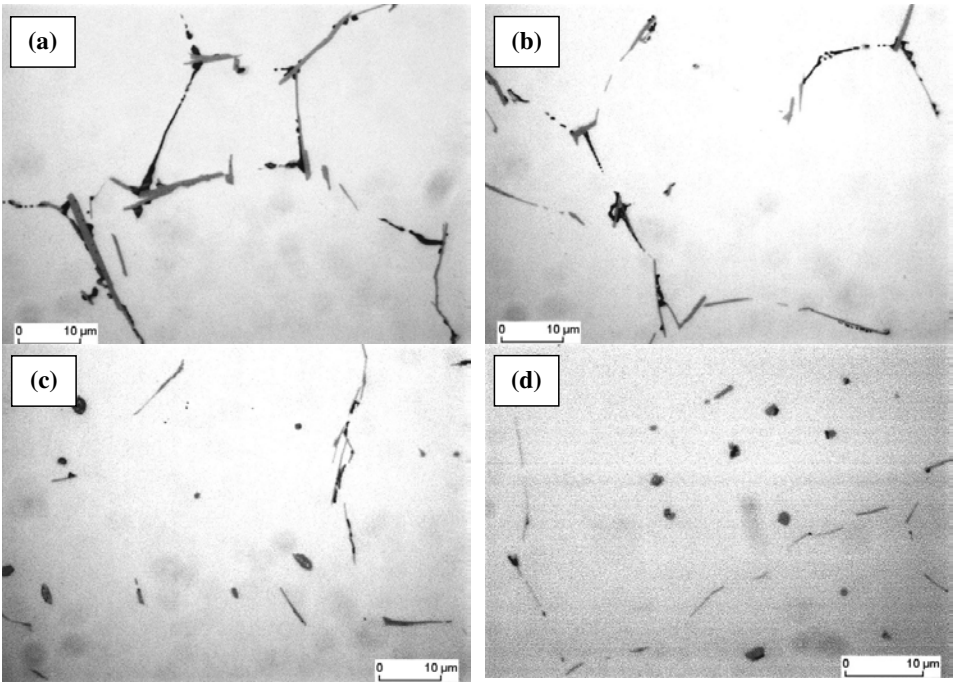

Figure 100: Solidification structure for Alloy 6060 (a,b,c) castings and (d) welds at different cooling rates: (a) 6 °C/s, (b) 39 °C/s, (c) 58 °C/s, and (d) 42 °C/s.

5.3.2 Phase identification

Phase analysis was realized using scanning electron and transmission electron microscopy (SEM and TEM) for an Alloy 6060 weld with 0% 4043 filler dilution. SEM was employed to observe a deep-etched 6060 weld cross section without 4043 filler (application of Etch E4, Table 6) shown in Figure 101. Note the presence of a feather-like phase at the grain boundary (Arrows numbered 1, 2, 4, and 9, Figure 101) with a high iron content (Table 30), and a globular phase (numbered 7, Figure 101) having element proportions close to the π-$Al_8FeMg_3Si_6$ phase (Table 30). Unfortunately, the large SEM-EDX measuring spot in regard to the small phase sizes (on the order of 1 µm) resulted in high aluminum content due to the matrix.

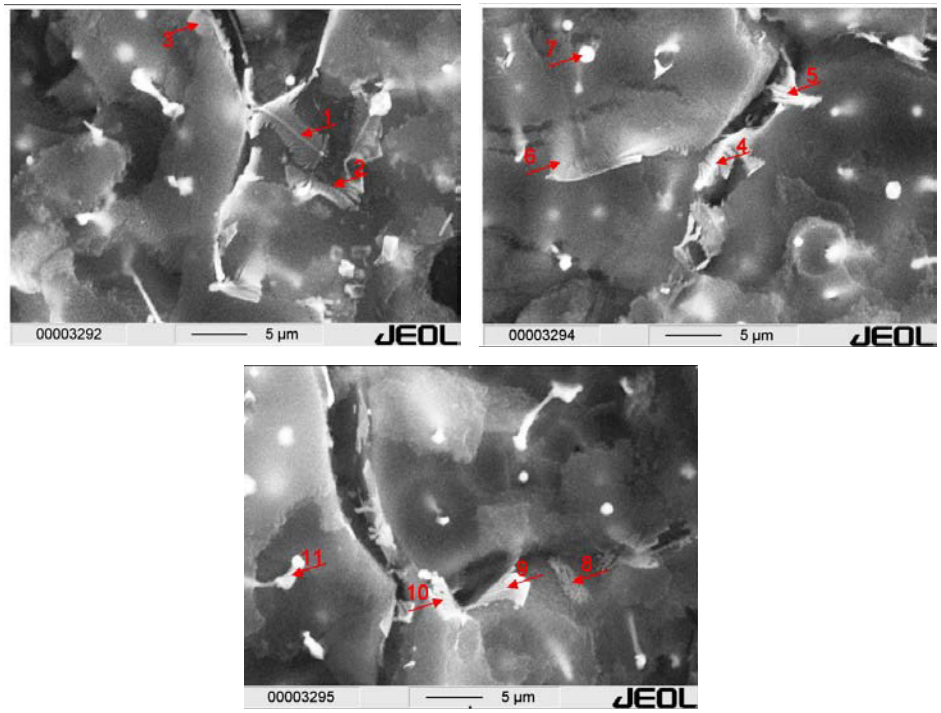

Figure 101: SEM observation of deep-etched Alloy 6060 weld cross-section. Composition measured at numbered arrows are given in Table 30.

Table 30: Measured Analysis for Phases in Aluminum Alloy 6060 Weld using SEM. Numbers reactions correspond to numbered arrows in Figure 101

Phase n°	Composition (wt.%)								
	Al	Si	Mg	Fe	Mn	Cu	Cr	Zn	Ti
1	69.09	8.20	11.70	8.73	0.33	0.31	0.08	1.49	0.06
2	76.21	5.59	7.96	8.75	0.27	0.51	0.08	0.38	0.26
3	77.86	10.34	8.78	2.49	0.15	0.06	-	0.21	0.10
4	76.61	5.49	6.57	9.35	0.42	0.62	0.16	0.56	0.22
5	77.87	9.97	9.45	2.40	0.15	-	0.06	-	0.09
6	61.52	7.33	15.21	13.95	0.67	0.39	0.13	0.59	0.21
7	49.29	30.49	13.90	4.28	0.37	1.01	0.10	0.44	0.12
8	76.14	9.65	10.22	2.38	0.55	0.68	0.01	0.18	0.19
9	69.32	5.07	7.10	15.00	0.42	0.72	0.01	2.27	0.11
10	77.94	3.55	5.25	6.38	0.32	1.65	0.00	4.73	0.17
11	62.16	11.23	8.07	17.52	0.19	0.54	0.08	0.12	0.09

Use was also made of TEM for element mapping and diffraction analysis on a polished Alloy 6060 weld cross-section. A Si-rich and Fe-rich needle shape (Figures 102 and 103) was likely a β–Al_5FeSi phase. The peak in Si along this phase (Figure 103) suggests this phase to be the “ternary β" (reaction 8 in Table 29). Another phase, shown in Figure 104, appears as a mixture of Ti-rich phase (probably $TiAl_3$, reaction 1 in Table 29), Mg-rich phase,

and Fe- and Si-rich phase. Unfortunately, these phases could not be identified. A round phase (Figure 105 and 106), similar in shape to phase numbered 7 (Figure 101), appears as a inhomogeneous mixture of Mg, Si, Fe, and Al, with an Fe- and Si-rich spot. Element scanning (Figure 106) suggests that this phase could be a mixture of Mg_2Si, Si, and π-$Al_8FeMg_3Si_6$ (reaction 10 in Table 29). Finally, a smaller phase (Figure 107), approximately 250 nm large and rich in Fe and Si, is likely α–Al_8Fe_2Si (reaction 4 in Table 29). The reactions suggested in Table 29 appear coherent with these measurements.

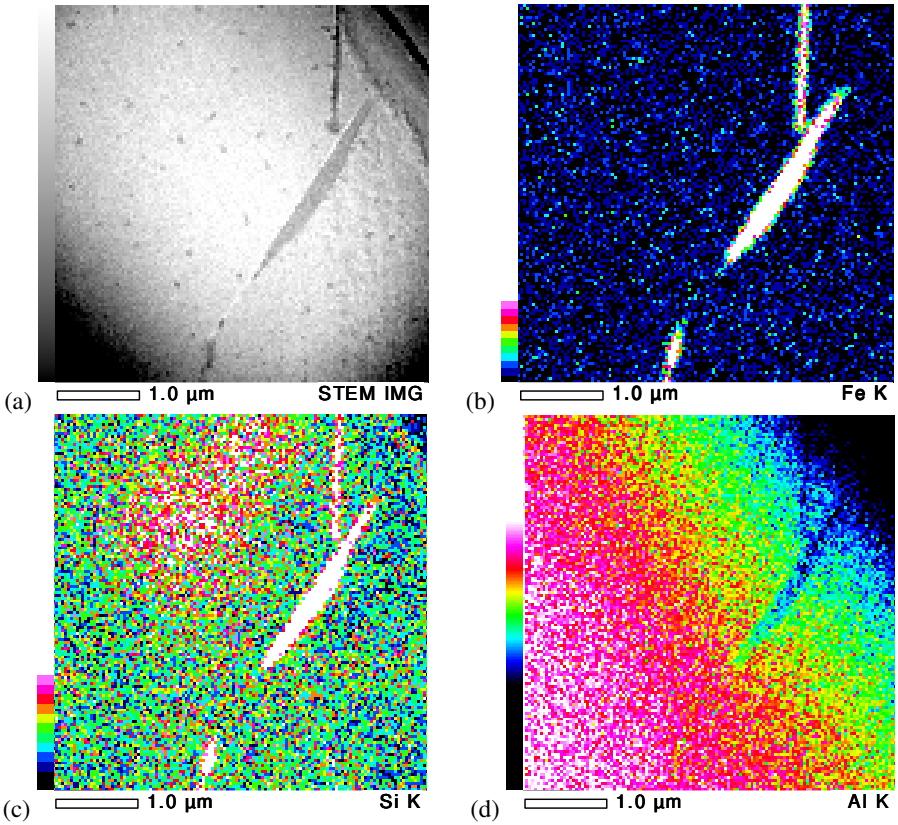

Figure 102: (a) TEM and EDS maps of (b) Fe, (c) Si, and (d) Al of a needle shape phase in Alloy 6060 weld cross-section.

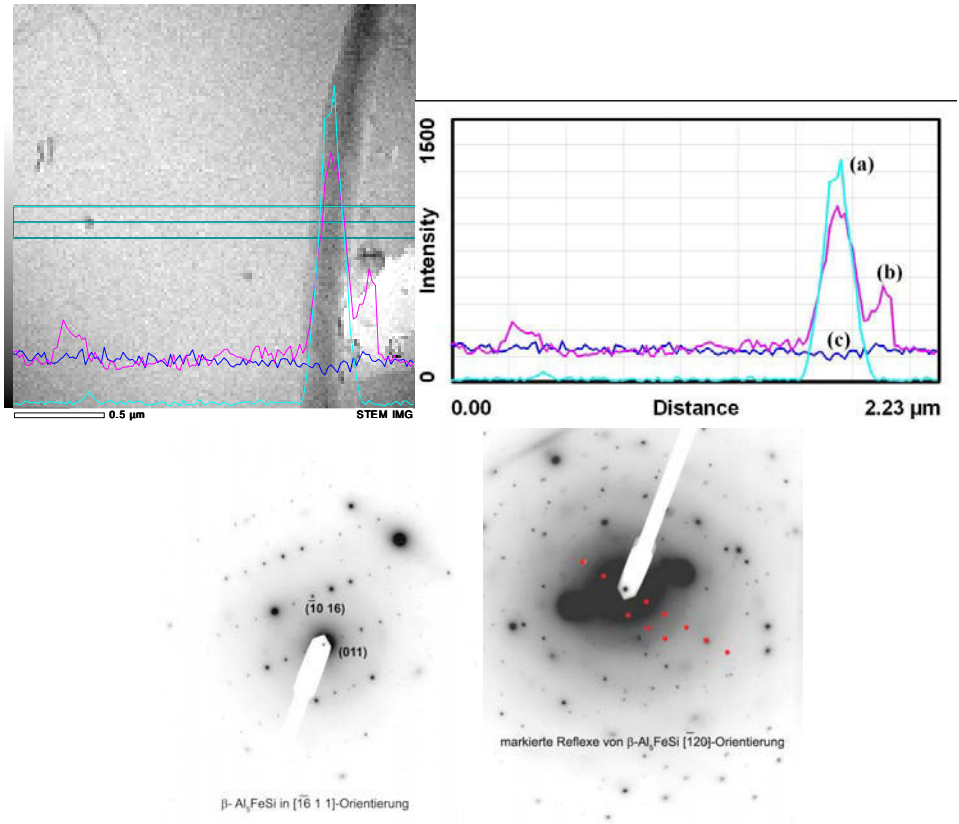

Figure 103: (a) Fe, (b) Si, and (c) Mg element scanning across needle phase shown in Figure 102 and corresponding TEM diffraction analysis.

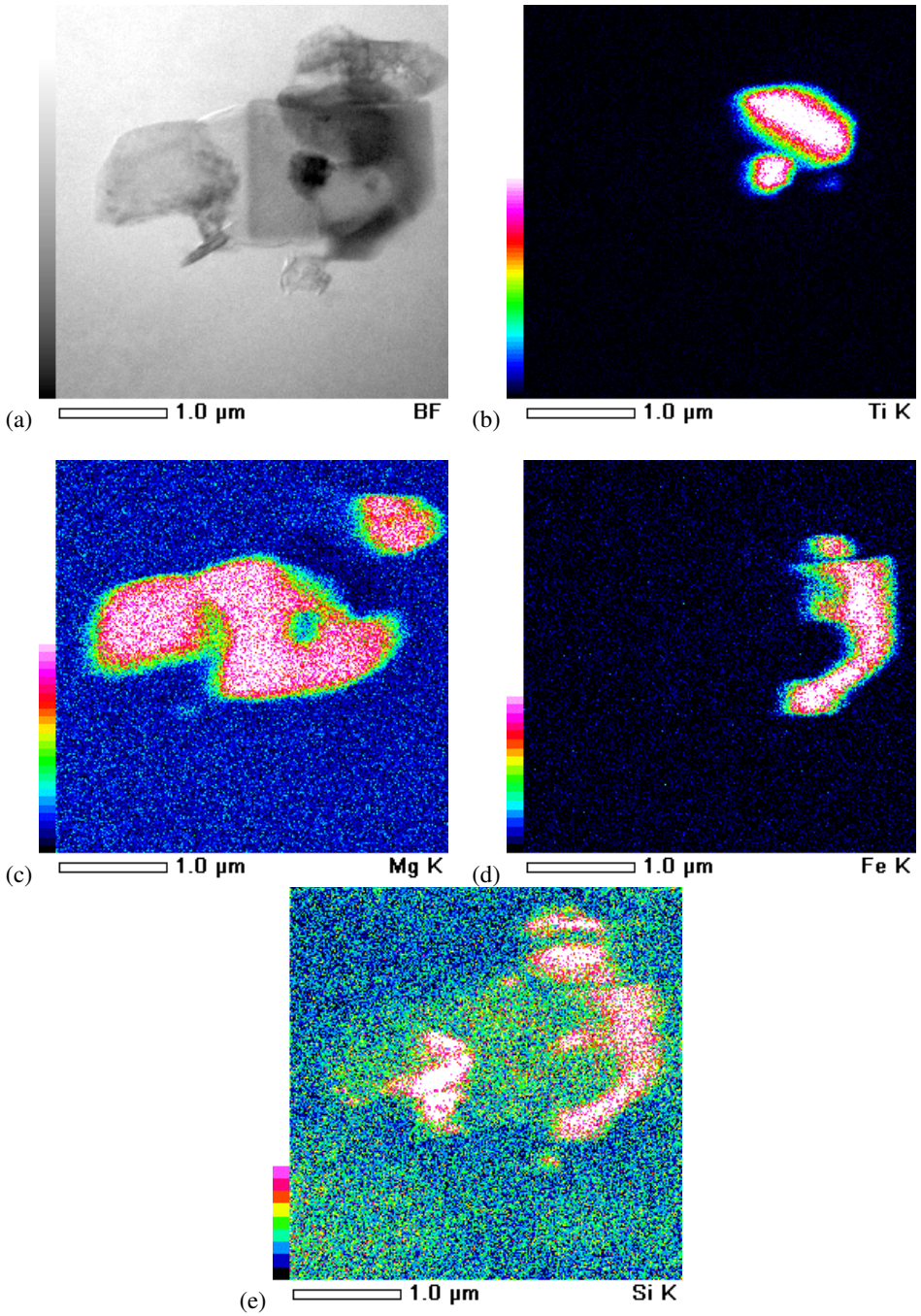

Figure 104: (a) TEM and EDS maps of (b) Ti, (c) Mg, (d) Fe, and (e) Si in Alloy 6060 weld cross-section.

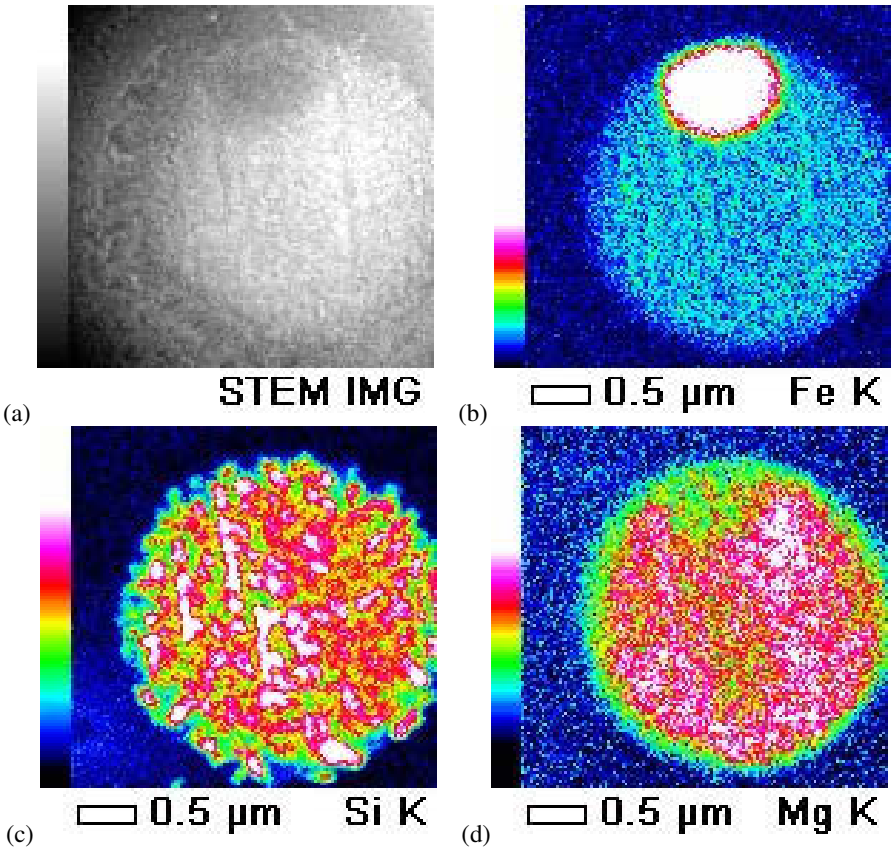

Figure 105: (a) TEM and EDS maps of (b) Fe, (c) Si, and (d) Mg of a round phase in Alloy 6060 weld cross-section.

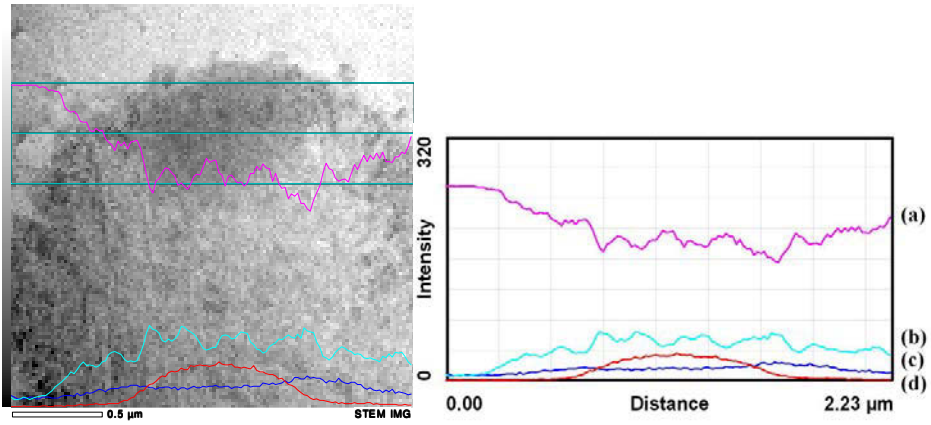

Figure 106: (a) Al, (b) Si, (c) Mg, and (d) Fe element scanning across round phase shown in Figure 105.

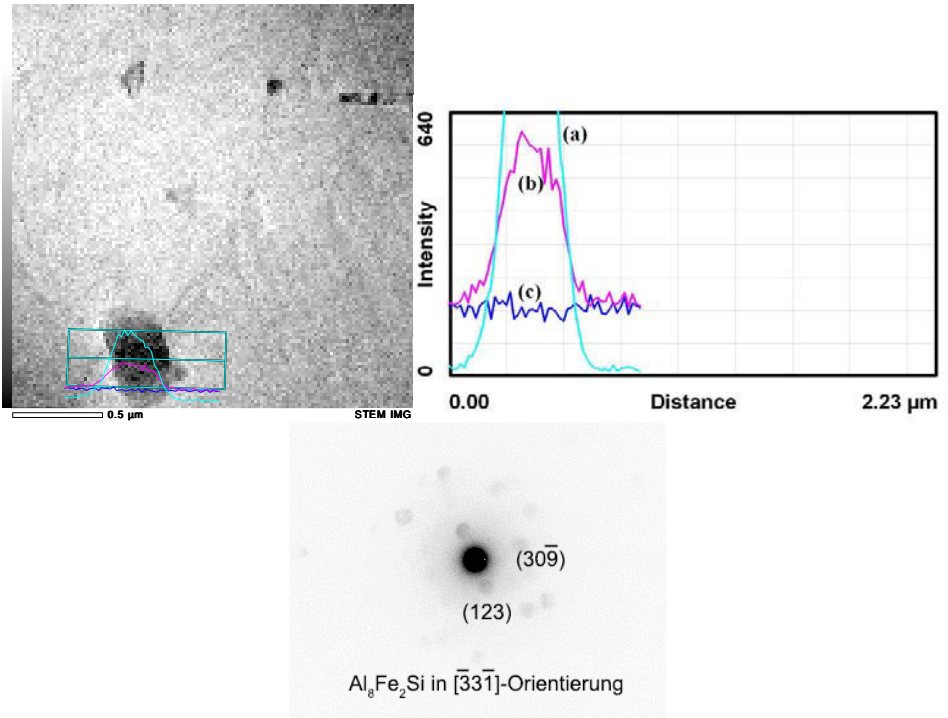

Figure 107: (a) Fe, (b) Si, and (c) Mg element scanning across small phase in Alloy 6060 weld cross-section and corresponding TEM diffraction analysis.

5.3.3 Summary

Based on thermal analysis, microstructure observations and available literature, small increases in Si content has a major effect on cast 6060 solidification path. Increased Si from 0.42 to 1.39 wt.% drops the solidus temperature from 577 to 509°C, increases the quantity of interdendritic constituent from 4 to 22%, and results in different phase formation. Binary β–Al_5FeSi and Mg_2Si phases are replaced with ternary β–Al_5FeSi, π–$FeMg_3Si_6Al_8$, and a low melting quaternary eutectic. Higher Si content also reduces solidification shrinkage. For gas-tungsten arc welds made on 6060, an increase in weld metal silicon content from 0.42 to 1.20 wt.% achieved by adding a 4043 filler metal, has no effect on solidification range (contrasting with 6060 castings), but reduces the temperature gradient from 27.5 to 21.7 °C/mm and thus lengthens the mushy zone from 6.0 to 7.6 mm. Also, higher Si content results in small grain refinement (from 63 to 51 µm) and stray grains disappearance. It is believed that both an increase in silicon and faster cooling rates promote the formation of low temperature reactions involving ternary β and quaternary eutectic.

Considering the shrinkage-feeding concept of Feurer [77], the higher amount of interdendritic liquid and lower solidification shrinkage should improves the weldability while the longer mushy zone should reduce it. These contradictory consequences when adding 4043 filler result in an improvement of alloy 6060 weldability, which should be predicted by cracking models.

The effect of cooling rate on 6060 solidification microstructure has also been examined. When going from slow to fast cooling, there is a transition in microstructure going from a continuous network of interdendritic phase constituents to isolated pools of constituents, with continuous phases at grain boundaries. This transition occurred at a cooling rate between 39 and 58 °C/s for cast 6060, and could be related to the nucleation of constituent phases.

6 Modeling Crack Initiation and Growth Mechanisms

Modeling solidification crack initiation and growth mechanisms is required to better understand the underlying causes. Based upon crack surface and in-situ observations, it is generally assumed that solidification cracking occurs at high solid fractions, and results from the fracture of a thin but continuous liquid film along grain boundaries. Implementing the experimental data from the present work in solidification cracking models helps to identify the mechanisms involved in solidification cracking formation generated by the CTW test within Alloy 6060 welds. Details are given below.

6.1 Experimental Input to Model

The reason for the improvement in weldability with filler dilution is not completely understood, but there is likely a combined influenced from grain refinement, bead shape, and solidification conditions. The critical local strain rate values from the CTW test at 0% and 16% filler dilution, i.e. –0.06 and +0.35 %/s respectively (recall Table 14), provide experimental input to cracking models in order to determine the underlying mechanisms involved in solidification crack initiation and growth within Alloy 6060 arc welds. Also, important to the RDG pressure drop evaluation, the solid fraction – temperature curve, determined from the thermal cooling curve for a 6060 a casting (recall Figure 94), is shown in Figure 108 compared against an approximated curve for a weld, corrected for differences in liquidus, solidus, and coherency temperatures (recall Tables 27 and 29), and assuming a same solid fraction at the coherency point (recall Figure 95). Unfortunately, the solid fraction – temperature relationship could not be determined for welds using the method previously applied to Alloy 6060 castings because no external source of heat, e.g. welding arc, is taken into account in Eq. 36.

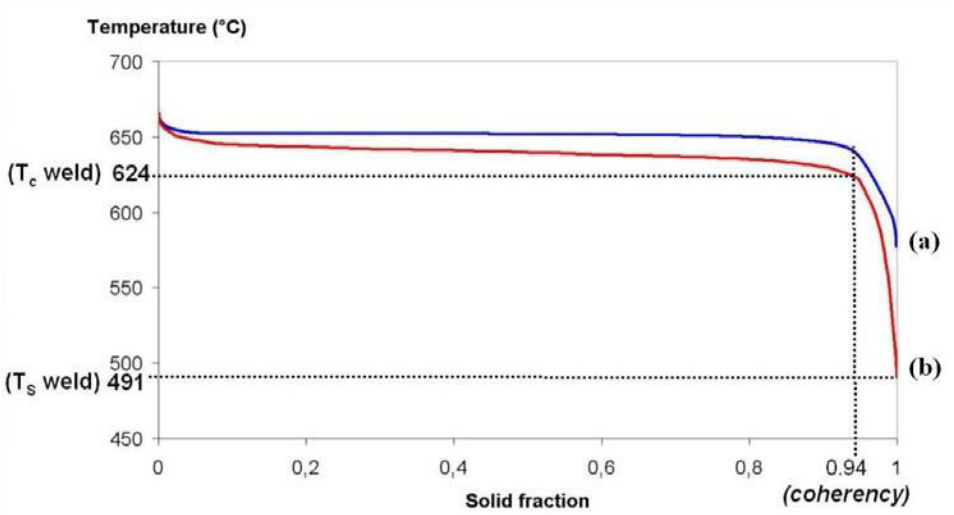

Figure 108: Solid fraction versus temperature curves for Alloy 6060 (a) measured in casting and (b) approximated in weld.

6.2 Strain Partitioning in Mushy Zone

Cracking most often occurs along a single grain boundary located near the weld centerline. Thus, defining how the local strain rate around the weld pool gets partitioned between grain boundaries in the mushy zone is of particular importance to modeling. Because experimental input to the model consists of local displacement measurements made across the mushy zone with an extensometer (recall Figure 61), it is convenient to consider this measured displacement (δ) as equally divided between N adjacent grains of equal size separated by liquid films of equal thickness [91], treating the mushy zone as a composite material consisting of parallel strips of liquid and solid phases. It assumes that strain is distributed equally among all grains in the mushy zone. While this is amounts to a crude approximation that ignores curvature effects, it serves a useful purpose in this study and must suffice until considerably more work can be devoted to this little explored subject. Likewise, if a differentiation is made between liquid (δ_L) and grain (δ_G) displacement, the displacement rate per grain from Figure 109 can be given as:

$$\frac{\dot{\delta}}{N} = \dot{\delta}_L + \dot{\delta}_G \tag{38}$$

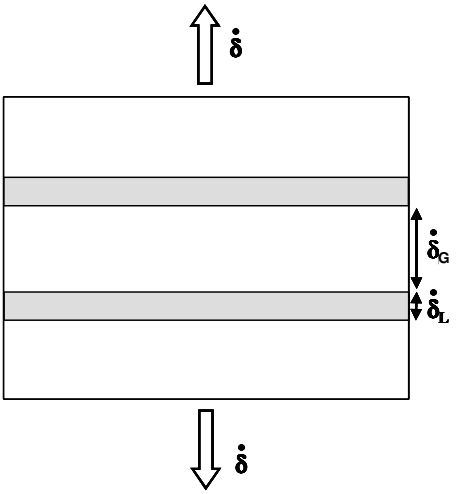

Figure 109: Schematic showing deformation rate across mushy zone ($\dot{\delta}$), grain ($\dot{\delta}_G$), and grain boundary liquid ($\dot{\delta}_L$) as considered by strain partition model in Eq. 38.

Grains in the mushy zone consist of packets of parallel dendrites surrounded by liquid, where the deformation rate $\dot{\delta}_G$ can be taken as the sum of solidification shrinkage ($\dot{\delta}_{G/sh}$) and deformation originating from the liquid pressure drop ($\dot{\delta}_{G/\sigma}$). The strain rate $\dot{\varepsilon}_{G/\sigma}$ was estimated from an expression relating the rheological behavior of semi-solids to stress σ (i.e. pressure drop):

$$\sigma = \sigma_0 \exp(\alpha f_S) \exp\left(\frac{mQ}{RT}\right) (\dot{\varepsilon}_{G/\sigma})^m \tag{39}$$

, where Q is activation energy, T is absolute temperature, m is strain rate sensitivity coefficient, α and σ_0 are material constants, and R is the gas constant. Approximate values were taken from work of Braccini et al. for an Al-4.5wt.%Cu binary alloy with a columnar structure [91]: m = 0.26, Q = 160 kJ·mol^{-1}, α = 10.2, and σ_0 = 4.5 Pa. Using these values for Alloy 6060 in the mushy state will not give an exact, but at least a rough order of magnitude of the solid deformation rate. Equal pressures are assumed within the grain and at the grain boundary, i.e. the stress σ equals the liquid pressure drop originating from the deformation rate $\dot{\delta}_L$. The grain deformation rate $\dot{\delta}_{G/\sigma}$ was calculated from $\dot{\varepsilon}_{G/\sigma}$ in Eq. 39, multiplied by grain size.

The grain solidification shrinkage ($\dot{\delta}_{G/sh}$) contributes to the tension at grain boundaries. A volume solidification shrinkage of 6% was assumed [163], giving a linear shrinkage of $\sqrt[3]{6} = 1.82\%$, applied between the coherency and solidus temperatures, and assuming a shrinkage proportional to the solid fraction (i.e. 0.0182% by every 1% solid fraction). The number of grains *N* is given by dividing the weld pool width (7.5 and 8.0 mm) with the grain size (63 and 51 μm), for 0 and 16% 4043 filler dilution, respectively.

The RDG analysis for interdendritic liquid pressure drop (recall Eq. 11) was applied to aluminum welds using the physical parameters listed in Table 31 and was likewise assumed to apply at grain boundaries. Grain boundary strain rate values were assumed that comply with Eqs. 38 and 39. An iterative process was applied until the boundary conditions (i.e. experimentally measured local strain rates in Table 14) were satisfied. The weld temperature gradient *G* was determined from thermocouple data; isotherm velocity ν_T was taken to be the welding speed; primary dendrite arm spacing λ_1 was assumed to be 10 μm; and the solid fraction – temperature relationship for welds in Figure 108 was used.

Pressure drop values were calculated for the grain boundary liquid deformation rate $\dot{\delta}_L$ up to 0.98 solid fraction. Beyond this point, the strain resistance due to interdendritic bridging is assumed sufficient to resist cracking. Results show an interdendritic pressure drop near the dendrite root (i.e. at 0.98 solid fraction) of 0.11 and 0.55 atm (0.011 and 0.055 MPa) for 0 and 16% filler dilution, respectively.

Table 31: Values of Constants used for Calculations in Eqs. 38-52

Parameter	Symbol	Value	Reference
Shrinkage Factor	β	0.06	[118]
Liquid Viscosity	μ	$1 \cdot 10^{-3}$ Pa.s	[118]
Thermal Gradient	G	25,000 $K.m^{-1}$	
Velocity of Isotherms	ν_T	0.004 $m.s^{-1}$	
Primary Arm Spacing	λ_1	$1 \cdot 10^{-5}$ m	
Permeability	K	$\frac{\lambda_1^2 \cdot (1-f_S)^2}{8\pi}$ m^2	[191]
Hydrogen Partition Coefficient	k_H	0.05	[116]
Liquid Surface Tension	γ	0.814 Nm^{-1}	[116]

Results from strain partitioning analysis, summarized in Table 32, demonstrate that the grain deformation rate $\dot{\delta}_{G/\sigma}$ can be neglected. This follows from basic assumptions made in the model where coherency within the grains provides resistance to deformation, whereas at grain boundaries there is assumed no coherency. The external straining is also mostly partitioned only between the grain boundary liquid films, as suggested a long time ago by

Pellini (recall Figure 10) and as experimentally observed in welds using the MISO technique [62]. In reality, there may be some coherency at grain boundaries, depending upon grain orientation and dendrite structure [85], but this is expected to always be less than within the grains. Accordingly, assuming strain rate sensitive cracking mechanisms, this helps to explain why cracks are typically always associated with grain boundaries. This also helps to explain the beneficial role of grain refinement in reducing cracking susceptibility [5,140,178]. For comparison, the pressure drop calculated in cast Al-Cu binary alloys under critical strain rate conditions is on the order of 0.02 atm [81], and the nominal stress to form solidification cracking in cast Al-0.5wt.%Cu binary alloy on the order of 0.22 atm [26]. The next paragraphs aim to put forward a liquid fracture mechanism involving these low pressure drop values.

Table 32: Summary of Deformation Rates from Strain Partition Model (negative rates indicate movement toward weld centerline)

Inputs and Outputs from Strain Partition Model	Aluminum Alloy Weld	
	6060	6060 + 16% 4043
Local Strain Rate (%/s), 10.5 mm gage	-0.06	+0.35
Number of Grains *N*	119	157
Local Deformation Rate $\dot{\delta}$ (μm/s)	-4.5	+28.0
Grain Boundary Liquid Deformation Rate $\dot{\delta}_L$ (μm/s)	+0.03	+0.30
Grain Deformation Rate $\dot{\delta}_{G/sh}$ (μm/s)	-0.06	-0.12
Maximum Grain Deformation Rate $\dot{\delta}_{G/\sigma}$ (μm/s) within Coherent Region	3.10^{-11}	1.10^{-6}
Maximum Interdendritic Liquid Pressure Drop (atm)	-0.11	-0.55

6.3 Modeling Crack Initiation Mechanism

Initiating a crack has been related to the liquid fracture under a pressure drop due to hindered liquid feeding [22,77], suggesting that liquid rupture occurs if the pressure falls below the cavitation pressure [81]. The model proposed here relates crack initiation to formation of a stable micropore, which provides crack initiation source. Based upon the present experimental inputs and literature data, a mechanism suitable for initiating a crack in Alloy 6060 arc welds will be proposed.

6.3.1 Pore Nucleation

The possibility of nucleating a void is discussed in this section using pore nucleation theories and liquid fracture properties. Unfortunately, interfacial energy data for many systems of interest are not available. However, an approximation using literature data is

possible regarding conditions required to nucleate *vapor* and *dissolved gas pores* within Alloy 6060 welds.

6.3.1.1 Vapor Pore Nucleation

As detailed in paragraph 2.1.3, by applying classical nucleation theory of Fisher [102], Campbell [22] showed that a tensile hydrostatic fracture pressure (P_f) of 30,500 atm (3,050 MPa) is needed for homogeneous vapor pore nucleation (i.e. cavitation) in pure molten aluminum at 660°C. Recall from Eq. 28, a lesser value of 1,760 atm (176 MPa) is required for heterogeneous vapor pore nucleation on Al_2O_3 oxides, poorly wet by liquid aluminum (wetting angle 160° [106]). Still, these values far exceed the actual pressure drop associated with the conditions in aluminum welding ($\approx 10^{-1}$ atm, recall Table 32). From this it appears that vapor pore nucleation (i.e. nucleation), usually cited as a possible mechanism to initiate solidification cracking [81,88,91], is not likely to occur under these assumed conditions. This has lead some researchers to ignore pore nucleation mechanisms and assume pre-existing pores (recall Figure 21) [96]. Even when considering high strain rates experienced in trans-varestraint tests (near 100%/s), the RDG model predicts a liquid pressure drop within Alloy 6060 welds without filler addition of approximately 18 atm, still two orders of magnitude under the values required for vapor pore nucleation (1,760 atm). Furthermore, the fracture strength of semi-solid alloys is usually less than 2 MPa, i.e. 20 atm [92,132]. This suggests that transverse strain alone cannot nucleate a vapor pore, and that other mechanisms must be involved in liquid fracture, in particular dissolved gas.

6.3.1.2 Gas Pore Nucleation

Of interest is the possible beneficial effect of dissolved gas contributing to the internal pressure needed for liquid fracture, with hydrogen serving as the sole source of porosity in aluminum [22,116]. In the discussion of this work, gases other than hydrogen are not taken into account and only welds made without filler are considered. It is assumed that hydrogen is partitioned between solid and liquid, that no hybrides are formed [116], and that none of the gas escapes by outgassing. Hydrogen is partitioned heavily to the liquid during solidification (k_H=0.05 [116]), with concentrations increasing in the interdendritic liquid. Excess hydrogen is nucleated as gas bubbles, which requires some initial supersaturation [22,99,116]. Unfortunately, with limited data regarding hydrogen equilibrium in aluminum alloys, values for pure aluminum have been used for partition coefficient, surface tension, and hydrogen solubility as listed in Table 31.

Adapting Eq. 29 for hydrogen in Alloy 6060 weld metal, the liquid fracture pressure P_f equals:

$$P_{H2} - P_e = P_f \tag{40}$$

, where P_{H2} is hydrogen partial pressure and P_e external pressure. P_e is the combined sum of the hydrostatic pressure (P_h), atmospheric pressure (P_a), and pressure drop due to solidification shrinkage (ΔP_{sh}) and external strains (ΔP_ε). For welds, P_h is negligible, P_a equals 1 atm, and the sum $\Delta P_{sh} + \Delta P_\varepsilon$ is approximately 0.1 atm (recall Table 32). Accordingly, since the fracture pressure P_f of pure aluminum liquid is at least 1,760 atm, Eq. 40 can be approximated by:

$$P_{H2} = P_f \tag{41}$$

According to Sievert´s law, P_{H2} (atm) is directly proportional to the square of the dissolved hydrogen content in the liquid $[H]_L$ (ml/100g), expressed as:

$$P_{H2} = \left(\frac{[H]_L}{K_S} \right)^2 \tag{42}$$

, where K_S is the Sievert´s constant represented by the Van´t Hoff Equation for pure aluminum [116]:

$$K_S = \exp\left(\frac{-2{,}700}{T} + 2.72 \right) \tag{43}$$

, where T is absolute temperature (K). In Alloy 6060 welds, values for K_S vary over a solidification temperature range of 165°C (recall Table 29), from 0.84 (dendrite tip) to 0.44 (dendrite root). Assuming equilibrium at the solid-liquid interface and complete mixing in the liquid, two possibilities exist for calculating hydrogen concentration $[H]_L$, considering either equilibrium (Lever law, Eq. 44) or non-equilibrium (Scheil equation, Eq. 45):

$$[H]_L = \frac{[H]_0}{(1-k_H)*(1-f_S)+k_H} \tag{44}$$

$$[H]_L = [H]_0 * (1-f_S)^{(k-1)} \tag{45}$$

, where f_S is solid fraction, k_H hydrogen partition ratio, and $[H]_0$ initial hydrogen content in the weld pool. The appropriate equation in the case of the Alloy 6060 weld is determined based

upon the diffusion distance of hydrogen into aluminum dendrites. The hydrogen diffusion coefficient D_H in pure solid aluminum (cm²/s) is given, according to [118]:

$$D_H = 0.11 \exp\left(\frac{-40{,}880}{RT}\right) \tag{46}$$

, where T is absolute temperature (K) and R is the gas constant. The diffusion distance X (cm) of hydrogen in solid aluminum during the time t (s) equals:

$$X = \sqrt{D_H \cdot t} \tag{47}$$

Plotting the hydrogen diffusion distance into solid aluminum during 1 second versus temperature (Figure 110) reveals a diffusion distance of 140 µm at 490°C (solidus, recall Table 29). Since the weld solidification time for Alloy 6060 is on the order of 1 second (recall Figure 97) and half the dendrite thickness is 5 µm (Table 31), the diffusion distance (140 µm) far exceeds the dendrite size. Hence, equilibrium conditions can be assumed, and the Lever law (Eq. 44) appears more suitable to represent hydrogen partitioning during weld solidification, and is used hereafter to calculate the hydrogen concentration in the liquid.

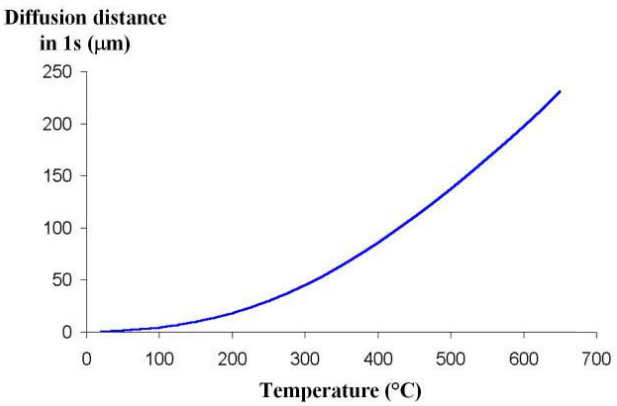

Figure 110: Diffusion distance of hydrogen in solid aluminum in 1s versus temperature.

Taking the estimated solid fraction – temperature curve for a 6060 weld (recall Figure 108), the hydrogen partial pressure is calculated using the Lever law (Eq. 44) for initial hydrogen contents in the weld pool between 0.1 and 0.8 ml/100g (Figure 111), i.e. close to the hydrogen solubility in pure aluminum (0.88 ml/100g H_2) [116], and up to 0.98 solid fraction. Beyond 0.98 solid fraction, the resistance to applied strain is assumed sufficient to

avoid cracking [81]. Results revealed that initial hydrogen contents of 1.60 and 6.65 ml/100g are required in the weld pool to achieve gas pressure of 1,760 and 30,500 atm respectively at the dendrite root (f_s=0.98). In comparison, to get microscopic gas porosity, only 0.15 ml/100g H_2 is commonly needed in aluminum castings [116], and 1.00 ml/100g H_2 in Alloy 6061 GMA welds with 4043 filler (Table 33).

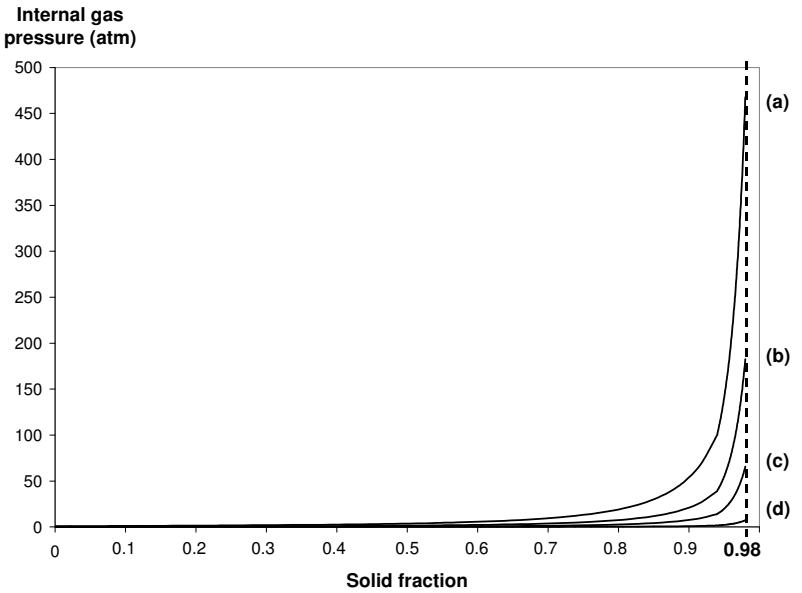

Figure 111: Hydrogen dissolved gas pressure versus solid fraction for initial hydrogen contents in the weld pool of (a) 0.1, (b) 0.3, (c) 0.5, and (d) 0.8 ml/100g. Calculation based upon Lever law (Eq. 44).

Table 33: Threshold Weld Metal Hydrogen Content to Get Porosity for Different Aluminum Alloys and Welding Processes

Welding Process	Aluminum Alloy	Threshold Hydrogen Content (ml/100g)
Autogenous GTA Weld [192]	2219	0.45
	Al-6.5wt.%Zn	0.50
	1100	0.70
	Al-1wt.%Mg	0.75
	3003	0.95
	5083	1.10
	Al-1wt.%Zn	1.15
	Al-6.5wt.%Mg	1.25
	7039	2.30
GMA Weld [192] (Base Metal/Filler Metal)	1100/1100	0.70
	6061/4043	1.00
	5083/5183	1.20
GMA Weld [119] (Base Metal/Filler Metal)	6061/5356	1.15
	5083/5356	1.20

From the analysis above, it appears that interdendritic gas pore nucleation is unlikely to occur for weld pool hydrogen contents lower than 1.60 ml/100g. However, experience suggests that pores can readily form under such conditions. One possible explanation for this apparent dilemma is that metastable pore nuclei may already exist in the liquid. Liquid metals are believed to contain micron sized pores that cannot escape during processing because of limited buoyancy [22]. These micropores may be nucleated by radiation damage from decay of radioactive matter and occasional passage of cosmic rays, where high-energetic α-particles cause small regions within the liquid to become vaporized [110]. Pore nuclei can also take the form of double-sided oxide films [125] or minuscule regions of gas trapped at the apex of oxides [103]. Double-sided oxides may originate as pores in cast ingots that are then collapsed and compressed by subsequent forming operations [125]. E.g., when hot rolling cast ingots, the gas pores, reduced in size, persist in the hot rolled plate in the flattened form, and are finally enclosed between oxides films.

Double-sided oxides may be entrained in the weld pool upon fusing the base plate, and become deposited at the solidification interface. Their rate of collapse is not likely controlled simply by inertial and surface-tension forces or volume diffusion of gas, but also by the mechanical rigidity of the oxide skin [125]. Such metastable pore nuclei must survive for a long enough period of time until favorable conditions are met to activate and expand them into stable micropores. Should these micropores form in the coherent region of the mushy zone, this could conceivably provide a source for crack initiation. Indeed, vapor bubbles and crack responsible for the failure of liquids have been observed to grow from extremely small nuclei [102]. Regarding aluminum castings, oxide particles were invariably found in association with bubbles or small pores at the grain boundaries [103], reducing oxides being found to decrease metal porosity amount [124]. Moreover, aluminum melts rich in hydrogen have been shown incapable of nucleating bubbles in the absence of inclusions [104]. High-resolution synchrotron X-ray micro-tomography revealed that cast aluminum alloys contain a huge number of small micropores, on the order of the micron in size [115]. The origin of these pores is not clear. However, higher densities of micropores were observed in cast Al-Mg aluminum alloys than in high purity aluminum (99.999wt.%) for a same hydrogen content [115], suggesting a major role played by particles in pore formation.

6.3.2 Porosity-Based Crack Initiation Model

Conditions needed to expand a pre-existing pore nuclei include i) hydrogen content in the liquid must exceed its solubility [22,109,116] and ii) pores must satisfy stability criterion. Grandfield et. al [96] combined the stability criterion as defined by Campbell [22] and the

RDG pressure drop calculation [81], where the internal pressures that contribute to expansion (i.e. hydrogen partial pressure P_{H2}, and pressure drop due to solidification shrinkage ΔP_{sh} and thermal contraction ΔP_{ε}) must exceed the external pressures that act to collapse the pore (atmospheric pressure Pa and surface tension pressure $P\gamma$):

$$P_{H2} + \Delta P_{sh} + \Delta P_{\varepsilon} > P_a + P_{\gamma} \tag{48}$$

Pore stability calculations were made using the physical property values listed in Table 31, with P_{H2} defined by Eqs. 40-44, Pa taken as 1 atm, and the sum ($\Delta P_{sh} + \Delta P_{\varepsilon}$) assumed to be 0.1 atm. Pores are assumed to be spherical at the moment of their expansion, with the surface tension pressure P_{γ} defined by:

$$P_{\gamma} = \frac{2\gamma}{r} \tag{49}$$

, where r is pore radius and γ liquid-vapor surface tension. The surface tension of pure aluminum liquid has been shown to be unaffected by hydrogen amount, but is lowered by the presence of surface oxides [193]. Impurities also affect the gas-liquid surface energy, and a variety of values found in the literature for the molten aluminum surface tension varying between 0.712 and 1.007 $N.m^{-1}$ [105,107,116,193], where smaller surface tensions, facilitating pore formation, are measured for extensive oxide layer present along the pore surface. A mean value of 0.814 $N.m^{-1}$ [116] is taken for the surface tension in this study.

The concept for a porosity-based crack initiation model, i.e. formation of a crack from a micro-pore, is illustrated in Figure 112. Three possibilities exist assuming the hydrogen concentration exceeds its solubility limit and that pre-existing nuclei are present. When formed ahead of the coherency region, a stable pore may either be expelled in front of the advancing dendrites as a macropore, or become entrapped between the dendrites as a micropore. This distinction is determined by whether or not the stable pore diameter ($2r$) exceeds the interdendritic spacing at the point of formation:

$$\begin{aligned} 2r &> (1 - f_s) \cdot \lambda_1 \rightarrow macropore \\ 2r &\leq (1 - f_s) \cdot \lambda_1 \rightarrow micropore \end{aligned} \tag{50}$$

, where λ_1 is primary dendrite arm spacing. However, if a stable micropore forms within the coherency region, it then becomes a potential crack initiation site. Indeed, in-situ observations revealed weld solidification cracking to possibly form from a pore [19]. The surface tension pressure P_{γ} (recall Eq. 49) increases at higher solid fractions, as the liquid film thickness decreases, reaching a value of 163 atm at 0.98 solid fraction. This must be

counterbalanced by high hydrogen content, if a stable micropore is to form at the dendrite root.

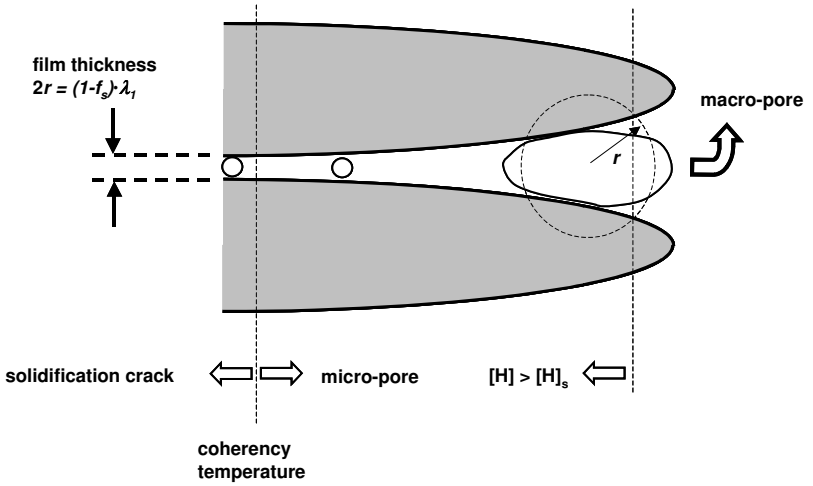

Figure 112: Schematic representation of porosity-based crack initiation model illustrating three different possibilities for formation of i) macropore, ii) micropore, and iii) solidification crack.

For a 6060 weld without filler addition, a minimum of 0.10 ml/100g H_2 is required in the weld pool to exceed the hydrogen solubility (0.88 ml/100g H_2) [116] at the coherency point (f_s = 0.94), and thus to get macroporosity since the corresponding stable pore diameter ($2r$ = 24 µm) exceeds the interdendritic spacing at the coherency point (0.6 µm). This is close to the minimum value reportedly needed to generate porosity in aluminum castings (0.15 ml/100g H_2) [116], but smaller than found for aluminum welds (recall Table 33). Rearranging Eq. 48, a stable micropore can form when the term (P_{H2} - P_γ) exceeds the term (P_a- ΔP_{sh} - ΔP_ε), which equals approximately 1 atm. Plotting (P_{H2} - P_γ) as a function of solid fraction for initial hydrogen contents in the weld pool between 0.1 and 0.8 ml/100g (Figure 113) the formation of stable micropores after coherency requires a minimum initial weld pool hydrogen content of 0.49 ml/100g H_2, i.e. pore-related solidification cracking is not possible below 0.49 ml/100g H_2. Applying similar arguments to 6060 welds with 16% 4043 filler dilution, minimum weld pool hydrogen contents of 0.10 and 0.40 ml/100g H_2 are required to form a macropore and micropore, respectively.

Since the term (P_{H2} - P_γ) can vary over a hundred atmospheres, the term ΔP_{sh} + ΔP_ε (≈ 0.1 atm) can be neglected. This demonstrates that the initiation of pore-related solidification cracking in aluminum welds does not depend upon local strain rate conditions, but rather on dissolved hydrogen content. This agrees with the work of Sigworth and

Wang [194], which revealed that the liquid pressure drop in castings of A356 aluminum alloy and steels is too small to contribute significantly to pore formation.

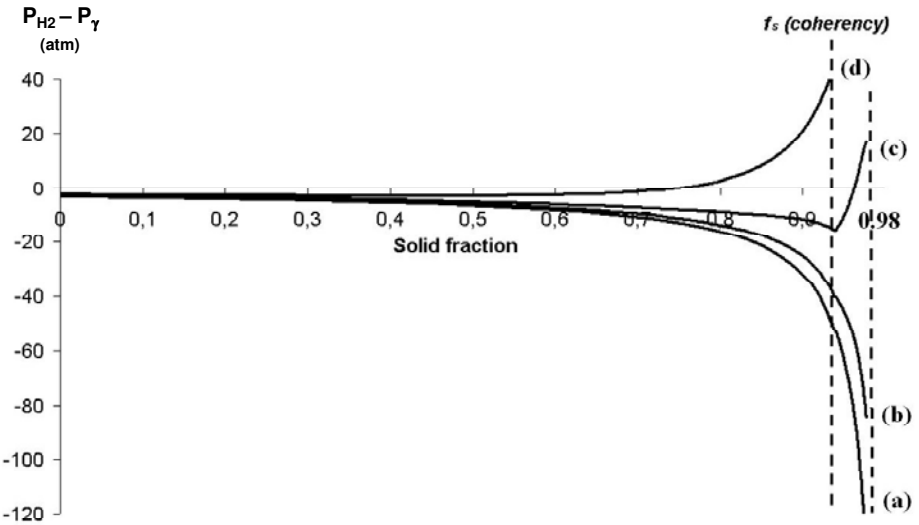

Figure 113: Difference between hydrogen partial pressure P_{H2} and surface tension pressure P_γ versus solid fraction for initial hydrogen content in weld pool of (a) 0.1, (b) 0.3, (c) 0.5, and (d) 0.8 ml/100g. Hydrogen gas pressure calculated using Lever law (Eq. 44).

6.3.3 Summary

The initiation of pore related solidification crack has been associated to the formation of a stable micropore within the coherent region, providing crack initiation source. Calculations show that pores are unlikely nucleated in alloy 6060 arc welds. A porosity-based crack initiation model has been developed, relating pore formation to the expansion of a pre-existing nucleus. Initiating a crack does not depend upon local strain rate conditions, the overriding factor being dissolved hydrogen content. A model is hereafter proposed regarding conditions required to grow a crack following crack initiation.

6.4 Model for Crack Growth

A crack that initiates from pre-existing pore nuclei, but does not grow, will not result in a solidification crack. To examine this aspect of the problem, a solidification crack growth model was developed. In addition, it was demonstrated in the last section that strain rate

does not affect crack initiation. It follows therefore that the observed dependence of cracking on critical strain rate (recall Table 14) must relate to critical conditions for crack growth.

Pressure-balance and mass-balance models have been considered for crack growth. Since the pressure-balance model considers crack growth controlled by Eq. 48 through the term ΔP_ε [96], this concept is deemed not applicable to alloy 6060 welds, where the term ΔP_ε is negligible compared to P_{H2} and P_γ. The mass-balance crack growth model [92], however, is particularly well suited to the boundary conditions of welding, where a crack must grow in a continuous manner (i.e. steady state) behind the weld pool.

Considering two grains separated by a liquid film of thickness h as depicted in Figure 114, this model relates the transverse deformation rate $\dot{\delta}_L$ needed to grow a solidification crack at a rate $\dot{x}$ equal to the weld travel speed, 4 mm/s, following from weld in-situ observations [27]. Such behavior is expected. If the crack were to grow faster than the torch, it would advance toward the weld pool and encounter conditions for high liquid feeding. If it were to grow slower than the torch, the crack tip will drop behind the solidus temperature, and thus immediately stop to propagate. This suggests that there exists a critical strain rate, below which the growth cannot be maintained for a given liquid feeding condition.

(L–x) is taken as the length of liquid film exposed to transverse strain in the region of dendrite coherency. Above the coherency point, the mushy zone is composed of suspended grains in a continuous liquid. The transverse deformation rate $\dot{\delta}_L$ is compensated by both advancement of the crack and liquid feeding (flow rate v_L) in the form of a mass balance:

$$\dot{\delta}_L (L - x) = \dot{x} h_1 + v_L h_2 \tag{51}$$

, where h_1 and h_2 are the liquid film thickness at the crack tip and coherency point positions. At a solid fraction f_s, the liquid film thickness h equals (1- f_s)·λ_1, where λ_1 is primary dendrite arm spacing.

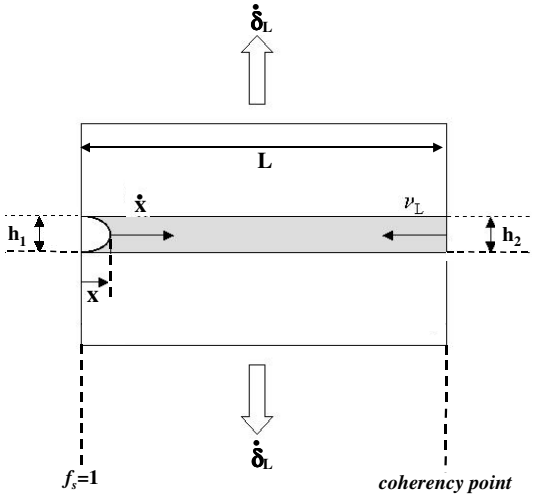

Figure 114: Schematic of liquid film at boundary between two grains, demonstrating mass-balance controlled crack growth.

In applying this model it is assumed that the crack tip is located at 0.98 solid fraction (x=0.98), occurring at 542 and 507°C for 0% and 16% filler dilutions respectively, as shown for 0% filler dilution in Figure 108b. Beyond 0.98 solid fraction, the strain resistance due to interdendritic bridging is assumed sufficient to resist cracking [81]. The coherency point is located at 0.94 and 0.82 solid fraction for 0 and 16% 4043 filler dilution, respectively. Under these conditions, the liquid film distance (*L-x*) equals 2.92 and 4.77 mm for 0% and 16% filler dilution, arising due to different temperatures at 0.98 solid fraction and lower cooling rates encountered with higher filler dilution (recall Figure 97). The liquid flow v_L was calculated from Darcy´s law:

$$f_L \cdot v_L = \frac{-K}{\mu} \frac{d(\Delta P_{sh} + \Delta P_\varepsilon)}{dx} \tag{52}$$

, where f_L is liquid fraction at the point of initial coherency, with K and μ values listed in Table 31. The pressure gradient was estimated using RDG pressure drop calculations (recall Eq. 11).

The crack growth model predicts a critical transverse deformation rate $\dot{\delta}_L$ of 0.47 and 0.33 µm/s for 0 and 16% filler dilution, respectively, promoting a pressure gradient (recall Eq. 52) on the order of 10^4 Pa/mm within the coherent region. This demonstrates a deformation rate dependence for crack growth, which could account for the observed relationship between crack formation and applied strain rate in weldability tests (recall

Tables 14 and 15). However, the slightly lower critical deformation rate predicted for higher filler dilution appears to contradict observed behavior, where filler dilution is known to improve weldability. The increased mushy zone size (from 2.92 to 4.77 mm) arising from a lower cooling rate is apparently not compensated by an increase in interdendritic liquid and feedability associated with a higher Si content. This nonconformance may be linked to oversimplifications in the model (e.g. grain boundary structure) or other approximations (e.g. solid fraction-temperature curve, and location of coherency point and crack tip). For example, the disappearance of columnar centerline grains at higher filler dilution (recall Figure 87) is not taken into account, nor is grain curvature considered. This suggests the need for a three-dimensional approach. The influence of grain boundary morphology may be illustrated with the CTW laser steel welds (see Appendix), where the centerline solidification crack was contained within the weld metal for austenitic and duplex stainless steels with tortuous grain boundaries and exited both crown and root surfaces with the super-austenitics probably due to their straight grain boundaries.

For crack velocities slower than the welding speed, i.e. less than 4 mm/s, crack growth will terminate when it falls behind the solidus. However, if the conditions for crack initiation are still satisfied, a new crack may form, resulting in a succession of several small cracks instead of one long continuous crack. Under these conditions, the boundary for small successive cracks is represented by a crack tip velocity of 0 mm/s, above which cracks grow, and corresponding to a predicted critical transverse deformation rate ($\dot{\delta}_L$) of +0.07 and +0.11 μm/s for 0 and 16 % 4043 filler dilution, respectively. Experimentally, discontinuous cracking is usually observed when close to the critical conditions required for weld solidification crack formation (recall Figure 75b). At the other extreme, if the crack grows faster than the torch, it will advance toward the weld pool and encounter conditions for rapid liquid feeding, which will slow down the crack tip velocity.

From Eq. 51 it is found that by reducing the extent of the coherency region, i.e. lowering the distance (L-x), there is an increase in the critical deformation rate $\dot{\delta}_L$ needed for crack growth. This follows from the ease of feeding liquid over shorter distances. This also agrees with welding practice, where alloys with a small solidification range typically demonstrate lower cracking susceptibility [50,51].

The strain partition model was used to convert grain boundary liquid deformation rate into local strain rate, comparable to what was measured experimentally using weld width as a gage length. As shown in Table 34, the critical local strain rates needed to grow a crack are +0.64 and +0.41 %/s for 0% and 16% 4043 filler dilution. Compared with experimental

values, the predicted critical strain rate for the 6060/4043 weld was within 17%, but for the 6060 weld the predicted value was off by an order of magnitude.

Table 34: Comparison between predicted and measured (recall Table 14) critical local strain rates for crack growth in Alloy 6060 welds with 0 and 16% 4043 filler dilution. Negative values relate to movement towards weld centerline

Weld Metal	Critical Local Strain Rate for Crack Growth (%/s) 10.5 mm gage	
	Predicted	Experimentally Measured
6060	+0.64	-0.06
6060 + 16% 4043	+0.41	+0.35

This model could help explain why, for the same alloy and grain size, weldability varies with the grain refiner used, scandium or titanium-boron, where titanium-boron is more efficient [5]. According to the proposed mass-balanced based crack growth model, the higher efficiency of titanium-boron may be due to the displacement of the coherency point towards lower temperature (recall Figure 58) or to the mechanism involved to promote grain refinement. Indeed, titanium promotes grain refinement with the peritectic reaction $L + TiAl_3 \rightarrow Al$ at 665°C [163] forming grains ahead of dendrite tip, while scandium refines the grain structure through a eutectic reaction $L \rightarrow Al + ScAl_3$ at 655 °C [163], forming grains between existing dendrites and thus limiting liquid feeding.

The proposed strain partition model includes the effect of solidification shrinkage and grain size upon local strain rate calculation. Their effect is investigated assuming the critical grain boundary liquid deformation rates fixed and given by the mass-balance based crack growth model for Alloy 6060 welds (i.e. +0.47 and +0.33 μm/s for 0 and 16% 4043 filler dilution, respectively). Reducing the solidification shrinkage from 1.82 to 0% slightly increases the predicted critical local strain rates from +0.64 to +0.75 %/s and from +0.41 to +0.65 %/s, for Alloy 6060 weld with 0 and 16% 4043 filler dilution, respectively (Figure 115). The predicted better weldability at lower solidification shrinkage is in agreement with the shrinkage feeding theory of Feurer [77]. However, the strain partition model shows grain refinement to be more efficient in improving Alloy 6060 weldability (Figure 116). Refining the grain size from 60 to 30 μm increases the predicted critical local strain rates from +0.69 to +1.48 %/s and from +0.31 to +0.86 %/s, for Alloy 6060 welds with 0 and 16% 4043 filler dilution, respectively. Hence, the model suggests that grain refinement could override the effect of reduced solidification shrinkage at higher filler dilution (recall Figure 96), as experimentally observed using the CTW test (recall Figure 82).

Interesting is to note that, for Alloy 6060 welds without filler, when considering the crack tip to be not at 0.98 solid fraction (as assumed previously) but at 502 °C (i.e. close to

the solidus temperature, Table 29), the mass-balance based crack growth model predicts a critical grain boundary liquid deformation rate of 0.14 μm/s, which, using the strain partition model, corresponds to a critical local strain rate of +0.12 %/s, close to the critical local strain rate measured (-0.06 %/s, Table 14).

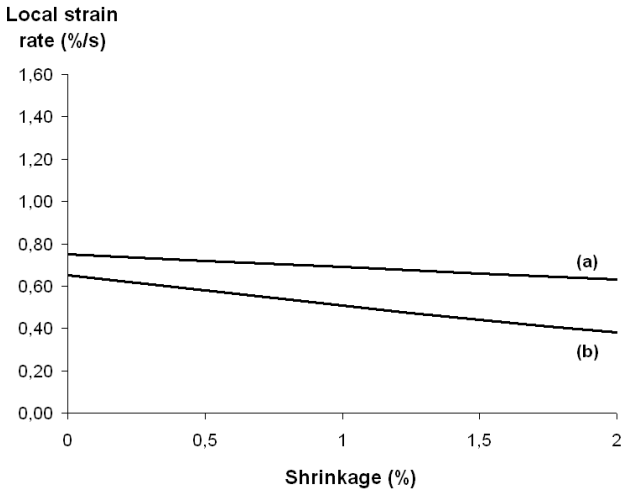

Figure 115: Predicted critical local strain rate versus solidification shrinkage for Alloy 6060 welds with (a) 0 and (b) 16% filler dilution, assuming grain boundary liquid deformation rate of (a) +0.47 and (b) +0.33 μm/s as given by mass-balance based crack growth model.

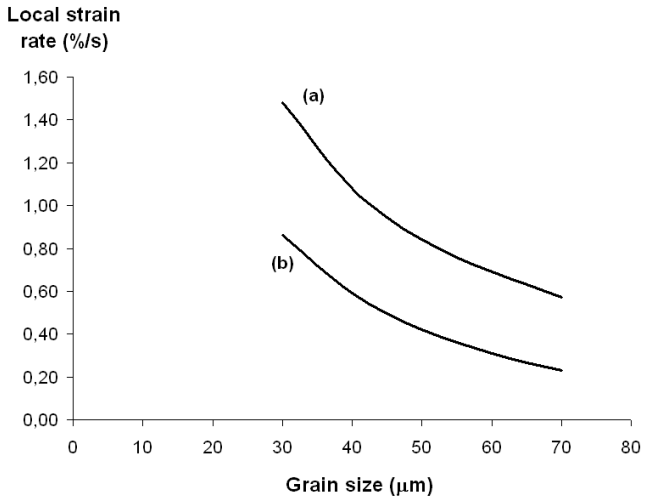

Figure 116: Predicted critical local strain rate versus grain size for Alloy 6060 welds with (a) 0 and (b) 16% filler dilution, assuming grain boundary liquid deformation rate of (a) +0.47 and (b) +0.33 μm/s as given by mass-balance based crack growth model.

6.5 Discussion

The proposed cracking models attempt to characterize the mechanisms for solidification crack initiation and growth within Alloy 6060 welds, as illustrated in Figure 117. The porosity-based crack initiation model shows that a crack is not likely initiated by the nucleation of a pore, but from a pre-existing pore nucleus. It also shows that the formation of a potential crack initiation site is not dependent upon local strain rate conditions, but upon hydrogen amount present in the metal. Once initiated, the mass-balance based crack growth model reveals that crack growth is strain rate dependent, and alloy weldability should be improved by reducing its solidification range or by shifting the coherency point to lower temperatures. Finally, a strain partition model provides a link between predicted and experimentally measured conditions for crack formation, which are on the same order of magnitude. However, the models predict lower weldability at higher filler dilution, the increase in interdendritic liquid quantity with higher Si contents not counteracting the deleterious effect on weldability of lengthened weld mushy zone.

The models outlined above represent a comprehensive approach for relating observed behavior with mechanisms for crack initiation and growth in aluminum 6060/4043 weld metal. Combining experiment with mechanistic models has allowed the quantification of grain boundary conditions needed for cracking to occur. By their simplified nature, however, the assumptions made in these models also limit the accuracy of their predictions, aside from the uncertainties in material constants.

Partitioning of thermal strain in the mushy zone, for example, must involve a complex interaction between grain morphology, grain coherency, and grain boundary orientation relative to strain. Grains located along the weld centerline, where cracking is most often observed, are typically the only grains oriented normal to transverse strain, and should experience a proportionately higher strain rate. The addition of 4043 filler was shown to refine the weld metal grain structure, eliminating columnar centerline grains (recall Figure 87). This effect alone could provide an overriding influence on improving cracking resistance.

If the proposed models are correct, the critical strain rate values measured in the CTW test represent the conditions needed for crack growth, whereas hydrogen concentration is critical to crack initiation. Combining these two factors together defines the conditions needed for cracking as shown in Figure 118 (continuous boundary lines). At sub-critical strain rates it is possible to get elongated pores. That hydrogen should be associated with weld solidification cracking is not a new concept [22,121]. Both porosity and cracking involve the formation of a liquid-vapor interface.

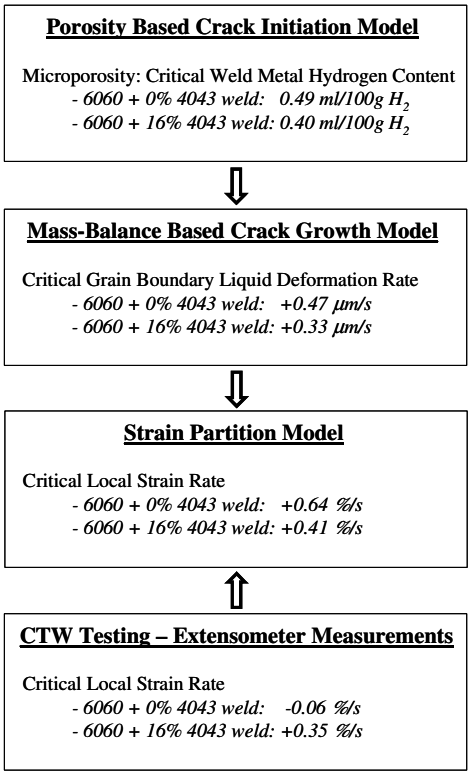

Figure 117: Overview of proposed cracking models, with comparison between predictions and measurements.

When evaluating crack growth, the mass-balance approach was deemed particularly applicable to the steady-state conditions of continuous crack advancement behind the weld pool. However, it is appreciated that in the early transient stage of crack formation and growth, gas pressure may also serve to advance the pore in the direction of cracking and, hence, may be partially dependent upon hydrogen concentration, as illustrated by the dashed lines in Figure 118. The exit of cracks to the surface at the weld crown or root, however, would clearly eliminate any pressure effect. Likewise, the presence of through-thickness cracks will also influence local straining conditions, with strain partitioned directly to the crack, leading to lower strain rates needed to terminate as opposed to initiate crack growth.

The proposed cracking models suggest that hydrogen plays a major role in solidification crack formation. To examine this further, experimental investigations were performed to characterize the effect of hydrogen contamination on Alloy 6060 welds, as detailed below.

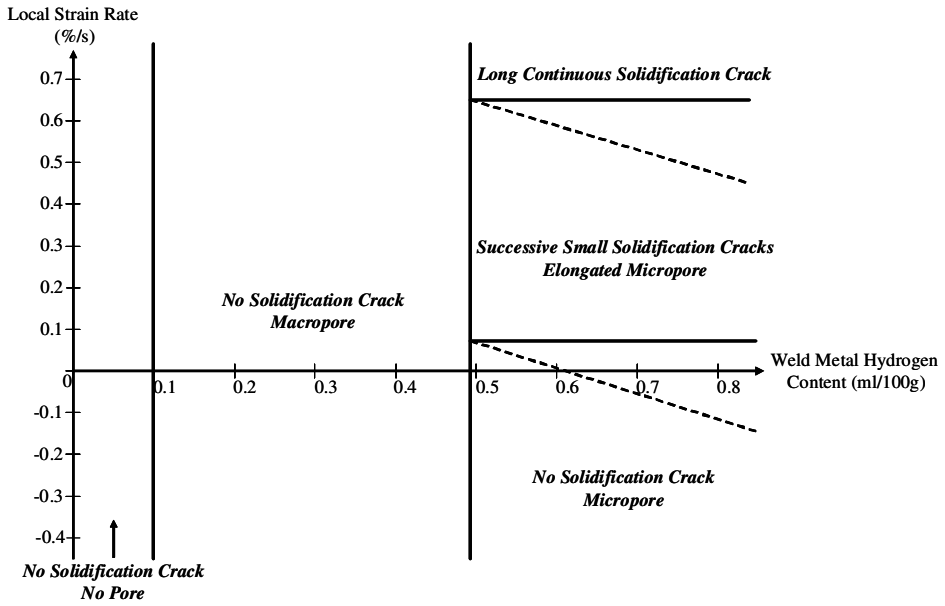

Figure 118: Critical strain rate – hydrogen map demarking regions for cracking versus porosity as applied to an alloy 6060 weld. The possibility that hydrogen may affect crack growth is indicated by dashed lines.

6.6 Model Verification: Effect of Hydrogen on Weldability

Combining the crack initiation and growth models suggest that hydrogen and strain rate, respectively, determine crack formation, and that hydrogen may possibly also affect crack growth. Therefore, experimental investigations were conducted to characterize the effect of hydrogen on *crack initiation* and *crack growth* in Alloy 6060 autogenous arc welds.

6.6.1 Hydrogen Contamination

Bead-on-plate welds were made using hydrogen contaminated shielding gas. Helium flow rate was maintained constant (0.33 L/s) and mixed with gas from Ar+2%H_2 pre-mixed bottles with flow rates varying from 0.000 to 0.083 L/s, resulting in a hydrogen content in the shielding gas between 0% and 0.40% (Figure 119). Among all welds, it has been observed that adding as low as 0.10% H_2 in the welding gas leads to a cleaner weld bead surface by eliminating a dark oxide layer, in agreement with other investigations [195]. This demonstrates that hydrogen serves as an effective oxide reducing element.

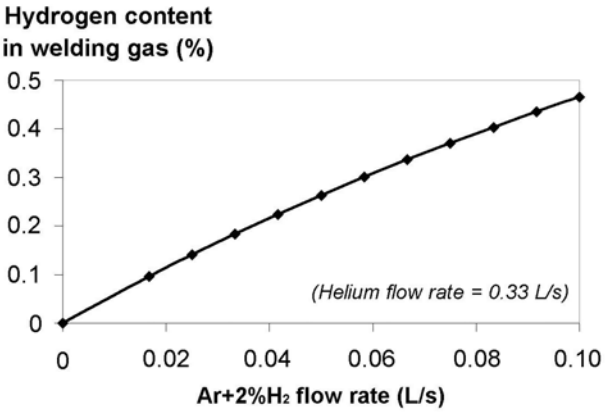

Figure 119: Calculated relationship between Ar+2%H_2 flow rate and hydrogen content in welding gas, helium flow rate being maintained constant (0.33 L/s).

6.6.2 Effect of Hydrogen on Crack Initiation

Solidification crack initiation has been associated with the formation of a stable micropore within the coherent region. Therefore, threshold hydrogen contamination contents were investigated for the formation of micro- and macro-pores in restrained bead-on-plate Alloy 6060 autogenous arc welds.

6.6.2.1 Porosity Characterization

Porosity was characterized to relate weld metal hydrogen contamination and porosity amount. Porosity was examined using X-ray radiography, with a detectability limit of approximately 0.6 mm pore diameter (Figure 120), and also on weld cross-sections at both low (Figure 121) and high magnification (Figure 122). A centerline solidification crack is formed in every weld (Figure 120). This is not surprising since Alloy 6060 was welded autogenously, this welding condition being known to be highly crack sensitive (recall Table 14). However, it was interesting to know if hydrogen bubbles would feed shrinkage and avoid cracking as suggested by the two-phase model of M´Hamdi and Mo [89] … apparently not.

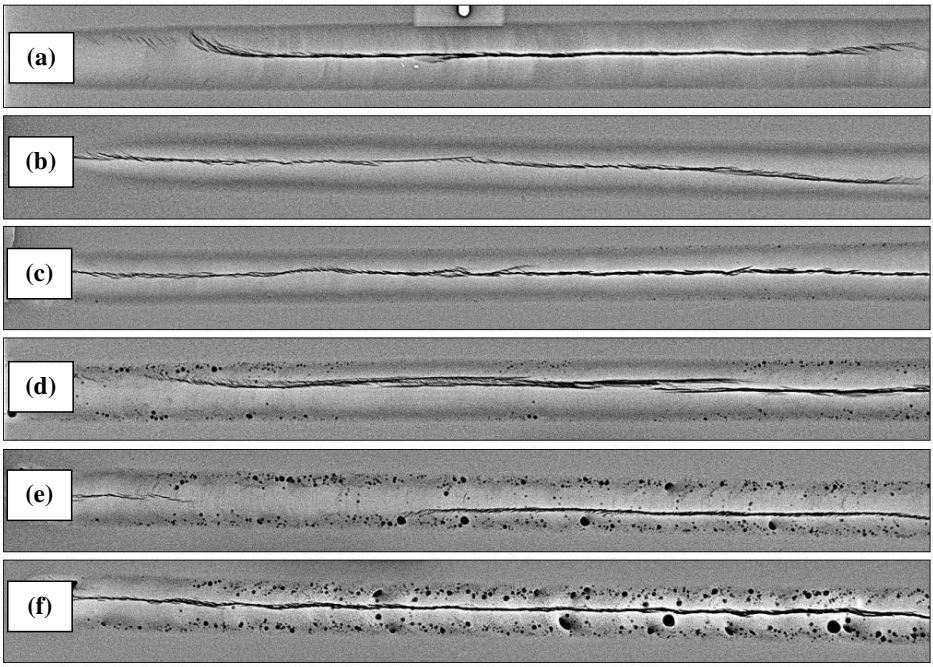

Figure 120: Radiography of welds as seen from top, welded using a percentage of hydrogen in the welding gas of (a) 0%, (b) 0.10%, (c) 0.18%, (d) 0.26%, (e) 0.34%, and (f) 0.40%.

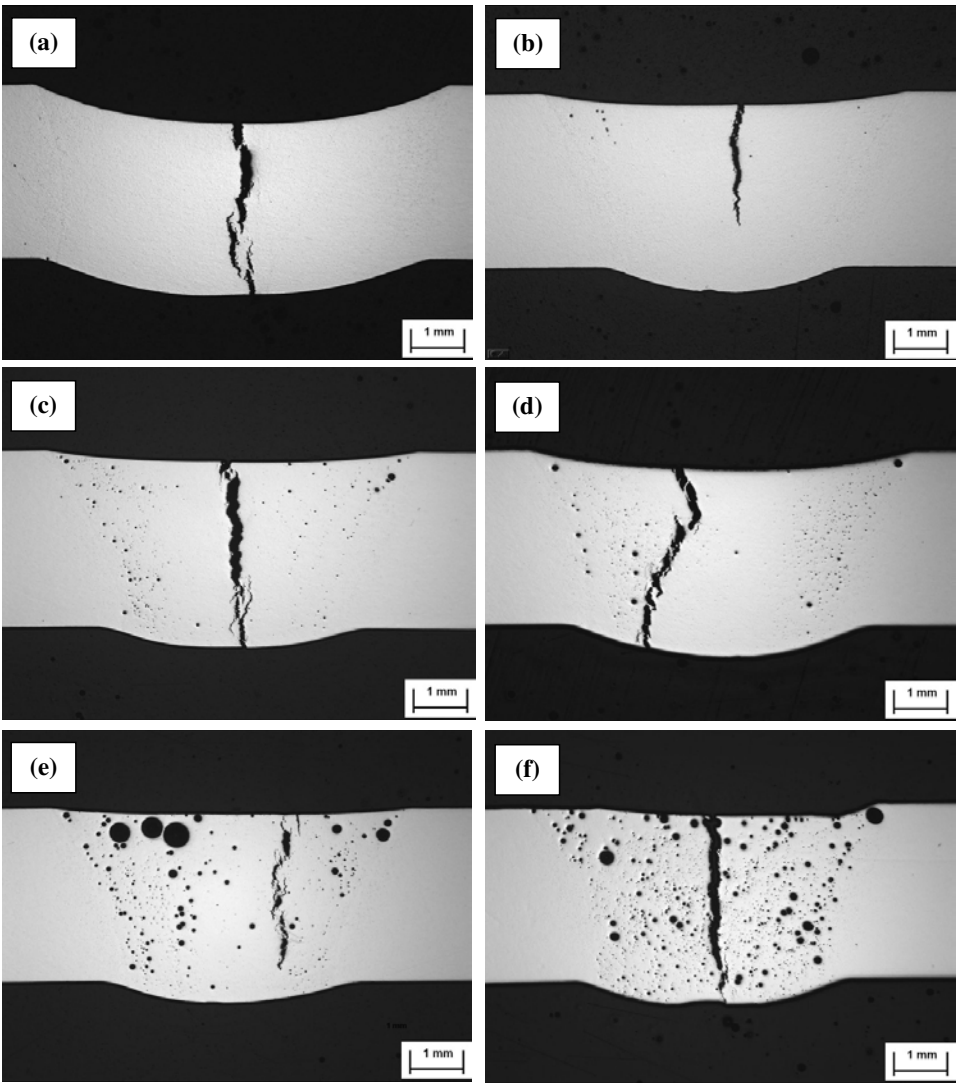

Figure 121: Weld cross-section at low magnification for hydrogen content in welding gas of (a) 0%, (b) 0.10%, (c) 0.18%, (d) 0.26%, (e) 0.34%, and (f) 0.40%.

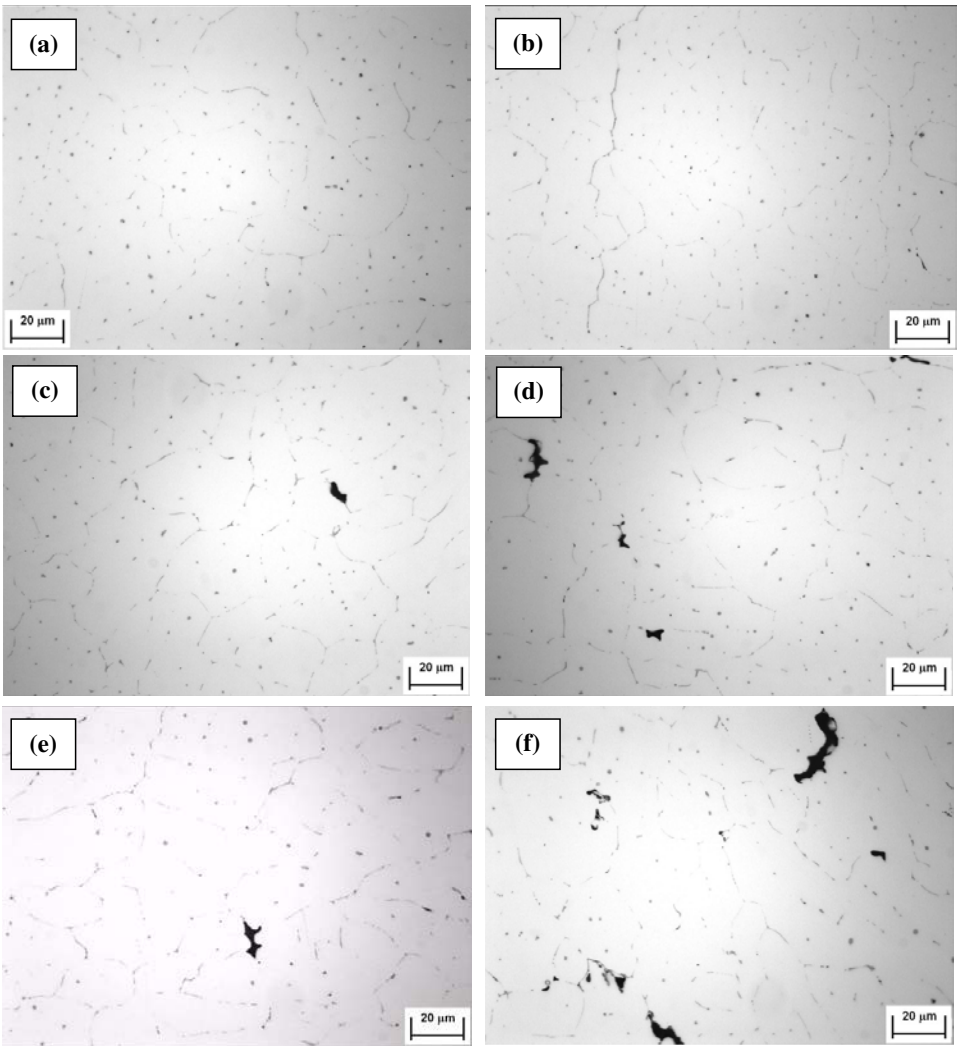

Figure 122: Weld cross-section for hydrogen content in welding gas of (a) 0%, (b) 0.10%, (c) 0.18%, (d) 0.26%, (e) 0.34%, and (f) 0.40%.

Round shaped macropores were first detected for hydrogen content in welding gas as little as 0.18% H_2 by X-ray radiography (Figure 120c) and 0.10% H_2 in weld cross-sections (Figure 121b), forming preferentially along the weld fusion line as observed by other researchers [98]. Further increase of hydrogen content in welding gas increases size and number of pores, especially close to the weld centerline (Figures 120d to 120f, and Figures 121c to 121f). Observing weld cross-sections at higher magnification (Figure 122), micropores were detected for contents higher than 0.18 % H_2 (Figure 122b), verifying the model prediction that macropores form at lower weld metal hydrogen contents than micropores. However, over-head welding would be a better way to verify the present measurements because macropores with large radii (recall Eq. 48 and 49) may escape from weld pool under buoyancy forces. Moreover, even when welding with pure helium, the formation of a solidification crack does not always coincide with the presence of observable micropores (Figure 122a), perhaps not detected because of their small size and low quantity. As to compare, a stable micropore formed at 0.98 solid fraction has a diameter of 0.2 μm when assuming a primary dendrite arm spacing of 10 μm, whereas normal optical metallographic observations have a resolution on the order of 1 μm.

With the aid of image analysis on weld cross-sections, porosity was characterized in terms of porosity area percentage, pore number density, and equivalent radius of the largest pore (Figure 123). Pores with radii exceeding 0.5 μm were considered. With increasing hydrogen content in welding gas from 0 to 0.26 %, the porosity area percentage slightly increases from 0 to 0.58 %, the equivalent radius of the largest pore varied from 0 to 66 μm, and the pore number density varied from 0 to 30 pores/mm². Increasing the hydrogen content in welding gas from 0.26 to 0.34 % did not affect significantly the pore number density (from 30 to 33 pores/mm²), but significantly increased the porosity area percentage from 0.58 to 6.11 % because of larger pores formed with an equivalent radius increasing from 65 to 280 μm. Further increase to 0.40 % H_2 in welding gas increases mostly the pore number density from 31 to 116 pores /mm² and thus, because of the limited weld metal volume, limits the pore expansion, reducing the equivalent radius of the largest pore to 167 μm, causing a drop in porosity area percentage to 5.20 %. This increase in porosity area percentage with increasing hydrogen content in shielding gas has been observed by other researchers [196]. These large bubbles are believed to be pushed ahead of the solidification front until they are mechanically trapped, the spherodicity being preserved possibly because the metal contacting the bubble wall freezes in place [120].

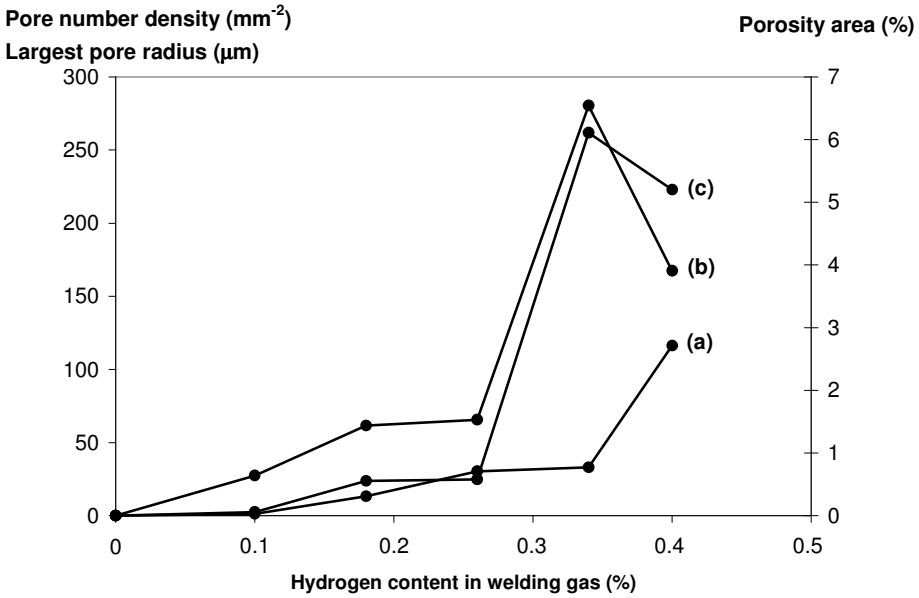

Figure 123: Image analysis on Alloy 6060 weld cross-sections showing (a) pore number density, (b) largest pore equivalent radius, and (c) porosity area percentage depending upon hydrogen content in welding gas.

6.6.2.2 Hydrogen Content Measurement

Weld metal hydrogen content was measured using the hot extraction test. Since measurements were made by maintaining the test coupon in solid state, only diffusible hydrogen, i.e. monoatomic hydrogen trapped in weld metal, was measured. Melting is indeed required to get the "total" hydrogen, i.e. diffusible hydrogen plus diatomic hydrogen trapped into micro- and macro-pores. Unfortunately, melting of test coupons was not possible due to technical limitations in the test equipment.

After having first defined the hot extraction test parameters using Alloy 6060 base metal (e.g. extruded bars), hydrogen content present in Alloys 6060 welds was measured with the aid of the hot extraction technique. Results are given below.

6.6.2.2.1 Hot Extraction Parameters

Measuring hydrogen by heating a specimen coupon requires the determination of temperature and duration of the hot extraction test. The temperature must be high enough to release diffusible hydrogen from trap sites (recall Figure 110). Therefore, since solidus temperatures were measured as low as 490°C (Tables 27 and 29), the test temperature was

fixed at 450°C. Using Eq. 47, the time required for hydrogen to diffuse through half the thickness of the extruded bars (i.e. 2 mm) at 450°C is 330 seconds. Thus, the duration of hot extraction tests was fixed at 900 seconds, to ensure complete diffusion. The machine was calibrated by injecting controlled amounts of hydrogen (Figure 124), the integration of the thermal conductivity detector (TCD) output over time being directly proportional to the injected amount of hydrogen (Figure 125).

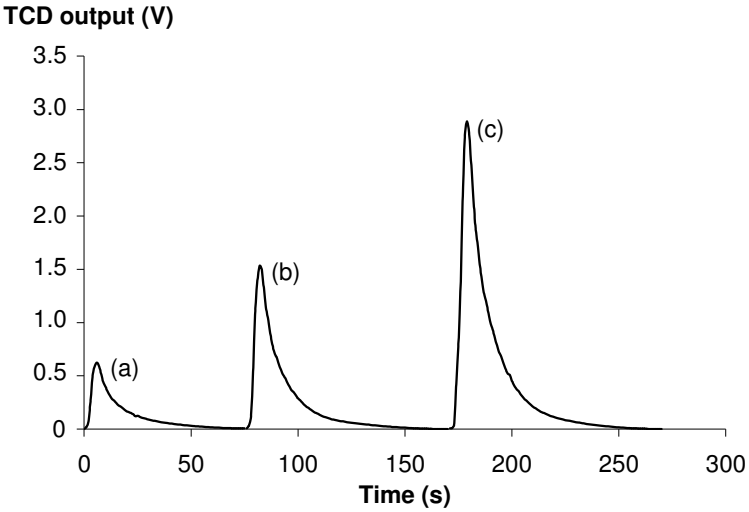

Figure 124: Thermal conductivity detector (TCD) output when injecting (a) 0.1, (b) 0.3, and (c) 0.5 ml of hydrogen.

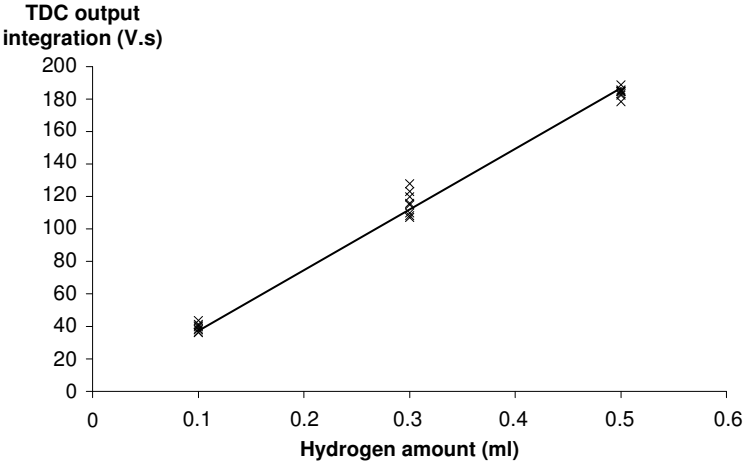

Figure 125: Integration of thermal conductivity detector (TCD) output over time versus hydrogen amount.

Material processing is known to affect measured hydrogen content. Indeed, using the hot extraction technique, Huismann et al. [197] measured the hydrogen content of Alloy 6061 base metal at the same temper, but from fifteen different manufacturers (Figure 126). Hydrogen is always present and varies between the coupons from 0.5 to 3.3 ml/100g H_2 in the as-received condition, and from 0.2 to 2.4 ml/100g H_2 when eliminating the surface oxide layer, contaminated by water (e.g. water-cooled plates during forming). The lower hydrogen values observed when eliminating surface oxide layers is best illustrated by specimen 4 (Figure 126), with a drop from 3.4 to 1.3 ml/100g H_2. Note that the high hydrogen contents far exceeds the theoretical solubility limit for pure aluminum liquid (0.88 ml/100g H_2) [116]. According to the solidification cracking models proposed above, such scattering in hydrogen contents should lead to weldability variations, indicating that threshold hydrogen values should be defined in material specifications.

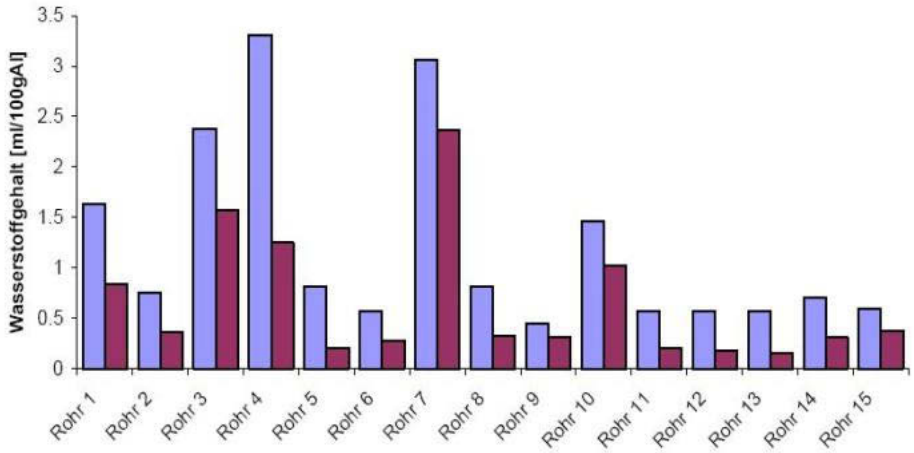

Figure 126: Hydrogen content measured in aluminum alloy 6061 fifteen different manufacturers and measured : (blue) as-received condition and (red) chemically etched to eliminate surface oxide layer [197].

In the present work, the influence of the specimen preparation was investigated on coupons cut from Alloy 6060-T4 and 6060-T6 extruded bars (Figure 127). Coupon preparations included degreasing with acetone (condition (a), Figure 127), cleaning with water (condition (b), Figure 127), mechanical polishing plus degreasing with acetone (condition (c), Figure 127), and etching (Etch E1, Table 6) plus degreasing with acetone (condition (d), Figure 127), with at least three measurements for each experimental condition. Scattering is observed, imposing at least two measurements for each condition. When cleaning with water (condition (b), Figure 127), the hydrogen measurement values rise

up to 2.5 ml/100g H_2, possibly because of water absorption or poor grease removal upon the specimen surface. Moreover, as observed by Huismann et al. (Figure 126), the mean value for hydrogen when eliminating surface oxide layers drops from between 1.8 and 2.0 ml/100g H_2 (Figure 127, conditions (a)), to between 0.6 and 0.7 ml/100g H_2 (Figure 127, conditions (c) and (d)). The contamination of the top surface is believed to come from the rolling process, where water and lubricant used to cool down the material penetrates a small distance into the surface.

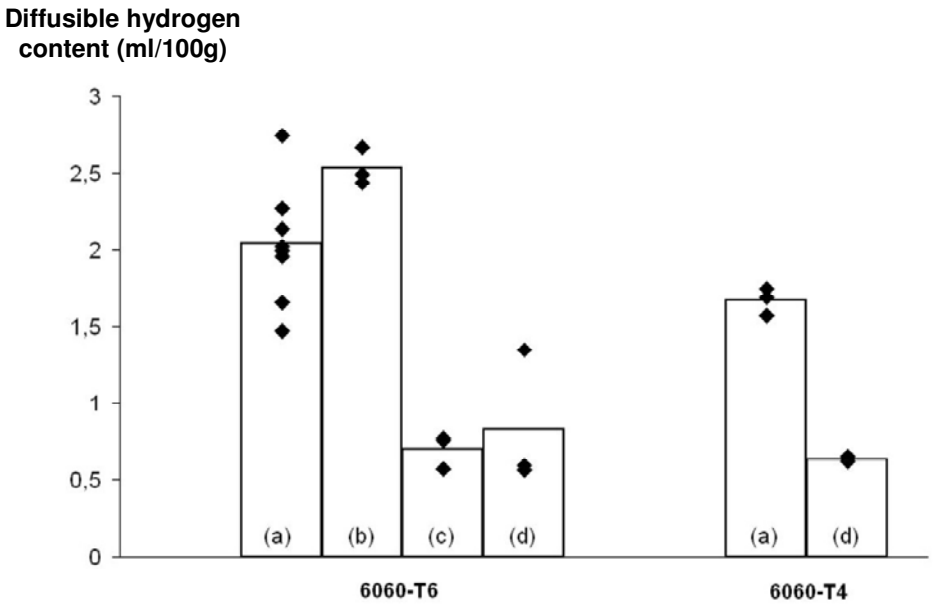

Figure 127: Diffusible hydrogen content measured with hot extraction technique for Alloy 6060-T4 and 6060-T6 base metals at 450°C with different specimen preparations: (a) degreasing with ethanol, (b) cleaning with water, (c) mechanically polishing plus degreasing with ethanol, and (d) chemically etching (Etch E1, Table 6) plus degreasing with ethanol. Note the drop in diffusible hydrogen content with removal of surface oxides (conditions (c) and (d)).

6.6.2.2.2 Diffusible Hydrogen Content in Weld Metal

Regarding Alloy 6060 welds, the effect of specimen preparation was investigated for specimens welded with pure helium shielding gas. The following diffusible hydrogen contents were measured for the different coupon preparations: between 2.5 and 2.8 ml/100g H_2 when degreasing with acetone, 3.0 ml/100g H_2 when mechanical polishing plus degreasing with acetone, and 3.2 ml/100g H_2 when etching (Etch E1, Table 6) plus degreasing with acetone. These small variations suggest that the hydrated oxide surface

layer is already removed, and thus degreasing with acetone was chosen as a standard coupon preparation. A Λ–shape curve is found for diffusible hydrogen in weld metal versus hydrogen in welding gas (Figure 128). Increasing hydrogen amount in welding gas from 0 to 0.40 % first results in an increased diffusible hydrogen amount in weld metal from 2.9 to 4.0 ml/100g (at 0.26 % hydrogen in welding gas), i.e. supersaturation, and then decreases to approximately 3.0 ml/100g. The lower dissolved weld metal hydrogen for higher welding gas hydrogen (above 0.26 % hydrogen) can be related to the appearance of huge macropores (Figure 121), which regulate the weld metal hydrogen content by absorbing dissolved hydrogen from weld metal. These macropores also act as traps for diatomic hydrogen [116]. Since only monoatomic hydrogen can diffuse through solid aluminum, the hot extraction performed here could not measure the gas content trapped in pores, only measurable if the sample is melt. Large macropores representing bigger traps, more hydrogen is retained and thus less is extracted and quantified during the hot extraction. Therefore a Λ–shape curve is found for diffusible hydrogen in weld metal versus hydrogen in welding gas, but the total weld metal hydrogen content (i.e. diffusible hydrogen plus diatomic hydrogen trapped in pores) is likely to continuously increase with increasing hydrogen content in welding gas. Note that the high hydrogen contents far exceed the theoretical solubility limit of for pure aluminum liquid (0.88 ml/100g H_2) [116] and are close to the measurements of Huismann et al. (Figure 126). Higher hydrogen contents than the theoretical solubility limit were also measured in Alloy 6061 welds with Alloy 5356 filler addition (1.15 ml/100g H_2) [119], and were related to a supersaturation effect under non-equilibrium conditions.

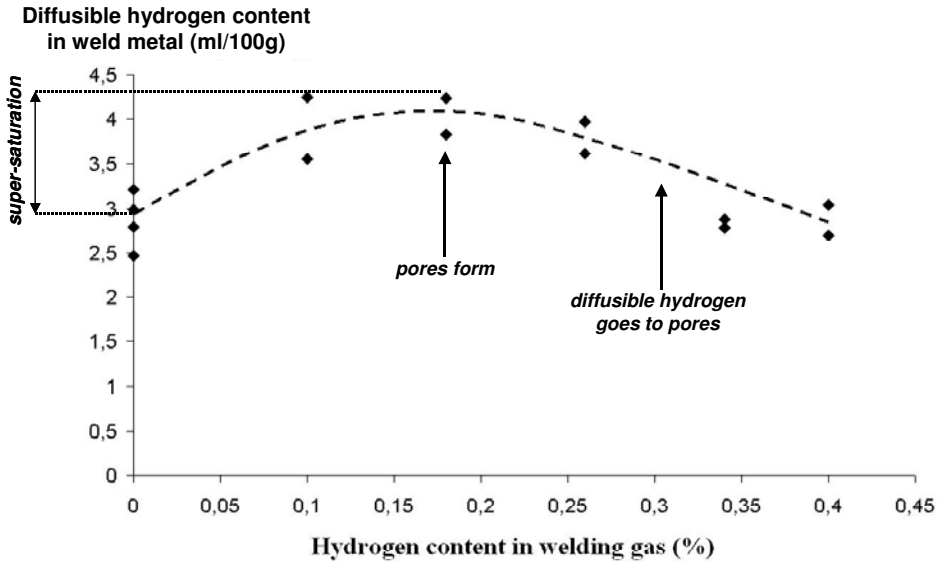

Figure 128: Diffusible Hydrogen content in Alloy 6060 weld metal versus hydrogen content in welding gas, measured using hot extraction technique at 450°C.

6.6.3 Effect of Hydrogen on Cracking Susceptibility

The effect of hydrogen on solidification cracking susceptibility is not clear, although theoretical aspects have been considered [121]. In the present work, the weldability of Alloy 6060 was characterized for various hydrogen contamination levels making use of the modified varestraint test (MVT).

6.6.3.1 Characterization of MVT porosity

Unetched cross-sections of Alloy 6060 welds performed using welding currents of 95 A (Figure 129) and 105 A (Figure 130) reveal porosity present in all welds, increasing with hydrogen content in welding gas, but decreasing for higher welding current. It is believed that higher welding current, i.e. higher heat input, resulting in lower cooling rate, ensures longer weld pool residence time and thus enabling more bubbles to float up and escape [120]. See Table 11 for detailed test parameters.

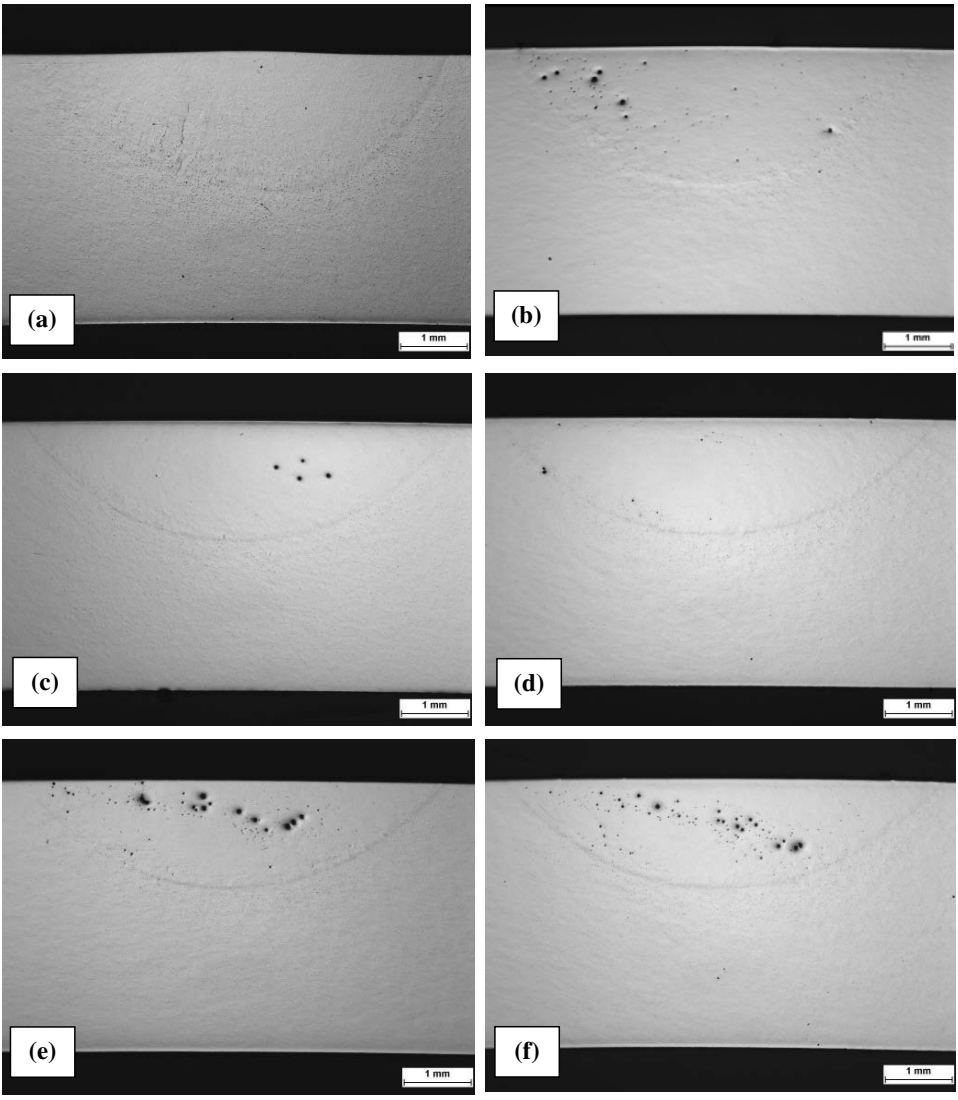

Figure 129: Weld cross-section at low magnification for hydrogen content in welding gas of (a) 0%, (b) 0.10%, (c) 0.14%, (d) 0.18%, (e) 0.22%, and (f) 0.26%. Welding current 95 A.

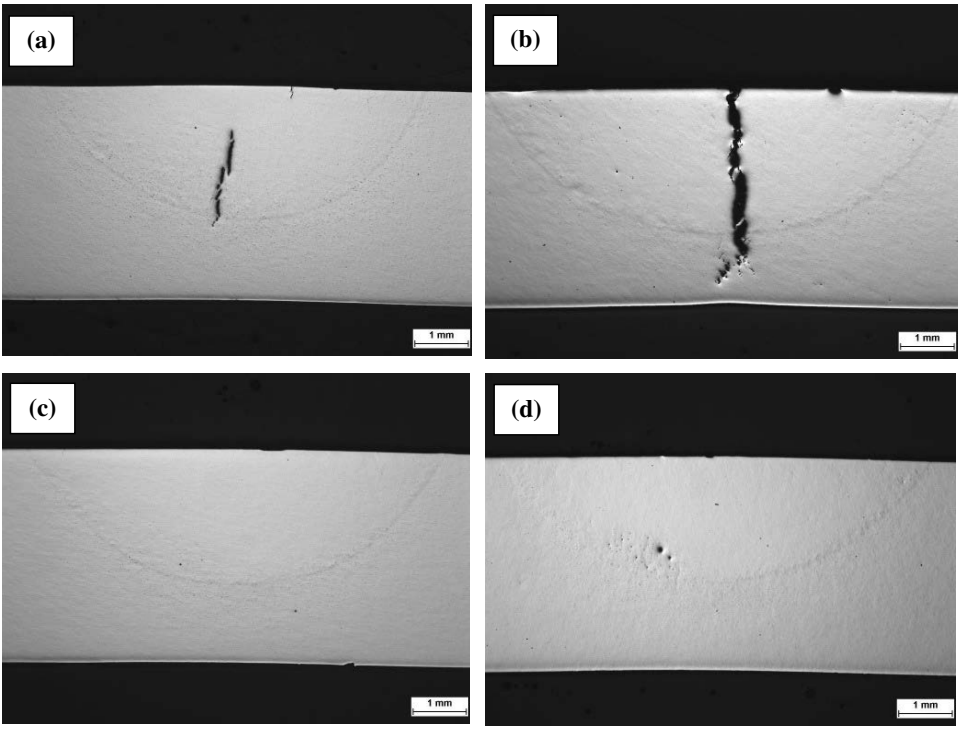

Figure 130: Weld cross-section at low magnification for hydrogen content in welding gas of (a) 0%, (b) 0.10%, (c) 0.14%, and (d) 0.18%. Welding current 105 A.

6.6.3.2 MVT Local Strain Measurement

The modified varestraint test (MVT) has been conventionally used at fixed ram speed followed by a ranking of the alloys based upon total crack length measurement at a given applied strain [152]. However, this test is used here in a manner similar to the slow bending trans-varestraint test [12,67], where the local strain rate in the vicinity of the mushy zone is varied by systematically varying the globally applied strain rate (i.e. ram speed) which allows a critical strain rate (i.e. critical ram speed) to be determined.

With the aid of a strain gage attached to the surface at specimen mid-length, strains on a coupon were measured during a MVT test performed cold (i.e. without welding) for a mandrel with a radius of 250 mm at different ram speeds. Under these conditions, the maximum measured strain, i.e. when the test coupon is against the mandrel, varied between 0.80 and 0.97 %, with an average value of 0.91 %. The theoretical calculation (recall Eq. 34) predicts a local strain of 0.80 %, in agreement with experimental measurements. Local strain measurements also reveal that a constant ram speed (set prior to the test) promotes a non-linear increase of the strain in the weld coupon, i.e. non constant strain rate during the

MVT test. For example, application of a 0.08 mm/s constant ram speed results in a variable strain rate, first increasing up to 0.22 %/s at 0.7% strain and then decreasing to 0 %/s at saturation, i.e. when the test coupon is against the mandrel (Figure 131). This result is in contradiction with observations of Arata et al. [12] who found a linear increase of strain at constant ram speed using the indentation recording film technique on the slow bending trans-varestraint test.

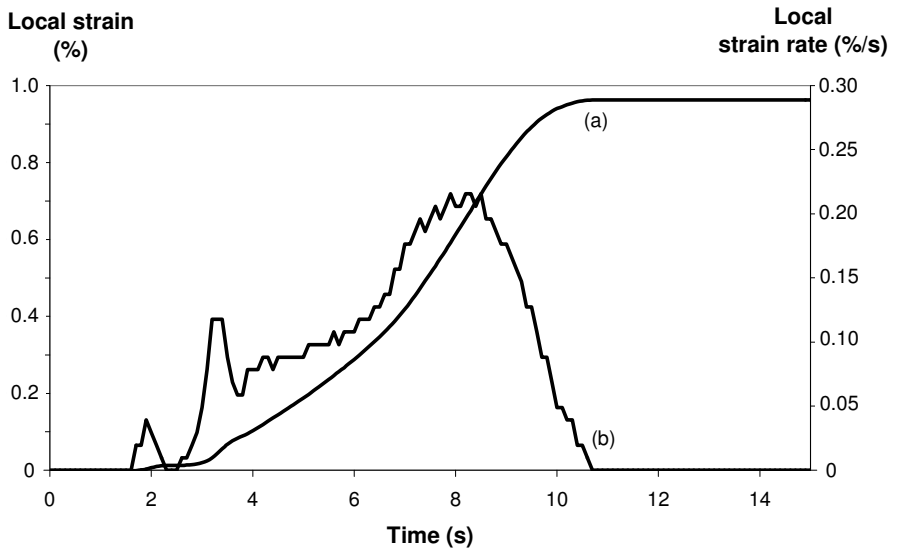

Figure 131: (a) Strain and (b) strain rate measured with strain gage along centerline of a coupon during a MVT test performed cold (i.e. without welding) at a 0.08 mm/s applied ram speed.

For ram speeds between 0.05 and 0.10 mm/s, the maximum local strain rate varied from 0.12 to 0.25 %/s (Figure 132), on the same order of magnitude as previous results (recall Table 14). Solidification cracks were found to form beyond the point where strain was first applied, and then grow continuously until the end of ram speed application. Cracks initiated sooner for those tests run at higher ram speeds, i.e. higher strain rates. Since solidification crack formation depends upon exceeding a critical local strain rate (recall Figure 75b), the ramping up of local strain rates with time in the MVT test could explain the non-instantaneous formation of cracking with bending application.

The non-constant strain rate at constant ram speed makes it difficult to measure a true critical strain rate needed for cracking. Nevertheless, MVT tests were performed at variable hydrogen contents to look for possible effects as discussed in the next section. An attempt was also made to use the MVT in a more traditional manner, i.e. as a trans-varestraint test

with “instantaneous” bending [148]. The MVT reaches a maximum ram speed of 6.1 mm/s, which results in a maximum local strain rate of 5.7 %/s with a 0.80 % strain applied in approximately 300 ms. According to in-situ observations of Robino et al. [27] detailed in the paragraph 2.1.5.2.2, a local strain rate of 5.7 %/s is too slow to relate crack length to any significant temperature characterizing solidification cracking susceptibility (i.e. brittle temperature range). Therefore, the MVT was not used in this “instantaneous bending” configuration.

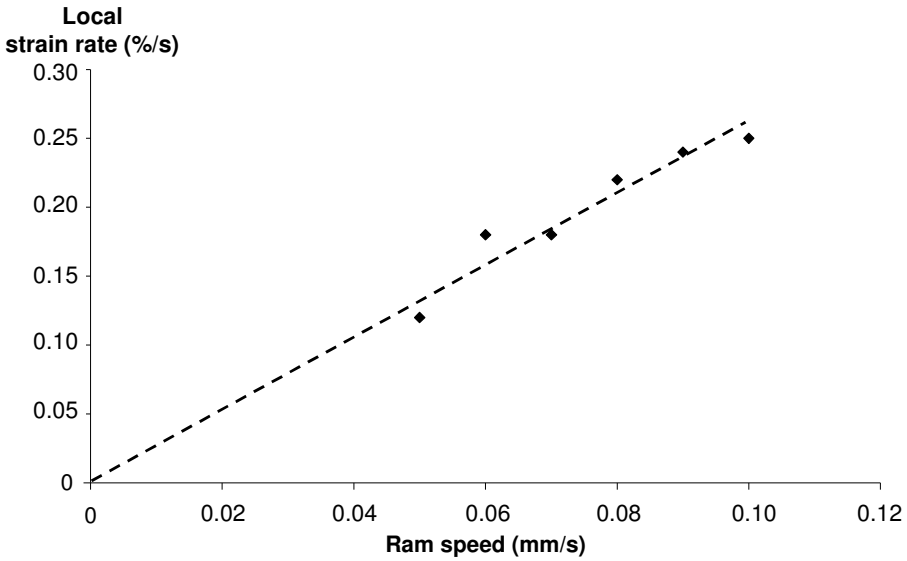

Figure 132: Maximum local strain rate versus ram speed measured with strain gage along centerline of a coupon during a MVT test performed cold (i.e. without welding).

6.6.3.3 MVT Cracking Susceptibility Evaluation

For different hydrogen content in the welding gas, the critical ram speed to form a solidification crack in Alloy 6060 autogeneous welds was investigated for welding currents of 95 A (Figure 133a) and 105 A (Figure 134a). A crack - no crack boundary, approximated with dashed line (Figures 133a and 134a), clearly shows a Λ-shape curve, with a peak in cracking susceptibility near 0.10 % H_2 in welding gas. In case of a 105 A welding current and 0.10% H_2 in welding gas (Figure 134a), the critical ram speed was set to 0 mm/s since solidification cracks formed even without bending application.

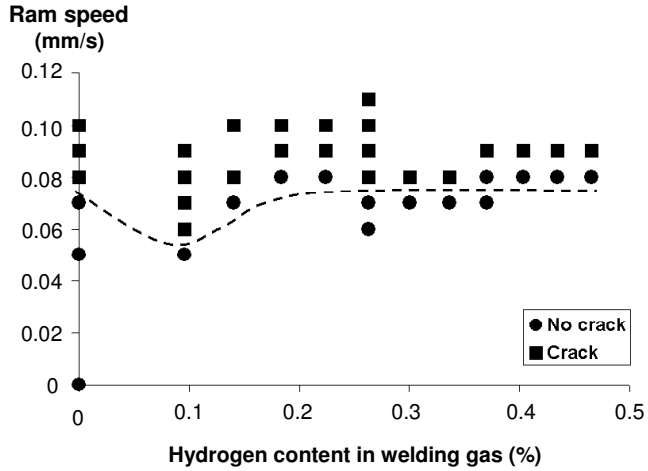

(a)

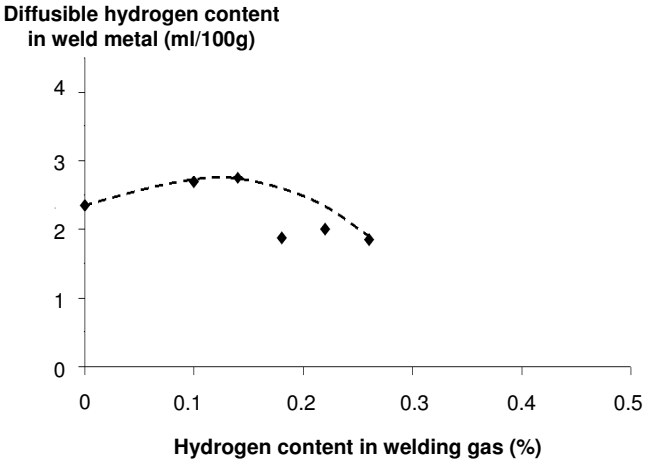

(b)

Figure 133: Alloy 6060 weld (a) critical ram speed and (b) hydrogen content versus hydrogen content in welding gas. Welding current 95 A.

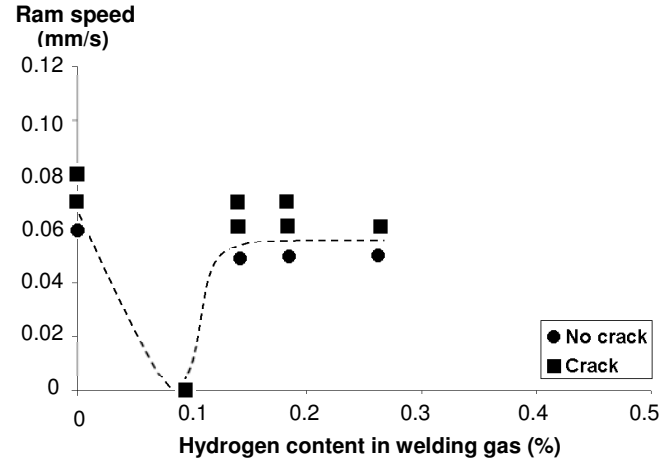

(a)

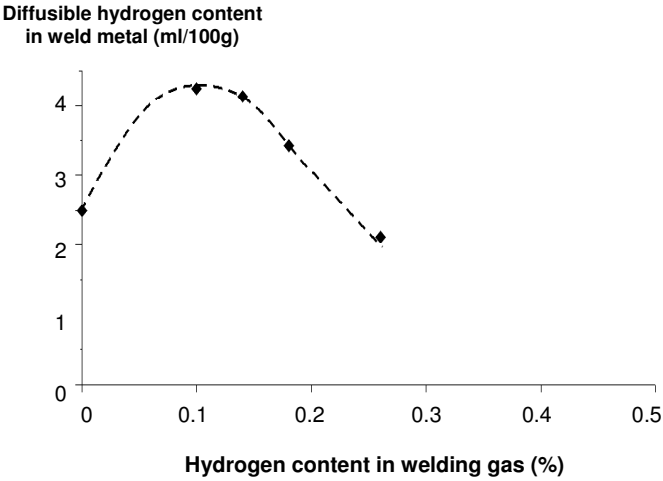

(b)

Figure 134: Alloy 6060 weld (a) critical ram speed and (b) hydrogen content versus hydrogen content in welding gas. Welding current 105 A.

As found previously (recall Figure 128), a Λ-shape curve is revealed when plotting hydrogen amount in weld metal versus hydrogen in welding gas (Figures 133b and 134b), with hydrogen amount in weld metal once again exceeding the solubility limit (up to 4.2 ml/100g H_2), similar to hydrogen contents measured previously (recall Figure 128). According to the proposed mass-balance based crack growth model (recall paragraph 6.4), hydrogen should have no effect on crack growth. The results of the MVT tests support this

model, with a critical ram speed for cracking almost constant, e.g. 0.07 and 0.06 mm/s for 95 and 105 A, respectively.

However, a drop in weldability is observed at the highest diffusible hydrogen content in weld metal (Figures 133 and 134). For this given condition, this may possibly be related to a different solidification cracking mechanism involving cavitation at the hydrogen peak saturation. Vapor pores nucleation, i.e. cavitation, is likely promoted at a rate high enough to support crack growth.

6.6.3.4 Suggestions Regarding Weldability Improvement

The results presented in Figures 133 and 134 combined with the solidification cracking models proposed in this work suggest a new approach for improving the weldability of Alloy 6060 in particular, and aluminum welds in general. The traditional approach to improve weldability consists of adding alloying elements through filler wire that shifts the critical strain rate to a higher value, the mass-balance crack growth model (recall paragraph 6.2) and the CTW test results (recall Figure 75b) suggesting a strain rate dependence for solidification crack growth. However, the porosity-based crack initiation model (recall paragraph 6.1) and the MVT test results (recall Figures 133 and 134) has demonstrated a connection between Alloy 6060 weldability and weld pool hydrogen contamination hydrogen. Therefore, addition of freon, chlorine, or fluorine to the shielding gas, which are known to be effective in reducing hydrogen (freon, chlorine, fluorine) and oxides (fluorine), and hence to result in sound aluminum alloy castings [104] and welds [120,198], should be efficient in improving aluminum alloy weldability, even if great care should be taken when using such toxic elements.

From a contamination standpoint, the control and minimization of hydrogen in plate, filler wire, and welding process (e.g. shielding gas and joint preparation) may provide an opportunity to improve the weldability of aluminum alloys. There is typically a large variation in hydrogen content from one heat of material to another (recall Figure 126) that may explain inconsistencies in weldability behavior (e.g. Figure 76). More efficient removal of oxide films with filters during ingot production could likewise improve weldability and consistency. The weldability improvement at lower dissolved gases content may possibly be generalized to any ferrous or non-ferrous alloy.

7 Conclusion

The objective of the present work was to characterize the effect of 4043 filler dilution on Alloy 6060 weldability, and examine the mechanisms involved for solidification crack initiation and growth in aluminum welds. With the aid of the CTW test and the new critical strain rate – dilution mapping concept, a crack – no crack boundary has been determined revealing that higher local strain rates require higher filler dilutions to avoid cracking. Increasing filler dilution results in grain refinement, concave bead shape, reduced solidification shrinkage, higher interdendritic liquid quantity, and reduced temperature gradient. However, it does not affect weld solidification temperature range.

Three comprehensive models have been developed that characterize the underlying mechanisms involved in solidification cracking. A porosity-based crack initiation model has been proposed that links cracking to the formation of a micropore within the coherent interdendritic region. Pores are assumed to form from pre-existing pore nuclei, controlled primarily by hydrogen content and surface tension. Following crack initiation, a mass-balance controlled crack growth model has been proposed that gives the critical transverse strain rate needed to sustain growth at the welding speed. With the aid of a strain partition model, the critical local strain rate measured in the CTW test has been related to the critical grain boundary strain rate needed for crack growth. Measured and predicted critical strain rate to form cracking are on the same order of magnitude. However, due to a longer mushy zone at high filler dilution, the model predicts a reduced Alloy 6060 weldability at higher 4043 filler dilution, counter to observed behavior. This discrepancy is believed to come from the grain boundary morphology not taken into account and from inaccuracies in solid fraction – temperature curves.

With the aid of the modified varestraint test (MVT) and a controlled hydrogen contamination system, results revealed that hydrogen has little effect on crack growth, providing support to the proposed cracking models. However, a drop in weldability corresponding to the peak in weld metal hydrogen supersaturation suggests, for this given condition, a different solidification cracking mechanism, where cavitation supports crack growth.

From a mechanical standpoint, local strain rates are difficult to measure and control, and are related to specific thermal, material, and restraining conditions. Critical strain rate, however, represents a unique measure of a material's weldability. The accurate prediction of critical strain rate, through modeling, will permit the useful assessment of weldability. But

this requires a more detailed understanding of grain boundary coherency and segregation than is currently available.

Based upon this work, a new approach has been proposed to improve aluminum alloy weldability. Reducing weld pool hydrogen and oxide content is believed to improve the alloy´s weldability by hindering initiation of solidification cracks. This could be achieved by adding oxide reducing elements (e.g. F_2) to the shielding gas, by using higher quality filler and base metal, and by using extra care in weld joint preparation to minimize contamination.

8 Future Work

Based upon results from the present thesis, the following topics are provided as a framework for future research studies to expand our understanding of cracking behavior.

The newly developed CTW test and critical strain rate – dilution maps have been shown effective in evaluating critical conditions for solidification crack formation, and in enabling comparison between predictions and measurements. Using this map, a weld procedure (including filler dilution) can be developed based upon local strain rate measurements. Such measurements could conceivably be made during welding using a sensor attached to the torch, where a laser scans across the mushy zone. Although the data from this study is limited to the Al 6060-4043 alloy system, a similar type of map could be generated for any ferrous or non-ferrous alloy, and also possibly to other welding processes. Clearly, however, better ways to characterize local weld pool strain and strain rate are needed.

The proposed models also need development, especially a three-dimensional approach to better take into account the grain structure. Moreover, the ability to accurately predict the onset of cracking from a theoretical standpoint requires the knowledge of material information that is lacking to date, including surface tension, hydrogen solubility, and hydrogen partition coefficient. Also needed is the modeling of grain boundary segregation, where presently the concentration of segregates at weld metal grain boundaries is not well understood or quantified. Indeed, while models for cracking so far have considered idealistic interdendritic conditions for reasons of simplicity, it is clear that intergranular conditions are more appropriate. Furthermore, the solidification path of an alloy, and its corresponding solid fraction versus temperature curve, is an important input to the solidification cracking models. It is of particular interest to better understand the effect of cooling rate on phase formation, especially for weld solidification crack prediction, since cooling rate changes significantly the constituent phase distribution in addition to the finer dendrite spacing and grain structure.

However, the most important future investigations suggested by the present work regards the relationship between hydrogen content and solidification cracking. Indeed, according to the proposed solidification cracking models, eliminating dissolved hydrogen in weld metal should avoid the formation of a micropore, i.e. crack initiation source, regardless of the mechanism for hydrogen pore formation. Moreover, experimental results suggest that cavitation may support crack growth at the hydrogen peak saturation in weld metal. Further research should also be initiated on two major themes: defining a threshold hydrogen content for manufacturers, and developing “getters” of hydrogen to reduce its content in the weld

pool. Regarding the second point, this may be accomplished by looking for hybrid former elements or by eliminating hydrogen during the welding process (e.g. fluorine addition to welding gas). Moreover, the idea that a solidification crack cannot initiate without dissolved gases should also be extended to other metal and gas systems.

References

[1] J.H. Dudas and F.R. Collins (1966). Preventing Weld Cracks in High-Strength Aluminum Alloys. *Welding Journal* **45 (6)**: 241s-249s.

[2] P. Cavaliere and F. Panella (2008). Effect of Tool Position on the Fatigue Properties of Dissimilar 2024-7075 Sheets Joined by Friction Stir Welding. *Journal of Materials Processing Technology*. In press.

[3] J.A. Liptak and F.R. Baysinger (1968). Welding Dissimular Aluminum Alloys. *Welding Journal* **47 (4)**: 173s-180s.

[4] M.G. Mousavi, C.E. Cross, Ø. Grong, and M. Hval (1997). Controlling Weld Metal Dilution for Optimized Weld Performance in Aluminum. *Sci. Tech. Weld. Joining* **2 (6)**: 275-278.

[5] M.G. Mousavi, C.E. Cross, and Ø. Grong (1999). Effect of Scandium and Titanium-Boron on Grain Refinement and Hot Cracking of Aluminum Alloy 7108. *Sci. Tech. Weld. Joining* **4 (6)**: 381-388.

[6] P.H. Jennings, A.R.E. Singer, and W.I. Pumphrey (1948). Hot-Shortness of some High-Purity Alloys in the Systems Aluminum-Copper-Silicon and Aluminum-Magnesium-Silicon. *J. Inst. Metals* **74**: 227-248.

[7] B. Chalmers (1964). *Principles of Solidification*. John Wiley.

[8] J.D. Dowd (1952). Weld Cracking of Aluminum Alloys. *Welding Journal* **31(10)**: 448s-456s.

[9] A.R.E. Singer and P.H. Jennings (1947). Hot-Shortness of some Aluminum-Iron-Silicon Alloys of High Purity. *J. Inst. of Metals* **73**: 273–284.

[10] W.I. Pumphrey and J.V. Lyons (1948). Cracking during the Casting and Welding of the More Common Binary Aluminum Alloys. *J. Inst. Metals* **74**: 439-455.

[11] J. Verö (1936). The Hot-Shortness of Aluminum Alloys. *The Metal Industry* **48**: 431-494.

[12] Y. Arata, F. Matsuda, K. Nakata, and K. Shinozaki (1977). Solidification Crack Susceptibility of Aluminum Alloy Weld Metals (Report II) - Effect of Straining Rate on Cracking Threshold in Weld Metal During Solidification. *Trans. of JWRI* **6 (1)**: 91-104.

[13] F. Matsuda (1990). Hot Crack Susceptibility of Weld Metal. In: Advances in Welding Metallurgy, Miami, FL: Am. Welding Soc. / Jap. Welding Soc. / Jap. Welding Eng. Soc.: 19-35.

[14] T. Zacharia (1994). Dynamic Stresses in Weld Metal Hot Cracking. *Welding Journal* **73 (7)**: 164s-172s.

[15] F. Matsuda, H. Nakagawa, S. Ogata, and S. Katayama (1978). Fractographic Investigation on Solidification Crack in the Varestraint Test of Fully Austenitic Stainless Steel – Studies of Fractography of Welded Zone (III). *Trans. of JWRI* **7 (1)**: 59-70.

[16] J.C. Borland (1979). Fundamentals of Solidification Cracking in Welds. *Welding and Metal Fabrication*: 99-107.

[17] Y. Arata, F. Matsuda, S. Katayama, and S. Ogata (1977). Solidification Crack Susceptibility in Welds Metals of Fully Austenitic Stainless Steels (Report III) – Effect of Strain Rate on Cracking Threshold in Weld Metal During Solidification. *Trans. of JWRI* **6 (2)**: 197-207.

[18] F. Matsuda and H. Nakagawa (1977). Some Fractographic Features of Various Weld Cracking and Fracture Surfaces with Scanning Electron Microscope - Studies on Fractography of Welded Zone (I). *Trans. of JWRI* **6 (1)**: 81-90.

[19] B. Dixon (1988). Weld Metal Solidification Cracking in Steels. IIW Asian Pacific Regional Welding Congress, Hobart, Tasmania: 731-751.

[20] Y. Arata, F. Matsuda, K. Nakata and I. Sasaki (1976). Solidification Crack Susceptibility of Aluminum Alloy Weld Metals (Report I) – Characteristics of Ductility Curves During Solidification by Means of the Trans-Varestraint Test. *Trans. of JWRI* **5 (2)**: 53-67.

[21] J.A. Brooks and J.J. Dike (1998). Modeling Weld Solidification Cracking Behavior in Aluminum Alloys - Analysis of Fracture Initiation. In: Trends in Welding Research, Proc. 5th Int. Conf. Pine Mountain, Georgia, USA: 695-699.

[22] J. Campbell (1991). *Castings.* Butterworth-Heinemann.

[23] Z. Ploshikhin, A. Prikhodovsky, A. Ilin, M. Makhutin, C. Heimerdinger, and F. Palm (2006). Influence of the Weld Metal Chemical Composition on the Solidification Cracking Susceptibility of AA6056-T4 Alloy. *Welding in the World* **50 (11/12)** Doc. IIW-1758-06 (ex-doc. IX-2220-06/IX-NF-07-06): 46-50.

[24] W.S. Pellini (1952). Strain Theory for Hot Tearing. *Foundry*, 80: 125-199.

[25] J.B. Mitchell, S.L. Cockcroft, D. Viano, C. Davidson, and D. StJohn (2007). Determination of Strain during Hot Tearing by Image Correlation. *Met. Mat. Trans.* **38A (10)**: 2503-2512.

[26] C. Davidson, D. Viano, L. Lu, and D. StJohn (2006). Observation of Crack Initiation During Hot Tearing. *International Journal of Cast Metals Research* **19 (1)**: 59-65.

[27] C.V. Robino, M. Reece, G.A. Knorovsky, J.N. DuPont, and Z. Feng (2005). Prediction of Maximum Crack Length in Longitudinal Varestraint Testing. In: Proc. 7th Int. Conf. Trends in Welding Research, ASM Int: 313-318.

[28] F. Matsuda, H. Nakagawa, and K. Sorada (1982). Dynamic Observation of Solidification and Solidification Cracking during Welding with Optical Microscope (I) - Solidification Front and Behavior of Cracking. *Trans. of JWRI* **11 (2)**: 67-77.

[29] I. Farup, J.-M. Drezet, and M. Rappaz (2001). In Situ Observation of Hot Tearing Formation in Succinonitrile-Acetone. *Acta Mater.* **49**: 1261-1269.

[30] P.-D. Grasso, J.-M. Drezet, I. Farup, and M. Rappaz (2001). Direct Observation of Hot Tear Formation in Organic Alloys. Presented at the 7th Conference on Advanced Materials and Processes, EuroMat 2001, Rimini.

[31] D.G. Eskin, W.H. Suyitno, and L. Katgerman (2004). Mechanical Properties in the Semi-Solid State and Hot tearing of Aluminum Alloys. *Progress in Materials Science* **49**: 629-711.

[32] D.G. Eskin and L. Katgerman (2007). A Quest for a New Hot Tearing Criterion. *Met. Mat. Trans.* **38A (7)**: 1511-1519.

[33] Suyitno, W.H. Kool, L. Katgerman (2005). Hot Tearing Criteria Evaluation for Direct-Chill Casting of an Al-4.5 Pct Cu Alloy. *Met. Mat. Trans.* **36A (6)**: 1537-1546.

[34] C.E Cross (2005). On the Origin of Weld Solidification Cracking. In: Hot Cracking Phenomena in Welds, Springer Pub.: 3-18.

[35] A. Norton (1914). Hot-Shortness Testing Machining for Aluminum Alloys. *Trans. ASME* **8**: 124.

[36] Archbutt, Grogan, and Jenkin (1928). Properties and Production of Aluminum Alloy Die-Castings. *J. Inst. Metals* **40**: 219.

[37] R.A. Chihoski (1972). The Character of Stress Field Around a Weld Arc Moving on Aluminum Sheet. *Welding Journal* **51 (1)**: 9s-18s.

[38] R.A. Chihoski (1979). Expansion and Stress Around Aluminum Weld Puddles. *Welding Journal* **58 (9)**: 263s-276s.

[39] Z. Feng (1994). A Computational Analysis of Thermal and Mechanical Conditions for Weld Metal Solidification Cracking. *Welding in the World* **33**: 340-347.

[40] J. Langlais and J.E. Gruzleski (2000). A Novel Approach to Assessing the Hot Tearing Susceptibility of Aluminum Alloys. *Materials Science Forum* **331-337**: 167-172.

[41] V.N. Saveiko (1961). Theory for Hot Cracking. *Russ. Cast. Prod.*: 453-456.

[42] C.H. Dickhaus, L. Ohm, and S. Engler (1994). Mechanical Properties of Solidifying Shells of Aluminum Alloys. *AFS Trans.* **101**: 677-684.

[43] D.J. Lahaie and M. Bouchard (2001). Physical Modeling of the Deformation Mechanisms of Semisolid Bodies and a Mechanical Criterion for Hot Tearing. *Met. Mat. Trans.* **32B (8)**: 697-705.

[44] H. Murakawa, H. Serizawa, M. Shibahara (2003). Prediction of Welding Hot Cracking using Temperature Dependent Interface Element. In: Mathematical Modelling of Weld Phenomena 7, Maney: 539-554.

[45] J.A. Williams and A.R.E. Singer (1968). Deformation, Strength, and Fracture Above the Solidus Temperature. *J. Inst. Metals* **96**: 5-12.

[46] F. Matsuda, K. Nakata, and S. Harada (1980). Moving Characteristics of Weld Edges During Solidification in Relation to Solidification Cracking in GTA Weld of Aluminum Alloy Thin Sheet. *Trans. of JWRI* **9 (2)**: 83-93.

[47] F. Matsuda, K. Nakata, K. Tsukamoto, and A. Kohzoh (1983). Effect of Additional Alloying Element on Weld Solidification Crack Susceptibility of Al-Zn-Mg alloy. *Trans. of JWRI* **12 (2)**: 93-102.

[48] V. Ploshikhin, A. Prikhodovsky, M. Makhutin, A. Ilin, and H.-W. Zoch (2005). Integrated Mechanical-Metallurgical Approach to Modeling of Solidification Cracking in Welds. In: Hot Cracking Phenomena in Welds, Springer: 223-244.

[49] W.I. Pumphrey and P.H. Jennings (1948). A Consideration of the Nature of Brittleness and Temperature Above the Solidus in Castings and Welds in Aluminum Alloys. *J. Inst. Metals* **75**: 235-256.

[50] C.E. Cross and D.L. Olson (1986). Hot Tearing Model to Asses Aluminum Weldability. In: Conf. Proc. Aluminum Alloys, Charlottesville: 1869-1875.

[51] J.C. Lippold (2005). Recent Developments In Weldability Testing. In: Hot Cracking Phenomena in Welds, Springer: 271-290.

[52] A.R.E Singer and S.A. Cottrell (1947). Properties of the Aluminum-Silicon Alloys at Temperatures in the Region of the Solidus. *J. Inst. of Metals* **73**: 33-54.

[53] L. Bäckerud, E. Krol, and J. Tamminen (1986). *Solidification Characteristics of Aluminum Alloys*. Vol.1. Skanaluminum, Oslo.

[54] B.I. Medovar (1954). On the Nature of Weld Hot Cracking. *Automat. Svarka* **7**: 12-28.

[55] J.C. Borland (1960). Generalized Theory of Super Solidus Cracking in Welds and Castings - an Initial Development. *Brit. Weld. J.* **7 (8)**: 508-512.

[56] F. Matsuda, H. Nakagawa, and S. Tomita (1986). Quantitative Evaluation of Solidification Brittleness of Weld Metal During Solidification by In-Situ Observation and Measurement (Report III) – Effect of Strain Rate on Minimum Ductility required for Solidification Crack Initiation in Carbon Steels, Stainless Steels, and Inconel Alloy. *Trans. of JWRI* **15 (2)**: 297-305.

[57] G.K. Sigworth (1996). Hot Tearing of Metals. *AFS Trans.* **104**: 1053-1062.

[58] W.M. van Haaften, W.H. Kool, and L. Katgerman (2002). Tensile Behaviour of Semi-Solid Industrial Aluminum Alloys AA3104 and AA5182. *Mat. Sci. Eng.* **A336**: 1-6.

[59] N.N. Prokhorov (1956). The Problem of the Strength of Metals While Solidifying During Welding. *Svar. Proiz.* **6**: 5-11.

[60] K. Nakata and F. Matsuda (1995). Evaluations of Ductility Characteristics and Cracking Susceptibility of Al Alloys during Welding. *Trans. of JWRI* **24**: 83-94.

[61] T. Senda, F. Matsuda, G. Takano, K. Watanabe, T. Kobayashi, and T. Matsuzaka (1971). Experimental Investigations on Solidification Crack Susceptibility for Weld Metals with Trans-Varestraint Test. *Trans. JWS* **2 (2)**: 141-162.

[62] F. Matsuda, H. Nakagawa, K. Nakata, H. Kohmoto, and Y. Honda (1983). Quantitative Evaluation of Solidification Brittleness of Weld Metal During Solidification by Means of In-Situ Observation and Measurement (Report I) - Development of the MISO Technique. *Trans. of JWRI* **12 (1)**: 65-72.

[63] B. Magnin, L. Katgerman, and B. Hannart (1995). Physical and Numerical Modelling of Thermal Stress Generation during DC Casting of Aluminum Alloys. In: Modeling of Casting, Welding, and Advanced Solidification Processes VII, TMS: 303-310.

[64] N.N. Prokhorov and M.P. Bochai (1958). Mechanical Properties of Aluminum Alloys in the Crystallization Temperature Range During Welding. *Svar. Proiz.* **8**: 1-6.

[65] N.N. Prokhorov (1962). The Technological Strength of Metals while Crystallizing During Welding. *Welding Production* **4**: 1-8.

[66] N.N. Prokhorov and M.N. Gavrilyuk (1971). Strain Behaviour of Metals During Solidification After Welding. *Welding Production* **13 (6)**: 8-13.

[67] Y. Arata, F. Matsuda, K. Nakata, and S. Katayama (1977). Solidification Crack Susceptibility in Weld Metals of Fully Austenitic Steels (Report II) – Effect of Ferrite, P, S, C, Si, and Mn on Ductility Properties of Solidification Brittleness. *Trans. of JWRI* **6 (1)**: 105-117.

[68] I.I. Novikov (1966). Hot Shortness of Non-Ferrous Metals and Alloys [in Russian]. Nauka, Moscow: 205.

[69] I.I. Novikov and O.E. Grushko (1995). Hot Cracking Susceptibility of Al-Cu-Li and Al-Cu-Li-Mn Alloys. *Materials Science and Technology* **11**: 926-932.

[70] F. Matsuda, H. Nakagawa, K. Nakata, and H. Okada (1979). The VDR Cracking Test for Solidification Crack Susceptibility on Weld Metals and its Application to Aluminum Alloys. *Trans. of JWRI* **8**: 85-95.

[71] H. Herold, M. Streitenberger, A. Pchennikov (2000). Prevention of Centerline Solidification Cracking During One Side Welding. IIW-Doc. IX-2000-01, II-C-220-01.

[72] H. Herold, M. Streitenberger, A. Pchennikov (2001). Modelling of the PVR Test to Examine the Origin of Different Hot Cracking Types. In: Mathematical Modelling of Weld Phenomena 5, IOM, London: 783-792.

[73] H. Herold, A. Pchennikov, and M. Streitenberger (2004). Assessment of Hot Cracking Initiation by Laboratory Test Procedures and FEM- Simulation Associated Experimental Measurements During Welding of Large Weld Components. *J. Japan Weld. Soc.* **22 (2)**: 211-217.

[74] H. Herold, A. Pchennikov, and M. Streitenberger (2005). Influence of the Deformation Rate of Different Tests on Hot Cracking Formation. In: Hot Cracking Phenomena in Welds, Springer: 328-346.

[75] H. Herold and M. Streitenberger (2007). Consideration of the Welding Process as a Thermo-Physical Mechanism to Control Weldment Cracking. In: Hot Cracking Phenomena in Welds II, Springer, 2008, in press.

[76] Y. Arata, F. Matsuda, K. Nakata, and K. Shinozaki (1977). Solidification Crack Susceptibility of Aluminum Alloy Weld Metals (Report III) - Effect of Straining Rate on Crack Length in Weld Metal. *Trans. of JWRI* **6 (2)**: 47 to 52.

[77] U. Feurer (1977). Influence of Alloy Composition and Solidification Conditions on Dendrite Arm Spacing, Feeding, and Hot Tear Properties of Aluminum Alloys. In: Proc. Int. Symp. Eng. Alloys, Delft: 131-145.

[78] M. Holt, D.L. Olson, and C.E. Cross (1992). Interfacial Tension Driven Fluid Flow Model for Hot Cracking. *Scripta Metallurgica et Materialia* **26**: 1119-1124.

[79] T.W. Clyne and G.J. Davies (1979). Comparison between Experimental Data and Theoretical Predictions relating to Dependence of Solidification Cracking on Composition. In: TMS Proc. Int. Conf. Solidification-Sheffield: 275-278.

[80] L. Katgerman (1982). A Mathematical Model for Hot Cracking of Aluminum Alloys During D.C. Casting. *Journal of Metals*: 46-49.

[81] M. Rappaz, J.-M. Drezet, and M. Gremaud (1999). A New Hot-Tearing Criterion. *Met. Mat. Trans.* **30A**: 449-455.

[82] J.-M. Drezet and M. Rappaz (2001). Prediction of Hot Tears in DC-Cast Aluminum Billets. In: Light Metals 2001, TMS, New Orleans, Louisiana: 887-893.

[83] J.-M. Drezet and D. Allehaux (2008). Application of the Rappaz Drezet Gremaud Hot Tearing Criterion to Welding of Aluminum Alloys. In: Hot Cracking Phenomena in Welds II, Springer: 19-38.

[84] W. Rindler, E. Kozeschnik, N. Enzinger, and B. Buchmayr (2002). A Modified Hot Tearing Criterion for Steels. In: Mathematical Modelling of Weld Phenomena 6, Woodhead Publishing Limited: 819-835.

[85] M. Rappaz, A. Jacot, and W.J. Boettinger (2003). Last Stage Solidification of Alloys: Theoretical Model of Dendrite-Arm and Grain Coalescence. *Met. Mat. Trans.* **34A (3)**: 467-479.

[86] S. Vernède, P. Jarry, and M. Rappaz (2006). A Granular Model of Equiaxed Mushy Zones: Formation of a Coherent Solid and Localization of Feeding. Acta Materialia **54**: 4023-4034.

[87] I. Farup and A. Mo (2000). Two-Phase Modeling of Mushy Zone Parameters Associated with Hot Tearing. *Met. Mat. Trans.* **31A (5)**: 1461-1472.

[88] M. M´Hamdi, A. Mo, and C.L. Martin (2002). Two-Phase Modeling Directed Toward Hot Tearing Formation in Aluminum Direct Chill Casting. *Met. Mat. Trans.* **33A (7)**: 2081-2093.

[89] M. M´Hamdi and A. Mo (2005). On Modelling the Interplay between Microporosity Formation and Hot Tearing in Aluminum Direct-Chill Casting. *Mat. Sci. Eng. A*: 105-108.

[90] A. Stangeland, A. Mo, M. M´Hamdi, D. Viano, and C. Davidson (2006). Thermal Strain in the Mushy Zone Related to Hot Tearing. *Met. Mat. Trans.* **37A (3)**: 705-714.

[91] M. Braccini, C.L. Martin, M. Suéry, and Y. Bréchet (2000). Relation Between the Mushy Zone Rheology and Hot Tearing Phenomena in Al-Cu Alloys. In: Modeling of Casting, Welding, and Advanced Solidification Processes IX, Shaker Verlag Aachen: 19-24.

[92] M. Braccini, C.L. Martin, M. Suéry, and Y. Bréchet (2000). Hot Tearing Phenomena in Al-Cu Alloys: Grain Refinement Effect. *Materiaux et Techniques* **5-6**: 19-24.

[93] C. Monroe and C. Beckermann (2005). Development of a Hot Tear Indicator for Steel Castings. *Mat. Sci. Eng.* **413A-414A**: 30-36.

[94] Suyitno, D.G. Eskin, and L. Katgerman (2006). Structure Observations Related to Hot Tearing of Al-Cu Billets Produced by Direct-Chill Casting. *Mat. Sci. Eng.* **420A**: 1-7.

[95] Suyitno, W.H. Kool, L. Katgerman (2002). Micro-Mechanical Model of Hot Tearing at Triple Junctions in DC Casting. *Materials Science Forum* **396-402**: 179-184.

[96] J.F. Grandfield, C.J. Davidson, and J.A. Taylor (2001). Application of a New Hot Tearing Analysis to Horizontal Direct Chill Cast Magnesium Alloy AZ91. In: Light Metals 2001, Warrendale TMS: 895-901.

[97] Suyitno, W.H. Kool, L. Katgerman (2003). Evaluation of Mechanical and Non-Mechanical Hot Tearing Criteria for DC Casting of an Aluminum Alloy. In: Light Metals 2003, Warrendale: TMS: 753-758.

[98] F.R. Kulikov et al. (1975). The Development and Prevention of Porosity in the Fusion Welding of Thick Titanium Alloys. *Svar. Proiz.* **11**: 26-31.

[99] S.F. Jones, G.M. Evans, and K.P. Galvin (1999). Bubble Nucleation from Gas Cavities – a Review. *Advances in Colloid and Interfaces Science* **80**: 27-50.

[100] D.C.F. Couzens and D.H. Trevena (1969). Critical Tension in a Liquid under Dynamic Conditions of Stressing. *Nature* **222**: 473-474.

[101] R.B. Dean (1944). The Formation of Bubbles. *J. Appl. Phys.* **15**: 446-451.

[102] J.C. Fisher (1948). The Fracture of Liquids. *J. Appl. Phys.* **19**: 1062-1067.

[103] S.N. Tiwari and J. Beech (1978). Origin of Gas Bubbles in Aluminum. *Metal Science*: 356-362.

[104] K.J. Brondyke and P.D. Hess (1964). Filtering and Fluxing Processes for Aluminum Alloys. *Trans. AIME* **230**: 1553-1556.

[105] R. Asthana (1994). An Empirical Correlation Between Contact Angles and Surface Tension in Some Ceramic-Metal Systems. *Met. Trans.* **25A (1)**: 225-230.

[106] P.S. Mohanty, F.H. Samuel, and J.E. Gruzleski (1993). Mechanism of Heterogeneous Nucleation of Pores in Metals and Alloys. *Met. Trans.* **24A (8)**: 1845-1856.

[107] T. Shinoda, H. Liu, Y. Mishima, and T. Suzuki (1991). Interfacial Compatibility in Ceramic-Fibre-Reinforced Metal Composites. *Mat. Sci. Eng.* **A146**: 91-104.

[108] T.M. Valentine (1977). On the Use of Critical Energy Techniques for the Measurement of Suface Energies of Ceramics. Part 2. The Temperature Variant Method. *Mat. Sci. Eng.* **30**: 211-218.

[109] E.L. Rooy (1992). Mechanisms of Porosity Formation in Aluminum. *Modern Casting:* 34-36.

[110] J. Campbell (1968). Pore Nucleation in Solidifying Metals. *The Solidification of Metals Iron and Steel Institute*: 18-26.

[111] C.G. Kuper and D.H. Trevena (1952). The Effect of Dissolved Gases on the Tensile Strength of Liquids. In: Proc. Of The Physical, Society of London: 46-54

[112] P.D. Lee, R.C. Atwood, R.J. Dashwood, and H. Nagaumi (2002). Modeling of Porosity Formation in Direct Chill Cast Aluminum-Magnesium Alloys. *Mat. Sci. Eng.* **A328**: 213-222.

[113] T.S. Piwonka and M.C. Flemings (1966). Pore Formation in Solidification. *Trans. Of Met. Soc. of AIME* **236**: 1157-1165.

[114] Ch. Pequet, M. Gremaud, and M. Rappaz (2002). Modeling of Microporosity, Macroporosity, and Pipe-Shrinkage Formation during the Solidification of Alloys Using a Mushy-Zone Refinement Method: Applications to Aluminum Alloys. *Met. Mat. Trans.* **33A (7)**: 2095-2106.

[115] H. Toda, T. Hidaka, K. Minami, M. Kobayashi, K. Uesugi, Y. Suzuki, and T. Kobayashi (2008). 3-D Tracking of Hydrogen Micropores during Aluminum Production Process. In: Proceedings of the 11th International Conference on Aluminum Alloys, Wiley-VCH: 575-581.

[116] D.E.J. Talbot (2004). *The Effects of Hydrogen in Aluminum and Its Alloys*. Maney Pub.

[117] Ö. Savaş and R. Kayikci (2007). Application of Taguchi´s Methods to Investigate some Factors Affecting Microporosity Formation in A360 Aluminum Alloy Casting. *Materials and Design* **28**: 2224-2228.

[118] K.R. Van Horn (1967). *Aluminum Properties, Physical Metallurgy, and Phase Diagrams, vol.1*. American Society of Metals, Ohio.

[119] R.P. Martukanitz and P.R. Michnuk (1982). Sources of Porosity in Gas Metal Arc Welding of Aluminum. *American Society of Metals*: 315-330.

[120] J.H. Devletian and W.E. Wood (1993). Factors Affecting Porosity in Aluminum Welds – a Review. *Welding Research Council Bulletin*, **Bulletin 290**, ISSN 0043-2326: 1-18.

[121] C.E. Cross, D.L. Olson, and G.R. Edwards (1993). The Role of Porosity in Initiating Weld Metal Hot Cracks. In: Int. Conf. Proc. On Modeling and Control of Joining Processes, AWS, Oak Ridge National Laboratory: 549-557.

[122] L.I. Sorokin and A.I. Golubev (1974). Quantitative Evaluation of the Influence of Alloying Elements on Porosity in the Welding of Nickel Alloys. *Avt. Svarka* **7**: 70-71.

[123] H. Fujii, H. Umakoshi, Y. Aoki, and K. Nogi (2004). Bubble Formation in Aluminum Alloy During Electron Beam Welding. *Journal of Materials Processing Technology* **155-156**: 1252-1255.

[124] G. Laslaz and P. Laty (1991). Gas Porosity and Metal Cleanliness in Aluminum Casting Alloys. *AFS Transactions* **99**: 83-90.

[125] J. Campbell (1968). The Tribonucleation of Bubbles. *Brit. J. Appl. Phys.* **1 (2)**: 1085-1088.

[126] J.W. Holl (1960). An Effect of Air Content on the Occurrence of Cavitation. *Journal of Basic Engineering*: 941-946.

[127] D.J. Lloyd (1989). The Solidification Microstructure of Particulate Reinforced Aluminum/SiC Composites. Composi*tes Science and Technology* **35**: 159-179.

[128] N.I. Kakhovskii, L.S. Zakharov, and V.N. Lipodaev (1978). The Prevention of Weld Porosity in the Welding of Austenitic Steels with High-Efficiency Electrodes. *Avt. Svarka* **8**: 9-13.

[129] Z. Sun and H.Y. Han (1992). Hot Ductility of Simulated Stainless-Steel Weld Metals. *Journal of Materials Science* **27**: 1311-1316.

[130] Z.-J. Lu, W.J. Evans, J.D. Parker, and S. Birley (1996). Simulation of Microstructure and Liquation Cracking in 7017 Aluminum Alloy. *Mat. Sci. Eng.* **A220**: 1-7.

[131] S.A. Metz and M.C. Flemings (1970). A Fundamental Study of Hot Tearing. Report of Research Project Sponsored by AFS Training and Research Institute: 1-8.

[132] A.K. Dahle and L. Arnberg (1997). Development of Strength in Solidifying Aluminum Alloys. *Acta Mater* **45 (2)**: 547-559.

[133] T.G. Nguyen, D. Favier, and M. Suery (1994). Theoretical and Experimental Study of the Isothermal Mechanical Behaviour of Alloys in the Semi-Solid State. *International Journal of Plasticity* **10 (6)**: 663-693.

[134] H. Zhang, L. Li, D. Yuan, and D. Peng (2007). Hot Deformation Behavior of the New Al-Mg-Si-Cu Aluminum Alloy During Compression at Elevated Temperatures. *Materials Characterization* **58**: 168-173.

[135] H. Heuser (2005). Value of Different Hot Cracking Tests for the Manufacturer of Filler Metals. In: Hot Cracking Phenomena in Welds, Springer: 305-327.

[136] J.C.M. Farrar (2005). Hot Cracking Tests – The Route to International Standardization. In: Hot Cracking Phenomena in Welds, Springer: 305-327.

[137] A.R.E. Singer and P.H. Jennings (1947). Hot Shortness of the Aluminum-Silicon Alloys of Commercial Purity. *J. Inst. of Metals* **73**: 197-212.

[138] F. Decultieux, P. Vicente-Hernandez, C. Levaillant (1993). Hot Tearing Test: Experiments and FEM Modelling. In: Modeling of Casting, Welding, and Advanced Solidification Processes VI, Warrendale TMS: 617-624.

[139] F.C. Hull (1959). Cast-Pin Tear Test for Susceptibility to Hot Cracking. *Welding Journal* **38 (4)**: 176s-181s.

[140] D. Warrington and D.G. McCartney (1989). Development of a New Hot-Cracking Test for Aluminum Alloys. *Cast Metals* **2 (3)**: 134-143.

[141] J.C. Borland and J.H. Rogerson (1962). Examination of the Patch Test for Assessing Hot Cracking Tendencies of Weld Metal. *Brit. Weld. J.* **9** : 464-498.

[142] T.W. Nelson, J.C. Lippold, W. Lin, and W.A. Baeslack III (1997). Evaluation of the Circular Patch Test for Assessing Weld Solidification Cracking, Part I - Development of a Test Method. *Welding Journal* **76 (3)**: 110s-119s.

[143] R.D. Stout, S.S. Tor, L.J. McGeady, and G.E. Doan (1946). Quantitative Measurement of Cracking Tendency in Welds. *Welding Journal* **25 (9)**: 522s-532s.

[144] P.T. Houldcroft (1955). A Simple Cracking Test for Use with Argon-Arc Welding. *British Welding Journal* **2**: 471-475.

[145] F. Matsuda and K. Nakata (1982). A New Test Specimen for Self-Restraint Solidification Crack Susceptibility Test of Electron-Beam Welding Bead - Fan Shaped Cracking Test. *Trans. of JWRI* **11 (2)**: 87-94.

[146] P.W. Jones (1957). A Summary of Recent Work on the Murex Hot Cracking Test. *British Welding Journal* **4**: 189-197.

[147] W.F. Savage and C.D. Lundin (1965). The Varestraint Test. *Welding Journal* **44 (10)**: 433s-442s.

[148] N. Bailey and G.R. Regelous (1976). Recent Developments in Transvarestraint Testing. *Weld. Inst. Res. Bul.*: 201-204.

[149] F. Matsuda, K. Nakagawa, H. Kohmoto, Y. Honda, and Y. Matsubara (1983). Quantitative Evaluation of Solidification Brittleness of Weld Metal During Solidification by In-Situ Observation and Measurement (Report II) – Solidification Ductility Curves for Steels with the MISO Technique. *Trans. of JWRI* **12 (1)**: 73-80.

[150] H. Tamura, N. Kato, S. Ochiai, and Y. Katagiri (1977). Cracking Study of Aluminum Alloys by the Variable Tensile Strain Hot Cracking Test. *Trans. JWS* **8 (2)**: 16-22.

[151] K. Wilken and H. Kleistner (1982). The MVT-Test - A New Universal Procedure for Testing the Hot Cracking Sensitivity During Welding (in German). *Material und Technik* **1**: 3-10.

[152] T. Kannengiesser, M. Wolf, and H. Schobbert (2005). Recent Developments in Nickel Base Material Shielding Gas on the Hot Cracking Resistance. *Stainless Steel World* **7**: 20-29.

[153] P.W. Turner and C.D. Lundin (1970). Effect of Iron on the Hot Cracking of Uranium Weld Metal – Part 1. *Welding Journal* **49 (12)**: 579s-587s.

[154] H. Schobbert, Th. Böllinghaus, and M. Wolf (2003). Hot Cracking Resistance of Laser and Hybrid Welded Austenitic Stainless Steels. In: Trends in Welding Research, ASM: 76-81.

[155] C.E. Cross and Th. Böllinghaus (2006). The Effect of Restraint on Weld Solidification Cracking in Aluminum. *Welding in the World* **50**: 51-54.

[156] G.M. Goodwin (1987). Development of a New Hot-Cracking Test: the Sigmajig. *Welding Journal* **66 (2)**: 33s-38s.

[157] K. Nishimoto and H. Mori (2004). Hot Cracking Susceptibility in Laser Weld Metal of High Nitrogen Stainless Steels. *Sci. Tech. Adv. Mat.* **5**: 231-240.

[158] Th. Kannengiesser, T. McInerney, W. Florian, Th. Böllinghaus, C.E. Cross (2002). The Influence of Local Weld Deformation on Hot Cracking Susceptibility. In: Mathematical Modeling of Weld Phenomena 6, Maney: 803-817.

[159] L. Johnson (1973). Formation of Plastic Strains during Welding of Aluminum Alloys. *Welding Journal* **52 (7)**: 298s-305s.

[160] L. Johnson (1974). Moire Techniques for Measuring Strains During Welding. *Exp. Mech.* **14**: 145-150.

[161] W.H. Peters and W.F. Ranson (1982). Digital Imaging Techniques in Experimental Stress Analysis. *Optical Engineering* **21 (3)**: 427-432.

[162] M.A. Sutton, W.J. Wolters, W.H. Peters, W.F. Ranson, and S.R. McNeil (1983). Determination of Displacements Using an Improved Digital Correlation Method. *Image and Vision Computing* **1 (3)**: 133-139.

[163] L.F. Mondolfo (1976). *Aluminum Alloys-Structure & Properties*. Butterworths.

[164] A.G.C. Gwyer and H.W.L. Phillips (1928). The Constitution of Alloys of Aluminum with Silicon and Iron. *J. Inst. Metals* **40**: 297-358.

[165] The Aluminum Association (2006). International Alloy Designations and Chemical Composition Limits for Wrought Aluminum and Wrought Aluminum Alloys.

[166] N.A. Belov, A.A. Aksenov, and D.G. Eskin (2002). *Iron in Aluminum Alloys*. Taylor and Francis, London.

[167] T.O. Mbuya, B.O. Odera, and S.P. Ng'ang'a (2003). Influence of Iron on Castability and Properties of Aluminum Silicon Alloys: Literature Review. *International Journal of Cast Metals Research* **16 (5)**: 451-465.

[168] L. Wang, M. Makhlouf, and D. Apelian (1995). Aluminum Die Casting Alloys: Alloy Composition, Microstructure, and Properties-Performance Relationships. *International Materials Reviews* **40 (6)**: 221-238.

[169] L. Bäckerud, E. Krol, and J. Tamminen (1986). *Solidification Characteristics of Aluminum Alloys*. Vol.2. Skanaluminum, Oslo.

[170] L. Bäckerud, E. Krol, and J. Tamminen (1986). *Solidification Characteristics of Aluminum Alloys*. Vol.3. Skanaluminum, Oslo.

[171] P. Skjerpe (1987). Intermetallic Phases Formed during DC-Casting of an Al-0.25 Wt Pct Fe-0.13 Wt Pct Si Alloy. *Met. Trans.* **18A**: 189-200.

[172] H. Westengen (1982). Formation of Intermetallic Compounds During DC Casting of a Commercial Purity Al-Fe-Si Alloy. *Z. Metallkde.* **73**: 360-368.

[173] W. Khalifa, F.H. Samuel, and J.E. Gruzleski (2003). Iron Intermetallic Phases in the Al Corner of the Al-Fe-Si System. *Met. Mat. Trans.* **34A (3)**: 807-825.

[174] P.N. Crepeau (1995). Effect of Iron in Al-Si Casting Alloys. *AFS Trans.* **103**: 361-366.

[175] T. Magnusson and L. Arnberg (2001). Density and Solidification Shrinkage of Hypoeutectic Aluminum-Silicon Alloys. *Met. Mat. Trans.* **32A (10)**: 2605-2613.

[176] L.A. Tarshis, J.L. Walker, and J.W. Rutter (1971). Experiments on the Solidification Structure of Alloy Castings. *Met. Trans.* 2: 2589-2597.

[177] L. Lu and A.K. Dahle (2005). Iron-Rich Intermetallic Phases and their Role in Casting Defect Formation in Hypoeutectic Al-Si Alloys. *Met. Mat. Trans.* **36A (3)**: 819-835.

[178] M.J. Dvornak, R.H. Frost, and D.L. Olson (1989). The Weldability and Grain Refinement of Al-2.2Li-2.7Cu. *Welding Journal* **68 (8)**: 327s-337s.

[179] M.M. Guzowski, G.K. Sigworth, and D.A. Sentner (1987). The Role of Boron in the Grain Refinement of Aluminum with Titanium. *Met. Trans.* **18A**: 603-619.

[180] E. Cicala, G. Duffet, H. Andrzejewski, D. Grevey, S. Ignat (2005). Hot Cracking in Al-Mg-Si Alloy Laser Welding - Operating Parameters and their Effects. *Mat. Sci. Eng.* **395A**: 1-9.

[181] O. Hunziker, D. Dye, S.M. Roberts, and R.C. Reed (2005). A Coupled Approach for the Prediction of Solidification Cracking During the Welding of Superalloys. In: Hot Cracking Phenomena in Welds, Springer: 299-319.

[182] M. Shibahara, H. Serizawa, and M. Murakawa (2005). Finite Element Method for Hot Cracking Analysis Using Temperature Dependent Interface Element. In: Hot Cracking Phenomena in Welds, Springer: 253-267.

[183] W.F. Savage and A.H. Aronson (1966). Preferred Orientation in the Weld Fusion Zone. *Welding Journal* **45**: 85s-89s.

[184] C.D. Lundin and C.P.D. Chou(1983). Hot Cracking Susceptibility in Austenitic Stainless Steel Weld Metals. *Welding Research Council Bulletin 289*.

[185] B.T. Alexandrov and J.C. Lippold (2005). Relationship Between the Solidification Temperature Range and Weld Solidification Cracking Susceptibility of Stainless Steels and Ni-base Alloys. IIW Doc.IX-2163-05.

[186] B.T. Alexandrov and J.C. Lippold (2006). A New Methodology for Studying Phase Transformations in High Strength Steel Weld Metal. In: Proc 7th Int Conf Trends in Welding Research, ASM Int: 975-980.

[187] W.O. Blodgett (1966). *Design of Welded Structures*. The James F. Lincoln Arc Welding Foundation.

[188] H. Hanemann and A. Schrader (1941). *Atlas Metallographicus, 3*.

[189] T. Senda, F. Matsuda, and G. Takano (1973). Studies on Solidification Crack Susceptibility for Weld Metals with Trans-Varestraint Test. *J. Japan Weld. Soc*. **42**: 48-56.

[190] J.J. Dike, J.A. Brooks, and M. Li (1998). Comparison of Failure Criteria in Weld Solidification Cracking Simulations. In: Mathematical Modeling of Weld Phenomena 4, IOM, London: 199-222.

[191] S. Ganesan, C.L. Chan, and D.R. Poirier (1992). Permeability for Flow Parallel to Primary Dendrite Arms. *Mat. Sci. Eng.* **A151**: 97-105.

[192] R.A. Woods (1974). Porosity and Hydrogen Absorption in Aluminum Welds. *Welding Journal* **53 (3)**: 97s-108s

[193] J.P. Anson, R.A.L. Drew, and J.E. Gruzleski (1999). The Surface Tension of Molten Aluminum and Al-Mg-Si Alloy under Vacuum and Hydrogen Atmospheres. *Met. Mat. Trans.* **30B**: 1027-1032.

[194] G.K. Sigworth and C. Wang (1993). Mechanisms of Porosity Formation During Solidification: A Theoretical Analysis. *Met. Trans.* **24B (4)**: 349-364.

[195] M. Onsøien, R. Peters, D.L. Olson, and S. Liu (1995). Effect of Hydrogen in an Argon GTAW Shielding Gas: Arc Characteristics and Bead Morphology. *Welding Journal* **74 (1)**: 10s-15s.

[196] R.F. Ashton, R.P. Wesley, and C.R. Dixon (1975). The Effect of Porosity on 5086-H116 Aluminum Alloy Welds. *Welding Journal* **54 (3)**: 95s-98s.

[197] G. Huismann, F. Wittemann, T. Behrendt, and H. Krüger (2004). Determining Pore Formation in Aluminum Welding by Hydrogen Analysis. Commision IX Nonferrous, June 2004: 1-11.

[198] M.B. Kasen and A.R. Pfluger (1958). Chlorine Additions for High-Quality Inert-Gas Metal-Arc Welding of Aluminum Alloys. *Welding Journal* **37 (6)**: 269s-276s.

[199] T.J. Linert and J.C. Lippold (2003). Improved Weldability Diagram for Pulsed Laser Welded Austenitic Stainless Steels. *Sci. Tech. Weld. Joining* **8**: 1-9.

[200] J.C. Lippold (1994). Solidification Behaviour and Cracking Susceptibility of Pulsed-Laser Welds in Austenitic Stainless Steels. *Welding Journal* **73**: 129s-139s.

[201] T.W. Juhl and O.O. Flemming (2003). Assessment of Hot Crack Properties of Laser Welded Stainless Steel Alloys. In: Proc. 1st Int. Symp. High-Power Laser Macroprocessing: 224-229.

[202] J.C. Lippold and D.J. Kotecki (2005). *Welding Metallurgy and Weldability of Stainless Steels*. Wiley Pub.

[203] J.A. Brooks, A.W. Thompson, and J.C. Williams (1984). A Fundamental Study of the Beneficial Effects of Delta Ferrite in Reducing Weld Cracking. *Welding Journal* **63**: 71s-83s.

[204] F.C. Hull (1967). Effect of Delta Ferrite on the Hot Cracking of Stainless Steel. *Welding Journal* **49**: 399s-409s.

[205] J.W. Elmer, S.M. Allen, and T.W. Eagar (1990). The Influence of Cooling Rate on the Ferrite Content of Stainless Steel Alloys. In: Recent Trends in Welding Science and Technology, ASM: 165-170.

[206] W. Kurz and R. Trivedi (1995). Modern Solidification Theory Applied to Welding. In: Trends in Welding Research, ASM, 1995: 115-120.

[207] D. Kosecki and T.A. Siewert (1992). WRC-1992 Constitution Diagram for Stainless Steel Weld Metals- a Modification to the WRC-1988 Diagram. *Welding Journal* **71 (5)**: 171s-178s.

[208] Ö. Hammar and U. Svensson (1979). Influence of Steel Composition on Segregation and Microstructure During Solidification of Austenitic Stainless Steels. In: Solidification and Casting of Metals, The Metals Society: 401-410.

Appendix: Application CTW to Stainless Steel Laser Welds

Unknown is the potential of the CTW test to characterize weldability in other materials and welding processes. Of particular interest is the application of the CTW test to laser welds. Also of great interest is a quantification of the weldability of new lean (low Ni, high Mn) stainless steels. Thus, modifications in CTW test procedure were done in this preliminary study to evaluate the solidification cracking susceptibility of stainless steel laser welds. A test procedure was specifically developed for CO_2 laser, through-thickness keyhole welds made on 3 mm thick plate for a variety of austenitic and duplex stainless steel alloys. Details of this test procedure and its limitations are outlined here and results from this preliminary study are presented. A ranking of the CTW laser weldability for these stainless alloys is made and compared with expected behavior based upon available literature.

Background

The formation of centerline solidification cracks can sometimes prove troublesome when laser welding certain crack sensitive stainless steel alloys. It would be beneficial, for purposes of alloy selection and process development, if a reliable testing method could be used to rank different stainless alloys as to their relative laser weldability. Also of interest is to quantify critical cracking conditions for purposes of mechanistic modeling. The use of standard weldability test methods and crack evaluations for arc welding are not always suitable for laser welding.

With the availability of new high power (20 kW) fiber lasers, there is a trend toward the use of higher travel speeds (20-50 mm/s). This results in high solidification rates and temperature gradients that produce unique differences in grain structure, solidification mode, segregation, and weldability. From a metallurgical standpoint, alloy rankings based upon arc welds do not necessarily reflect accurately upon laser weldability. One case in point is the possibility for favoring primary austenite solidification when laser welding, thereby lowering weldability. Keyhole instability is another factor that may influence cracking susceptibility.

Similarly, the local strain distribution around rapid moving laser welds is expected to react differently to global restraining forces. It follows, therefore, that a weldability test is needed that is compatible with the laser welding process and conditions. Only a limited number of laser weldability studies have been made to date [154,157,199-201].

Laser Weldability Testing. Laser weldability testing to date has been largely limited to evaluating bead-on-plate welds made under controlled conditions. This has proven useful in providing comparisons of alloys based simply upon crack-no crack observations [199,200]. They have demonstrated an extension in primary austenite solidification (and associated cracking susceptibility) to higher Cr/Ni ratios for laser welding.

A few researchers have either developed or adapted weldability tests specifically for laser welding. Schobbert et al. [154], using a special test based upon the varestraint test concept [147], compared two different austenitic stainless steel alloys (alloys 309 and 304), establishing critical deformation rates needed to form cracks. The 309, with its lower Cr/Ni equivalent ratio, was found to solidify as primary austenite at high travel speeds. Consequently, the critical deformation rate to form cracking was found to be less than for 304, which consistently solidified as primary ferrite. Nishimoto and Mori [157], using the preloading tensile strain (PLTS) test based upon the Sigmajig test concept [156], investigated the weldability of CO_2 laser welded 304 stainless steel with variable nitrogen content. It was convincingly shown that the upper Cr/Ni equivalent ratio boundary for primary austenite solidification increases with dendrite growth velocity (i.e. weld travel speed).

Weldability of Stainless Steels. The weldability of stainless steels, examined in terms of susceptibility to solidification cracking in the weld metal, has been shown to be predominantly controlled by alloy composition and impurity content [202]. The primary solidification mode is known to have a predominant effect on weldability. Alloys that solidify as primary austenite, corresponding to equivalent Cr/Ni ratios less than 1.48 for arc welds, are most susceptible to cracking. The well-defined, straight and continuous nature of the grain boundaries associated with this mode of solidification is believed responsible for its high cracking susceptibility [203].

For alloys with Cr/Ni equivalent ratios higher than 1.48, where primary solidification occurs as ferrite and, in addition, austenite forms as a peritectic-eutectic, the resistance to cracking is exceptional. For these alloys, weld metal grain boundaries are irregular and ill-defined [203]. Also, it has been argued, impurity liquid films do not wet austenite as well as ferrite [204]. However, for alloys still higher in Cr/Ni ratio which solidify completely as ferrite, susceptibility to cracking increases. The nature of grain boundaries reverts back to being straight and continuous, and wettability improves in the absence of austenite.

In the case of laser beam welds, there is a complicating factor affecting weldability ratings established for arc welds. Under solidification conditions characteristic of beam welding, e.g. high temperature gradient and (in some cases) high growth rate, there is higher undercooling experienced at the solidification front favoring austenite [205,206]. This has the

general effect of shifting the upper Cr/Ni ratio limit for primary austenite solidification to higher values [200]. Also, there is observed the possibility to have both modes of solidification (primary austenite and primary ferrite) occur intermixed within the weld metal.

Material

A variety of different types of austenitic and duplex stainless steels have been investigated in this study as listed in Table 35. Alloys are grouped in this table as super-austenitic (310, 904L, 254 SMO), austenitic (304L, 301L, 201L, 316L, 321), and duplex (2205, 2304, LDX 2101). The super-austenitics are highly alloyed for exceptional corrosion resistance, but traditionally exhibit very poor weldability due to their solidification as primary austenite. Alloy 304L is a low carbon version of the standard 304 (18-10) stainless steel, used to avoid sensitization during welding. Alloy 301L is a slightly lower alloy (lower cost) replacement for 304L, with reduced corrosion resistance, and alloy 201L is a low cost (high Mn) replacement for 301L. Alloys 316L and 321 are different variations on the 304L grade, where 316L contains molybdenum for improved pitting resistance, and 321 is stabilized against sensitization with titanium. Alloy 2205 is the standard grade of duplex, and 2304 is a low molybdenum version of 2205. LDX 2101 is a lean duplex, containing high manganese as replacement for nickel content.

Each test coupon (30mm x 150mm x 3mm thick) was arc welded between two larger 304 stainless steel plates (150mm x 250mm x 8mm thick) suitable for clamping into the CTW test frame. A single bead-on-plate laser weld was made along the 150 mm direction for each weldability test. Following welding, the weld coupon was cut out for analysis and the large clamping plates reused.

Table 35: Measured Compositions for Investigated Stainless Steel Alloys (in wt.%)

Alloy	C	Si	Mn	P	S	Cr	Ni	Mo	N	Cu	Ti
310	0.046	0.56	0.99	0.012	0.001	25.06	19.36	0.13	0.038	0.1	0.001
904L	0.015	0.35	1.61	0.019	0.001	19.99	23.93	4.4	0.049	1.42	0
254	0.014	0.39	0.55	0.014	0.001	20.04	17.75	6.06	0.194	0.76	0
304L	0.015	0.35	1.74	0.031	0.001	18.15	8.44	0.41	0.069	0.25	0.001
301L	0.023	0.5	1.02	0.024	0.002	17.17	7.18	0	0.122	0	0
201L	0.025	0.39	6.7	0.023	0.004	16.45	4.21	0	0.14	0	0
316L	0.022	0.49	1.7	0.027	0.002	16.82	10.49	2.52	0.043	0.33	0
321	0.039	0.5	1.42	0.025	0.001	17.32	9.08	0.48	0.012	0.37	0.47
2205	0.018	0.38	1.4	0.019	0.002	22.46	5.8	3.22	0.188	0.23	0.003
2304	0.023	0.39	1.46	0.025	0.002	23.2	4.83	0.45	0.116	0.22	0.001
2101	0.025	0.65	5.13	0.019	0.001	21.57	1.56	0.28	0.229	0.3	0

Welding Parameters

All welds in this study were made with a 6 kW carbon-dioxide laser, run at full power at a travel speed of 25 mm/s. The laser beam was focused 1 mm below the plate surface, with a 200 mm focal distance. Welds were made bead-on-plate, through thickness, in a keyhole mode. A mixture of argon and helium (50/50) was used for shielding gas. Coupons were degreased with acetone just prior to welding. It is believed that these parameters provide significantly higher heat input than the minimum needed to achieve full-penetration welds, thus producing a wider bead and a higher propensity for cracking.

CTW Weldability Test

A series of tests are run for a given alloy, each at progressively higher cross-head speeds, until a critical speed is found that produces a continuous centerline crack near the weld mid-length. Critical cross-head speeds were observed over a range between 0 and 1 mm/s for the alloys examined. The CTW test sequence consisted of the following steps:

1. clamp test plate into CTW test frame (500 kN capacity)
2. apply 2 kN pre-load
3. initiate beam and travel 5 mm from edge of plate (parameters given above)
4. initiate strain application (fixed cross-head speed) 32.5 mm after weld start
5. limit cross-head travel to 1 mm or weld stop (which ever occurs first)
6. stop beam and travel at 120 mm weld length
7. remove test plate, cut-out weld coupon for radiography

Crack Detection

Whenever the critical strain rate was exceeded for a given alloy, a continuous crack was normally found to occur along the weld centerline, contained within the weld metal (i.e. not visible at the surface). An exception to this was found with the super-austenitics, where the centerline crack exited both crown and root surfaces. Thus, radiography was routinely used to detect and characterize crack formation for each test. Cracks were routinely found to form near the weld mid-length (either before or after), roughly 30-40 mm beyond the point where strain was first applied, and then grow continuously to different lengths. Cracks initiated sooner for those tests run at higher strain rate.

Development of CTW Test Procedure

The general concept and procedure for operating this test was based upon experience gained from the work presented in this thesis examining the solidification cracking in gas-tungsten arc (GTA) welded aluminum. However, there were notable differences in procedure and behavior observed that are outlined here. The most notable behavioral difference being that cracks did not form instantaneously with strain application, as was the case with aluminum GTA welds. This delay in crack formation regarding the strain application may be related to the at higher travel speeds (50 mm/s) for the same welding power (6 kW), where higher cross-head speeds were required to form cracking. Indeed, in the case of alloy 301L welded using 6 kW, a critical cross-head speed to form a crack was observed to increase from 0.66 to 0.83 mm/s when increasing the welding speed from 16.7 to 50 mm/s.

With higher welding speeds used for laser welding (laser: 25 mm/s, GTA: 4 mm/s), the corresponding time for testing is much shorter (laser: 6s, GTA: 25s). Also, higher cross-head speeds were required (laser: 0-1 mm/s, GTA: 0-0.1 mm/s). This means that with laser CTW testing of stainless steel, higher maximum strains are encountered and, due to a higher elastic modulus, higher loads are generated (up to 185 kN). This resulted in problems with failure in auxiliary welds used to join the coupon to the clamping plates, at the high end of cross-head speed.

To avoid auxiliary weld failure, the maximum cross-head displacement was limited to 1 mm, thus limiting the maximum load to below 180 kN. This means that for the high end of cross-head speed, strain could only be applied for one second (i.e. 25 mm weld travel). It is conceivable that for highly weldable alloys requiring even higher cross-head speeds in order to crack, this limitation in the application of strain over distance may prove unworkable.

Critical Cross-Head Speeds

The 301L weld cross-section with 0.67 mm/s applied cross-head speed (Figure 135) illustrates a typical continuous crack occurring along the weld centerline, contained within the weld metal, and thus requiring X-Ray radiography to be detected.

Weldability Predictions

A comparison of Cr/Ni equivalent ratios for the alloys examined in this study is given in Table 35. Two different formulations for Cr and Ni equivalents have been used: one based upon WRC-1992 [207] and one based upon Hammar and Svensson [208]. The former does not account for the alloying element Mn, which probably does not represent as well the high

Mn alloys 201 and 2101. However, the general trend between the three groups remains the same with the super-austenitics having the lowest ratios and the duplex alloys having the highest.

Figure 135: Weld cross section of alloy 301L for 0.67 mm/s applied cross-head speed.

Table 36: Comparison of Cr/Ni equivalent ratios for the Stainless Steel Alloys in Table 35 ([207] [208])

Alloy	Cr_{eq}/Ni_{eq}- WRC 1992 [207]	Cr_{eq}/Ni_{eq}- H&S [208]
310	1.16	1.22
904L	0.95	0.99
254	1.17	1.33
304L	1.78	1.83
301L	1.65	1.84
201L	2.08	1.93
316L	1.59	1.69
321	1.65	1.84
2205	2.51	2.88
2304	2.95	3.68
2101	3.08	3.16

A diagram comparing the crack-no crack test results for different alloys and CTW cross-head speeds is given in Figure 136. In particular, the location of crack formation is indicated relative to the weld mid-length. It is observed that there is a consistent trend for each alloy, where the crack forms further from the point of strain application with increasing cross-head speed. The bars for each alloy indicate approximately the cross-head speed where the crack forms close to the weld mid-length. Cracks formed at the lowest cross-head

speeds for the super-austenitic stainless steels (0.3-0.4 mm/s), reflecting upon their poor weldability. This agrees with welding practice, where stainless steels with equivalent Cr/Ni ratios less than 1.48, solidifying as primary austenite, have been found highly susceptible to solidification cracking. Note the exceptionally good behavior of the 301L alloy among the austenitic stainless steels.

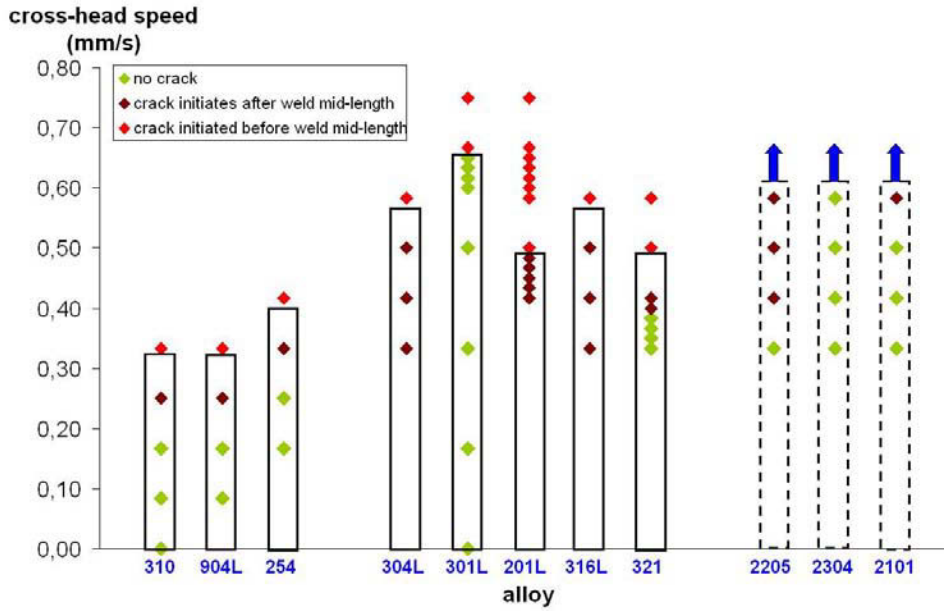

Figure 136: Comparison of CTW test results for super-austenitic, austenitic, and duplex stainless steels showing observed solidification cracking behavior varying with applied cross-weld deformation rate (i.e. cross-head speed).

Summary

Adapted to stainless steel laser welds, the CTW test enables a ranking of the alloys regarding their susceptibility to cracking. Results reveal the austenitic stainless steels to have the highest solidification cracking susceptibility, in accordance with the literature data. However, measurement of local strain rates is still required to characterize the local straining conditions around the moving weld. Moreover, a new sample configuration is required to enable higher loading ability without failure in auxiliary welds, and to permit longer welds for higher welding speeds, because of the delay in crack formation compared to cross-head speed application.

List of Figures

List of Tables

Publications

N. Coniglio and C.E. Cross (2006). Characterization of Solidification Path for Aluminum 6060 Weld Metal with Variable 4043 Filler Dilution. *Welding in the World*, IIW-1755-06, **50 (11/12)**: 14-23.

N. Coniglio, C.E. Cross, Th. Michael, and M. Lammers (2008). Defining a Critical Weld Dilution to Avoid Solidification Cracking in Aluminum. *Welding Journal* **87 (8)**: 237s-247s

N. Coniglio and C.E. Cross (2008). Weld Parameter and Minor Element Effects on Solidification Crack Initiation in Aluminum. In: Hot Cracking Phenomena in Welds II, Springer: 277-310.

C.E. Cross and N. Coniglio (2008). Weld Solidification Cracking: Critical Conditions for Crack Initiation and Growth. In: Hot Cracking Phenomena in Welds II, Springer: 39-58.

N. Coniglio and C.E. Cross (2008). Effect of Cooling Rate and Silicon Content on Solidification Path and Phase Constituents in 6060 Aluminum Castings and Weld Metal. In: Proceedings of the 11th International Conference on Aluminum Alloys, Wiley-VCH: 1889-1896.

N. Coniglio and C.E. Cross (2008). The Role of Hydrogen in Aluminum Weldability: Mechanisms for Solidification Crack Initiation and Growth. Submitted to *Met. Trans.*